BEDROCK TO SOIL:

IN-SITU MEASUREMENT AND ANALYTICAL TECHNIQUES FOR INITIAL WEATHERING OF PROGLACIAL ENVIRONMENTS

by

Karsten Leopold Lorentz

A thesis submitted to Victoria University of Wellington
In fulfillment of the requirements
in Geology for the degree of
Master of Science

February, 2019

School of Geography, Environment and Earth Sciences

A debt of gratitude:
To Kevin Norton for the coffee+bike rides,
Brian Anderson for coding assistance+lessons on bush navigation,
and the both of them for their superb academic support, logistical facilitation, and calm insight.

Special thanks to:
Huw Horgan-Coding and bike rides
Lauren Vargo-Coding and bike rides
Darcy Mandeno-Bike rides
Ross Whitmore-Chats about everything
Aidan McLean-Rogaine Adventures
Ben Nistor-Alpine distractions and infallible friendship
Ricardo Delgado-Abrazos muy fuerte
Schewart Cunningham-Laughter and pork buns
All the office mates-Gelato adventures
Jeff Lee-Relentless banter
Conor Neilson-More games than you can shake a stick at
Natasza Lorentz-Commiseration and Exercise Challenges
Will McGuinness-Helping me get here

Dedicated to my mother and father, Dr. Alexandra Lewis-Lorentz and Casimir Lorentz, for introducing me to the wonders of the natural world and the power of observation with a scientific mindset.

"It only takes two points to make a line…"
-Ross Whitmore

Bedrock to Soil
Karsten Leopold Lorentz

FULBRIGHT NEW ZEALAND
TE TŪĀPAPA MĀTAURANGA O AOTEAROA ME AMERIKA

Victoria UNIVERSITY OF WELLINGTON
Te Whare Wānanga o te Ūpoko o te Ika a Māui

I. Abstract

Dirt. It is more important than one might think. Soil, along with its bedrock-derived components, provides a nexus in the earth system for energy, nutrient, and atmospheric control; yet it is a finite resource. Soils are consumed, transported, and replenished by natural and anthropogenic forces. Weathering—both physical and chemical—is the key process breaking down and regenerating the ions and mineral constituents of soils, facilitating the pathways from solid bedrock to soil to the rest of the global ecosystem. Yet our understanding of weathering is incomplete and the available methods to investigate these processes are limited. Here, the fundamental processes of weathering are questioned by studying them at their origins, the rock surface. New techniques were developed in pursuit of quantifying weathering at small scales in-situ, to obtain the highest resolution measurements possible. These were carried out in the proglacial regions of two New Zealand glaciers, Brewster Glacier and Franz Josef Glacier.

Proglacial bedrock environments provided a clean-slate model from which to measure incipient weathering at increasing exposure ages. To mitigate error, a holistic approach encompassing weathering signals from multiple angles was taken. Spatial characterisation was completed through the capture of structure-from-motion photogrammetry (SFM) at multiple scales of observation. The resultant three dimensional surface models had an average error of 1.06×10^{-1} mm. The models were characterised for weathering using roughness as a novel multi-point analysis of surface features, through two separate novel methods utilising global polynomial interpolation filtering and continuous wavelet transform analysis. Physical samples were collected from the field for cosmogenic radionuclide surface exposure age dating. Compositional analysis was performed through X-ray fluorescence, as well as electron microprobe analysis (EPMA). Nano-scale structural and compositional trends were investigated through optical analysis of backscatter electron imaging and secondary electron imaging.

Non-directional roughness and volumetric analysis patterns present compelling information to support negligible weathering occurring on bedrock surfaces in

proglacial environments. Lithologic variation was identified as a strong influence on the results. Compositional analysis demonstrated insignificant levels of chemical alteration between sites, corroborating the spatial modelling results. The lack of surficial weathering in highly productive weathering environments necessitates the role of additional weathering factors. Deep subsurface weathering was investigated and presents the strongest case as a major contributor to chemical denudation. Validating the presence of deep weathering in many environments critically alters the knowledge required to evaluate and predict patterns of landscape evolution. By establishing a better understanding of how bedrock weathers in-situ, the groundwork is laid for making more accurate and educated forecasts on how the earth system will respond to changes in the future.

II. Table of Contents

III. List of Figures

IV. List of Tables

1. Introduction

The world we live on is the most complex and interconnected system yet known in the observed universe (Ward and Brownlee, 2000). The earth system as an interconnected set of components, controls the way in which the world is shaped around us, and no single piece is independent of the others. The breakdown of specific minerals from bedrock influences everything from plant growth to oceanic phytoplankton proliferation and global climate regulation through facilitated atmospheric carbon dioxide reduction (Raymo et al., 1988; Siever, 1991; Drever, 1994). Silicates are one class of such minerals, which are present in many rocks around the world, and whose behavior has large potential impacts. The fate of these silicates is a crucial component to maintaining the balance of the earth system, though there is still uncertainty surrounding how these minerals are liberated and introduced into the environment (White, 2008). By establishing a better understanding of how bedrock weathers in its natural environments, the groundwork is laid for making more accurate and educated forecasts on how the world will evolve in response to changes within the system.

It should be stressed that soil is an ecosystem, an organic world that is a link in the nutrient cycle of the earth (Raich and Schlesinger, 1992). It takes a long time to form and can indeed develop to facilitate bountiful life. Yet we have discovered that this life yielded by fertile soils in turn plays a huge role in steering the subterranean environment of available nutrients and minerals (Baumeister et al., 2015).

As defined by National Research Council's Committee on Basic Research Opportunities in the Earth Sciences, the Critical Zone is the "living, breathing, constantly evolving boundary layer where rock, soil, water, air, and living organisms...regulate the natural habitat and determine the availability of life-sustaining resources" (CZO, 2018).

The primary purpose behind establishing the Critical Zone was to design a tool which would facilitate interdisciplinary collaboration on research within the scientific community. This incorporates a coalescence of multiple fields, and ultimately draws upon intellectual perspectives from each area to establish a complete and holistic understanding of the processes under investigation (Brantley et al., 2007). The resources available through this network often lead to conclusions that are impossible to obtain while operating through the lens of a single field.

Currently, there remains great uncertainty surrounding the mechanisms which dictate soil erosion and landscape evolution (Herman and Champagnac, 2016; Willenbring and Jerolmack, 2016; Norton and Schlunegger, 2017). This is not aided by the sparse number of available methods for measurement (White, 2008). The production of soils is fundamentally controlled by weathering, where the breakdown of rock enables soil development (Heimsath et al., 2012). Weathering is divided into two principal categories: physical and chemical. Physical weathering is the mechanical breakup of material into smaller constituent components, while chemical weathering is the process of geochemical ion exchange and mineral dissolution as a result of compositional properties. Physical weathering produces increased surface area for chemical weathering to occur, facilitating mineral availability. The two processes jointly promote soil development over a wide range of environments, relying on their combined forces in various roles of dominance to develop landscapes. Influences can vary from up to 45% of material transport load due to chemical weathering, to the other end of the spectrum with more than 90% from physical weathering (Berner and Berner, 1996). The former occurs in mild landscapes such as low fluvial plains with minimal topographic relief and high residence time of water and material, with the latter physical-weathering dominated regime in regions of high topographic relief such as the Himalaya (Berner and Berner, 1996).

Elucidating the nature of how weathering processes have acted over time, and their behavior in the present moment, is essential for metering the changing

environments of the world. It is crucial for generating predictions as to how the world will respond to changes in the future, and determining what responses will be towards managing resources. Unfortunately, there are few accurate methods for measuring these processes (White, 2008). The primary issue within the quantification of weathering rates is that all of the compound variables in a select environment must be accounted for. There are many factors governing these processes—such as broad-spectrum biogeochemical interactions of plant responses to the environment—of which many are third order and contain further variables themselves. The signals are extraordinarily complex and ultimately are typically ignored in favor of an idealized system. There are inherent flaws in this, which must be addressed to obtain more accurate data.

In order to approach this problem from a new perspective, research from the fields of geomorphology, computer science, and mechanical engineering are utilised as the basis for development of novel analytical research methods (Rosso, 2001; Raja, 2002; Krizbergs, 2006; Tingbo, 2012; Miles et al., 2017). The methods developed are designed to operate independently of environmental variables by selecting against them in field areas, and employing model parameters that successfully account for them, which promotes higher confidence in field tests.

Long term trends of chemical depletion have been studied in great detail to elucidate the nature of weathering over thousands and millions of years (Pavich, 1986 ;Stonestrom et al., 1998; White et. al. 1998). Yet very little is known regarding short term trends and mechanisms for weathering. Studies into the first stages of solute genesis, or incipient weathering, have been completed and begin to elucidate the nature of chemical alteration within soils and bedrocks (Dixon et al., 2005; Amusan, 2009; Baumeister et al., 2015). White and others (1998) reviewed several weathering measurement techniques, yet were unable to generate compelling results with statistical significance above dataset variance, citing a lack of precision in data and a need for more accurate measurements. Though nearly two decades ago, the lack of techniques is still apparent. In 2012, P.J. Kelly investigated the

behavior of rock strength during incipient weathering, and despite modern techniques was unable to draw correlations between rock strength and the degree of chemical alteration in the minimally weathered rocks studied (Kelly et al., 2012). Numerous other studies such have been performed to simulate weathering environments and processes in laboratory settings (Wright et al., 1998; Anderson et al., 2000; White and Brantley, 2003; Smith et al., 2005). Theoretically a laboratory reproduction of weathering conditions could selectively compensate for external forcings, and produce more accurate results. Despite the wide variety of approaches, there is a large disparity in weathering results between the experimental values and recorded field measurements (Anderson et al., 2000; Smith et al., 2005; White and Brantley, 2003; Wright et al., 1998). Ultimately, even for small scale weathering in the most isolated regions possible, there are an excessive number of variables that are impossible to comprehensively simulate in a laboratory environment. While extraordinarily useful for the relative study of mechanisms, the difference in applied contextual processes is too great between experimental weathering reactors and field environments to directly extrapolate to natural processes.

A potential solution to help bridge the chasm of observational scales would be an intermediate environment with a compromise between basin-scale and isolated-reactor levels of variables, within which to measure weathering rates. The primary focus of this thesis is to develop and implement a novel method of in-situ weathering rate quantification by combining existing proven methods in such a way as to eliminate the maximum number of naturally occuring confounding variables. With the joint application of structure from motion photography, volumetric modelling, roughness frequency analysis, and tailored glacial field areas, this study generates the potential for more accurate surface characterisation and weathering rate calculations in geomorphology.

1.1. Applications

Weathering rates are the elusive yet often sought after measurements in the field of geomorphology. The pace of weathering shapes our world. Exhibiting strong controls on landscape evolution dynamics, accurately measured weathering rates for different environments are key components for all landscape evolution models. While relatively simple to conceptualize, weathering rates are notoriously complex and challenging to quantify (Oleschko et al., 2004; Moses et al., 2014). The ability to determine a specific weathering rate requires a mechanical understanding of the various active weathering processes, as well as their roles in responding to multiple system inputs and relative impacts for system outputs. With the added complexity of lithology, biogeochemical interactions, and foreign matter introduction such as dust flux, it becomes nearly impossible to make accurate measurements which exceed their cumulative error. Current methodologies of measuring weathering rates often fall short of accounting for all of these factors.

1.1.1. River Load Proxy

Measurement of dissolved and suspended loads in hydrologic systems is one of the most prevalent methods of acquiring general weathering rates. The river load, commonly equated with landscape weathering flux, is the combination of solids being physically transported at all scales and the concentration of total dissolved solids measured in mass of minerals per liter (J. Gaillardet et al., 1999). Interestingly enough, to cut down on independent variables these models often ignore the mass of sands transported along the river bed despite the fact that they constitute up to ten percent of river load (Milliman, et. al., 1995). There are two primary points that prevent this model from establishing comprehensive weathering readings. First, this method assumes that the dissolved load at any point in the river represents the cumulative upstream weathering output. This prevents the scale of observation at a given point from being any more precise than the entire drainage basin upstream of the sampling site. Due to this, it is very difficult to distinguish the effects of local variations in slope, elevation, and bedrock morphology on weathering rates. The calculated rate must be averaged over the whole basin, which

will generate inaccurate rates on both ends of the spectrum. Secondly, the model assumes that the volume of dissolved load in the stream originates from the bedrock studied, which often is not the case. Plants, pollutants, and foreign introduced materials often comprise a significant portion of measured river loads (Milliman, et. al., 1995).

1.1.1.1. Anthropogenic Influence

When utilizing this technique of weathering rate calculation from river dissolved loads, there is an ever-shrinking limit on data accuracy over scales due to anthropogenic forcings. In any dissolved-load and discharge measurements taken downstream of an area that has seen human interaction, the mineral and nutrient content are likely to have non-natural inputs to the system from fertilizers and agricultural products, which would artificially boost the relative concentrations measured (Mendiguchía et al., 2007). Often, water use by humans has a significant impact in reducing the discharge of a river due to increasing residence time by diverting for agriculture and storage. This increases the concentration of dissolved and suspended load relative to the volume of water observed. For example, the modern discharge of the Nile, 0.3 $km^3\ yr^{-1}$, is over seven orders of magnitude less than its natural discharge of 83 $km^3\ yr^{-1}$ (Gaillardeta et al., 1999). The impact on water quality due to this reduction is astronomical in magnitude.

1.1.1.2. Aerosols

When using weathering products to calculate a volume deficit and reconstruct original environments, it is often inaccurate to assume that 100% of measured materials are sourced from the target area. This is often the case in the widely applied concept known as steady-state soils equilibrium. Steady-state equilibrium proposes that for a given drainage basin, the measure of local bedrock eroded should be equal to the material flux both solid and dissolved of the hydrological system leaving the basin. Unfortunately, this does not account for introduction of foreign materials such as rainwater chemistry, nor does it consider weathering

products transported by non-hydrological processes such as aerosolized dust (Durand, et al. 1991; Jacobson et al., 2003).

In populated areas, anthropogenic contamination due simply to airborne pollutants can account for over seven percent of dissolved load in rivers (Roy et al., 1999). However, atmospheric pollutants are present in most locations around the world and in varying environments. Rainfall chemistry of a mountainous area in southern France was shown to be significantly affected by three main factors: long-range pollutants, aerosolized sea-salt, and aeolian dust from a desert more than one thousand kilometers away (Durand, et al. 1991). Any of these as a single source of contamination would have strong influences on weathering calculations if not carefully accounted for. Each of these externally introduced aerosols are not limited by proximity to their sources, and can indeed have profound effects on environments from a great distance regardless of topographic relief. It is possible to recognize and largely compensate for these factors, yet the sheer number of and complexity within each introduced variable presents a challenging case for maintaining acceptable values of error.

These trends of foreign atmospheric inputs perpetuate to most environments around the world, and the study sites chosen for this research are not an exception. Local to the region studied, research completed by A. D. Jacobson and others (2003) presented the case that meteoric inputs have a dramatic impact on measured dissolution rates. It was found that rainwater contribution to stream water dissolved ion loads can account for nearly ten percent of measured silicate flux and up to between fifty and one hundred percent of major cation concentrations (A. D. Jacobson et al., 2003). With these dissolved load signals interfering with the major traditional methods of quantifying weathering rates, it is essential to have strong controls and understanding of all system inputs to generate strong correlations within models.

1.1.2. Soils Weathering

The other main approach to determining chemical weathering rates is through mass balance considerations in the weathered regolith itself (Riebe et al., 2003). This method relies on the relative enrichment of immobile elements, such as zirconium, in weathered regolith due to mass loss of relatively more mobile elements. While long-term trends in weathering have been addressed with this method (Riebe et al., 2001; Norton and von Blackenburg, 2010; Dixon et al., 2009; among others), the method relies on an assumption of steady state. As such, the derived weathering rates average over long time-scales, with associated long response times (Norton et al., 2014). Making direct inferences about how changing climate will affect chemical weathering rates is therefore challenging.

Not only are weathering rates challenging to quantify, but the resultant values are extremely difficult to partition and attribute to specific weathering processes. Taking into consideration lithology, climate, precipitation, and landscape morphology characteristics, it is still a very difficult task to determine whether physical or chemical weathering is responsible for the dominant forcings on landscape evolution. How does one simplify the equation to control as many variables as possible? How can the outputs of a system be accurately quantified, and attributed to specific processes? The ability to understand and differentiate the dominance of multiple weathering processes is critical to interpreting, understanding, and projecting the way an environment functions and responds to changing inputs.

It is clear that new methods of analysis are needed to accurately characterise the nature of weathering in most environments.

1.1.3. Weathering Without Soil

The presence of soil is a requisite factor most weathering measurement techniques. There are already many thoroughly tested quantitative approaches to characterizing natural chemical weathering rates in evolving landscapes, yet the vast majority of them rely on solid or dissolved mineral distributions across a landscape with developed soil horizons (A. White & A. Blum, 1995; S. Anderson et al., 1997; J. Gaillardet et al., 1999; S. Anderson et al., 2000; R. Anderson, 2002; A. D. Jacobson et al., 2003; A. White, 2008). Soil pit analysis with depth, solid mass transfers, and steady state soils examination all require a soil-mantled environment—even within very young studies (<150a) (Mavris et al., 2010). The moment a chemical weathering study steps up and out of regions with extant regolith, numbers of available methods for quantification are dramatically reduced.

1.1.4. Minimising Variables

Employing Occam's Razor, the best results are likely to come from the least complex solution. A way of simplifying the methods is to eliminate as many variables which need compensation as possible. Calculating weathering rates using a medium which is impervious to external material flux would be a large step in the correct direction. Studying material loss in-situ from bedrock is an elegant solution, as 100% of the studied material is present in the source. If studied along a weathering transect starting with a sample with little to no weathering as a reference, quantitative measurements of difference should be relatively simple to extract. Glacial basins present an attractive case for field sites, as their endemic geomorphic processes generate these precise conditions in proglacial areas.

Following the same principles, observational scale often presents great challenges for obtaining accurate results. As seen with dissolved load analysis, results must be averaged over large areas which are composed of different materials in various stages of weathering. As both physical and chemical weathering operate on scales as small as the crystalline level, reducing the window size for analysis should not

produce any functional issues (Turcotte, 1995). The fresh bedrock exposed in the wake of a retreating glacier presents the optimal conditions for analysis on a centimeter scale. At this size and substrate, variables such as solute residence time and biogeochemical contributions can be ignored as there is no soil present to act as a sink, or facilitate ion transfer catalysing unexpected reactions. This leaves us free to explore the few remaining factors which control weathering of bedrock surfaces, such as time, lithology and morphological characteristics.

Small scale precision measurement techniques of weathering are currently extremely limited. One example is the use of a micro erosion meter, which offers increased precision over other methods which utilise optical determination with a clear plastic ruler (Stephenson, 1996; Nicholson, 2009). Having the ability to measure the evolution of a surface in situ with little to no destructive sampling would open doors to increase the accuracy of all calculated weathering rates. Results may be scaled up for improvement in larger scale measurements, and calibrated against existing measurement techniques, allowing empirically backed solutions to be proposed for some of the great landscape evolution questions of our time.

1.2. Aims and Objectives

The research conducted for this thesis aims to closely investigate the greater question of how rocks weather in alpine settings, by understanding the various active weathering processes at their point of inception. This is pursued from a quantitative standpoint, in an attempt to approach these ideas with an empirical perspective. The developed methods should provide the highest accuracy of data—which is crucial when dealing with such small measurements.

It is recognized that surface roughness plays a role in affecting the magnitude of weathering processes, but it is yet unclear as to precisely what defines roughness or how this functions in the greater context of landscape evolution within the earth system. The active weathering processes studied will be cross examined with

surface characteristics to elucidate what relationships they have to terrain morphology as expressed by roughness.

In the following thesis, weathering processes and surface roughness are investigated through a novel technique which aims to generate accurate quantitative measurements of each in a non-destructive and cost-effective manner that will prove complementary to existing measurement techniques. The data gathered from this method will in turn be analysed using novel combinations of currently employed techniques, with the hopes of proofing and presenting an additional viable method of research analysis for use in the field of geomorphology.

Changes through time in weathering rate and active processes within proglacial environments are studied. Analysis is performed through the development and application of new micro-scale structure from motion photogrammetry techniques along with novel weathering feature analysis utilising global polynomial interpolation filters and wavelet transform analysis. Geochemical characterisation of the bedrock links patterns in roughness to changes rock chemistry, providing evidence for regional weathering behaviors.

2. Field Sites

Glacial bodies act as powerful erosive forces capable of resurfacing massive areas and driving landscape evolution at an incredible rate. The erosional potential that glaciers exert upon bedrock surfaces, functions as the reset button of an atomic clock for the weathering system as measured though cosmogenic radionuclide surface exposure dating. Prior to glaciation, a given location will have characteristics and exposure ages that temporally contextualize the samples. Present not only on the surface, but often at depths up to 10cm, these characteristics will produce signals overlapping from multiple periods of history, adding complexity to the process of age determination (Wieler and Graf, 2001). Glacial bodies, unlike most other erosional forces, operate at magnitudes where entirely erasing such signals is a trivial matter. Similarly, in order to calibrate observations of physical surface variations, an ideal example of the original surface prior to weathering must be locally observed. For outcrops of great exposure ages, it is nearly impossible to definitively declare what the original surface morphology was prior to weathering. Yet at the base of an actively retreating glacial body, clean slate surfaces are continuously being exposed, and serve as excellent outcrops to calibrate against as zero age surfaces.

2.1. Why New Zealand?

The study of in-situ initial weathering processes could theoretically be done anywhere, yet New Zealand was chosen as the host country for this research. As one of the few geographic locations with easily accessible sites experiencing active glaciation, NZ is a particularly attractive field study location. The morphology of New Zealand's Southern Alps, Ka Tiritiri o te Moana, is famous for its jagged ridges and highly prominent peaks created by relatively weak lithology and exposure to the aggressive climate of the Tasman Sea. This supplies evidence of high weathering rates, which are a favorable condition for study in real time. Further, within the context of chemical weathering and soil development, the exceptionally clean air circulating in the low-mid latitudes of the southern

hemisphere impart a uniquely sterile atmospheric environment for New Zealand, particularly when compared with glaciated regions in the northern hemisphere (Schwikowski, 2004).

2.2. Why Glaciers?

In order to address the research question with sufficient precision, the investigation was conducted with an emphasis on preservation of detail. The capture of high resolution observations begins with quality field sites, which need to be chosen carefully. Above all, two basic factors remain most important for accurately measuring weathering rates. For one, in order to measure the amount of material removed from a given surface, we need to know what the surface morphology would have been at the time of initial exposure. This is to say that we must have a "start point" from which to compare all the other subsequent samples. Very few geomorphic agents act in this way, and on the timescales necessary to produce a young enough start point or origin of weathering. Secondly, in order to accurately measure the rate of material removal it is necessary to have at a minimum three data points along a temporal transect. Two data points are needed to calculate a span of time with a start and end date, and additional points function to define changing rates in more detail. This requires a field site that has active mechanisms which can guarantee a succession of easily identifiable relative exposure ages to ensure proper initial sample collection. Glaciers, as extremely powerful geomorphic agents, fill this niche perfectly. As glaciers retreat, they expose freshly eroded bedrock at a measurable rate. So long as the glacier studied is still active, and conditional upon lithologic continuity, the region directly adjacent to the present ice margin should accurately represent the original surface structure of the older exposures serve as a "start point" to back calculate volumetric deficiencies.

In addition to this pair of key factors, there were many other requirements to take into consideration when choosing field sites. In order to reduce the complexity of data processing, it was necessary to have field sites which did not exhibit multiple signals of weathering processes. This includes both the agent and the substrate. A

field site that is heavily vegetated and full of active fauna is likely to have overabundant weathering signals prohibiting accurate interpretation on such small scales. Sites which vary too much in compositional character and lithology along a transect are certain to have compounding variables affecting relative weathering rates due to bedrock chemistry and hardness. On a similar note, a field site needs to have the capacity to provide a transect of sampling venues at relatively even intervals with exposed bedrock. If parts of a site are buried under sediments, shielded from cosmic rays, or unavailable for sampling due to complex topography, they will not be able to provide the necessary research materials for the study. Once again, the erosional capacity of glaciers facilitates this by providing a proglacial environment typically devoid of vegetation and developed soil horizons. Lithologic variability is solely controlled by regional site selection.

2.3. Why These Glaciers?

Brewster Glacier and Franz Josef Glacier made it into the running for potential field sites because they fill the vast majority of the aforementioned criteria. Each site has a relatively continuous lithology, presents sampling venues at regular intervals along a clear transect, and does so at a consistent slope which is reproducible at each sampling site. Both Brewster Glacier and Franz Josef Glacier were ultimately chosen above the rest of the available field sites due to their ease of accessibility; academically, logistically, and financially. Each field site had been visited by scientific parties in the past for multiple investigations. As such, there was supplemental information available for familiarization with the area prior to arrival. Logistically, each field site had well documented and established means of access, with each having suitable locations and adjacent facilities for helicopter travel. Brewster Glacier had the added convenience of a Department of Conservation hiking track leading to the vicinal peak of Mt. Armstrong, affording travel on foot to the field site in favorable conditions. Financially the two selected field sites were made very attractive with the advent of simultaneous adjacent research being conducted by other research faculty, which fostered collaboration and support for

the project through sharing utility costs as well as assisting with sample and field data collection.

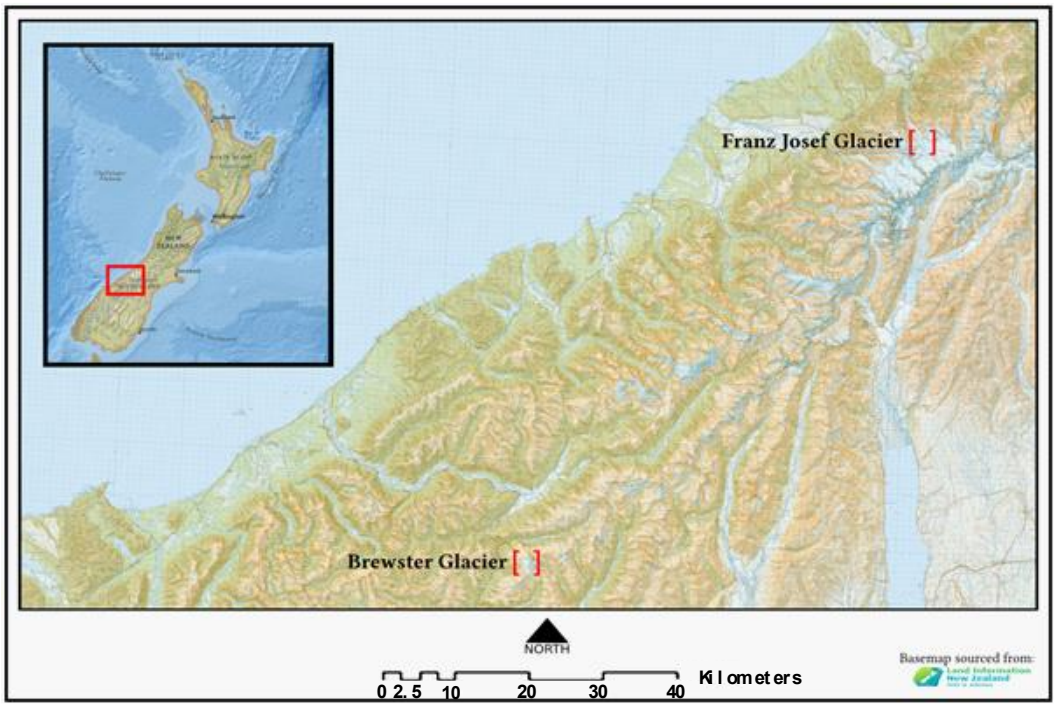

Figure 001
Topographic map showing relative position of the two field sites studied, Brewster Glacier and Franz Josef Glacier, with inset map providing context for main map extent.

This combination of factors presented Brewster Glacier and Franz Josef Glacier as the most logical choices for field sites. However, neither site was without its drawbacks. The lithology at each site contained greater levels of variability both locally and across the transect than desired. The research parameters originally designed favored ideal geologic conditions such as uniform rocks with little to no lithological or structural variability between sampling sites along the transects chosen. Unfortunately the ubiquitous country rock of New Zealand is greywacke, a metasedimentary rock with local variability in metamorphic grade, mineralogical composition, and a penchant for complex structural fabric (Figure 002).

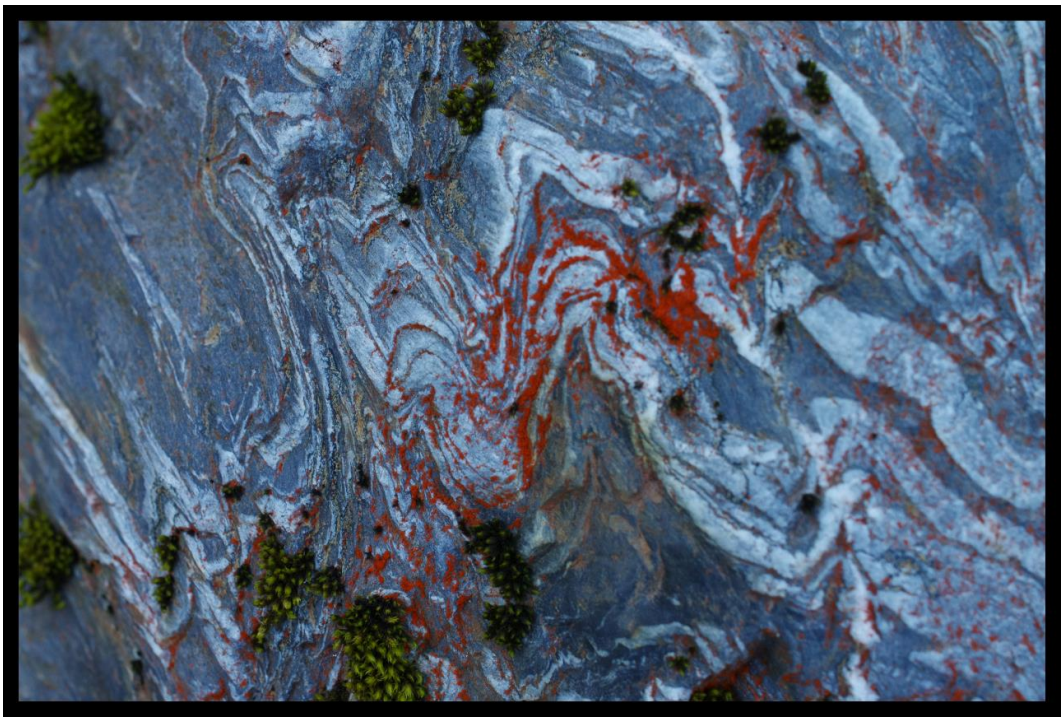

Figure 002

Metamorphically altered bedrock at Franz Josef Glacier. Structural foliations and crenulations are visible throughout. Photo capture area is approximately 60cm^2.

Additionally, the conceptual model for this research was initially developed for sampling along the low-angle centerline of the glacial valley which would allow for uniform sample collection and function to eliminate additional weathering signals generated by variations in slope and aspect. Utilizing samples along the centre and base of the proglacial area would theoretically create a direct correlation through proxy between distance along the recession track of the glacier terminus and sample age. Ultimately, due to the terrain caused by the aggressive erosional nature the vast majority of New Zealand glaciers possess, few to no glaciers exist with exposed bedrock along the central channel as their excessive sediment loads immediately fill the proglacial area with till. This issue was addressed by selecting transects along the hillslope perpendicular to glacial flow. By applying this sampling method, the relationship between sample age and distance along a vector of glacial retreat can be preserved. This functions well by correlating glacial retreat

as a function of volumetric deflation and mass balance measured by vertical relief rather than longitudinal regression.

2.4. Brewster Glacier

Forty two kilometers East from where the mouth of the Haast River opens into the Tasman Sea, Mt. Brewster and Brewster Glacier cap the northwestern corner of the Young Range of New Zealand's Southern Alps, Ka Tiritiri o te Moana. Extending forty five kilometers to the south and covering a land area of approximately 82,000 hectares, the Young Range sports dozens of peaks of which Mt. Brewster is the most prominent at 2,516 m above sea level (ASL) at its summit. Cradled in the hanging valley just below and to the southwest of Mt. Brewster sits Brewster Glacier. With an average elevation of 1700 m and a small set of glacial lakes at its base, the glacier is a perfect location for retreat sampling along its exposed bedrock flanks.

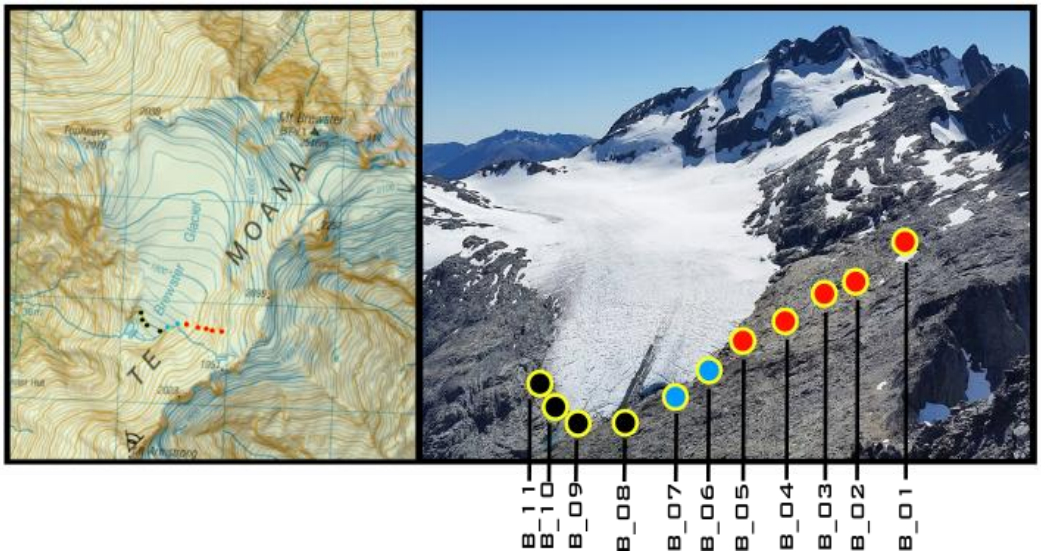

Figure 003
On left: Brewster Glacier field site and sampling areas located on hybrid NZ topo50 (sourced from Land Information New Zealand; LINZ) and terrain DEM. Grid square overlay is 1 kilometer per side. Multi-colored circular markers denote sampling sites as referenced by GNSS. On right: Oblique photograph taken from Mt. Armstrong overlooking the Brewster Glacier field site. The sampling transect

is demarcated by multicolored circles corresponding to individual sampling sites. Red circles indicate a site with SFM modeling and physical sample collection, with processing for cosmogenic radionuclide dating. Blue circles indicate a site where SFM photography was collected, but no cosmo dating has been undertaken. Black circles indicate sites where samples were collected, but no SFM imagery was captured.

2.4.1. Geologic Setting

The entire range of the Southern Alps is part of the Haast Schist formation (Rattenbury et. al. 2010). Permian to Jurassic in age, the lithology of the Brewster Glacier study site sits specifically within two of its members known as the Torlesse Composite terrane and the Rakaia terrane (Rattenbury et. al. 2010). Bordered on its western edge just thirty kilometers away lies the great Alpine Fault. Rocks from the Rakaia terrane become increasingly deformed and metamorphosed as they near in proximity towards to Alpine fault (Rattenbury et. al. 2010). Mt. Brewster and the Brewster Glacier catchment lie within zone IIB of this deformation, as classified by the Institute of Geological & Nuclear Sciences. Composed of foliated sandstone and mudstone schist, this region of the Haast Schist is bordered to the east by the Dingle Fault and the Barrier Range, which contain the un-metamorphosed parent rock of the Young Range: undifferentiated sandstone and mudstones with rare mafic igneous rocks (Rattenbury et. al. 2010). Within the region of study, this parent rock is metamorphosed to psammitic and pelitic semi-schist and greyschist, punctuated by small areas of metavolcanics, conglomerates, and chert.

2.4.2. Glacial Setting

Brewster Glacier resides in a hanging valley at the base of Mt. Brewster. Sitting 40 kilometers inland of the west coast, roughly 30 kilometers of mountain ranges which make up the westernmost flank of the Southern Alps sits in this space and shields Brewster Glacier from some of the more intense weather systems. Unlike many of the alpine glaciers in Southern Alps, Brewster Glacier is quite slow to respond to local climate. Reconstructed ELAs from snowline photography show a positive mass balance within Brewster Glacier for 21 years of a 38 year study from

1978-2017 (Willsman et. al., 2015). Since 1981, Brewster has been at a stand still with a minor advance in 1990 (Cullen et al., 2017). The glacier flows ~2.5 kilometers south, initially along a south-westerly slope of 31 degrees which grades down to a 10 degree southerly slope for the majority of the glacial body (Cullen et. al., 2017). Extending for less than two kilometers on its longest axis, Brewster Glacier is a relatively small glacier with an associated accumulation basin of around 200 hectares. For the last nine years, the Brewster Glacier terminus has been retreating at an average rate of ~12m/y, and in the years since 1981, the terminus has retreated up valley 365 ± 12m (L. Vargo et. al., 2017). The recent retreat activity of Brewster glacier allows for sample collection and site investigation at the terminus and sampling transects which begin in the wake of the glacier at these newly exposed areas which provide "zero date" samples.

2.4.3. Sample Selection

The sampling transect at Brewster Glacier was selected subsequent to arrival on site, following a local survey on foot. While surrounded on three of its four sides by bedrock exposures, the eastern flank of the glacier was ultimately chosen for sampling. As visible in figure 003, the valley side to the east has a large continuous exposure of bedrock propagating from the eastern lateral edge of the glacier terminus up to the arete which joins Mt. Brewster to Mt. Armstrong in the south. The great extent of bedrock exposure with a westerly aspect at this location presented a strong case for minimal snow cover during the winter months and constant residence times. The terrain is also relatively low angle with regularly spaced terrace-like features parallel to glacier flow, likely a product of the geologic structural fabric and large scale glacial weathering. The repetitive landscape stepping allowed for collection of samples at different elevations and evenly spaced distances from the glacier, with in-situ near zero slope environments, presenting the opportunity to eliminate slope as a weathering factor. Prominent meltwater streams and sheet flow were observed further down section to the south, and staying above them reduced the likelihood of incongruent meteoric water exposure between sites.

Samples were collected from the highest point in the transect and progressing downslope. The altitude and location of the primary sample was determined following the initial site survey, where it was discovered that approximately 25% of the remaining distance up to the arete exhibited signs of glacial scouring from an alternative source. It was observed that there was a small accumulation basin directly below the summit of the arete which appeared to have influenced the formation of a tributary glacier feeding into the Brewster Glacier from the northeast (figure 004). Evidence for this could be seen clear down to the waypoint for the first sample, by means of channels and glacial striations all pointing prominently southwest at about 273°. At this point, in both directions laterally the bedrock showed a ubiquitous change in striation azimuth all the way to the terminus, from 273° to between 055° and 065°, which parallels the direction of glacial flow from Brewster Glacier. Each subsequent bench feature encountered from this point downslope was sampled and photographed, making for seven total points along the transect utilised in this study. The latitude/longitude coordinates of these sampling locations can be found in a table within appendix 9.9.

Figure 004

Image of meltwater lake formed in the small basin of the tributary glacier. Photo taken from the summit of the Eastern ridge along the basin, looking west.

2.5. Franz Josef Glacier - Kā Roimata o Hine Hukatere

Franz Josef Glacier is the second field site chosen, located ninety kilometers northeast of Mt. Brewster and twenty kilometers inland from the west coast. Named Kā Roimata o Hine Hukatere in Māori, or "the tears of Hine Hukatere" from ancient Māori legend. Two lovers, Hine Hukatere and Wawe, tragically caught in an avalanche climbing through the western alps which swept away and buried Wawe. The tears of Hine Hukatere were frozen by the gods cascading down the mountains and formed Te Tai o Wawe, or Franz Josef Glacier. Stemming from the heart of Ka Tiritiri o te Moana (Southern Alps of New Zealand) adjacent to the Tasman Glacier, Franz Josef glacier flows westward towards the Alpine Fault. The studied field area is just to the east of the Alpine Fault, and experiences the metamorphic influences of this proximity. A national heritage site, Franz Josef has been the location of countless scientific endeavors, and its active behavior continues to educate the community on new dynamics of glaciers and environment.

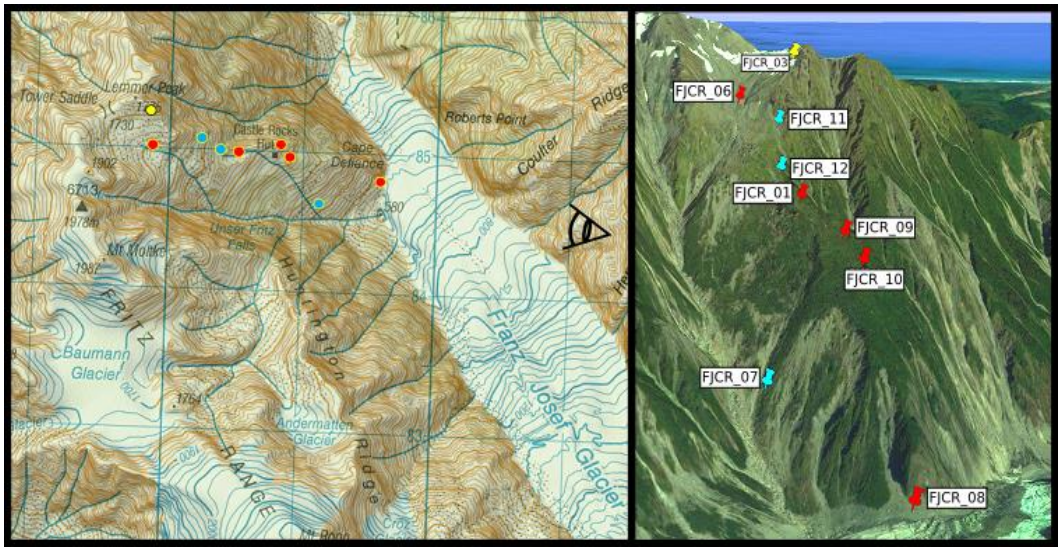

Figure 005
On left: Franz Josef Glacier field site and sampling areas located on hybrid NZ topo50 (sourced from LINZ) and terrain DEM. Grid square overlay is 1 kilometer on each side. Multi-colored circular markers denote sampling sites as referenced by GNSS. On right: Oblique modified rendering of photo-overlay DEM sourced from Google Earth database. Perspective as if captured from Hende Ridge

overlooking the Franz Josef field site of Castle Rocks on Cape Defiance Ridge. The sampling transect is demarcated by multicolored pins corresponding to individual sampling sites. Red indicates a site with SFM modeling and physical sample collection, with processing for cosmogenic radionuclide dating. Blue indicates a site where SFM photography was collected, but no cosmo dating has been undertaken. Yellow indicates sites where samples were collected, but no SFM imagery was captured due to snow cover.

2.5.1. Geologic Setting

Within the Rakaia terrane member of the Haast Schist, the Fox and Franz Josef Glacier Névés are primarily dominated by non-schistose to schistose quartzofeldspathic sandstone ("greywacke") interbedded with siltstone-mudstone ("argillite") of Triassic age (Cox, S.C., et. al. 2007). The area of study is contained within the Almer Syncline, a north-south striking structural feature that parallels the fabric of the Southern Alps along the Alpine Fault. The metamorphic deformation of the Alpine fault generates cleaved sandstone and mudstone semischist rocks within zone IIA of deformation, which is where the field area resides. In the short distance to the western boundary of the unit, lithology briefly shifts to metavolcanic greenschist before transitioning to the curly schist and schist-derived mylonite, cataclasite, and fault breccia that abuts the Alpine Fault boundary. To the east, the unit of study is bordered by the Main Divide Fault Zone and the Malte Brun Range, the lithology slowly grades out to schistose meta-sedimentary units of undifferentiated age.

2.5.2. Glacial Setting

Comprising 6% of the total ice volume within the Southern Alps of New Zealand, Franz Josef glacier extends just under 10.5 kilometers down from the west bank of the Southern Alps, nearly making it to sea level (Herman et al., 2011). The area of Franz Josef is approximately 3500 hectares, making it one order of magnitude larger than Brewster Glacier. The glacier flows northwest on approximately a 23.7 degree slope. The glacier experiences oscillating periods of retreat and advance, and in the recent past has had dramatic advances greater than most regional glaciers.

At its center Franz Josef Glacier flows an average of 2.5-3 m per day (H. Purdie et al., 2014). For the last century or more, the terminus of Franz Josef Glacier has been retreating at a rapid rate. The glacial body and its accumulation basin, as a function of their underlying slope and proximity to the Tasman Sea, are much more responsive and fast-flowing than Brewster Glacier, and have had several extended periods of rapid advance in the last two centuries. These sequences of advance and retreat provide a unique opportunity to study glacier dynamics and bedform interactions, as the repetitive cycles cover, expose, and again subsequently cover the same areas in quick succession. However, in the past 100 years the terminus has moved up valley 3110m ±25m overriding the signal from periods of advancement (H. Purdie et al., 2014).

2.5.3. Sample Selection

Photogrammetric surveys were conducted at previous sampling locations. Equipped with a Garmin 60CS series handheld receiver and 1:50,000 LINZ topographic maps, the previously sampled sites were located through the dense unmarked terrain and photographed for later structure from motion processing. Rough landscapes harkening to the tale of Hine Hukatere and Wawe surround the icy body of Franz Josef. The terrain in this region was considerably more rough than at Brewster Glacier, and the conditions fostered by high angle unconsolidated slopes necessitated technical experience with avalanches, alpine snow travel, steep loose terrain navigation, and knickpoint mitigation.

The primary transect studied at Franz Josef Glacier begins near the glacier base just up valley of Cape Defiance, close to the terminus. Proceeding up the longest unglaciated valley attached to Franz Josef, the sites dot the steeply sloping terrain from the glacial margin (601 m ASL)up to Castle Rocks (1157 m ASL) where there is a brief break in slope to shallower terrain, before again steepening up towards Tower Saddle and the summit of Lemmer Peak (1773 m ASL). As the sites visited were dictated by the provided sample suite, variability of sampling conditions and constraints on local morphology were much more loosely controlled. This

reintroduced several additional environmental variables which would need to be accounted for post-processing, such as slope angle, vegetation, and meteoric runoff flow. The latitude/longitude coordinates of these sampling locations can be found in a table within appendix 9.9.

3. Key Elements of the Proposed Approach

In order to study weathering and roughness of proglacial bedrock in-situ, new methods were needed to conceptualise and quantifiably characterise the ongoing processes. As existing methods largely rely on primary and secondary weathering products, an novel in-situ method was developed to investigate weathering processes at their source. A wide angle approach was made to develop a new method for accomplishing this, with multiple spatial, chemical, and optical analyses to provide overlapping comparative results.

The exploratory nature of the research questions required a combination of traditional analytical techniques with novel applications, as well as new techniques of original design to be employed. This experimental process of developing analytical methods led to a wide variety of approaches, some more effective than their counterparts. Prior to technical explanations of the methodology used, a well-laid theoretical groundwork is necessary to fully understand how the procedures here differentiate themselves from traditional approaches and the motivations behind their selection. The following section provides an overview of the theory and introduction to the methods behind this experimental design.

3.1. Structure From Motion

The underpinning of the entire project, structure-from-motion was the tool of choice for accurately modeling the field areas in a digital environment.

A new tool for high accuracy topographic modelling, structure-from-motion uses automated photogrammetric procedures to identify three-dimensional relationships projected from two-dimensional images. Photogrammetry in its most basic definition is the procedure of making measurements from photographs. The early concepts of photogrammetry were derived from mathematical models such as the coplanarity condition, used in generating scalable maps from aerial photography in the early 1950's and 1960's (Thompson, EH. 1965). By using stereoscopic parallax measurements from overlapping adjacent images, collinearity equations can link spatial data between photographs and calculate relative distances based on field of view (see figure 006). Once paired with known distances such as manually dimensioned landscape features or GNSS markers, the relative relationships between images can yield plentiful and accurate spatial data.

Figure 006
Conceptual diagram demonstrating parallax error used to calculate measurements in the third dimension using overlapping adjacent stereoscopic photography. The proximity of reference objects to the capturing sensor affects the magnitude of the parallax effect. Diagram reprinted from VLR stereoscopic setup, redway3d. Retrieved December 2017, from

http://www.redway3d.com/downloads/public/documentation/bk_ba_stereoscopy.html.

However, calculations such as these were very cumbersome to perform and photogrammetry practices were generally restricted to map making procedures. It was not until much later that new technologies emerged which allowed for precise measurements of spatial features to be made remotely. The three primary methods for generating complex digital models of landscapes are through GNSS mapping, Terrestrial Laser Systems (TLS) and Airborne Laser Systems (ALS) such as Light Detecting and Ranging equipment (LiDAR). GNSS mapping can be extremely effective for crude mapping of remote areas, particularly when determining elevations of road segments. By using a high accuracy Global Navigation Satellite System antenna and continually marking points along a route or transect, elevation data for specific areas can be gathered with precision (Webster and Dias, 2006; Racoviteanu et al., 2007; Hopkinson et al., 2004). Unfortunately, in order to generate higher spatial resolution reconstructions and coverage, the GNSS system must be manually placed where each point is desired, making it a logistically-prohibitive solution to measurement campaigns over large areas. Both TLS and ALS utilize laser scanning technology which incorporates laser range measurements with mobile and stationary receivers to rapidly acquire multiple terrain signals. TLS typically focuses on smaller scale regions as the laser scanners are mounted to a tripod or another affixed location. Using a beam of low divergence and scanning an area within a defined viewing angle, TLS can generate extremely high accuracy models from a single measurement perspective. This is most commonly used to map features at distances of up to eight hundred meters (Vastaranta et al., 2009). ALS operates on similar principles as TLS but over larger areas. Frequently airborne laser systems require a reflecting object to calibrate range measurements with GNSS accuracy and to triangulate the models (Hyyppä and Inkinen, 1999). Having LiDAR equipment mounted on aerial equipment greatly increases the capacity for increased scale measurement while simultaneously imposing restrictions such as resolution and cost. Unfortunately while TLS and ALS are ubiquitously associated with extraordinarily accurate

measurements, their shared characteristic of very high overhead costs makes them a relatively inaccessible technology for many researchers.

Only recently has computational capability become available facilitate the advancement of traditional photogrammetry techniques. The previous issues surrounding multiple-point-calibration of overlapping images have had workarounds developed through complex softwares. Early photogrammetry required intensive camera-calibration techniques to properly orient models, and had to employ strict restrictions on the level of overlap and scale between photos (Chandler ,1999). Structure-from-motion (SFM) is a type of photogrammetry which utilizes complex pixel-matching algorithms to establish relationships in three dimensions from multiple overlapping stereo-photographs (Westoby et al., 2012). Common features shared between photos are identified by software and their positions relative to camera position and capture angle is back calculated to generate accurate models without significant input. There are several different software packages containing algorithms that run SFM calculations, and while they all vary in discreet procedures the overall methodology is the same. A suite of overlapping oblique and/or grid-collected aerial photographs of the target area are collected with consumer-grade photographic equipment. It is best to utilize full-frame and digital single-lens reflex (DSLR) cameras to conserve as much detail throughout the modelling process, however satisfactory results can be obtained in certain situations with lower pixel-count sensors as small as the now ubiquitous smartphone cameras. Thanks to redundant automated calibration and alignment algorithms, the overlap between photographs can be far less to those previously required for photogrammetry. Indeed, a strong characteristic of SFM software is that it can reconcile data from large sets of images which are un-sorted, captured from various oblique perspectives at different scales, and without prior camera calibration procedures. The distortion properties of the lenses used to capture images can be automatically estimated by the software.

In order to generate dimensionally-accurate models reconcilable with the real world, shared markers between photographs need to be physically placed prior to capturing images. These markers are called Ground Control Points (GCPs) and a minimum of three points need to be present in multiple photographs of the target area. For larger regions of interest and models that are destined to be georeferenced with global coordinate systems, these must be placed with high-accuracy GNSS equipment in order to properly triangulate the models.

By matching shared features between overlapping photographs within the image set using a scale invariant feature transform (SIFT) algorithm, as parallax shifts from different viewing angles to determine distance, the common points are assigned coordinates in an arbitrary three-dimensional system. Based on the quality and number of photographs used, a three-dimensional grouping of points otherwise known as a sparse point cloud, will form between 5,000 and 150,000 coordinate points representing the target feature. Following several rounds of recalibration and alignment of the sparse point cloud, the number of points is amplified through a process using novel algorithms developed by Furukawa and Ponce (Furukawa and Ponce, 2010). By segmenting the point cloud into small workable sections called “patches” and using an expansion procedure that works through calibrated multiview stereo (MVS), this patch-based multiview stereo system (PMVS) can increase the number of shared points between overlapping photosets in a computationally efficient manner. A point-count increase by over two orders of magnitude is often yielded while simultaneously reducing error and maximizing accuracy of the image feature mapping. The resultant group of points is collectively referred to as a dense cloud, and within high resolution models consists of between 1,000,000 and 100,000,000 distinct feature points. Point clouds can then be exported in various formats to become three-dimensional models for analysis.

SFM photogrammetric modelling shows promise for being a viable method of remote sensing that can rival the quality of more expensive competitors at a fraction of the price. The fact that consumer grade digital cameras can be used in the stead

of expensive laser-ranging equipment makes SFM financially attainable for many more researchers. A benefit of the lower-technology equipment used for data capture is a reduction of expert technical knowledge required to perform the assessments. Excellent software packages are available with user-friendly formats which eliminate the vast majority of complex calculations otherwise requiring specialist knowledge, such as Agisoft Photoscan, 3D Flow's 3DF Zephyr, Context Capture, Memento, Reality Capture, and Pix4D (Nikolov and Madsen, 2016). The software packages can operate on small systems such as personal computers, though model generation can be greatly expedited through the use of high-performance-clusters. While less complex, expensive, and time consuming compared to other techniques, the accuracy of SFM model outputs does not reflect their ease of acquisition. Westoby and others performed a series of detailed tests to compare the quality of generated outputs between laser systems and structure from motion photography using consumer-grade cameras (Westoby et al., 2012). Their research validates the efficacy of SFM as not only an affordable way to produce results, but also a methodology that produces quality results precise enough to be competitive with more established and expensive systems.

The majority of photogrammetric modelling completed for this thesis was done through SFM in a programming suite produced by Agisoft LLC, known as Photoscan. The outputs of data can be variable depending on their intended use, but for this research all of the models were exported as Digital Elevation Models for further analysis.

3.2. Digital Elevation Model

Traditionally used for modeling landscapes over large areas, a Digital Elevation Model, or DEM, is a two-dimensional representation of a three-dimensional feature. A DEM consists of individual data points that represent specific points in space, as designated by a latitudinal and longitudinal coordinate pair which locate each point on a planar surface. Each of these points are coded with information

about the elevation at their specific location. By assigning a color gradient or greyscale to the elevation data for all the points, a visual depiction of three-dimensional characteristics can be generated. Alternatively, the data can be reorganized as points with three coordinate values (x,y,z) and input into a computer model to digitally simulate a three-dimensional space. This set of coordinates otherwise known as a point cloud, can then be manipulated with various softwares to make precise measurements and calculations.

Point clouds can be used many different ways, with the most common practices being conversion to raster datasets and triangular irregular networks (see figure 007). Raster datasets are used for generating height fields where the points are evenly distributed throughout a grid system and hold their elevation values. Rasters are a convenient way of packaging data in a simplified format that is easy for computers to reconstruct, but often comes at the sacrifice of reducing the complexity of the studied region. Triangular irregular networks are vector-based representations generated by interconnecting every coordinate in a point cloud to all adjacent points without intersecting lines, a process known as Delaunay's criterion (Weatherill and Hassan, 1994). This produces a triangular mesh that reconstructs the physical surface of the studied region. A higher quality triangular irregular network consists of more points and smaller triangles. This is an excellent format for graphically representing a surface with complex topography.

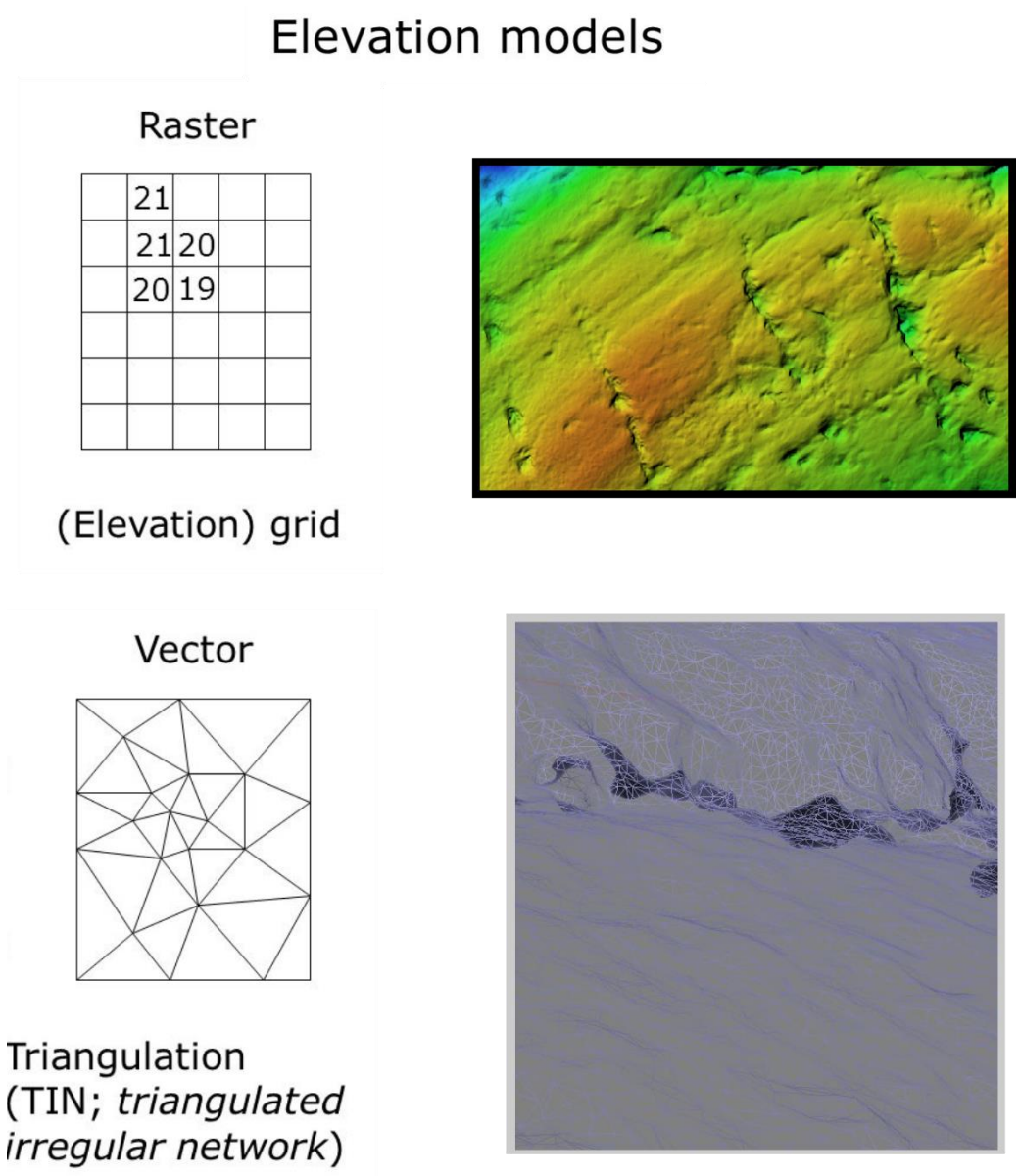

Figure 007
Two common styles of DEM graphical representations overlain on the same dataset from a Brewster Glacier sample. Model (a) is showing a color gradient corresponding to point elevation in a raster format, and (b) depicts the same feature at higher magnification with an opaque tessellated TIN to show surface structure.

Due to the source formatting for the studied datasets, using an Inverse Distance Weighting (IDW) method from individual points of the model to form a DEM dataset is preferred to using the Triangulated Irregular Network (TIN) as it preserves the detail of models without requiring additional interpolation steps for

the software, resulting in slightly faster calculations and processing times (Bartier and Keller, 1996). The data are stored and manipulated in raster form, and only modified with color gradients or translated into TIN meshes when visual confirmation is required.

The primary difference between commonly studied DEMs and the datasets in this research is in the scale of observation. The processes being investigated operate on macro and microscopic scales, and as such this research attempts to physically characterize their effects in the most accurate manner which involves taking measurements at the smallest possible level. When studying landscape evolution within geomorphology, most often DEM generation and analysis operate on hundred-meter scales to characterize entire drainage basins, mountain ranges, and hillslopes. Most of the target regions in this study being analyzed for volume and surface characteristics exist on the hand-sample scale, and cover less than one hundred centimeters square which is often two or more orders of magnitude less than the error on most landscape models (see figure 008).

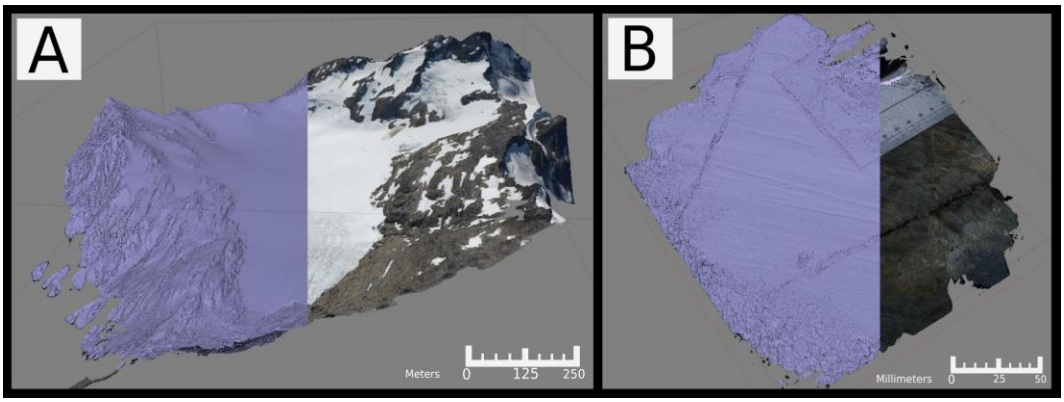

Figure 008
Examples of scale between DEM study areas. Model (a) shows the Brewster Glacier basin as a TIN mesh generated from aerial photography of just over one thousand photographs. Model (b) shows a TIN solid mesh surface of one sample from this study along a hillside transect near the glacier, the model was generated from about fifty photographs captured with a handheld DSLR camera. Note the level of detail between models and the size of sizes of features.

It is through these Digital Elevation Models that this research attempts to characterize volumetric changes over time and weathering relationships between samples extant in differing conditions. They are imported to several different software suites described below and analyzed against various parameters such as: surface reconstruction, volumetric analysis, slope and curvature isolation, textural feature wavelengths and dominant frequencies, roughness indices, and relative material weathering properties.

3.3. Model Analysis

Multiple lines of analysis were carried out on each model in a partially redundant nature with mapping, modeling, and engineering software. This provided the most accurate model outputs while corroborating analyses for precision calibration and evaluation of techniques.

Surface feature reconstruction was performed using the ArcGIS product suite, where each sample was normalised in resolution and spatial coverage by area prior to processing. The primary function of this was to determine the degree to which physical surface morphology has been altered by weathering between each sample, compared along the transect to a starting surface and with respect to each adjacent sample. To receive the most accurate and unbiased metrics, the surfaces were first normalised and filtered through global interpolation polynomials. This ensured that the volumetric measurements were representative of currently active processes (i.e. weathering), rather than the influence of regional morphology and past events, such as deep glacial striae. Polynomial interpolation also allowed for the cleaning up of digital artefacts such as high frequency error and model orientation, which are generated through model export and translation between different formats for each software suite used.

The second component of this characterisation was to analyse the missing material volume by identifying the depth and geometry of individual surface features.

Operator-subjective break values were set for data classifications to isolate the desired surface features characterising weathering. The amplitude and frequency of these features was determined and implemented into a novel roughness calculation described in section 3.5.2. to determine the magnitude of weathering trends present at the sampling sites.

In order to test whether the subjective threshold technique created substantial bias, the surface models were also analyzed using decompositional wavelet transform analysis to automatically extract pit characteristics. This was performed through MATLAB, with the aims to quantify the same weathering patterns using an alternative novel approach. With successful calculations, this more powerful and efficient tool for surface feature analysis of complex environments was introduced as a competent alternative to the ArcGIS approach.

3.4. Compositional Quantification

Concurrent to model simulation, a wide barrage of material characterisation was carried out to further contextualise the results. Following the preparation of sample billets and thin sections, the entire sample suite was subjected to X-ray Fluorescence (XRF) to gain primary elemental analysis on a parts-per-million scale. Each specimen was sub-sampled six times both at the standard beam energy level, and again at the amplified 50 kV beam level to enhance detection of heavy metals. This cumulative wide-spectrum analysis enabled objective detection of compositional shifts and redistributions between samples, with accurate quantification potential should variations be present. Due to logistic constraints, XRF was only performed on the Brewster samples.

Additionally, portions of sample billets were machined and polished to micron thickness and mounted uncovered on glass slides as ultra-thin billets. These were analysed with a multibeam scanning electron microscope. Secondary Electron Imaging (SEI) and Backscatter Electron (BSE) analysis were used to capture the

physical subsurface grain boundary morphology and mineral distributions present in each sample, respectively. Microprobe spot analysis was conducted throughout the investigation of each specimen, enabling confident identification of each mineral present. The captured BSE images were exported and mineral distribution quantification was carried out via false color image processing.

3.5. Roughness

This section provides an overview of roughness as currently defined in literature, in order to contextualise the novel techniques of weathering analysis performed on the spatial model outputs.

By James C. Bathurst's summary in the *Encyclopedia of Geomorphology*, the term “roughness” describes the texture of a streambed as a major contributing factor towards inhibiting channel water flow (Bathurst, 2004). This same basic conceptual framework of morphology as a static opposing force has been utilized to categorise aerodynamic roughness length for environments (Miles, et. al. 2017). The lens that roughness is investigated through in this study, however, is of additional dimensions. Roughness as a quantitative component of topographic morphology is measured in three dimensions and from all directions, rather than along a single two-dimensional vector. This alters the investigation from transect roughness to area roughness, adding further elements which may have an effect on results. Investigating roughness as a product of and active component within landscape evolution allows a view of how it changes through an environment both over time and space.

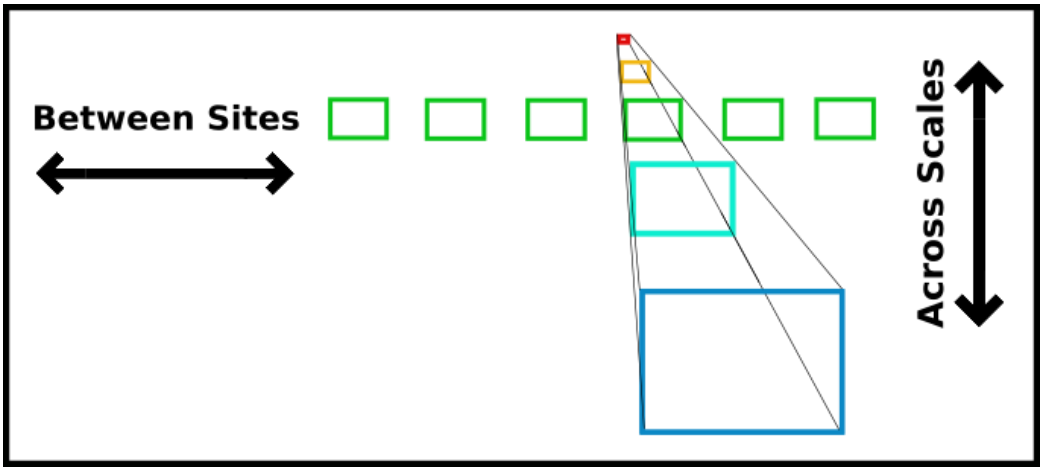

Figure 009
Theory diagram of the multi-dimensional approach of model analysis. Vertical integration across scales of observation provides spatial components, while the comparison between sites allows for a cross section of exposure ages to quantify the impacts of time on the system. By utilizing this technique, a single variable can be explored for cross-correlations over spatial and temporal settings simultaneously.

Roughness is first examined as a variable component of weathering. Based on the magnitude and form of roughness characteristics that a surface expresses, relationships to different styles of weathering—physical or chemical—are elucidated. Each region investigated in this study has a sampling transect which begins adjacent to the glacier and progresses further afield, minimising the number of controlling factors while increasing exposure age with distance. By comparing roughness between analogous sample sites along an age transect, the evolution of surface morphology over time is investigated. Observing how roughness changes in similar environments can provide data to assess the form and magnitude of active weathering processes. Looking at the components of each sampling site, the relative dominance of these processes can be determined and their relationships with roughness defined as a product and driver of landscape evolution within the system.

3.5.1. Exploring Roughness

When investigating roughness, it is important to differentiate between textural and structural aspects of roughness (Hyslip and Vallejo, 1997). Conceptualising structural roughness as the two-dimensional geometry of a feature perimeter is the most logical. However, geometry is challenging to quantify. The simplest method here would be to calculate the ratio of length between two axes of a feature. An initial calculation will determine how elongated a feature might be, and subsequent measurements along the axis of width will give a numerical picture of shape. Textural roughness is considered as a measure of the detail in the perimeter. The simplest calculation to determine this would be a comparison of the ratio between perimeter length and object area for the investigated object, compared to an ideal object of the same area, typically a circle.

These two components of roughness become more difficult to describe when a third dimension is added to the mix. Structural roughness components must now be investigated through a combination of the previous method with calculations that account for peak amplitude and slope. Textural roughness is now more or less the exact same measurement though in its higher order derivative form. Rather than measuring perimeter versus area, the measurement is between surface area and planar field-of-view area, otherwise known as the area-ratio. Unfortunately, these two components of roughness are no longer sufficient to account for all of the observed surface variations in three dimensions.

The first step in this to establish a definition of roughness in three dimensions. Though no single established definition exists in the field of geomorphology, a wide variety of terminologies have been applied to its study, including indices of peakedness (J. Krizbergs et al. 2006) and *waviness* (J. Raja et al. 2002), as well as *ruggedness* (Washtell et al. 2009), *rugosity* (Wilson et al. 2007), *microrelief* (Stone and Dugundji 1965) or *microtopography* (Herzfeld et al. 2000). Briefly discussed above, roughness as described in Bathurst's summary is the measure of resistance

to a directional flow imparted by surface texture. In three dimensions there are more spatial variables to account for.

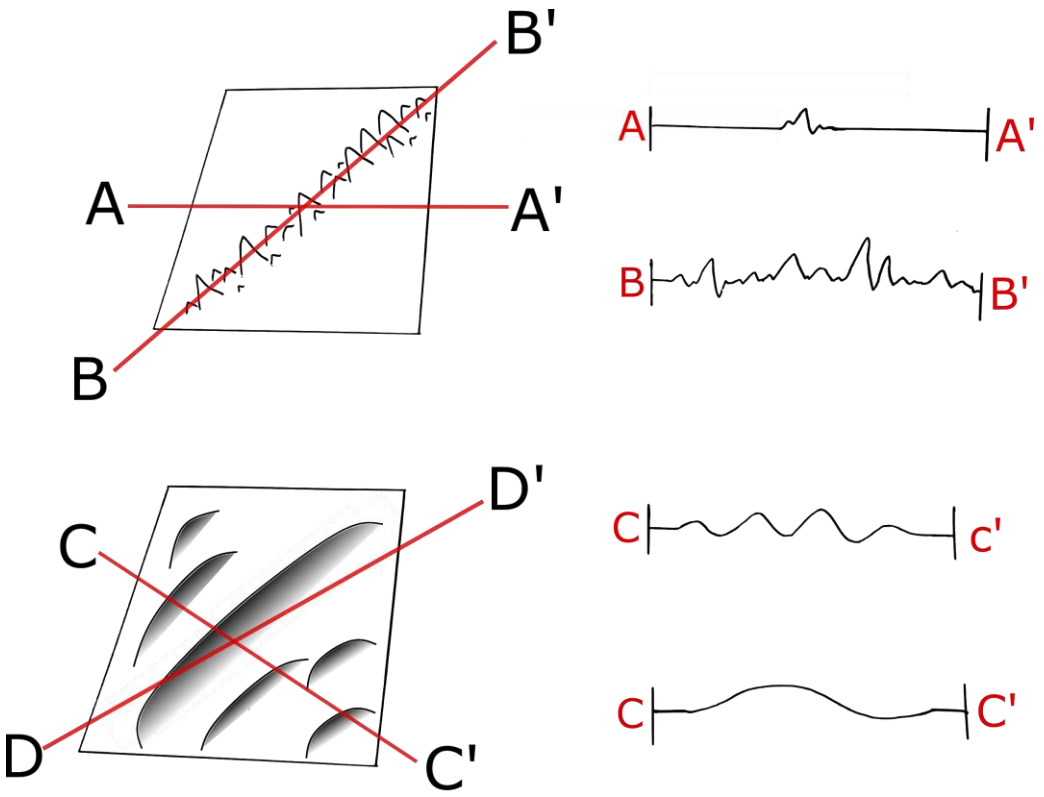

Figure 010
A simplified conceptual representation of how two and one-dimensional analytical techniques for roughness characterisation cannot simultaneously account for the number of spatial variables present in three-dimensional analysis.

With the added complexity of the third dimension, multiple additional metrics for surface morphology can be used. A multitude of analytical pathways are available for quantifying aspects of roughness. In reviewing literature nineteen distinct metrics were found (Hyslip, 1997; Grohmann, et. al., 2011; Ortega, 2012; Carvalho et. al, 2013). Of the nineteen explored, twelve are briefly described. Each of these methods have their own intrinsic strengths of qualitative and quantitative characterisation of surface texture, though only paint part of the picture needed to accurately represent roughness. The RIX ruggedness index works well for supporting effects of topography on wind predictions but, as an indicator of terrain

steepness, it cannot account for the frequency or size of textural features, leaving an incomplete approximation of roughness (Carvalho et. al, 2013). Variability of slope, standard deviation of slope, and standard deviation of profile curvature all suffer from the same shortcomings as the RIX ruggedness index. While the standard deviation of slope is touted as an efficacious metric for identifying separate textural features as a proxy for roughness, it lacks the ability to quantify magnitude when used individually. Vector dispersion is a precise tool for measuring the textural and geometric variability of features within a landscape, but has excessively high sensitivity to small scale and high frequency data, which allows the scale of observation and resolution of a dataset to have strong controls on model outputs. The standard deviation of residual topography struggles to pick up high frequency data and utilizes filtering which would eliminate small and medium sized textural features in the presence of infrequent high amplitude data with an overhead average (Grohmann, et. al., 2011). The Distributed Melton Ruggedness Number and the Modified Single Flow Model are powerful tools for characterising basin areas and mechanisms of formation, but are not easily scaled down and cannot account for volume of features or geometric identities (Ortega, 2012). Each of the single-dimensional analyses such as maximum profile depth, mean profile depth, mean peak width, and others all fail to account for at least two spatial factors which would accurately describe roughness in three dimensions. The primary issue with all methods of roughness characterisation that operate in two or less dimensions is the inability to generate a reading for a transect while simultaneously accounting for spatial variability across an area (figure 010). The only straightforward manner to utilise these metrics which are inherently two-dimensional or less with any sense of accurate spatial representation, is to perform the analyses using a parallel line method with an infinitesimally small measurement step length, or at least one which is less than half the size of the smallest feature of resolution, and repeat the process at a number of different angles approaching infinity (Hyslip, 1997). This technically can be done, but would require immense computational power and processing times bordering or exceeding prohibitive for viable study.

The area ratio of a site is described by the sum of all topographic surface area compared to the area as measured on a flat plane bounded by the circumferential coordinates of the study site (3D area:2D area). This measurement is controlled by two factors: scale of spatial observation and resolution. If the scale of observation is kept at a constant, proper representation of larger features will not be possible. This would prevent the objective analysis of regional properties that may change across scales such as roughness and curvature analysis. While at first the measurement of area ratio seems an excellent metric to compare textural differences between sites across scales, ultimately the observed changes could be entirely controlled by model resolution. If the ratio of resolution to scale is kept constant, larger observations would preclude small features, and thus provide an incomplete analysis of the surface. However, if resolution is preserved from the smallest scale of observation, any comparisons made across scales would exhibit a behavior of increase approaching infinity, as the relationship between resolution and surface area can be represented by a non-linear increasing function (Hobson 1967).

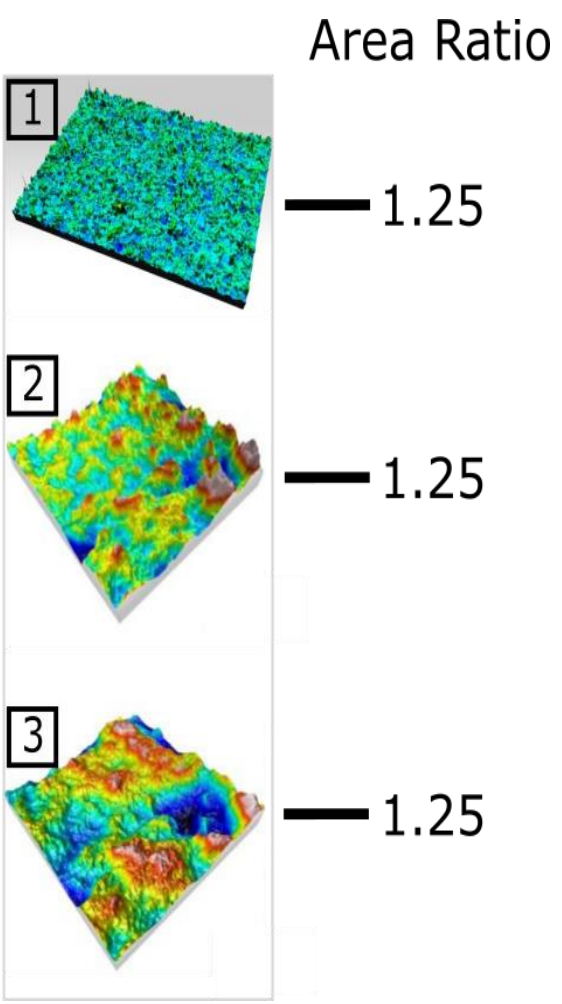

Figure 011
A simplified conceptual representation of the blind-spot presented by area-ratio analysis for roughness.

Even area-ratio, which paints a very simple yet effective metric for the complexity of a surface has several shortcomings. If we consider roughness to be the area-ratio for a specific region, in measuring a specific area for texture we get a set value of

x. However, we can generate the same area-ratio value of x for an entirely different textural regime. In figure 011, the image 1 shows a surface with numerous small amplitude features. The image 3 in figure 011 shows the same region size, but instead with fewer surface features of much higher amplitude. The image 2 in figure 011 again has the same region size but with a few surface features that have high amplitude, a few with a more moderate amplitude, and several with a very small amplitude. All three of these possible scenarios have very different surface textures, but using area-ratio all show the same numerical representation of roughness. In order to have a more accurate measurement of surface texture, the spatial and magnitudinal elevation variability of terrain must also be accounted for.

3.5.2. Novel Roughness Development

The definition of roughness as used to characterise surface morphology in this study has been generated using a multivariate hybrid approach to combine multiple models. This has been done in an effort to preserve the quality of observational conclusions through the translation to numerical representation. An appropriate quantification of roughness must account for surface complexity, stochastic feature coverage, and independent structural amplitude of objects. A single analytical metric does not exist to generate these measurements, but with a modified area-ratio calculation calibrated against the derivative of the relationship between feature density and relative element prominence, a holistic numerical representation of roughness can be established.

Area ratio is an excellent conceptual metric for roughness, and if constrained properly is one of the few methods of analysis which allows for a representation of the entire region of interest. As shown in figure 011, area-ratio has problems with lateral continuity of data across changing types of texture as it cannot account for relative differences caused by size or number of features. The outputs for area-ratio are also extremely susceptible to influence by variable study region sizes and data resolution. This can be mitigated by using areas of examination that cover identical spatial extents, and normalising the resolution of all DEMs tested to each other.

Prominence as measured is the quantification of height disparity or amplitude from an artefact peak to the established planar baseline. Prominence can be analysed for multiple scales of features should they exist by modifying the baseline height. Feature density as measured is the frequency of independent height artifacts on a given surface. The application of feature density will account for the distribution of textural features across a surface by number when paired with prominence for height. This ensures that the surfaces being measured at each site have a standard morphological coefficient of compliance (MCOC), meaning that they represent similar environments under study rather than radically variable surfaces generating model outliers.

Frequency is plotted against amplitude for the distribution of artefacts across a surface, and the resultant histogram speaks towards the texture of each surface. The relationship between amplitude and frequency is determined via interquartile statistics. The median as well as 25% and 75% interquartiles are calculated, and using the equation below, the relative distribution of features by size and frequency is determined, with each half of the equation representing the morphology of the distribution on either side of the median.

$$Interquartile\ Ratio\ (Z) = \frac{Q3 - median}{median - Q1}$$

The interquartile ratio for each category supplies the most information about a surface, by representing artefact size, size trend, and quantity. An interquartile ratio greater than one corresponds to an environment with a skewed distribution towards large amplitude features, while a value of less than one indicates a surface dominated by small amplitude features. This leaves a value equal to one to represent an environment with a symmetrical distribution of artefacts in all amplitude categories. Total number of features need not be considered in this event, as the lower and upper limits will be manifested in the area-ratio results.

As shown in figure 012, the interquartile ratio is plotted against the area-ratio values. For a given set of sites exhibiting dissimilar structure with identical area-ratio values, here depicted as the surface categories from figure 011, the vertical spatial disparity between points represents the degree of representativeness for the area-ratio measurements. The magnitude of disparity is recognized as the morphological coefficient of compliance (MCOC). Sites with dissimilar morphologies will have an MCOC value greater than zero and as a calibration, show the area-ratio readings to be inaccurate. As MCOC values approach zero, the area-ratio values are more likely to be accurate for the studied surface.

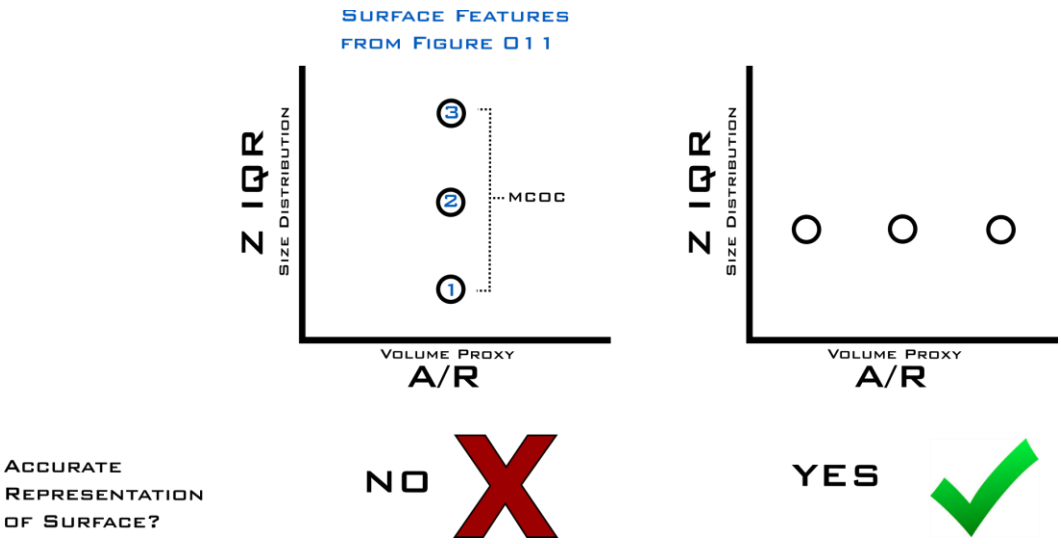

Figure 012
A simplified conceptual representation of the determination for morphological coefficient of compliance (MCOC). The interquartile ratio (Z) is plotted against area-ratio values (A/R).

The applications for the MCOC area-ratio calibration are explored further in figure 013. By linking the points in order of relative age, the positive or negative correlation in slope of the MCOC analysis can be used to represent different weathering regimes as a series of sites changes in roughness. The magnitude of the slope value of the MCOC analysis functions as a proxy for speed or intensity of landscape evolution. If a MCOC slope is negative, then the transect is experiencing

an increase in surface area along with a change in dominance from large to small features. This could be observed if the size of existing features remains unchanged while the number of new smaller features is increased, such as might be expected in the early stages of surface weathering. Similarly, if a MCOC slope value is positive, it implies the transect is experiencing an increase in surface area, but with a trend change from small to large artefacts. This could be observed if a site has the same number of features, but their amplitude is increasing. For a situation with weathering pits as artefacts, this would represent an increase in erosional pit depth, which would be expected for later stages of weathering as pits widen and deepen with time. Theoretically this could also be due to new larger amplitude artefacts being added to a site rather than existing feature growth, but the magnitude in area-ratio increase should reflect this with a different signal.

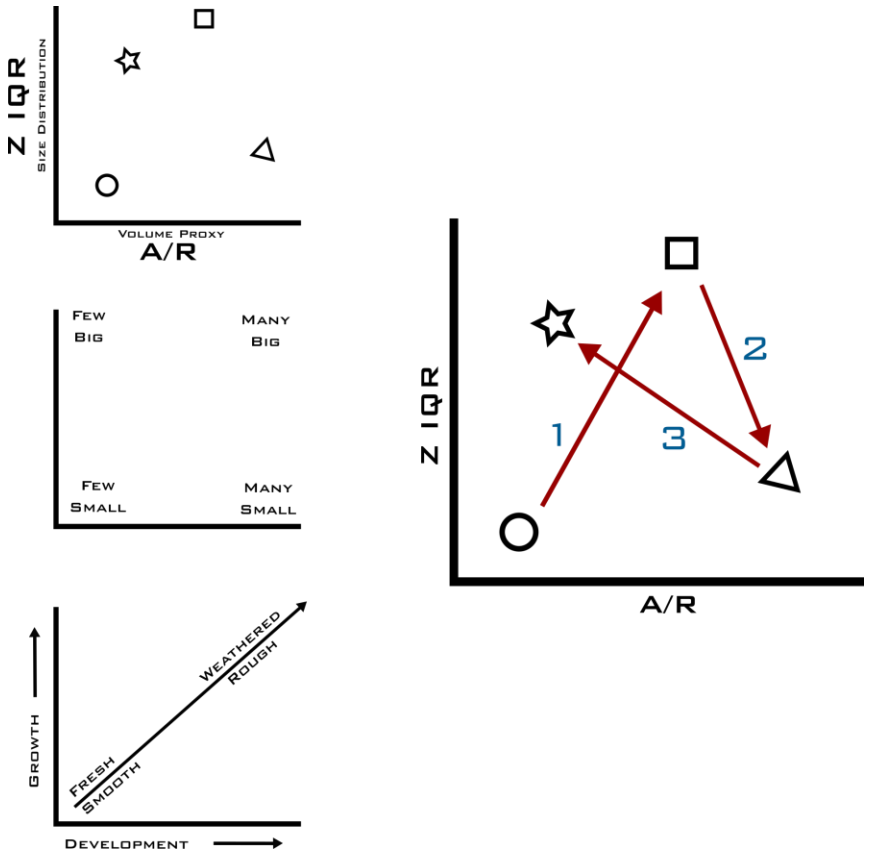

Figure 013
Examples of how the relationship between MCOC and area-ratio reflect changing roughness across a site, and the implications for weathering trends and intensities.

While figure 012 demonstrates area ratio for accurate quantification of roughness change in ideal situations, figure 013 demonstrates how the this method can be used to achieve the same results while also describing the nature of how roughness is changing, hinting at possible weathering patterns and mechanisms. Within figure 013, during trend 1 the surface area and size distribution are both increasing while the pits increase in number and size, which could represent a fresh surface being weathered. In trend 2, surface area is increasing while the size distribution changes to smaller pits. This could be a weathering surface eroding further, generating new small features more quickly than it is deepening existing ones. Trend 3 is characterised by a decrease in surface area with an increase in size distribution. This could be due to fewer small pits, as a surface experiences weathering at a higher rate than it can form new features.

There are dozens of possible permutations of the model, many which could be presented as a non-linear progression. This opens up the possibility of the MCOC model for interpretation of complex weathering regime reconstruction over regions with progressively developing landscapes.

3.6. Multiresolution Wavelet Decomposition Analysis

A marvelous phenomena of the natural world is the mechanical tendency to follow numerical patterns. Whether the mathematical concepts are derivatives of the natural world or the other way around, is an entirely different discussion. Nonetheless there are many unique observations that can be made of the natural world with the correct perspective. As with naturally occurring patterns of proportioning such as ferns which have shoots that develop a physical manifestation of fractal patterns, there are many other components of the earth system which can be modeled effectively using mathematics. Similar to resonant frequencies of objects with vibrational energy, the morphology of the physical world gives way to many shapes and processes which occur within certain ranges or scales. The mechanical properties of rocks allow for relatively predictable behavioral

responses, and as such lend themselves to generate structures at given frequencies. This can be observed in the fractal expansion properties of crystalline structure, where the microscopic fracture surfaces within crystal lattices or rocks develop patterns which can be observed on microscopic and regional scales. It is not uncommon to have fracture planes visible within the structure of a basin which repeat in a parallel manner down to microscopic levels (Turcotte and Huang, 1995). It is then reasonable assumption that surface roughness, a component of the earth system and a manifestation of weathering elements acting upon rocks, should also function across a series of distinguishable frequency scales.

Analysing surface roughness in three dimensions, however, is much more complex than a breakdown of optical frequencies from photographs, patterns within sound waves, or trends of properties along profiles. Typically, Fourier transforms function as an excellent mechanism for these types of analyses. Fourier transforms act within time-series datasets across a broad range of applications, to develop a frequency domain representation of the dataset by overlaying the interpreted signal with waveforms which are controlled over variable frequency and translational domains. Unfortunately, Fourier transforms are unfit for the decomposition of roughness signals because they operate on fixed resolutions in time and frequency domains, and as such cannot account for three-dimensional variable patterns who have variable frequency domains and scales (Zhaouani et. al, 1999). For the same reason, power spectral density analyses (PSD) are also inherently unfit for three-dimensional analyses. Though they can reconcile variable frequency domains, the roughness of a surface often occurs across different frequency scales within multiple spatial scales, and spectral analysis does not have the capacity to resolve multiple resolution datasets (Zhaouani et. al, 1999). The only way to resolve this analytical issue is to employ a method which can simultaneously account for variable spatial and frequency domains. This can be accomplished by a process which has a mobile compensating window, which can widen at lower frequencies and narrow at high frequencies to interpret all signals with the correct resolution.

The fully scalable modulated window of wavelet analysis successfully overcomes this problem and can generate signal readings for every spatial position in the spectrum of frequencies of a given sample. This is accomplished through the application of both discrete wavelet transforms (DWT) and continuous wavelet transforms (CWT). A wavelet in its most basic application is a type of simple curvilinear waveform used to interpret complex non-linear signal patterns. The wavelet is superimposed over the signal, and a fit metric is calculated to determine the accuracy of the match, often something comparable to an integral of difference in 1D.

As powerful tools for pulling out variable surface frequencies, their applications in a variety of fields are gaining popularity. For example, in the computer-numerically-controlled subtractive machining process of billet materials, high accuracy of geometric consistency is required to generate the optimum forms. Surface texture in these materials is analysed for quality control using wavelets to determine if defects are present in the forms, machining processes, or the equipment has dull or broken tooling (Rosso, et. al, 2001). In engineering, surface texture as characterised is split into three subsets: roughness, waviness, and form. Each of these categories corresponds to distinct types of surface features which exist across different scales and are tied to independent manufacturing processes. The issue is that these are not mutually exclusive—to the contrary they are almost always simultaneously extant—which results in the generation of complex compound signals within surface morphology. Various wavelet transform filter banks can be applied to these datasets, and with the correct parent wavelet matching and manipulation are very effective at isolating the various signal frequencies.

3.6.1. Wavelet Families

Each wavelet family has a different base morphology. It is beneficial to pick a wavelet family with a waveform that most closely resembles the signal being interpreted for accurate results. Examples of wavelet families can be seen in figure 014. Each wavelet family has unique properties which make them more well suited to certain applications than others (Chaudhary and Dhamija, 2013).

Figure 014
Examples of multiple wavelet families, with two-dimensional waveform morphologies shown. Image sourced from MathWorks Wavelet Toolbox (2018).

3.6.2. Wavelet Support

In order to ensure the best match between a wavelet and signal, the wavelet is manipulated in several different ways. The morphology of a wavelet is determined by its parent wavelet (i.e. the family that the wavelet belongs to) and wavelet order. As they are often significantly modified through the transform process, it is necessary to explicitly state the parent wavelet. Wavelet order, also known as wavelet support, corresponds to the number of vanishing moments of the wavelet and loosely indicates smoothness of the wavelet in use. Each time a wavelet signal oscillates and crosses an axis boundary, a vanishing moment is established, and the ability of the wavelet to interpret signals with higher order polynomial behavior

generated. It is a general rule that for all wavelets with N number of vanishing moments, a support value that is greater than or equal to one less than twice the number of vanishing moments is needed, or *2N-1* (Heller, 1995). A second order wavelet will typically have four vanishing moments, or waveform oscillations, whereas a twelfth order wavelet will have six vanishing moments and a correspondingly higher target frequency. Generally, wavelets with small support values have difficulty interpreting closely spaced features, and wavelets with large support conversely are not able to interpret widely spaced features with high accuracy. The relationship between wavelet support levels and signal morphology, both in two and three dimensions is demonstrated in figure 015. A product of the unique ability of wavelets to interpret spatiotemporal variability across signals, is the preservation of wavelet shape as it is manipulated for different frequencies. As a result, it is critical to understand the abilities of the wavelet chosen, and to ensure that it closely resembles the morphology of the signal under investigation. As of currently, there are no algorithms or mathematical expressions to aid in the determination of appropriate wavelet support for three-dimensional applications, resulting in the accepted practice of repeated trial with adjustment (Daubechies, 1988); (Abramovich and Benjamini, 1996). It is plausible that a geometric or volumetric coefficient of fit value could be calculated to represent the level of match between a wavelet and a studied signal, but the processing power and calculation time required to compute every possible ramification of wavelet-signal interaction would be many orders of magnitude greater than that required for visual determination.

Figure 015
The Daubechies wavelet, conceptualized by Ingrid Daubechies in 1998, is shown with multiple levels of support depicted in two-dimensional waveforms. Image sourced from: (Gupta, 2014).

3.6.3. Wavelet Scaling and Translation

The manner in which a wavelet breaks down and analyses a signal is controlled by two main variables, the scaling parameter and the translation parameter. Scaling parameters affect the frequency domains used for analysis, while translational parameters determine a frame of reference along the signal for each applied wavelet. These two factors determine to which detail and level of decomposition that a signal is interpreted, resulting in very different system outputs as they are varied. The scaling parameter functions to match the shape of the waveform to multiple amplitudes within a signal. This is done by compressing or dilating the frequency of each level of wavelet applied. Each time the scaling parameter is altered, the level of decomposition is equivalently modified, effectively halving or doubling the size of the analysis window within the frequency domain. Depending on the type of wavelet applied, as the number of scales *(a)* increase, the frequency domain reduces by a multiplier of *1/2(a)* (Young, 1993). The thresholding for determination of the scale parameter is calculable by a variety of different methods. Trial and error can be employed to see how many levels of decomposition are needed visually to best represent the frequency ranges present in the analysed signal. Other algorithms are based at least in part upon the Birgé-Massart strategy

which helps to determine the maximum cutoff for high frequency decomposition levels where additional scales begin to yield diminishing returns (Sidhik, 2015). When applied through a discrete wavelet transform, only the number of desired scales of analysis need to be specified, and their periods will be determined by wavelet transform filter bank analysis. Discrete and continuous wavelet transforms will be further characterised in section 3.6.4.

The translation parameter is a measure of distance along a signal within the frequency domain that a wavelet is applied. Once the wavelet scaling parameter has been established, the compressed or dilated waveform will be weighted against the signal at the period determined by the translation parameter for its full length. In discrete cases, the translation parameter is always proportional to the scaling parameter. This can be traced to the implementation of the fidelity factor *Q*, the ratio of center frequency of filter to the bandwidth, which allows the window to have a variable inverse size function compared to the frequency (V. Gadre, 2008). In figure 016, the parallel relationship between translation parameters can be observed.

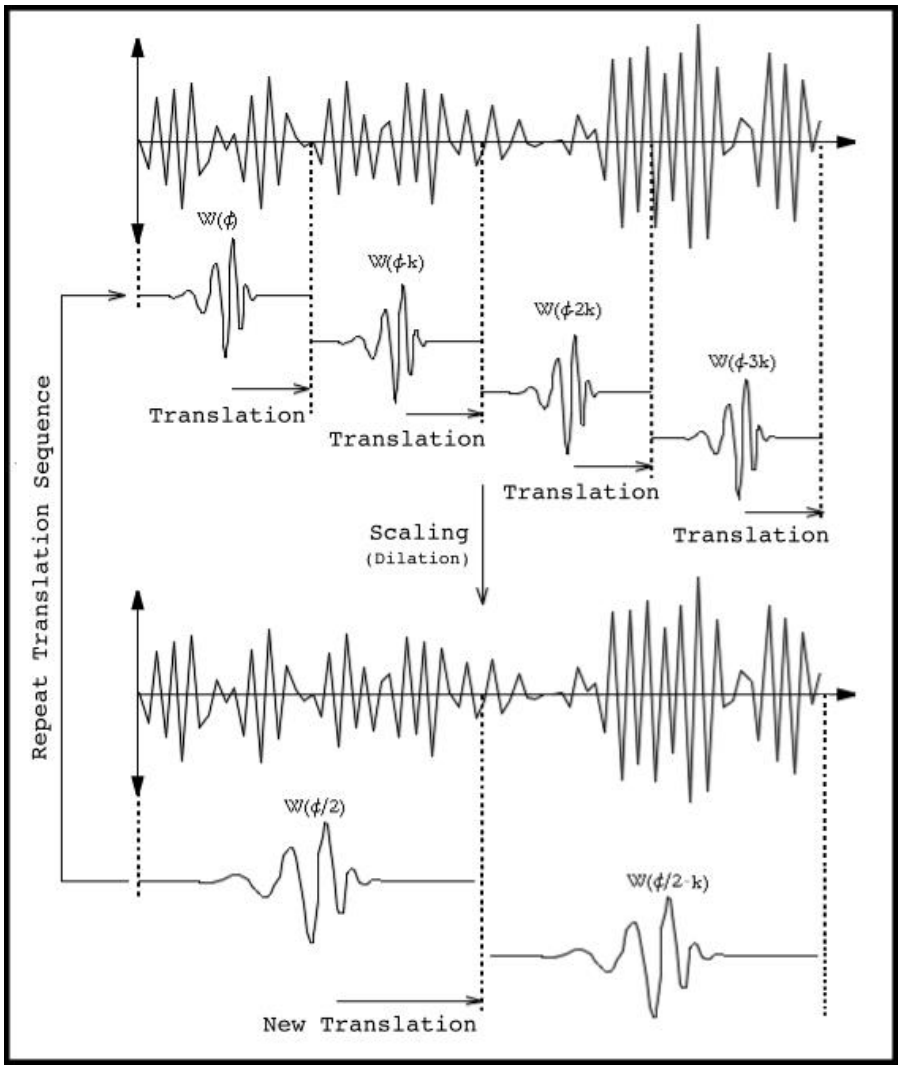

Figure 016
Conceptual model of wavelet transform analysis showing the functions of scaling and translation parameters on a db5 wavelet. Modified from a wavelet.org resource (wavelet.org, 2018).

3.6.4. Discrete and Continuous Wavelet Transforms

For interpreting different types of waveform signals for frequency data, there exist two types of wavelet transforms: Discrete and Continuous. Each wavelet transform has specific wavelet families that belong to it, and correspond to the style of analysis performed. The primary functions of both wavelets are the same: to analyse and filter complex and nonlinear signals for trends of frequency and scale. However, they each approach this task in a different manner.

Discrete wavelet transforms (DWT) are particularly effective tools for multiresolution decomposition analysis. With orthogonal wavelet analysis, discrete wavelet transforms function with a complete preservation of signal energy by interpreting signals operating 90 degrees from the basal plane, and as a result have the unique ability to generate perfect reconstructions with signal inversion (Daubechies, 1988; Pasti, 1999). This comes as a by-product of the discrete wavelet transform behavior of downsampling. Signal reconstruction accuracy allows for precision checks to ensure accurate wavelet function following interpretation, where a signal to noise ratio can be calculated for a signal prior to decomposition and weighted against the signal to noise ratio of the reconstructed signal after wavelet filtering (L. Pastia et. al, 1999).

Once the parent wavelet family and order are selected, they will remain unchanged for the duration of the wavelet transform analysis. The DWT waveform is then manipulated in two ways for multiresolution analysis. Discrete wavelet transforms control their scaling and translation parameters as a function of dyadic block sampling, which is a method of wavelet transforms following a geometric sequence based off a power of 2 (Josso et. al, 2002). As each subsequent scaling parameter increase splits the frequency band by a factor of two, the translation parameter is proportionately increased. Where a situation with a scale value of $2^{(a)}$ will result in a translation parameter of $(t)=2^{(a)}N$ (Josso et. al, 2002). Each wavelet family has a unique maximum scaling coefficient value. Based on these, the resultant fit between the wavelet and signal can be plotted separately for each level of frequency domain studied, resulting in a frequency-decomposed signal analysis. The resultant scales separated by DWT analysis can be recombined in various ways in order to represent surface features by morphology and frequency. Figure 017 is an example of multiscalar decomposition analysis by discrete wavelet transform. A surface is examined using a Daubechies db20 wavelet with 7 levels of decomposition.

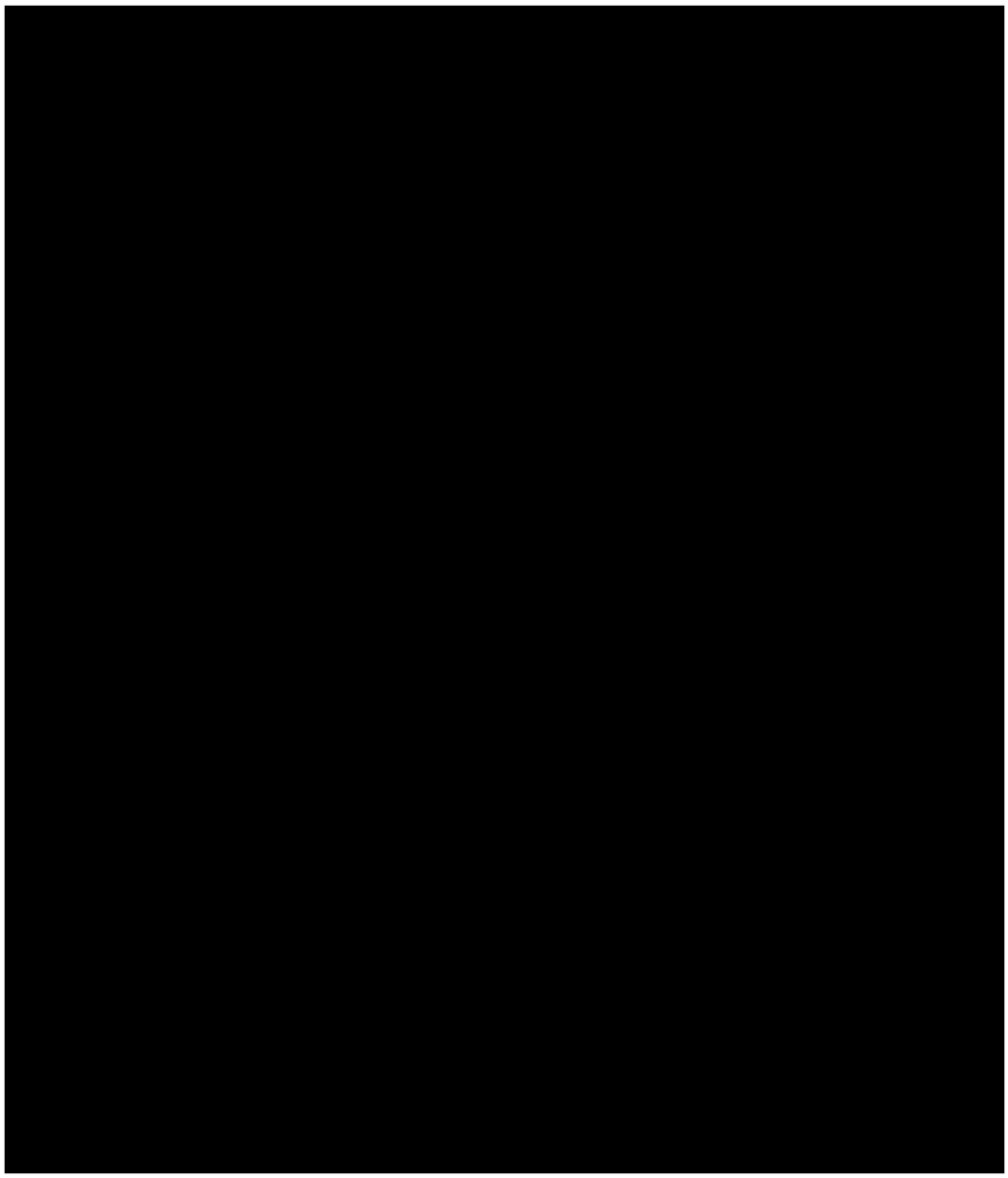

Figure 017
Discrete wavelet transform multiresolution decomposition analysis of surface texture, generated using seven scales of the Daubechies 20 discrete wavelet, and its frequency normalised equivalent. Each subsequent level is associated with a changing value of the scaling parameter, and represents the surface as it matches to the db20 wavelet's associated frequency domains. Image sourced from: (Josso et al., 2002).

The main difference between a discrete and continuous wavelet transform is in the modification of their scaling parameters. While discrete wavelet transforms alter the number of intermediate scales between the doubling of a frequency bandwidth

by a set factor of two with minimal resulting overlay, a continuous waveform is quite redundant in that it employs orders of magnitude more intermediate scales between a frequency doubling, which results in large amounts of overlap (O. Rioul, P. Duhamel, 1992). This is best represented by each waveform type's relationship to the factor of two, derived from the separation of high-pass and low-pass frequency filters applied during each transform. Where a DWT might utilize scaling factors at intervals of 2^x, a CWT would instead have scaling factors oscillating at a much faster rate such as $2^{1/2x}$.

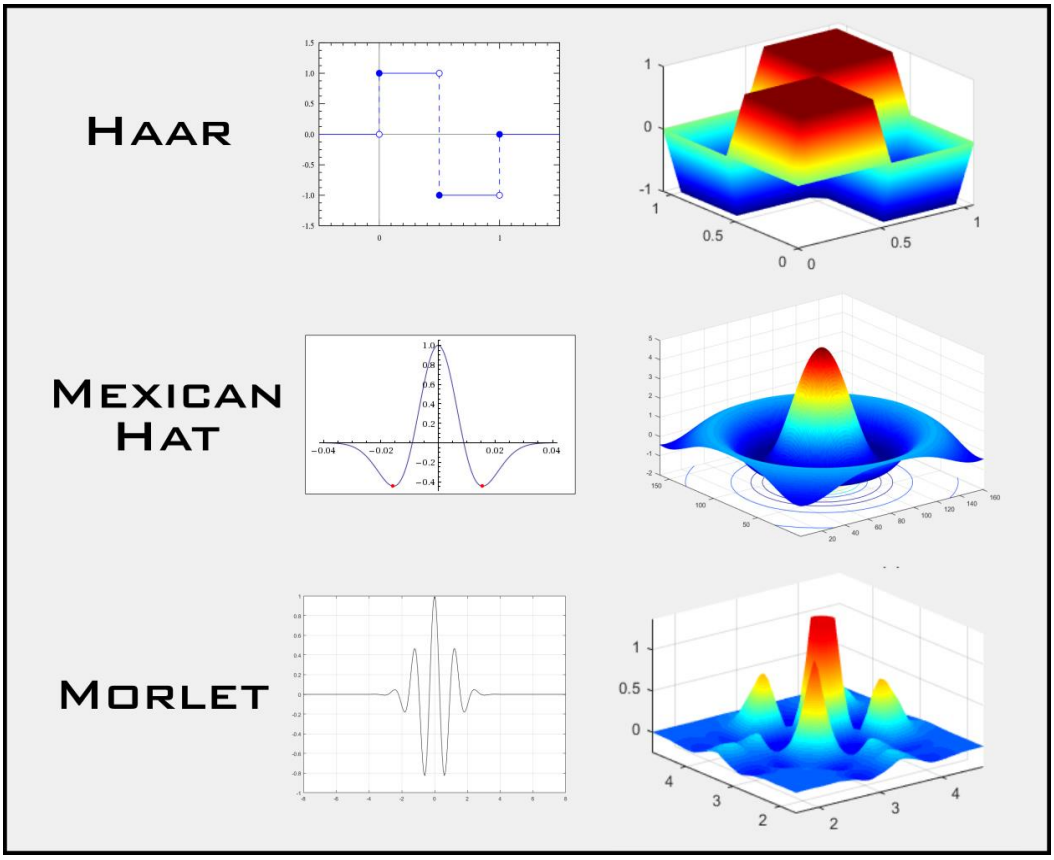

Figure 018
Wavelet family morphologies for the most commonly used continuous wavelet transform functions. Note that independent of wavelet support level, the waveforms have very different morphologies.

Continuous wavelet transforms operate on the same basic principles as discrete wavelet transforms, save for the period of analytical translation and increments of

waveform compression. The most digestible manner of conceptualizing this is with a moving window which interprets a signal, averaging readings over a near-infinite number of frames, capturing the same information multiple times. This redundancy results in a high assurance of accurate calculation, and functions to protect CWT analyses from signal noise, but comes at the cost of complexity and required computational resources (O. Rioul, P. Duhamel, 1992). This functions to move the three-dimensional wavelet across the entire area of study, looking to find optimal overlap with features that have similar morphology to the waveform along all applied scales. The scanning-wavelet method of analysis with CWT is very effective at targeting premeditated sets of surface artifacts.

The three most commonly utilised wavelets for continuous wavelet transform analysis are the Haar wavelet, Mexican Hat wavelet, and the Morlet. Each has a distinctly different parent waveform (figure 018), and targets datasets which have varying levels of complexity in morphology. The Haar wavelet, interestingly enough, represents the same waveform as a Daubechies wavelet with a support level of 1, which is evolved across a continuous transform (Fatma H. Elfouly et. al, 2008). The conceptual simplicity of the Haar wavelet makes it computationally very efficient, but limits the effectiveness for modeling complex signals to one dimensional analysis of two-dimensional data (M.Z. Lubis et. al, 2016). The Morlet wavelet family is well suited to identifying convoluted features, and would be useful for separating compound signals generated from more than one process, or targeting features with signal entanglement (Baoping Tang et. al, 2010). However, for the research in question the Mexican Hat wavelet should have the most useful application. The morphology of the Mexican Hat wavelet most closely agrees with the targeted features when inverted, namely erosion pits and single-curvature surface features (figure 019). The single dominant peak of the Mexican Hat wavelet makes it a ubiquitous proxy for many natural features: representing tree canopies, convolutions on sculpture manifolds, turbulence energy cascades, cosmic celestial body detection, electrocardiogram analysis, and landslide triggering factor analysis—truly any feature that can be vaguely represented with a parabolic arc—

which sees it as one of the most widely-used wavelets across fields (Falkowski et. al, 2006; Hou and Qin, 2012; Argoul et. al, 1989; Bernard et. al, 2004; Burke and Nasor, 2004; Tomás et. al, 2016).

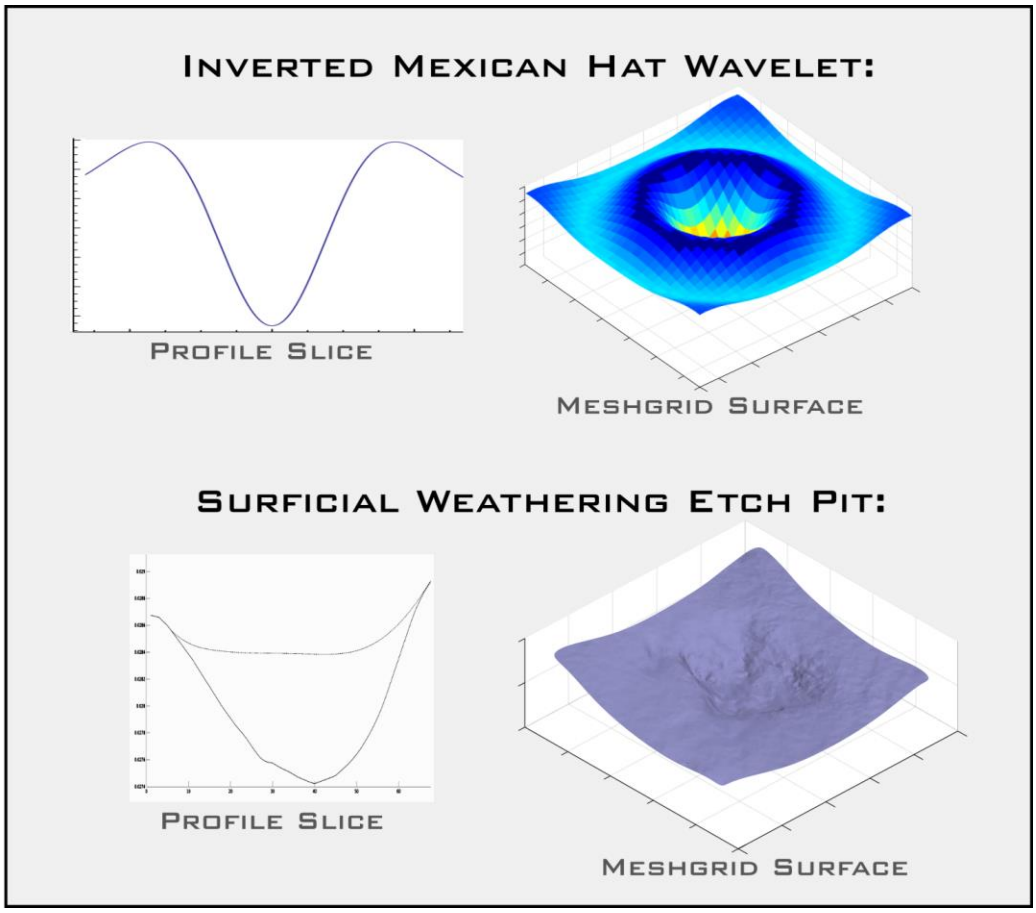

Figure 019
Conceptual diagram showcasing the exceptional ability of the Mexican Hat wavelet to match with common erosional features. Two and three-dimensional representations of the Mexican Hat wavelet and an etch pit from a Brewster Glacier sampling transect are depicted

3.7. Cosmogenic Radionuclide Surface Exposure Dating

The key component of gathering weathering rates in situ is to establish time constraints for volumetric changes between similar locations. The amount of material weathered from a surface is relatively inconclusive unless it can be contextualized by time boundaries.

Cosmogenic radionuclide surface exposure dating is a method of acquiring precise surface exposure ages by measuring the abundance of cosmogenic radionuclides present in a sample (Dunai, 2010). Cosmogenic radionuclides are specific isotopes generated from terrestrial elements through interaction with secondary high energy particles, mainly neutrons and muons (Dunai, 2010). In spallation, an energetic neutron collides with a target nucleus, spalling it into: gamma radiation, mesons (muons and pions) and smaller nucleons (protons and neutrons), as well as nuclear fragments (alpha particles), and larger remnant atoms (cosmogenic isotopes) (Lal, 1991; Gosse and Phillips, 2001; Dunai, 2010). There are two classifications for cosmogenic isotopes: meteoric and in-situ. Meteoric cosmogenic isotopes experience cosmic ray spallation in the atmosphere and as a result accumulate on the surface of the earth and in soils through precipitation and dry deposition (Dunai, 2010). In-situ cosmogenic nuclides undergo cosmic ray spallation while the parent material is still locked in the crystalline structure (typically in bedrock) which in turn contains the cosmogenic isotopes after synthesis. Many cosmogenic nuclides are isotopes that can only be generated by this singular process and because they have an assumed constant generation rate and accumulate in-situ, act as a unique signal for the amount of time a given surface has been exposed at the surface to cosmic rays.

Due to the mechanism by which accumulation of cosmogenic radionuclides occurs, several factors control its accuracy. The rates of accumulation are governed primarily by proximity to cosmic rays. If the sampling site experiences any topographic shielding, whether it be from a nearby mountain or adjacent topographic high such as a large boulder (greater than 60-70cm diameter) must be

taken into account (Heyman et al., 2011). As there is a finite rate of cosmic radiation entering Earth's atmosphere at any given moment in time, and each collision consumes some of the particle cascade's energy, the vast majority of cosmogenic nucleosynthesis occurs in the upper atmosphere as gas molecules are bombarded by rays. Therefore, elevation plays a significant role in the calibration of cosmogenic radionuclide accumulation. If a sample area exists at a low elevation, there will be more mass between the top of the atmosphere and the surface, reducing the cosmic ray flux. Thus, cosmogenic nuclide production rates are lower at low elevation when compared with higher elevation sites. For this reason, aspect and slope angle also play important roles in calibrating results.

There are many radioactive and stable cosmogenic isotopes that can be generated through cosmogenic nucleosynthesis, though the product is dependent on the elemental identity of the parent material and as such cosmogenic isotopes derived from abundant elements are more conducive for research. The most commonly used cosmogenic radionuclide isotope, and the one used exclusively in this study, is Beryllium-10 (^{10}Be). ^{10}Be is generated when a high energy galactic cosmic ray particle impacts an atom of oxygen and through spallation nucleons are shed from the oxygen molecule leaving behind a newly formed chemical element, ^{10}Be. ^{10}Be is chosen for its availability, though the true credit goes to its ubiquitous parent mineral, quartz. With the chemical formula of SiO_2 quartz not only holds a large reservoir of oxygen but also is one of the most abundant materials on the planet, making up an estimated twelve percent of Earth's crust (Okrusch and Matthes, 2005). The simple composition, chemical resilience and mechanical hardness of quartz make for a sublime experimental medium that can hold up to the natural processes that cosmogenic radionuclide dating requires.

The advent of this geochronological technique has been particularly beneficial in the field of geomorphology as it is one of the first methods that gives a look into the amount of time passed since a given feature has been exhumed (Dunai, 2010). Cosmogenic isotope dating provides insight into the chronology of weathering

mechanisms such as mass-wasting events, glacial cycles, and other agencies of landscape evolution. It is for this quality that cosmogenic radionuclide surface exposure dating was selected for this research. Further, the diversity of ages covered by this method make it an excellent tool for this type of research, as erosional surfaces can span a wide range of ages. Typically applicable between 10^7 and 10^2 years, the lower age limits for ^{10}Be is largely restricted by the sample collection, chemistry practices, and AMS measurement capabilities (Davis et al, 1999). The exposure age of a rock sample should perfectly correlate with the duration of weathering that it has experienced while at the surface, providing a chronology for the transects measured in this study. This acts as a proverbial atomic clock which is used to calculate the amount of time that the samples have been weathered following exhumation, in this case the span of time since the rock surfaces were exposed as the glacial body retreated. When paired with the volumetric difference calculated between samples, an empirically generated weathering rate can be calculated for a given sample with high correlation between theoretical and measurable values.

4. Methodological Approach

4.1. SFM Development and Photoscan Optimisation

Structure from motion technology (SFM) has been proven as an incredibly powerful and effective tool for analyzing environments in three dimensions through user-generated 3D models. SFM is most commonly utilized for studying macro scale objects, and as such the traditional techniques employed required modification for the unique application of this study. Due to the small scale of observation, caution had to be exercised for preserving as much accuracy as possible when scaling down experiments. The following is an overview of the modifications and techniques used to generate more accurate SFM models developed through running hundreds of algorithms over nearly twelve months.

4.1.1. Photography

Being that SFM uses sets of photographs to develop models, it is important to have a high level of detail in the starting material for the process, and develop an understanding of how to take the best photos. To capture the highest level of detail when photographing small samples, it is important to understand the mechanisms by which the SFM software generates data points. The software package utilized for this study was Agisoft Photoscan. Photoscan uses variations in shading and brightness to identify tie points and calculate parallax offsets between images. For this reason it is important to have sufficient lighting to capture the full detail of the sample, without washing it out. The best weather for these conditions is a bright overcast day. The cloud cover will create a uniform lighting environment and not wash out the lighter sections of sample as would occur on a clear sunny day. To ensure proper lighting always maintain aperture priority for the camera and keep the ISO and F-stop adjusted to optimize brightness and emphasize contrast within the sample. For all photos captured, the image stabilisation and auto-focus should be both turned "OFF", as these settings will omit specific photo metadata which the software uses to compensate for optical lens distortion. Above all, ensure that the same settings and environmental conditions are present when photographing each individual sample. The smaller the scale of observation, the larger the differences in output will be with varying conditions of observations as the software will have more difficulty reconciling the good from bad data.

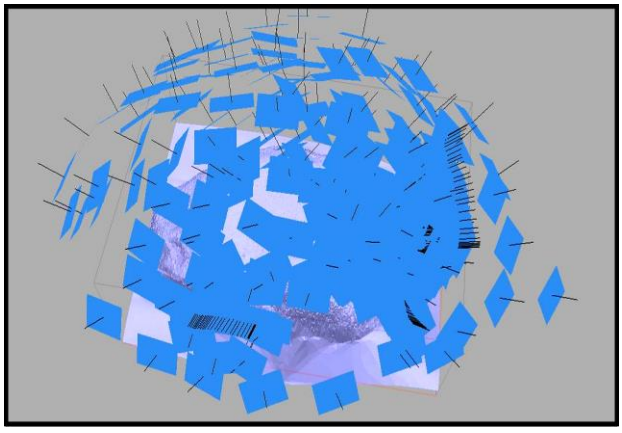

Figure 020
Model generation state in Agisoft Photoscan displaying camera locations. Note the tight spacing and variety of orientations of camera positions.

One of the most critical components of good SFM photographs is the field of view. Though the software can do a commendable job of matching photosets together with minimal overlap, greater overlap between photos will result in a more detailed model. With a larger field of view captured, more data points are available for correlation. Operating at very small scales, it is difficult to capture photographs with a traditional telephoto lens which keeps the majority of the field of view in focus with minimal optical distortion. The first set of photographs captured in the field were done with a Nikon D800E 32 megapixel sensor full-frame DSLR camera using a Nikon AF-S FX Nikkor 35mm f 1.8G lens. The detail in the photographs was high, but at the scale desired only a very small portion of the field of view was ever in focus. This resulted in poorly correlated tie points between photographs and models with less than desirable quality. The remainder of field data collection was completed with a Pentax K-5II 16 megapixel sensor camera with a 35mm f/2.8 Macro Limited HD DA macro lens (figure 022). Though the Pentax is not a full-frame camera setup, the dedicated macro lens allowed a tremendous amount of detail to be imaged in the photographs, resulting in captures with much larger in-focus fields of view than the Nikkor (see figure 021). Using a lens that has a large focused capture area at the scale of interest has a great impact on the quality of models produced. Due to the small size of the features observed at this scale, it is very important to capture as many overlapping photos as possible, and from as many angles as possible. If all the photos are taken from an overhead view the height field generated will have difficulty representing the third dimension of the model with accuracy.

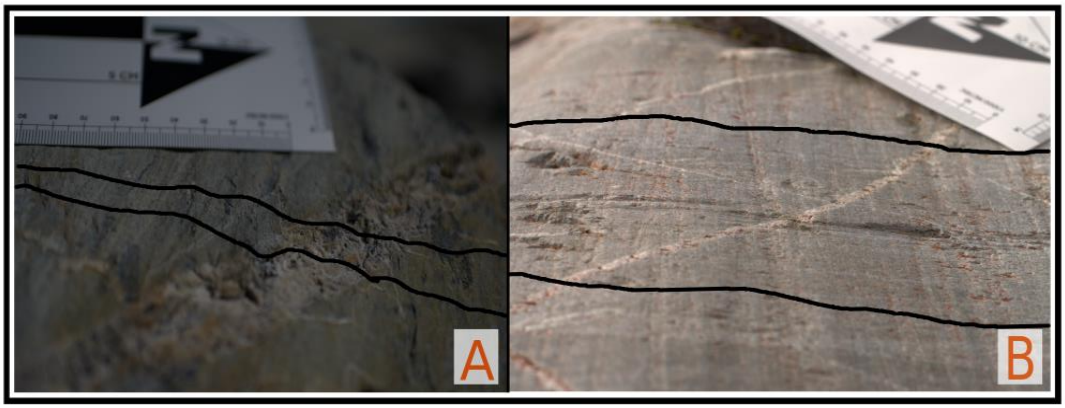

Figure 021
Side by side comparison of the two cameras used. The field of view for the Nikon with wide angle lens in image (a) has much less area in focus than the field of view for the Pentax with the macro lens in image (b), even though it is taken at a more oblique angle. Both images were shot in similar light conditions, and illustrates the poor light reception from the Nikon as its aperture must close tightly to preserve focus with the attached lens.

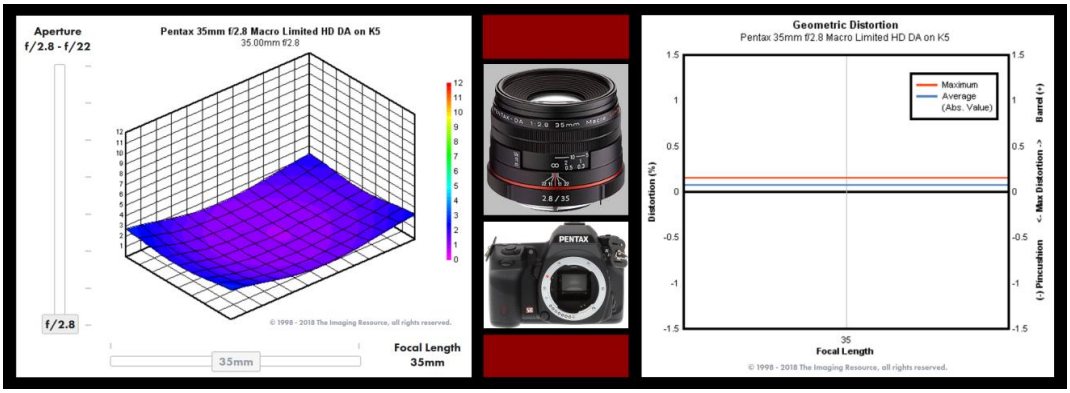

Figure 022
Lens blur and geometric distortion for the 35mm Pentax macro lens used to capture the majority of photos in the field (imaging-resource.com, 2018). The lack of distortion from the lens makes calibration and geometric corrections a simple order of business for SFM processing.

Once transferred to a computer the photographs can then be converted to a traditional file format—.tiff is favored by Photoscan—and imported as unmodified images into the SFM software.

4.1.2. Spatial Control

Preservation of scale is imperative to accurate analysis of models generated from photosets. Unlike traditionally scaled SFM models, this micro-scale modeling does not cover a large enough surface area (in the 10s of cms) to utilize GNSS-based ground control points and be anchored within a geographic coordinate system. However, without ground control points, a model cannot be exported or analysed as it has no physical dimensions. In order to rectify the situation, a scale object must be used in each photoset to allow for real world scaling of the models. The scale object should have at least three easily identifiable points on it that are of known distances apart with x,y,z, coordinates (figure 023). To produce the most accurate models, the scale object should be in three or more photographs and remain in the same location for the duration of the photoset capture. It is recommended that the scale object be a rigid item capable of holding its shape in a variety of conditions. A flexible scale object can severely damage the resolution of a SFM model by forcing the algorithms to deform the point cloud to an inaccurate spatial ratio.

Figure (023)
On left: The scale used for collecting and grounding SFM photos has multiple scales on it and a high level of contrast to most samples, yet is flexible and prone to bending. When assigning GCPs to the scale, assuming a flat surface decreases the accuracy of dense cloud generation. A 1.5 inch cube of Tungsten or Aluminum, as shown on right, would better serve this purpose due to its capability to maintain a consistent three-dimensional form.

4.1.3. Model Optimisation

Once in the SFM software, the photographs need to undergo a preliminary alignment in order to more precisely match tie points later on. With the preliminary alignment, the accuracy is set to the highest setting, the “key point limit” is well in excess of what is expected—one million is a good place to start—and the software is using the “adaptive camera model fitting”. It is important to note that in this step and all subsequent steps in the protocol, any deviation from the “high” quality setting will result in the downscaling of resolution for the output model by a factor of four. In most situations, the sparse cloud generated from photo alignment will automatically size the bounding box which sets constraints for future analysis. To improve the cross-correlation accuracy at this point, it is good to trim the sparse cloud. Often, the sparse cloud generated will have many outlying points far away from the target area and occasionally in a different plane. The extent to which this happens depends on the perspective and quality of the photosets. After deleting the errant points from the sparse cloud, the easiest method of which is to select the desired area with the selection tools then invert the selection through the editing menu, the cameras should be realigned using the “optimize cameras” function in the toolbox. This will use the existing alignment and the changes to improve the accuracy and number of points matched between photographs prior to dense cloud generation. If the camera’s specifications are intimately known, a manual camera calibration routine can be setup to further improve accuracy, and account for minimal lens distortion. However, at the small scale observed this practice is not needed.

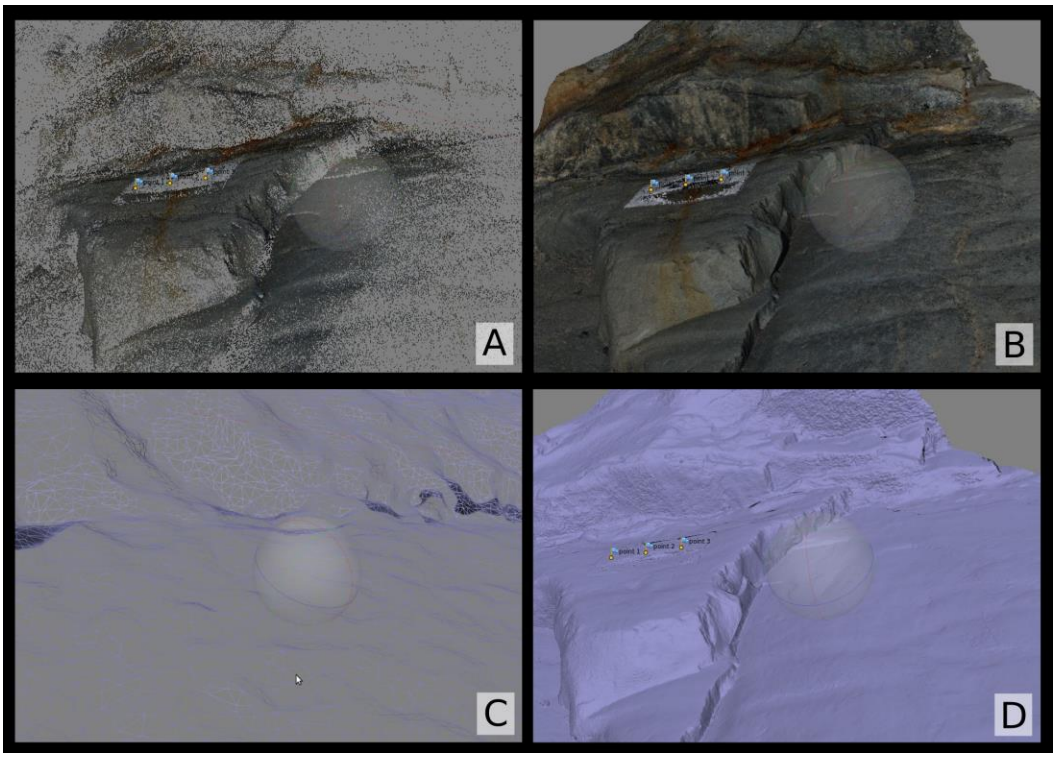

Figure 024
Screen capture images from within the Agisoft Photoscan software suite of a model generation at different points of processing. The difference between image (a) of the sparse cloud and image (b) of the dense cloud are striking. The sparse cloud is composed of 377,396 individual points, while the dense cloud has 40,473,583 points to it—a two-order of magnitude increase. Image (c) shows the framework of a TIN produced from a dense cloud when magnified greatly, while (d) represents the TIN-generated surface from the same perspective as (a) and (b). The spatial resolution of this model is 0.131 mm/pixel.

Dense cloud generation is the most computationally and time consuming function within Structure from Motion Photography. However, allocating the resources to properly run the dense cloud generation algorithms has the most profound impact on model output quality. The algorithm within photoscan takes the photo sets, and runs a series of redundant algorithms comparing the individual depth maps for each photograph against the spatial point cloud already generated, creating an increased point count usually up to an order of magnitude greater, while simultaneously orthorectifying the images (Anestis Koutsoudis et. al, 2014). The increase in precision gained by the advanced dense cloud generation process can be seen in figure 024 comparing parallel models at both levels of analysis. The observations

are visible in table 2 and table 3 in the results section for a number of analysed samples. When initiating a dense cloud generation sequence through Agisoft Photoscan for this type of small-scale data, there are a few setting tweaks that ensure the software is using the most efficient algorithms for the dataset. The quality of model which can be generated hinges upon the computational resources available to the researcher. Table 1 displays estimated general values correlating computational resource with model complexity. In this case, a high performance cluster server was available with 32 cores and 128GB of random access memory. However, due to the resolution and number of photos utilised, even this powerful machine could not successfully render dense clouds in the "highest" quality mode. Therefore, every model run for this research was done using the "high" quality setting. For the study of very small surface features—as was the case in these experiments—the depth filtering setting within the advanced properties must be changed from the default of "aggressive" to "mild. Depth filtering smooths out the high frequency data in a rendered surface, but must be set to a lower experimentally determined threshold so as not to mute the targeted signals.

Photos	20 - 50	100	200	500
Lowest quality	100 MB - 300 MB	150 MB - 450 MB	300 MB - 1 GB	1 GB - 3 GB
Low quality	500 MB - 1.5 GB	750 MB - 2.2 GB	1.5 GB - 4.5 GB	4 GB - 12 GB
Medium quality	2 GB - 6 GB	3 GB - 9 GB	6 GB - 18 GB	15 GB - 45 GB
High quality	8 GB - 24 GB	12 GB - 36 GB	24 GB - 72 GB	60 GB - 180 GB
Ultra high quality	32 GB - 96 GB	48 GB - 144 GB	96 GB - 288 GB	240 GB - 720 GB

Table 1. Processing resources in gigabytes of random access memory (RAM) required to generate a dense cloud model in "arbitrary" mode, based on the quality and number of photos used. The resolution, perspective, and focal quality of source photographs will greatly influence these values. Numbers drawn from the Agisoft informational website (Agisoft Inc., 2017).

Following a successful dense cloud generation, a surface mesh in the form of a triangular irregular network will be formed by connecting each datapoint with all of its adjacent brethren. Figure 024 images (c) and (d) illustrate the appearance of

the mesh and the final surface which results from the empty spaces between points being filled in as a surface. This step is the final point before the true quality of the rendered model can be visualised. Mesh generation settings optimised for small features should be as follows: Mesh type set to “arbitrary”, this setting rather than “height field” puts more processing focus into calculating the depth function with more accuracy, whereas “height field” is designed for perpendicular flyover aerial shots and calculates only 2.5D for the depth field. The source data should originate from the dense cloud using interpolation for all point classes with a high face count output. Following the tessellation of the TIN, the photographs have completed the full course of multi-dimensional alignment, and will now be spatially locked to one another for the coordinate system establishment.

Traditionally with a normal SFM landscape model this point in the procedure one would simply generate a DEM and be done with the process. However, due to the small size of the studied region, a traditional geographic coordinate system cannot be assigned, as the distance between points are simply too small to capture accurately with GNSS. Photoscan cannot generate a digital elevation model without spatial data, so a minimum of three markers must be placed on the model with known coordinates in the xyz space. In this case, ground control points are determined from secondary context targets rather than GNSS points. The scale item described in figure 023 functions as a spatially consistent platform for all ground control points. With the photos aligned, the procedure for assigning scale and GCPs is simple. The corners or marked areas on the scale item of known relative spatial orientation will be designated in the system by placing a marker at each location. A single photo from within the set which has the scale item in focus will suffice. Once the markers have been placed, the prior alignment of the photos will allow the software to automatically determine the location of the markers in every other aligned photograph.

The photos will now need to be re-aligned to incorporate the new spatial data. The “align photos” step can be omitted, while the “optimize cameras”, “build dense

cloud" and "build mesh" functions will need to be repeated with the exact same parameters. Before generating a DEM from the now properly dimensioned model, the surface will need to be oriented in space so the resulting exported surface has the correct azimuth. Photoscan does not currently have a function to accomplish this, so a workaround has been developed by Agisoft users and placed in the open source wiki, which utilises a small amount of python code (Agisoft, 2017). The bounding box can be resized and rotated around the model, and should be done so in order to have the target surface parallel with the bounding box surface, with the red face of the bounding box below the model. Be sure to examine the box-model system from all angles to ensure full containment, as there are no axial locks on adjusting the bounding box in 3D space so it is quite easy to place a point in the wrong location. Orient the view so the perspective is perpendicular to the surface, then run the python code through the photoscan console: "coordinate system to bounding box.py" (appendix 9.1.). The model should now be locked in the proper coordinate system and orientation. Depending on the desired secondary analysis method, this is a good step to trim the mesh to ensure the exported model is free of defects. Build and export the DEM using the mesh as the source data and keeping all other settings default. The tessellation of the mesh will generate the same quality DEM as the dense point cloud in hi-resolution mode, and is much easier to work with for window modification. The resulting .tiff file can be utilised for further analysis on a wide variety of software platforms.

4.2. Field Work

The field sites were visited and sample data collected as described in section 2.4.3. and 2.5.3. in accordance with the procedure outlined in section 4.1. The areas were scouted, transects selected, photography captured, and samples extracted. The resultant material was brought back to the Victoria University of Wellington campus for analysis.

Site and transect determination was particularly critical for this research, as the aim was to eliminate the influence from as many outside sources as possible. Keeping

the number of variables controlled was a priority to secure correlations between sites, and ensure that the changes between sites could prove statistically significant for the remaining variables in an effort to develop a ubiquitous set of observations from which to base the subsequent models. Variables left to account for, such as meteoric water exposure, annual snowfall residence time, and slope angle were considered. An attempt to maintain consistent lithology was made, though the complex parent rock at both sites precluded this without biased sampling. Despite having limited options for research areas based on accessibility and morphology, an attempt was made to select sampling transects that shared as many characteristics as possible.

As sample sites were chosen for photographic analysis, surface exposure ages and compositional determination, specific features were targeted for physical sample collection. Cosmogenic radionuclide surface exposure dating via ^{10}Be utilises quartz and as such any regions within an identified sample area with prominent quartz veins were identified as potential collection sites. However, the coherent nature of the partially metamorphosed rocks presented a notable challenge for physical removal. A portable electric rock saw was carried to site, but with limited battery resources the most favorable method of extraction was via sledgehammer.

Prior to sample collection, extensive photogrammetry at each site was conducted for future model generation and surface reconstruction. In accordance with the procedures detailed in 4.1.1. photographs were captured of the desired surfaces at multiple scales. Though memory volume available was not infinite, it played a role of little significance in dictating the number of photographs captured. At the closest scale from which the most detailed models would be generated, great care was taken to utilize every perspective possible with a variable depth of field (figure 025).

Figure 025
Capturing the most detailed photographs of samples often requires creative camera positions and stabilisation to preserve the best resolution of data. Hunting for the perfect lithological exposure amidst the moss and lichen on a large bedrock sample area above the Franz Josef Glacier.

Photographs were then captured from two larger scales—approximately 1 meter out, and again at 3-5 meters out from the proposed rock samples to be collected—and again in accordance with the protocol outlined in section 4.1., multiple perspectives were gained. Initially set to encompass four scales of observation for each sample when combined with a basin scale model, the 1 meter samples were taken standing next to the sample at waist height, and the larger scale 3-5m standing at various points on a perimeter holding the camera overhead for optimal perspective change.

Following photogrammetric surveying of each sample site, subsequent physical sample extraction gathered 1-2 kg of rock, depending on the lithology and relative size of quartz features present. The maximum depth of sampling in-situ varies with

material properties, though for the case of ^{10}Be generation in quartz, ten centimeters is the recognized maximum to avoid errors due to depth attenuation within datasets (Gosse and Phillips, 2001). This was taken into account, and each sample set was extracted ensuring to not source any sample material from deeper than 5cm—a feat easily facilitated by the hardness of the local bedrock at Brewster Glacier.

Prior to moving to the next sample area, cosmic ray shielding values were recorded, GNSS coordinates and elevations captured, and other notable site features such as striae orientation and planar strike captured.

4.3. Sample Preparation

The physical samples collected on site are slated to be analysed through multiple mediums, and as such must be prepared in the manner appropriate for each measurement technique.

Large rock samples must first be subdivided with a rock saw to isolate areas to preserve for more precise preparation, and to provide manageable pieces which fit into the rock crusher for the next step of cosmogenic sample preparation. Billets and uncovered thin sections were made from the desired areas before crushing, which preserved a cross section through the weathered surface of the rock.

The portions cut for billets and thin sections were cast in epoxy and set overnight, before being refaced and polished to the appropriate texture. Billets were analysed with XRF and SEM BSE microprobe analysis, while the uncovered thin sections were used for SEM BSE microprobe and SEI processing for mineral distribution identification as well as mineral grain boundary characterisation.

From this point forward, the physical sample processing was entirely focused towards quartz isolation for cosmogenic radionuclide analysis. The remainder of the rock body was crushed using a rotary-powered Boyd rock crusher. The products were separated and re-crushed until no fraction was larger than 1mm. Following

another round of sieving, any rock particulate larger than 750 µm were brought down to size using a ring mill with tungsten carbide dies.

Crushing products were first dry sieved and separated into fractions of 750-500 µm, 500-250 µm, and 250-125 µm. Any material less than 125 µm was set aside and labeled as "space dust" due to its resemblance to lunar regolith. While targeted as waste, this fraction was set aside in case it had future utility.

These fractions were then brought over for magnetic separation. The first step within magnetic separation was to remove the ferromagnetic component of the sample by passing a bar magnet through the sample multiple times in order to attract and subsequently remove the iron-containing minerals. This removed only a relatively small percentage of the sample, but was a crucial step to prevent the equipment in the next step from becoming clogged.

Following ferromagnetic filtration, the samples underwent paramagnetic separation by a Frantz Isodynamic Magnetic Separator. All of the remaining minerals in the sample are devoid of ferromagnetic components, but when subjected to intense magnetic fields can either be attracted (paramagnetism) or repelled (diamagnetism). With quartz famously diamagnetic, the Frantz separator enabled a mostly pure quartz fraction to be isolated from the remainder of the sample. Settings applied to the Frantz machine varied based on sample size, roundedness, and level of paramagnetic interaction. Each sample should be evaluated accordingly to optimise the various equipment parameters such as the tilt adjustments, as well as bed and feeder vibration frequency, in order to have the most efficient separation.

It was soon discovered after processing the majority of samples that, at the recommended separation fractions between 750 µm and 250 µm, the grain size was not small enough to establish breaks between the quartz and adjacent minerals. Investigating the magnetic waste samples showed a large number of quartz grains with small inclusions of magnetic material that were preventing them from being

properly separated on the Frantz. Yields from the 750-250 µm fractions were exceptionally low, on the order of 5-15g per kg of sample. For the later chemistry steps of cosmogenic radionuclide sample dating a target minimum of 40 g of sample is required in the processing steps, and in excess of 80g is strongly recommended.

The remaining 250-125 µm fraction was wet sieved to clean the excess powdered material from it which otherwise acted to clog the Franz channels. Yields were much more efficient for the smaller fraction. The "space dust" fraction of material less than 125 µm was investigated for potential quartz content.

An experimental procedure for isolating quartz from the ultra-fine waste material was developed. Dry sieving was quickly abandoned as the ambient static electricity charge prevented grains from becoming properly clean, which would then in turn clog the Franz separator. Two stage sample washing and wet sieving was eventually chosen as the preferred method.

Generous amounts of sample were placed on a 45 micron or No. 325 ASTM mesh sieve, and water added to fill the sieve part way. The mixture needs to be constantly agitated to clear material of the sieve surface and allow water and finer material to drain. The best method for doing so was to massage the mixture in the sieve with one hand, moving the fingers in a circular motion to clear particulate, while rotating the sieve base slowly with the other hand. Water must be constantly added during this stage, with careful consideration to the balance of flow rate and drainage rate of the system.

Once the mesh drains freely around the filtered material, it was transferred to a large beaker >500mL and immersion rinsed with turbulent flow several times to ensure no fine powder makes it through. The clean, separated fraction was placed in a foil drying tray, and the process was repeated 4-6 times until the full volume of each sample had been processed. The trays were placed in a 50°C desiccating oven for several days to completely dry.

The new clean extra fine fraction was passed through the Frantz again, with reduced bed tilt angle along both axes due to the increased flow rate of the smaller and more regular grains. Magnet voltage remained constant for improved pickup. The final products of Franz separation generated unexpectedly high yields, with one sample increasing from 5.26% quartz to 38.9% by mass.

Products of Franz separation we then taken to undergo gravimetric determination and the sample masses were recorded as the starting baseline for subsequent cosmogenic radionuclide testing analysis. Care was taken to keep size fractions separate for every sample, as in later chemistry steps, surface area increases Hydrofluoric Acid (HFA) reactivity and could cause sample to be consumed.

4.4. Cosmogenic Radionuclide Surface Exposure Dating

Following sample preparation, the protocol for ^{10}Be dating became largely chemistry-based and was carried out in Victoria University of Wellington's specialized Cosmogenic Nuclide Laboratory.

Following modified protocols built off the principal laboratory techniques of von Blackenburg and others (2004), the standard 750-250 µm fractions were dissolved, cleaned, solubilized, and separated for ^{10}Be. A series of HCl, HF, and Aqua Regia were utilised to clean and etch the samples and rid them of any foreign material other than pure quartz. The purified sample is then dissolved in concentrated HF and introduced to a series of cation exchange columns and precipitation steps to isolate the ^{10}Be from other elements present in the quartz.

The remaining extra fine 45-125 µm fractions were processed through an experimental version of the same protocols, currently in development with PhD student Ross Whitmore. These samples had to be treated with additional care, as their increased surface area introduced the possibility of quartz consumption via the

many strong acids used throughout the standard procedure. This dramatically reduces the margin of error with times surrounding solution introduction and rinsing, and to compensate, lower concentration analogous mixtures were employed.

The resulting isolated ^{10}Be samples are packed into targets and shipped off to an international facility for analysis with Accelerated Mass Spectrometry (AMS).

4.5. XRF

X-ray fluorescence (XRF) is a style of compositional analysis performed by exposing a sample to primary X-rays and measuring the secondary X-rays emitted as a response of excitation. An accurate report of elemental composition is generated for each sample. XRF is particularly attractive as it is a non-destructive technique, and has to potential to by employed in the field to analytically assess in-situ samples that cannot otherwise be collected for lab analysis.

XRF can be applied to both powderised and whole samples. For this study, XRF analysis was conducted on the billet samples for each sample area to gain bulk geochemistry values. Every site at Brewster glacier had a small and a large billet produced. Each billet was analysed at three different locations to gain the most accurate reading from which to approximate the sample's body composition. Each analysis was conducted at the standard voltage, and again with a 50 kV setting. The higher voltage increases the accuracy of the XRF analyser with respect to heavier elements, and facilitated readings for materials such as lead, thorium, and tantalum. This resulted in twelve representative XRF readings for each sample to be further analysed for compositional trends (see section 5.4. and appendix 9.7.).

4.6. SEM

With small scale and high accuracy in mind, Scanning Electron Microscopy was looked towards for both optical observation at the smallest scale possible, and compositional variations with microprobe point analysis. Backscatter electron imaging (BSE) received the most attention due to its ability to generate images showing elemental composition variation with representative optical contrast values, which were used in subsequent processing. Secondary electron Imaging (SEI) was utilised to investigate for variations in surface morphology, by looking at the physical separations of minerals along the surface profiles of each sample. Both wavelength-dispersive spectrometry (WDS) and energy-dispersive spectrometry (EDS) were utilised for full sample compositional analysis, as well as spot analysis on regions of interest to identify the composition of specific minerals. The equipment available for carrying out these specific procedures was Victoria University's JEOL JXA-8230 SuperProbe Electron Probe Microanalyser (EPMA). The instrument is a highly sensitive system featuring a combination of 5 wavelength dispersive X-ray spectrometers (WDS), a recently developed energy dispersive X-ray spectrometer (EDS) analyser featuring spectral imaging, a JEOL xCLent 3 cathodoluminescence (CL) spectrometer, and highly sensitive detectors for acquisition of backscattered electron (BSE) and secondary electron (SEI) images (Victoria, 2018).

An attempt was made towards the novel application of elemental fractionation of Germanium during cumulative weathering (Kurtz et al., 2002). Unfortunately, the presence of Germanium above detectable limits on the WDS was insufficient across the sample suite to be used as a viable method.

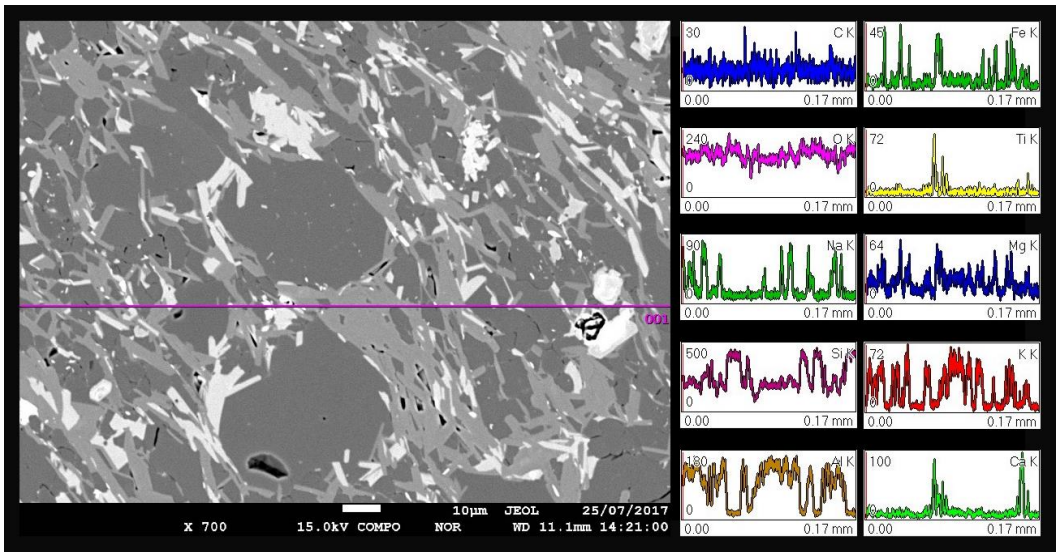

Figure 026
Linear elemental composition scan with EDS. Associated elemental concentrations with vertical axis maxima of parts per million relative to each element. Elemental identifications are noted in top right corners, and proceeding clockwise are: Carbon, Iron, Titanium, Magnesium, Potassium, Calcium, Aluminium, Silicon, Sodium, and Oxygen.

A general scan along a transect with EDS for each sample generated a reading of average compositional makeup. This is possible by designating a linear region throughout the amount of sample in the given window, and perform several thousand spot analyses along it. The data produced arrives in the form of a waveform for each element present, and its relative concentration along the chosen transect (figure 026).

Each prepared sample contained a profile through the surface of each sample, SEI was used to map and characterise variations in surface morphology. Images were captured between 200x and 1,100x magnification. The SEI images were exported to ImageJ, an imaging processing tool, to investigate the texture of the surface, and the presence of chemical alteration or mechanical breakup, if any, and the depth to which it occurred.

BSE played the largest role of SEM analysis, with each sample receiving at least ten separate images each with 3-10 microprobe spot analyses. This allowed for targeted analysis of specific regions of interest based on their arrangement of elements, otherwise not visible with standard imaging techniques. BSE images were collected along a wide spectrum of magnifications, ranging from 40x to 1,200x. The images were exported to a secondary image processing suite, ImageJ, and analysed for compositional variations.

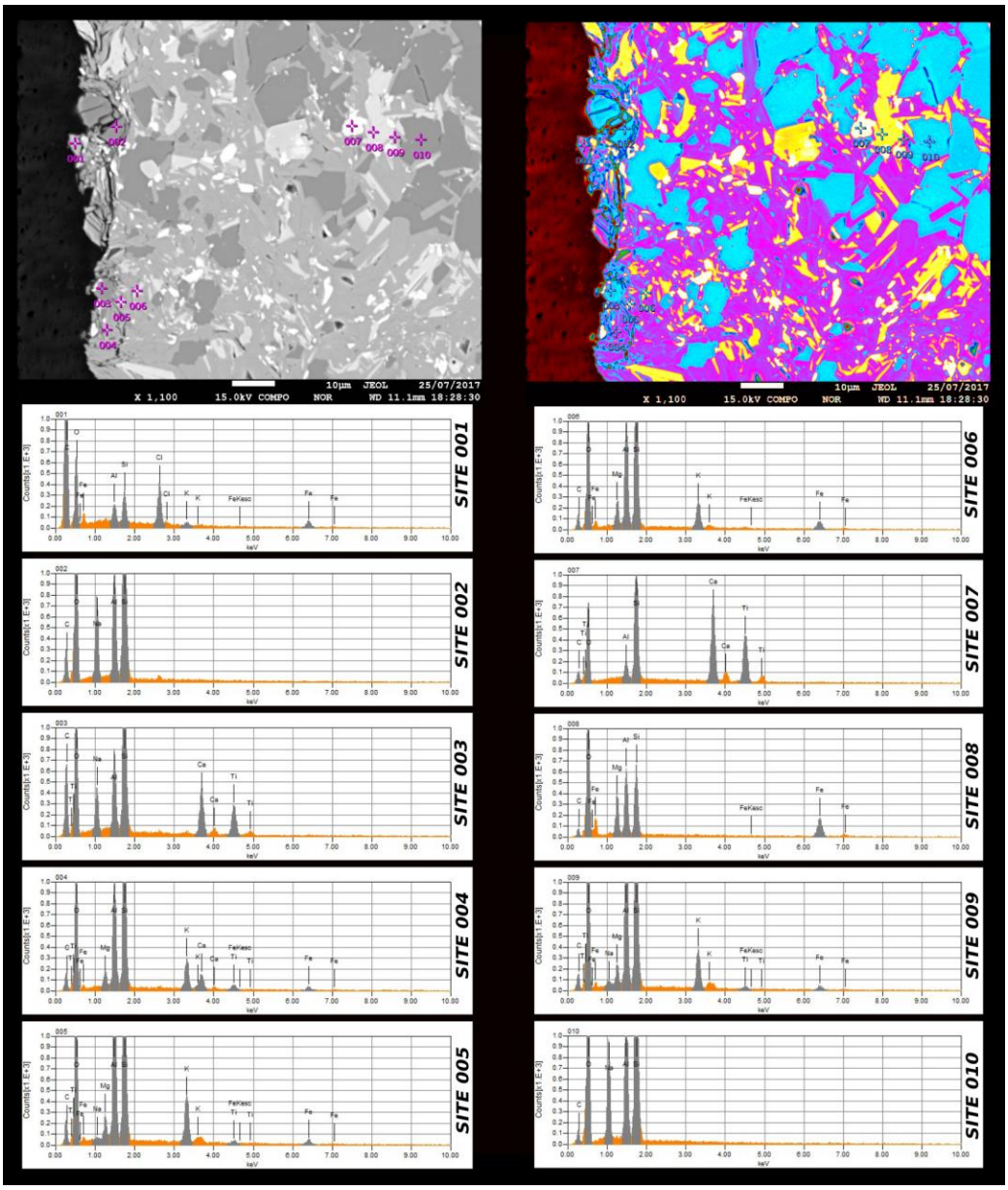

Figure 027
Backscatter electron imaging (BSE) of sample B_05 from Brewster Glacier. At left is the microprobe output greyscale image, and the right is the same image with a false-color filter applied. The microprobe spot analysis locations can be easily seen on the greyscale image, and their associated EDS spectra are listed below.

Within ImageJ, each image was converted to 8-bit color, and the greyscale BSE images had a false-color filter applied, which matches specific grey values of each pixel and assigns them a corresponding hue and saturation to generate an optically more contrasting image (figure 027). Subsequently, each image was analysed with

the Versatile Wand Tool, which allows all pixels of the same hue, saturation, and value within an image to be selected. Custom value tolerances were selected which helped to speed the process up and set boundaries for minerals. A value tolerance of 8 and the non-contiguous function were used for all analyses. Once all of the desired pixels of a select color were chosen, the "Cell Counter" plugin from the "Analyze" toolbox was used to quantify the number of pixels within the selected thresholds. To prevent recounts or skipped pixels, each value range selection was deleted prior to initiating the next count (figure 028 & figure 029). The recorded values represent the percent composition by area of each sample, and were exported to a spreadsheet program for future analysis.

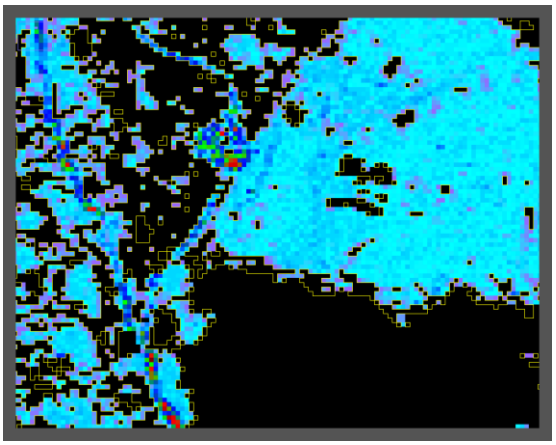

Figure 028
High-zoom screen capture during optical analysis of false color images. Note the pixelated nature of the window and the gradient of colors present.

Figure 029
View of sample BSE throughout the optical compositional quantification process. At left: The initial false-color image of the greyscale BSE prior to mineral selection. In center: The sample image during an intermediate stage where one mineral group has been quantified and removed. On right: The sample image is almost entirely empty following the quantification and elimination of the three remaining minerals.

Billets were investigated initially, and while they emitted strong signals for compositional analysis, the false color image analysis they would be used for proved ineffective due to the noise generated by polishing marks and the lack of contrast between solid samples. The mounting procedure for the billets was much more complex due to their non-uniform nature, and the mounting adhesive used to position them was adversely affected by the pump-down to full vacuum, often resulting in a shifted and out of focus sample. Furthermore, during the carbon-coating process the billets had a tendency to accept more carbon coat than required, which further distorted some of the images. The analysis was switched to the uncovered thin sections, which proved to be a superior medium for all avenues of analysis as the increased contrast allowed for more precise targeting while driving the multibeam microprobe.

4.7. Computational Lab Work

A large portion of data synthesis, model generation, and quantification analysis was executed on digital platforms. Personal computers, university workstations, and high-performance-cluster (HPC) servers were all utilised at different stages of analysis, often simultaneously to generate and synthesise the characteristics of the sample sites in two, three, and four dimensions.

4.7.1. Agisoft Photoscan

Structure from motion photogrammetry was carried out through the Photoscan software suite developed by Agisoft LLC. The procedure developed for use with exceptionally small scales of observation were followed as detailed in section 4.1.3. The model outputs were DEMs of exceptional spatial resolution, to be subsequently used for feature analysis.

Global polynomial interpolation filtering and continuous wavelet transform analysis were applied independently to the Phoscan output digital elevation models, with the objective of characterising weathering patterns via geometric and

volumetric quantification, explicitly surface area ratios and artefact population amplitude frequencies.

The aims the computational work on the digital elevation models generated through Photoscan, was to gain accurate numerical representations of two physical surface observations made at sampling sites. One was to obtain a volumetric quantification of weathering in-situ as represented by missing material of selected surface features. The ability to distinguish between the signals of weathering etch pits and pre-existing glacial striations was crucial. The second task was to develop a metric with which to accurately represent surface roughness. This required measurements of three-dimensional surface area as well as identification of all present surface features such as etch pits, and post-filtering quantify their maximum depth from an interpolated original surface reconstruction.

4.7.2. Global Polynomial Interpolation Filtering Analysis

The popular mapping software suite ArcMap from ESRI's ArcGIS package was used for volumetric analysis and feature classification. The protocol carried out in ArcGIS* was as follows:

* It is important to note that some of the analytical tools and procedures used are not operable in all versions of ArcGIS. Version 10.2.0.3348 was used.

1. Import data to ArcGIS with the "add data" function. Ensure that the imported raster is in GRID/ESRIgrid format.
2. Format the Map Layer Properties such that the map units and reference units agree. In this particular case, meters is the unit chosen.
3. It can be helpful to generate a hillshade for the starting DEM to ensure that the correct model has been imported before beginning processing.
4. Using the Clip tool in the Data Management Toolbox, crop the desired study area so as to include only the most precise features, and ensure that any edge

effects from improper DEM export are avoided. Again, ensure that the imported raster is in GRID/ESRIgrid format.

5. To ensure a preservation of raster resolution throughout the process, the preferred output cell size should be set to the clip file that has been created. This is done through the Raster Analysis function of the Environments tool, which can be found in the Geoprocessing drop-down menu. If cross-scalar analysis is desired, use the coarsest DEM resolution for each scale, and always reference this to normalize resolution. In the same line, a cubic or bilinear resampling method should be employed. The function can be found using Raster Storage->Resampling Method->CUBIC (or BILINEAR). This makes the resolution reduction process more accurate by interpolating for substitution values rather than picking adjacent values, which can often cause small features to be obscured.
6. Using the Geostatistical Wizard function of the Geostatistical Analysis Toolbox, apply a Global Polynomial Interpolation (GPI) to the newly clipped DEM using the Gridcode function for reference. Any order polynomial between 1 and 10 may be chosen. The function of a polynomial interpolation is to estimate the larger scale features such as topographic undulation, large glacial striae, artefacts of misaligned model export, and build a surface containing only these features. The difference between this surface and the starting DEM will produce a Dem of DIfference (DoD) which highlights the features of interest without distortion from larger scale artefacts (figure 030).

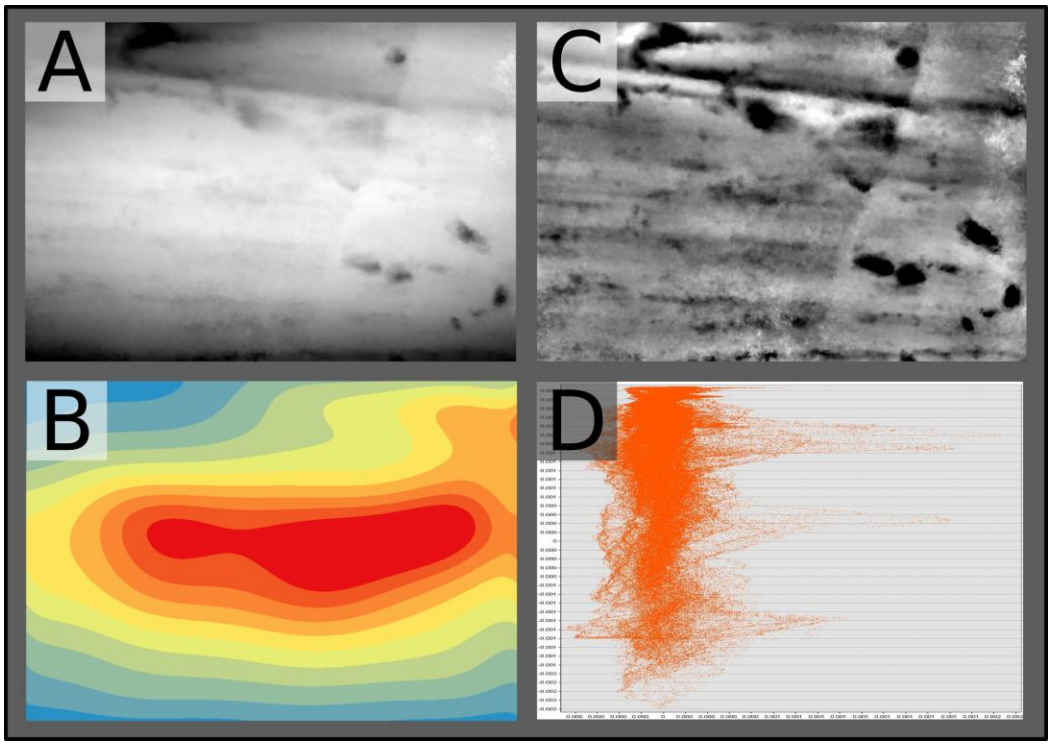

Figure 030
The function of a surface filter applied from a Global Polynomial Interpolation (GPi) is demonstrated here. (A) shows the original DEM, whose features are weakly expressed, and the edge effects of the curved surface projected onto the 2D format washes out the gradient applied for height determination. (B) shows the 10th order GPi generated from the original surface. The difference between (A) and (B) are shown in (C) as the modified surface now free of edge effects with increased sensitivity towards smaller features. (D) shows the distribution of points generated alongside the GPi, representing the accuracy of matching features by the polynomial.

7. Once the calculation has finalised, export the results table as a shapefile, which will be automatically imported into the current map layer.
8. It is recommended to repeat steps 5-7 with multiple levels of polynomials until the most accurate envelope is selected to eliminate local morphology without affecting the targeted small scale features (figure 031). For this research, the 10th order polynomial was chosen for its best fit capabilities.

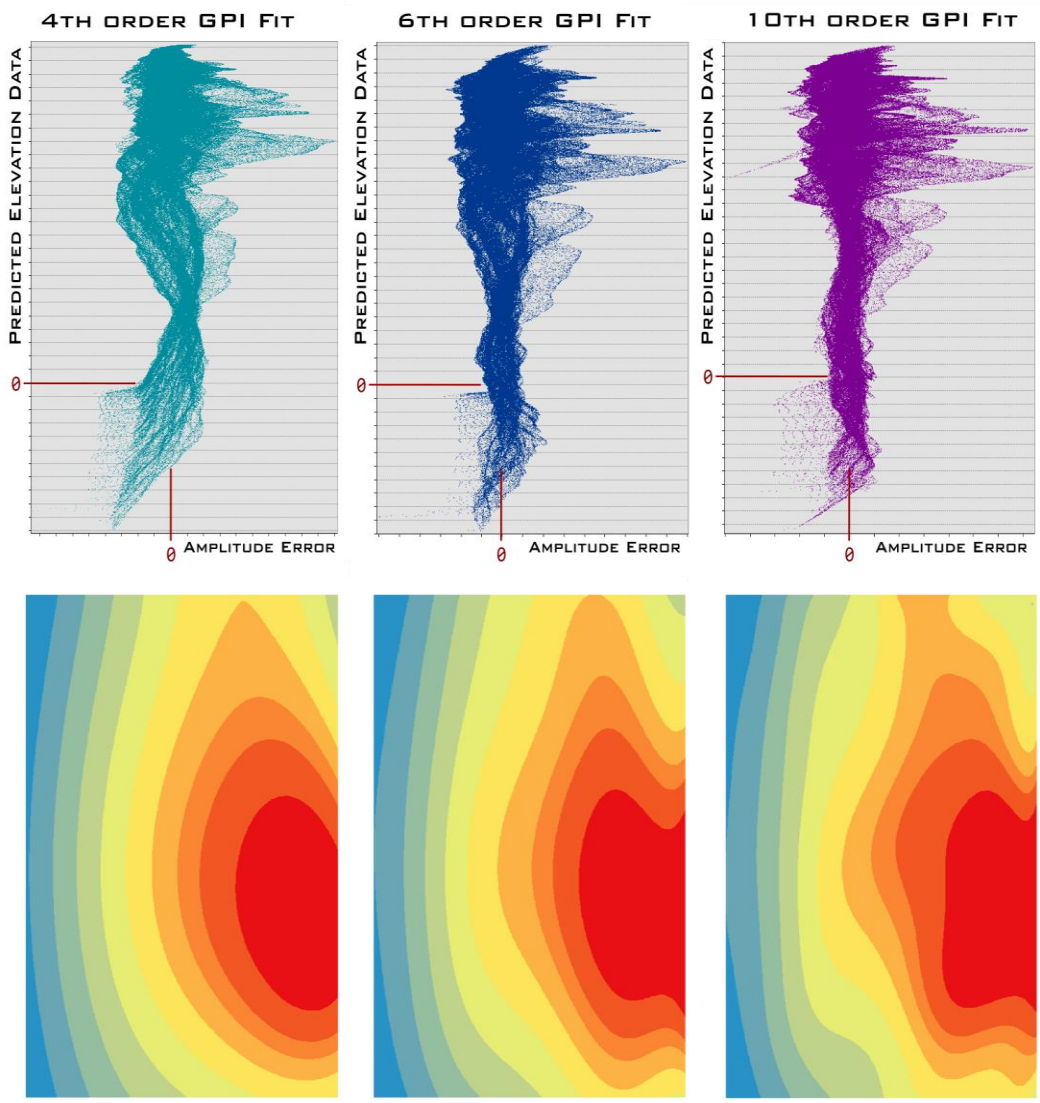

Figure 031
Depiction of three different orders of Global Polynomial Interpolations. The interpolated surface layer and level of fit point cloud are shown for each polynomial. From left to right: 4th order GPI, 6th order GPI, and 10th order GPI.

9. To speed processing time, it is recommended that the size of the exported GPI shapefile be reduced in the number of points. This is accomplished through altering the size of training feature subset to ten percent through the Subset Features function of the Geostatistical Analysis Toolbox.
10. The GPI layer (not the shapefile) will need to be exported to a raster format with the same processing extent as the original clipped source DEM. It is

imperative to set the cell size of the GPI raster export to the setting for the original clipped source DEM file, generated in step 4.

11. A DEM of Difference (DoD) will be created by subtracting the original clipped DEM from the GPI raster layer, using the *Raster Calculator* tool from the *Map Algebra* package of the *Spatial Analyst Tools*. This will show the roughness of the surface after being filtered by the GPI, and allow for more accurate amplitude measurements. The values will be inverted in order to highlight the negative relief features as positive integers, to make further processing more efficient.
12. The effectiveness of the polynomial interpolation used can be assessed by generating a scatter plot from the attribute table of the reduced count GPI shapefile and plotting the predicted values for elevation by the polynomial against the error generated from the DoD. The graph will closely resemble the one shown in figure 032. As values are inverted through the DoD, negative outliers on the graph will represent positive relief features, while the positive values will represent erosional features such as pits and striae. Points of high predicted value will be deepest, and the low values will be the smallest. Often, there is a low amplitude negative tail representing an imperfect fit with surface curvature. The targeted features, namely pits and high frequency striae will be represented by a series of high value positive peaks to the upper right of the graph. These can be selected and their associated features highlighted in map view for verification.

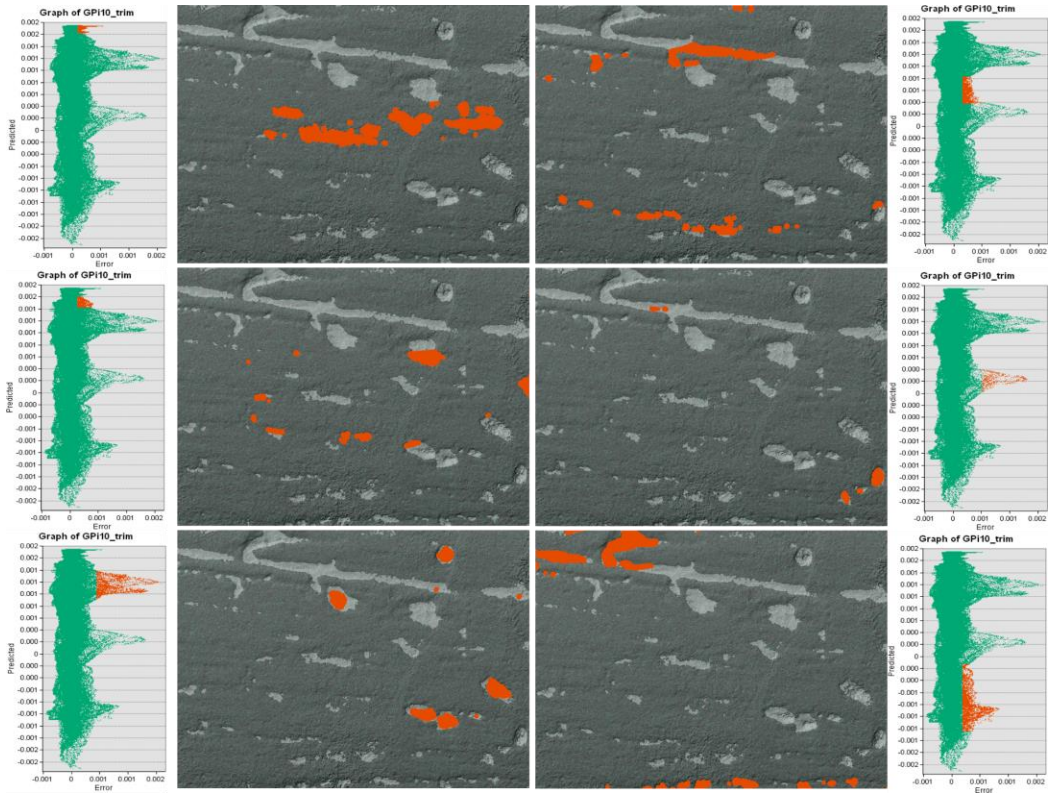

Figure 032
GPI calibration point cloud resampled to show different surface features. Points downsampled to 10% are representative of the accuracy of fit for the GPI filter. Points are graphed as GPI predicted value against error from true value. The highlighted regions of point cloud correspond to different surface features.

13. The classification ranges for the targeted features must be identified. By changing the break values in the Classification menu of the Symbology of the DoD along the histogram, this can be achieved. The best way to establish the most representative break values is to overlay the DoD layer on a hillshade of the original clipped DEM file, with the DoD transparency (found in the Display segment of the Layer Properties) set to 60%.
14. With the classification break values representing all of the desired features, Reclassify the DEM of Difference using the Reclassify tool within the 3D analyst toolbox. By using the Value Reclassification field, the break values set in step 13 will be imported, and each range will be assigned a number. With two groups a binary image will be produced. This will allow the

separation and objective analysis of the weathering features independent of the remaining surface.

15. In order to quantify frequency characteristics of the features, they must first be made independent of one another. Using the Region Group tool within *Generalization* subset of the *Spatial Analyst* toolbox, import the reclassified raster and group with four neighbors to group adjacent pixels, and separate independent groups of pixels (figure 033).
16. To gather amplitude and frequency distributions of features, Zonal Statistics are required. Using the *Zonal Statistics as Table* tool of the *Zonal* subset within the *Spatial Analyst Tools*, import the Region Group raster layer as the *feature zone data*, keeping the *Zone Field* at 'VALUE', and using the DoD raster as the *Input value raster*. The statistics type should be set to 'ALL'.

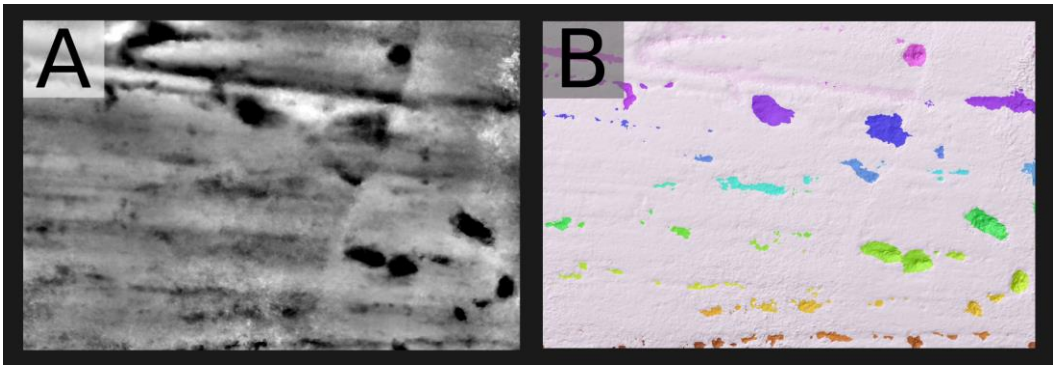

Figure 033
Visual representation of the products of a 'Region Group' function. (A) shows the DoD, with surface features defined by the darker values representing negative elevation. Following reclassification and grouping of adjacent pixels, the individual surface artefacts can be investigated separately. (B) shows the region group overlain on a hillshade for contrast.

17. To view the correlation between zonal statistics values and surface features within the model, the data must be connected between the Region Group and DEM of Difference using a 'Table Join'. This is not necessary, but very helpful to verify the accuracy of results before moving on.

18. The output table should supply values of pixel count, area, depth, and other characteristics of the independently grouped surface features. The *Max* category values will represent the maximum depth of each surface feature, as they are inverted from step 11. The distribution of these features will be determined by interquartile statistics so as to be ubiquitously applicable between samples of varying morphology and scale.
19. As the value to be calibrated by these features, area ratio must also be calculated. Using the *Surface Volume* tool of the *3D Analyst* toolbox, input the DoD generated in step 11, with the *Reference Plane* set to 'ABOVE', and all other option factors unchanged.
20. The output table will have values for the 2D area (planimetric) and 3D area (surface area). By dividing the surface area by the planimetric area, as discussed in section 3.5.1., the resultant value will be the area ratio—and the core metric of surface roughness.
21. Results are analysed using spreadsheet processing and the statistics program "R".

4.7.3. Continuous Wavelet Transform Analysis

MathWorks MATLAB 2016a version was used, performed on the Victoria University of Wellington Geology HPC server, tara. The 32-core, 128Gb RAM high performance cluster enabled more complex coding structures to be utilised for model analysis.

MATLAB was employed to perform the same calculations as carried out through ArcMap, but with a higher preservation of detail in every operation. The main shortcoming of ArcMap's procedure is the limit of Global Polynomial Interpolation levels accessible. With the discovery and adaptation of wavelets, MATLAB was explored as a more powerful and accurate processing alternative. The two methods were operated in tandem to allow for an objective comparison between the two methods of gathering the same data through vastly different procedures.

The data input to begin the procedure can either be a raw uncut DEM directly from the Photoscan export, or an edited one. Though the CWT function can ignore the majority of edge effects, it is a good idea to start with a trimmed DEM. As the ArcMap procedure had already been run, each sample site had a prepared clipped DEM at full native resolution.

The script can be run, and a continuous wavelet transform operation will be completed across the surface utilising the Ricker Wavelet—more commonly known as the "Mexican Hat Wavelet". The wavelet is shifted across the entire surface at variable scales and dilation parameters, with the end result being a selection of features that correlate with the physical 3D shape of the wavelet over the largest range of dilations below a specified threshold. The use of a CWT wavelet is critical, as it characterises features only on the similarity between waveforms, and as such is independent of orientation of the imported datasets and applicable across scales, negating the need for first order polynomial interpolation to prepare the surface. The superposition of wavelet transforms over a cumulative surface results in a four-dimensional dataset, in the form of a spatially varied time-series style dataset of changes in three-dimensional data, which can be complex to interpret. To circumnavigate this, the *'cwtft2'* function is applied, which generates the analysis in a 2D space and uses a Fourier transform-based algorithm in which the 2-D Fourier transforms of the input data and analyzing wavelet are multiplied together and inverted (Mathworks, 2018).

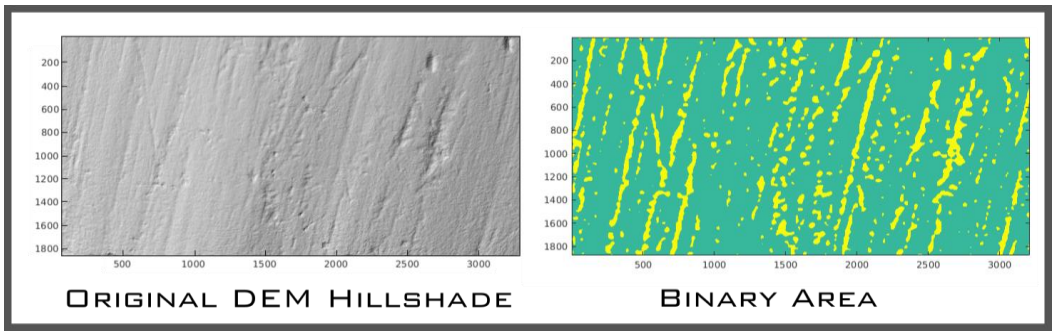

Figure 034
Sample B_04_Hi-Res as an original DEM Hillshade and the binary image output by MATLAB after analysing the DEM for surface features with a specified continuous wavelet transform algorithm.

The CWT function outputs are organised into binary images with thresholds to filter frequencies and distinguish extant features from signal noise (figure 034). For the selected models, threshold values for a real number was set to $1x10^{-2}$, which isolates the background noise of the TIN vertices and particularly deep striations which are presented as elongate pit artefacts, in effect setting a filter for our desired feature size. This $1x10^{-2}$ threshold binary dataset is to be used for the subsequent analysis, and for ease of function continuity the last line of code translates the desired data package into a format recogniseable by the pit statistics function.

The function '*pitstats2.m'* can now be run without the modification of any presets. Through this procedure, the binary image of pit area is imported as renamed in the last step of the previous function. The first routine beginning with *"bwimage"* creates a logical image from the data which facilitates improved processing times down the line.

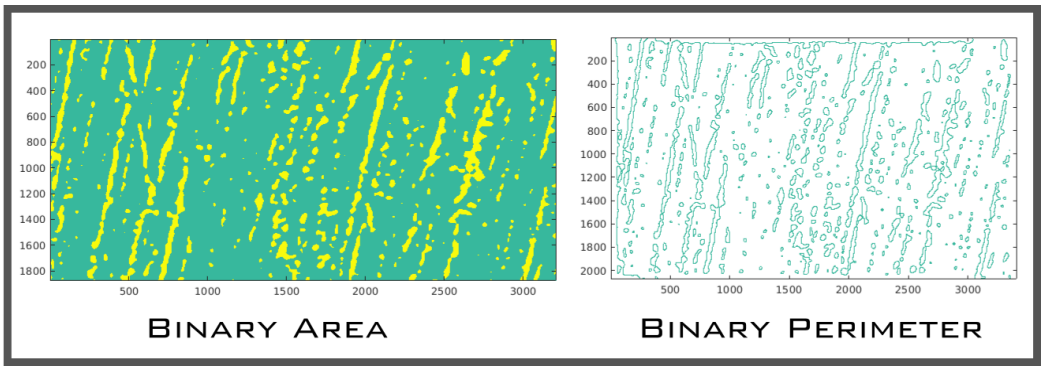

Figure 035
On left: Sample B_04_Hi-Res represented as the CWT generated binary image selecting for weathering pits. At right: The same sample with feature perimeter identified as part of the initial analysis for the pit statistics function.

Vector multiplication is then used to generate a new model of the surface, similar to the binary image found at the end of the CWT analysis, save with elevation data assigned to every pixel within the target features, and the surrounding area remaining at not-a-number values (nan). The equation for a contour matrix calculation is added, which operates as a surface interpolation characterisation method for reconstructing the original surfaces above etch pit features at an efficient rate (Figure 036). The perimeter of each surface feature which is representative by interconnected adjacent pixels with real number values is calculated (figure 035). A +5% margin outside of the calculated pit area is taken and added to the dataset for interpolation. Doing so assists in mitigating the edge effects often created as a feedback of surface interpolation of features with large drops or disparities in data. With perimeters determined in a binary system, the matrices can again be multiplied to generate a system with nan values inside and outside pit perimeters, with the perimeter pixels assigned their corresponding elevation values. The function "*imcontour*" is used to generate a gridfit interpolated surface, acting as the reconstructed original surface prior to pit formation.

The newly reconstructed artifact surfaces can be utilised to calculate max depth of each pit by elevation difference between the interpolated ceiling of the object and its lowest point, as well as overall volume contained within.

Total area, maximum depth, and volume datasets are exported for statistical analysis with R and other data management programs.

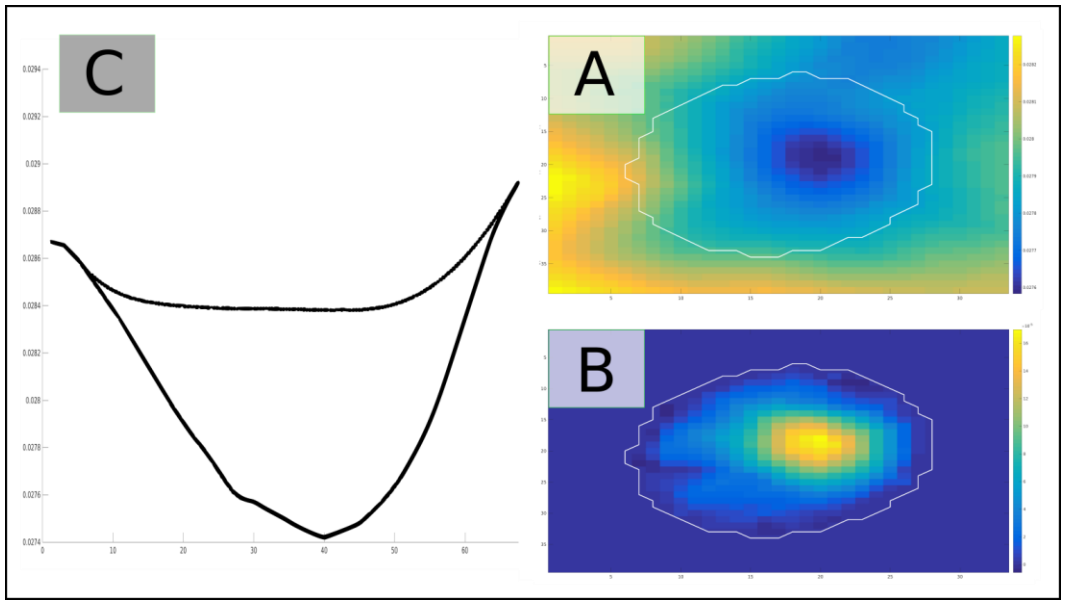

Figure 036
Output figures generated for a single weathering pit cluster from the 'pitstats2.m' script. The contour surface interpolation method takes into account the contextual morphology, and with the added handle of a +5% perimeter, approximates a pre-weathering surface of reasonable accuracy. The pit perimeter is located within the heightmap of the ful DEM (A). The lower image (B) shows the same colour filter applied with the area outside the feature perimeter set to 'nan', and as such the range decreases to show morphology in higher detail. A cross section of the pit (C) is printed and shows the level of conformity for the new surface contour (dashed line).

4.7.4. R Foundation for Statistical Computing

The use of R as a computational resource was relatively limited, due to the majority of dense calculations taking place upstream within the processes of ArcMap and MATLAB. However, it was exceptionally useful as a supplementary analytical tool for a large portion of primary bulk statistics and graph generation.

Exports from both model generation methods, predominantly in the form of 2D pixel count volumetric pixel area and maximum depth profiles, utilised R for analysis. Features were filtered for size to eliminate signal noise, selecting only pit areas with a positive value greater than 100 pixels. The depth profile statistics for all features present on given surfaces was used in the generation of the MCOC statistic, where R's functionality to perform interquartile range statistical calculations proved invaluable and superior to the capabilities of traditional spreadsheet softwares.

5. Results

5.1. Agisoft Photoscan Outputs

The primary focus for the duration of the model generation process from photographic capture to precise feature alignment was to capture and preserve the highest resolution details possible. This was largely achieved with the average exported DEM resolution reaching just fifteen hundredths of a millimeter, or $1.5x10^{-4}$m on the meter-scale applied to the model spatial system. Photoscan table 2 and table 3 showing the model parameters obtained through the structure from motion generation process.

Brewster Photoscan Model Outputs

Site I.D.	Number of photos	Aligned photos	Sparse Cloud points	Dense Cloud points	3D model faces	DEM resolution (mm/pix)
B_01_combo	59	55/59	424,647	48,122,317	9,624,413	0.171
B_01_Hi-Res	36	35/36	25,409	20,597,450	4,119,467	0.044
B_02_combo	62	48/62	333,710	33,230,584	6,646,065	0.241
B_03_combo	89	88/89	59,254	36,675,837	7,335,142	0.136
B_03_Hi-Res	61	61/61	115,325	18,189,282	3,637,808	.0477
B_04_combo	85	85/85	82,138	51,501,969	10,300,346	0.119
B_04_Hi-Res	57	57/57	215,570	31,127,302	6,225,433	0.0618
B_05_combo	92	92/92	353,356	34,021,274	6,804,221	0.115
B_05_Hi-Res	20	20/20	169,555	15,901,250	3,245,882	0.159
B_06_combo	84	84/84	53,399	51,011,574	10,202,269	0.211
B_06_Hi-Res	55	55/55	151,857	24,602,971	4,920,527	0.066
B_07_combo	67	66/67	377,396	40,473,583	8,094,671	0.131
B_07_Hi-Res	36	36/36	67,573	21,988,121	4,397,619	0.0514
Drone Scale	1173	192/1173	104,261	99,559,970	19,911,902	268.799

Table 2. Results of dense cloud generation and DEM export of models through Agisoft Photoscan for sampling sites at Brewster Glacier.

Franz Josef Photoscan Model Outputs

Site I.D.	Number of photos	Aligned photos	Sparse Cloud points	Dense Cloud points	3D model faces	DEM resolution (mm/pix)
FJCR_01_combo	48	48/48	44,015	16,118,553	3,233,705	0.377
FJCR_06_combo	30	30/30	797,133	11,048,592	2,209,706	0.347
FJCR_07_combo	72	72/72	1,334,525	24,867,217	4,973,410	0.092
FJCR_08_Hi_Res	99	99/99	43,518	26,237,213	5,247,435	0.0288
FJCR_08_combo	206	206/206	2,876,614	33,972,995	6,496,068	0.175
FJCR_09_combo	94	94/94	2,195,740	23,314,382	4,662,860	0.407
FJCR_10_combo	58	52/58	36,069	22,984,424	4,596,881	0.179
FJCR_11_combo	32	32/32	710,898	9,538,536	1,907,656	0.166
FJCR_12_combo	50	50/50	1,183,186	13,985,728	2,797,138	0.422

Table 3. Results of dense cloud generation and DEM export of models through Agisoft Photoscan for sampling sites at Franz Josef Glacier.

It is clear that while settings within Agisoft Photoscan can be optimised to generate models with high levels of detail preservation, much of the accuracy of the final product is determined by the subject on study, most namely the depth and visual contrast of surficial features which the software utilises to establish spatial markers. This is most clearly seen in the apparent lack of relationship between number of aligned photos, sparse cloud points, dense cloud points, and exported model resolution.

5.2. Photoscan Model Accuracy

Photoscan Model Accuracy

Site Model	DEM resolution (mm/pix)	Point 1 Average Error (mm)	Point 1 Total Error in pixels	Point 2 Average Error (mm)	Point 2 Total Error in pixels	Point 3 Average Error (mm)	Point 3 Total Error in pixels	TOTAL ERROR OF MODEL (mm)
B_01_combo	0.171	1.441E-03	0.118	2.839E-03	0.332	3.848E-04	0.099	9.388E-02
B_01_Hi-Res	0.044	2.160E-04	0.162	1.200E-04	0.09	1.173E-04	0.088	1.496E-02
B_02_combo	0.241	1.095E-05	0.001	1.095E-05	0.001	1.095E-05	0.001	7.230E-04
B_03_combo	0.136	3.041E-04	0.199	2.155E-04	0.141	9.474E-05	0.062	5.467E-02
B_03_Hi-Res	0.0477	3.910E-06	0.005	4.676E-06	0.005	7.038E-06	0.009	9.063E-04
B_04_combo	0.119	2.646E-04	0.189	5.250E-04	0.375	2.604E-04	0.186	8.925E-02
B_04_Hi-Res	0.0618	1.152E-04	0.082	3.680E-04	0.262	1.573E-04	0.112	2.818E-02
B_05_combo	0.115	2.413E-04	0.193	1.650E-04	0.132	1.075E-04	0.086	4.727E-02
B_05_Hi-Res	0.159	1.590E-05	0.002	1.590E-05	0.002	1.590E-05	0.002	9.540E-04
B_06_combo	0.211	5.413E-04	0.059	7.614E-04	0.083	5.871E-04	0.064	4.347E-02
B_06_Hi-Res	0.066	5.500E-06	0.004	1.490E-05	0.007	5.867E-06	0.004	9.900E-04
B_07_combo	0.131	3.593E-04	0.181	4.141E-04	0.098	1.330E-04	0.067	4.533E-02
B_07_Hi-Res	0.0514	1.271E-04	0.089	1.758E-04	0.106	2.641E-04	0.185	1.953E-02
FJCR_01_combo	0.377	5.451E-03	0.694	4.901E-03	0.624	4.390E-03	0.559	7.076E-01
FJCR_06_combo	0.347	2.406E-03	0.208	4.846E-03	0.419	2.441E-03	0.211	2.908E-01
FJCR_07_combo	0.092	6.133E-05	0.01	8.587E-05	0.014	3.422E-04	0.093	1.076E-02
FJCR_08_combo	0.175	5.886E-04	0.333	6.028E-04	0.341	6.169E-04	0.349	1.790E-01
FJCR_09_combo	0.407	1.324E-04	0.067	2.568E-04	0.13	1.245E-04	0.063	1.058E-01
FJCR_10_combo	0.179	2.209E-04	0.116	4.266E-04	0.224	2.114E-04	0.111	8.073E-02
FJCR_11_combo	0.166	3.039E-03	0.952	1.357E-03	0.425	1.781E-03	0.558	3.212E-01
FJCR_12_combo	0.422	8.308E-04	0.063	1.648E-03	0.125	7.913E-05	0.006	8.187E-02

Table 4. Accuracy and associated error calculated for each model generated through Agisoft Photoscan. 'Average Error' represents the average area in GCP displacement for each photograph in the photoset. 'Total Error' is the sum of all photograph GCP displacement errors in pixels. 'Total Error of Model' is the sum of all 'Total Error' calculations for all GCPs in a given model, combined with export resolution to give error in millimeters. As these models serve as the basis for all subsequent calculations and interpretations, their associated error will be extrapolated to each result as a baseline function error. The average error of all the models as calculated in mm displacement uncertainty of Ground Control Points is $1.06x10^{-1}$ mm, or roughly one tenth of a millimeter inaccuracy.

Table 4 shows the spatial error for each Agisoft model as calculated by total inaccuracy of displacement between GCP approximations for each photo with respect to each GCP. The calculation results in a displacement error magnitude displayed in pixels. This value is translated into dimensioned spatial displacement in millimeters by multiplying the pixel value by the native resolution of each exported DEM, which is presented as mm/pixel. The errors for each model are very small, and present an accurate and precise platform from which to make subsequent calculations.

With an average error of all models at $1.06x10^{-1}$ mm, or roughly one tenth of a millimeter inaccuracy, the number is difficult to believe within the context of its generation. However, with the use of a DSLR camera with a native resolution of at least sixteen megapixels (16,000,000 pixels) surveying an average region of 0.465 m^2 (~465,000 mm), a crude approximation of capture resolution is 0.029 mm/pix or twenty-nine thousandths of a millimeter (table 4 and information from section 4.1.3. used for values). This capture resolution approximation is nearly 75% smaller than the calculation error, rendering the 1.06E-01 mm inaccuracy plausible.

5.3. Model Outputs: ArcMap and MATLAB

Photoscan model exports are brought into two separate software suites, ArcMap and MATLAB, for parallel processing using two distinct methodologies. The objective outputs for ArcMap were the Area Ratio and feature amplitude distribution sorted by an interquartile ratio. For MATLAB, the objectives remained the same, with the addition of a volume per area ratio. Total volume was also recorded from the MATLAB processing, yet was not used as there were no cosmogenic date results available to combine with for rate calculation. The results as model outputs are shown below, as well as their distributions relative to one another.

Brewster Polynomial Interpolation Filter Analysis				
Site I.D.	Distance from Terminus (m)	Area Ratio	# of features	Z IQR
B_01_combo	500	1.0035604	50	0.7292
B_01_Hi-Res	500	1.0127942	16	0.5290
B_02_combo	430	1.0002895	108	2.8922
B_03_combo	380	1.0581312	170	2.0558
B_03_Hi-Res	380	1.0188962	66	0.8754
B_04_combo	210	1.0103144	25	1.6210
B_04_Hi-Res	210	1.0178823	64	2.9485
B_05_combo	130	1.0282466	31	5.5049
B_05_Hi-Res	130	1.0538057	85	5.0847
B_06_combo	80	1.1033117	80	1.8549
B_06_Hi-Res	80	1.0530774	58	3.3690
B_07_combo	5	1.0073339	28	1.4240
B_07_Hi-Res	5	1.0256593	65	1.8699

Table 5

ArcMap model outputs for Brewster Glacier sampling sites, yielding component values for roughness calculations.

Franz Josef Polynomial Interpolation Filter Analysis				
Site I.D.	Distance from Terminus (m)	Area Ratio	# of features	Z IQR
FJCR_01_combo	1740	1.0336325	35	1.6198
FJCR_06_combo	2550	1.0944344	35	2.2874
FJCR_07_combo	790	1.0818037	24	1.0546
FJCR_08_combo	100	1.0481668	32	1.7770
FJCR_09_combo	1440	1.1410702	79	2.5383
FJCR_10_combo	1250	1.0674358	49	2.6696
FJCR_11_combo	2290	1.0484436	30	1.0017
FJCR_12_combo	1950	1.0545476	68	2.7440

Table 6

ArcMap model outputs for Franz Josef Glacier sampling sites, yielding component values for roughness calculations.

Brewster Continuous Wavelet Transform Analysis					
Site I.D.	*Distance from Terminus (m)*	*Area Ratio*	*# of features*	*Z IQR*	*Volume/Area Ratio*
B_01_combo	500	1.0138	754	2.4793	203.7639
B_01_Hi-Res	500	1.0148	347	1.6573	677.7538
B_02_combo	430	1.0097	382	2.2646	160.9671
B_03_combo	380	1.0290	51	3.4361	441.6576
B_03_Hi-Res	380	1.0208	476	1.7007	784.4460
B_04_combo	210	1.0540	904	1.8327	340.3415
B_04_Hi-Res	210	1.0217	28	0.6389	282.2358
B_05_combo	130	1.0129	11	1.5674	59.7135
B_05_Hi-Res	130	1.0272	53	2.3361	212.5607
B_06_combo	80	1.0476	65	4.6095	516.2389
B_06_Hi-Res	80	1.0628	58	0.9652	799.7366
B_07_combo	5	1.0210	223	2.5800	114.9849
B_07_Hi-Res	5	1.0275	37	1.1575	304.9518

Table 7
MATLAB model outputs for Brewster Glacier sampling sites, yielding component values for roughness calculations.

Franz Josef Continuous Wavelet Transform Analysis					
Site I.D.	*Distance from Terminus (m)*	*Area Ratio*	*# of features*	*Z IQR*	*Volume/Area Ratio*
FJCR_01_combo	1740	1.0393	19	2.6395	271.5651
FJCR_06_combo	2550	1.1256	22	0.5281	348.7280
FJCR_07_combo	790	1.1144	113	1.6666	5224.2430
FJCR_08_combo	100	1.0618	99	1.7891	1834.5360
FJCR_09_combo	1440	1.0813	42	1.7039	485.7006
FJCR_10_combo	1250	1.0741	78	3.1337	2887.0202
FJCR_11_combo	2290	1.0576	29	1.7323	831.6434
FJCR_12_combo	1950	1.0592	24	2.7563	714.2009

Table 8
MATLAB model outputs for Franz Josef Glacier sampling sites, yielding component values for roughness calculations.

It is apparent that while the MATLAB approach was far more sensitive to weathering pit identification and characterisation at the Brewster Glacier site, it was evenly matched in accuracy with ArcMap at the sites from Franz Josef Glacier (figure 037). This is likely a function of the degree of weathering in the rocks present and the geometry of features that the models were parameterized towards. This is discussed in greater detail in section 6.7.2.

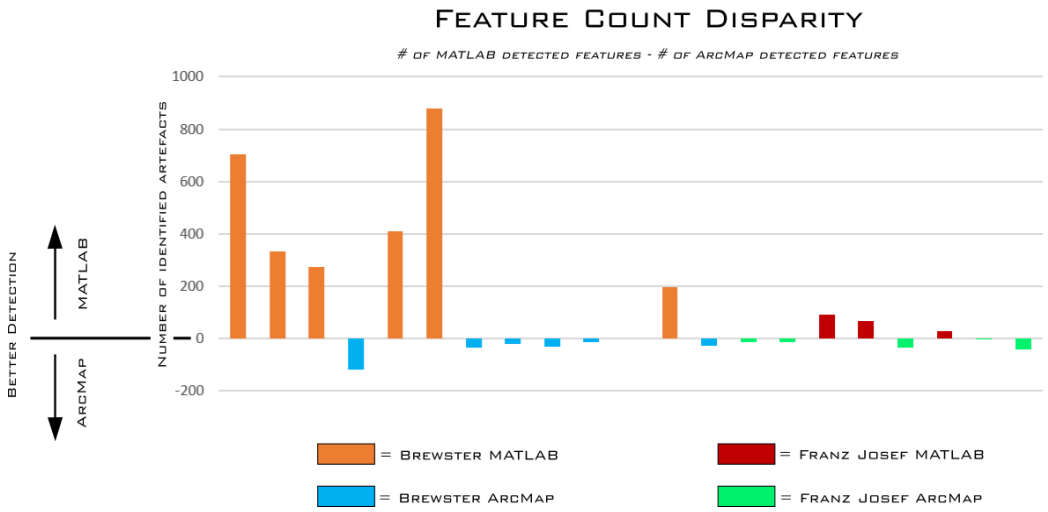

Figure 037
Comparison of ArcMap and MATLAB model sensitivity for feature identification at Brewster Glacier and Franz Josef sampling sites. Values were generated by subtracting ArcMap feature count from MATLAB feature count. All positive values represent higher MATLAB sensitivity, while all negative values represent higher ArcMap sensitivity.

Model outputs for Brewster and Franz Josef Glacier through both ArcMap and MATLAB are plotted independently for trend analysis. Expected linear progressive trends of weathering signals and surface features are not present in the datasets. Higher order analyses are presented in the discussion analysing relationships between specific datasets.

Area ratio patterns track more tightly between the two models used, whereas the interquartile range sees larger disparities between models and across samples.

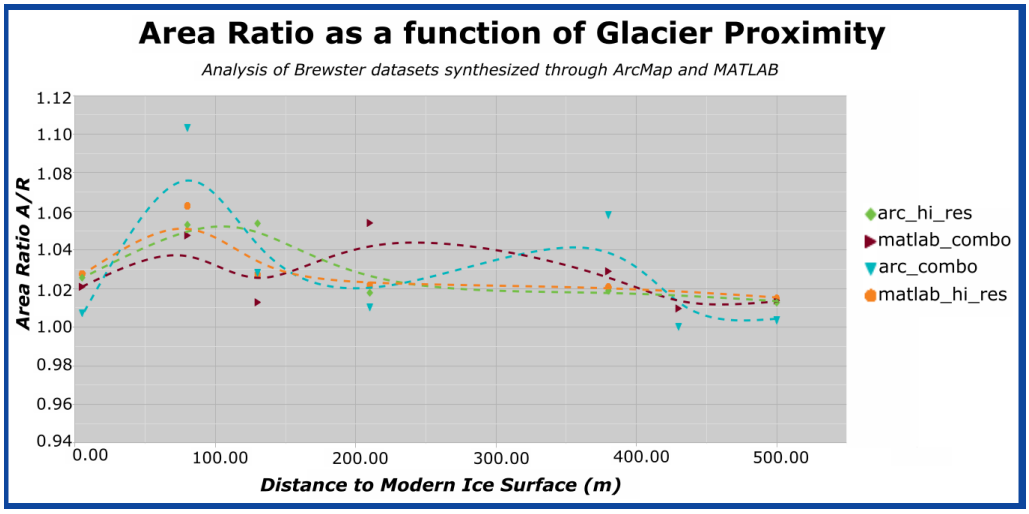

Figure 038

Overlay of area ratio model outputs generated for two scales of observation at Brewster Glacier, using both MATLAB and ArcMap. Tangential interpolation lines are used to represent data trends between the model output values.

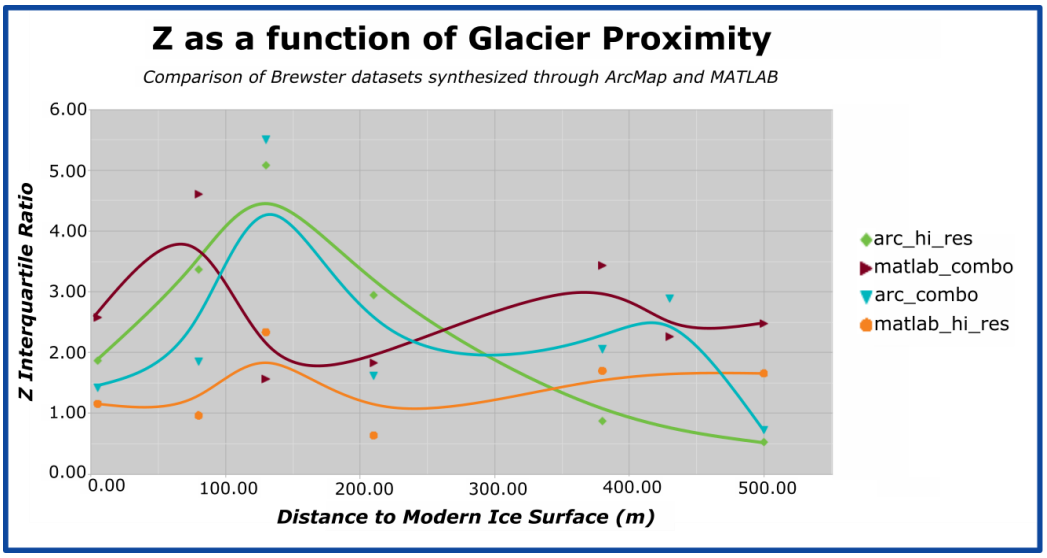

Figure 039

Overlay of feature amplitude and frequency model outputs as the interquartile range Z, generated for two scales of observation at Brewster Glacier, using both MATLAB and ArcMap. Tangential interpolation lines are used to represent data trends between the model output values.

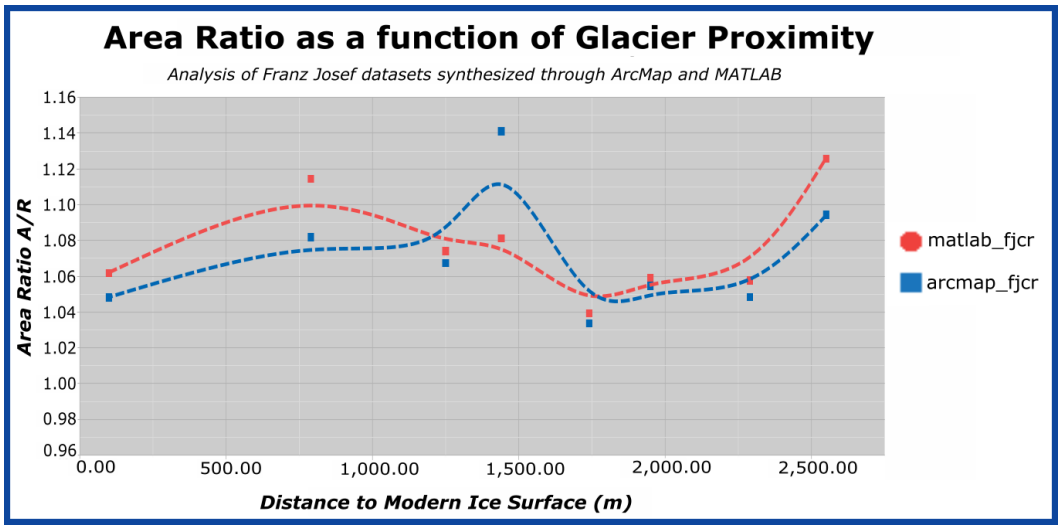

Figure 040
Overlay of area ratio model outputs generated for Franz Josef Glacier, using both MATLAB and ArcMap. Tangential interpolation lines are used to represent data trends between the model output values.

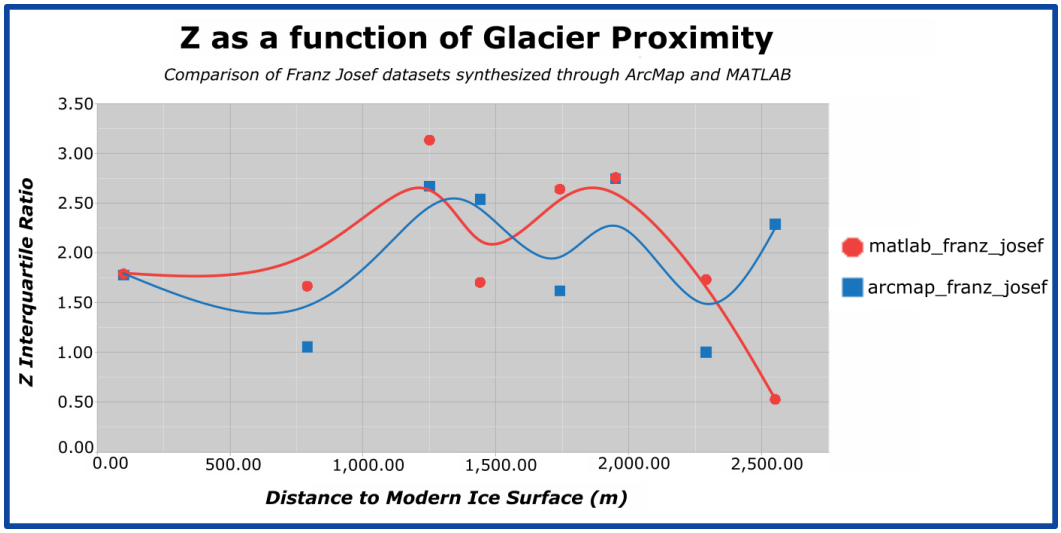

Figure 041
Overlay of feature amplitude and frequency model outputs as the interquartile range Z, generated for Franz Josef Glacier, using both MATLAB and ArcMap. Tangential interpolation lines are used to represent data trends between the model output values.

Though the two field sites are compared with one another, it is important to remember the difference in scale between the two. Figure 042 plots the area ratio results for both Brewster Glacier and Franz Josef Glacier on the same medium with constant axis dimensions, demonstrating the five-fold increase in distance covered by the Franz Josef sampling transect analysis. The features studied are scale-invariant as discussed in section 6.8. yet the same cannot be stated for the weathering processes active in these landscapes.

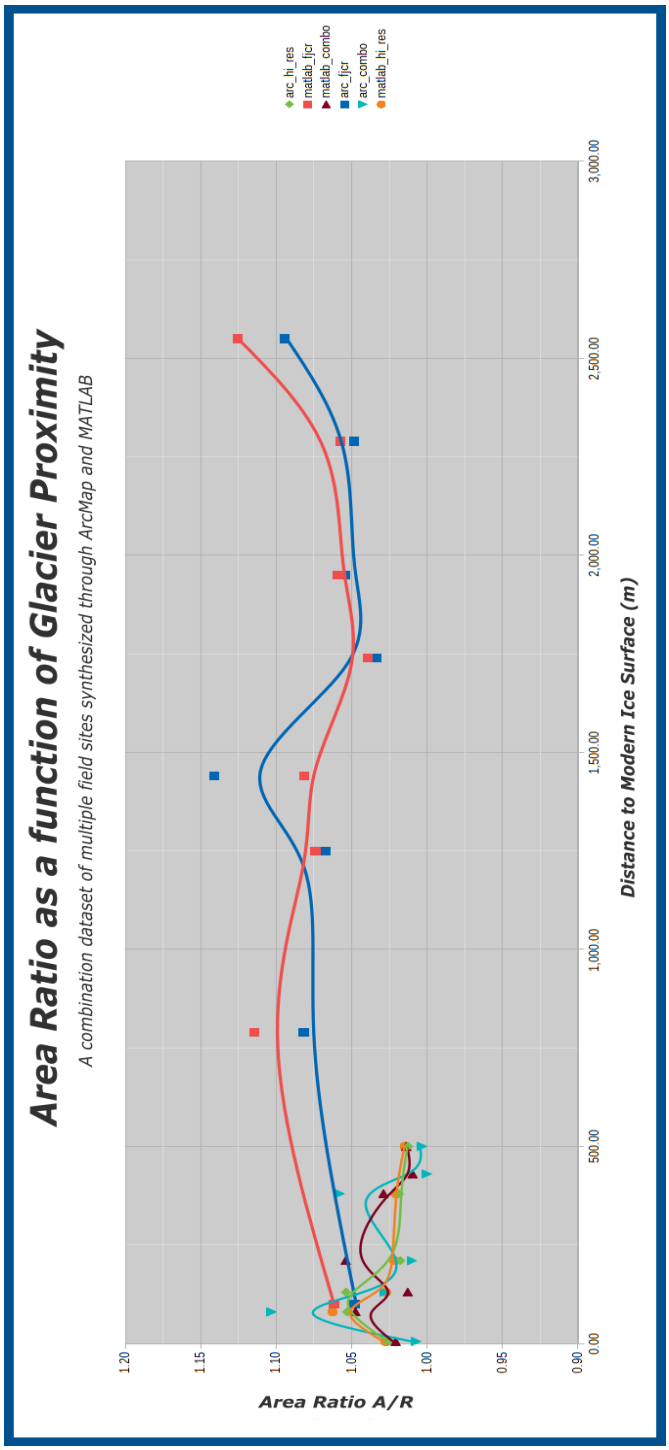

Figure 042

Overlay of area ratio model outputs generated for Brewster Glacier and Franz Josef Glacier, using both MATLAB and ArcMap. Axis scale is maintained for geometric preservation and demonstration of the spatial variation of observations between sites. Tangential interpolation lines are used to represent data trends between the model output values.

5.4. XRF Data

As discussed in section 4.5. XRF analysis was performed on two different samples each at three independent beam locations for every sampling site at Brewster Glacier. At each beam location, two readings were taken, one at the standard voltage and a second at 50kV for improved sensitivity to heavier elements. This resulted in twelve XRF measurements for each site, which were automatically calibrated by the internal software of the analyser to be exported as ppm.

Below are several graphical representations of readings for important elements investigated for compositional trends. Mobile elements, somewhat immobile elements, and very immobile elements are investigated as well as two suites of low ion lithophile elements (LILE) and high field strength elements (HFSE). The remainder of detectable elements will be visible in appendix 9.7. As some of the measurements are near the detection limits of the equipment utilised, a table of measurement error projection for each elemental reading can be found in appendix 9.7.1.

Mobile elements such as potassium and calcium are generally weathered quickly and easily from minerals. An expected trend for a continuous weathering environment would see a steady reduction of these elements in the rocks as the age of exposure is increased. However, looking at the potassium chart this is not evident. The lower component of figure 043, calcium does appear to have a gradual decreasing trend, though the spread of measurements produces weak correlations for a statistical trend.

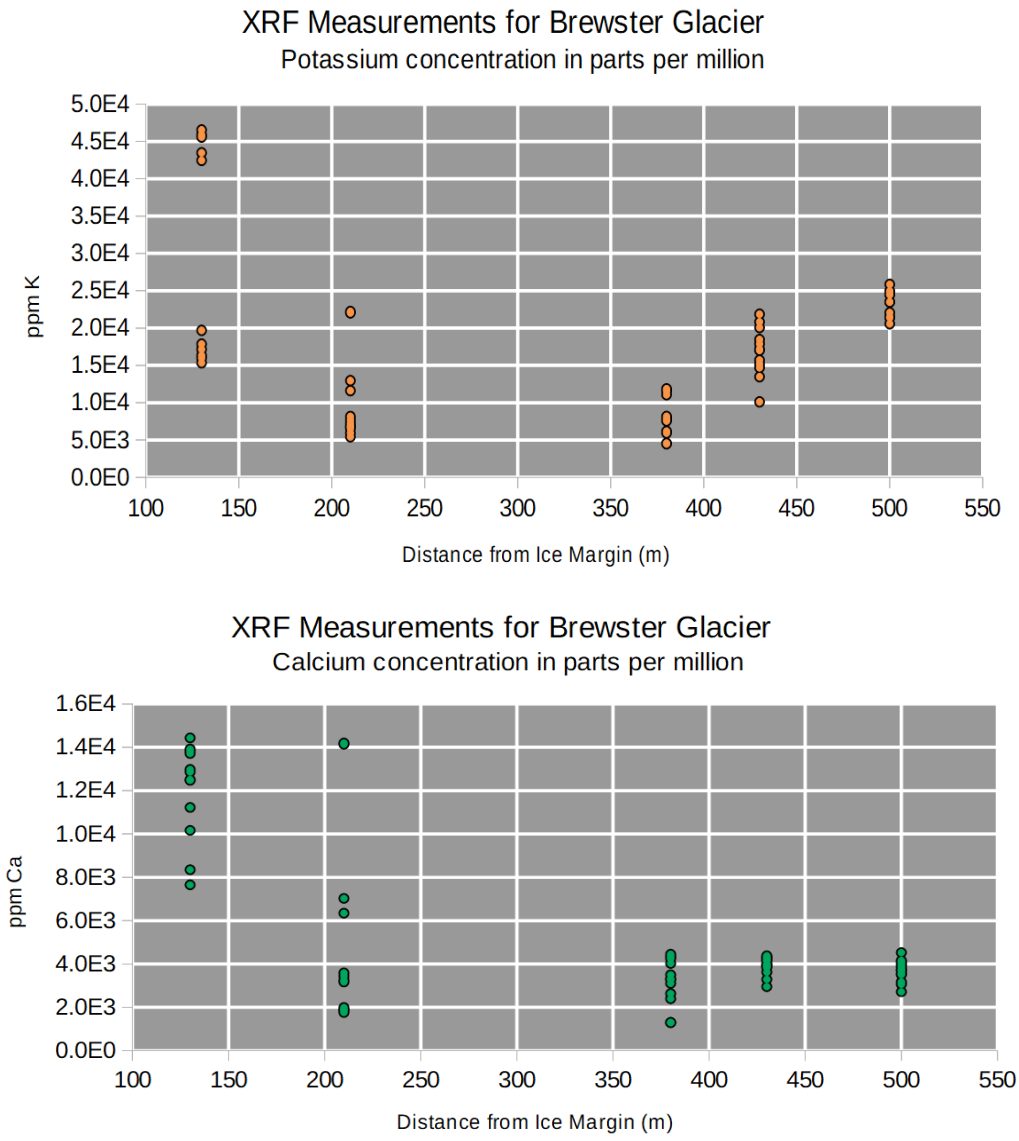

Figure 043

From top: Graphical representation of Potassium and Calcium trends, respectively, in samples from Brewster Glacier transect, grading from large to small displacement between sampling site and glacier terminus. Each sample site has 6 XRF Geochem readings at 10-40 kV, and 6 readings at 50kV.

Somewhat immobile elements such as silicon, manganese, aluminium, and iron are generally weathered much more slowly than the mobile elements. An expected trend for a continuously weathering environment would see a steady concentration of these elements in the rocks as the age of exposure is increased, caused by the relative increase in very immobile element concentrations and the relative decrease in mobile element concentrations. Looking at both charts in figure 044, there is a slight convex shape to the trend in data, though with the spread of measurements could easily be determined to be constant and thus fitting with the expected patterns. Aluminium and Iron as represented in figure 045 exhibit similar concave behaviors, with aluminium skewed slightly to an overall decrease in concentration and iron skewed slightly to an overall increase in concentration.

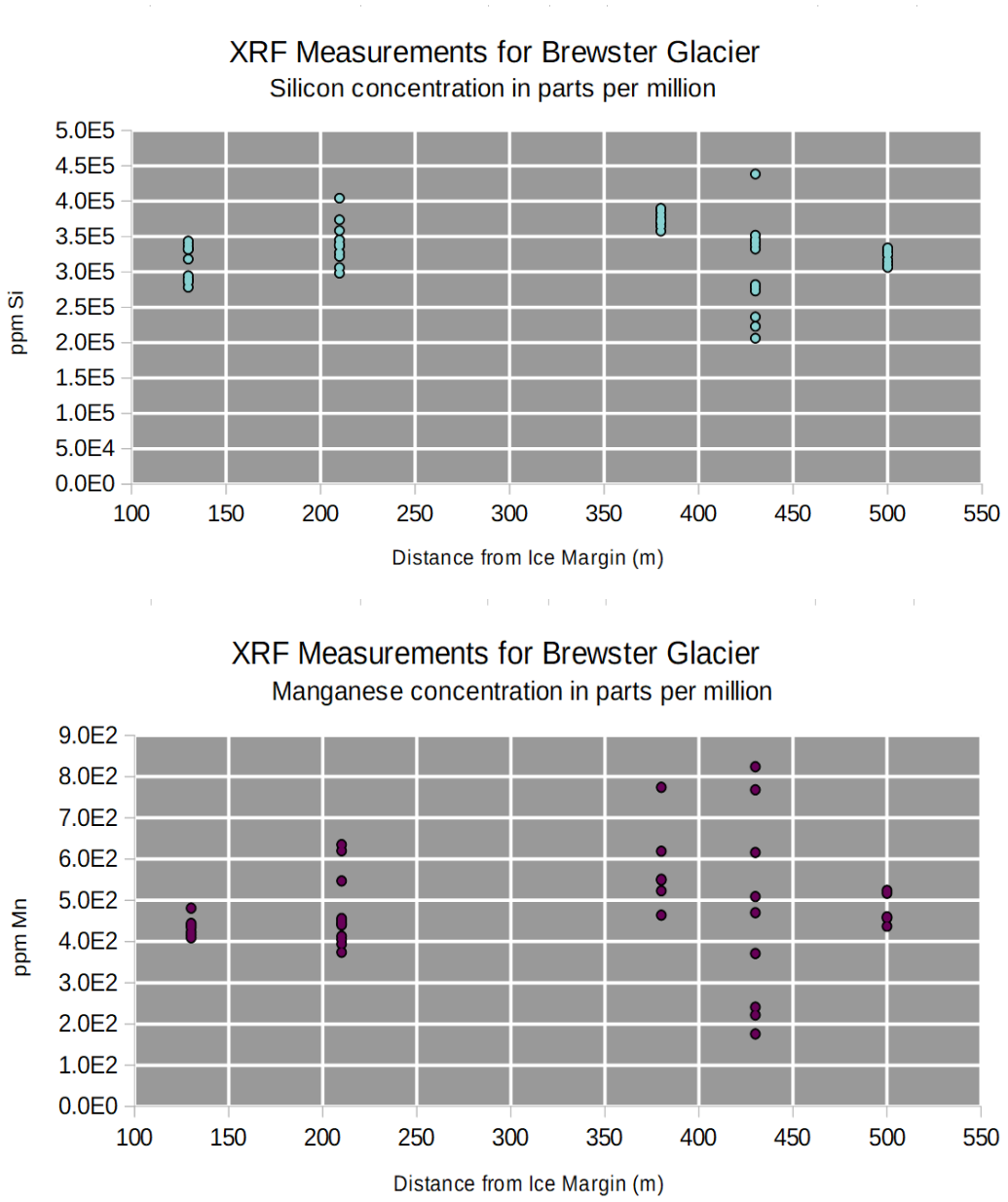

Figure 044

From top: Graphical representation of Silicon and Manganese trends, respectively, in samples from Brewster Glacier transect, grading from large to small displacement between sampling site and glacier terminus. Each sample site has 6 XRF Geochem readings at 10-40 kV, and 6 readings at 50kV.

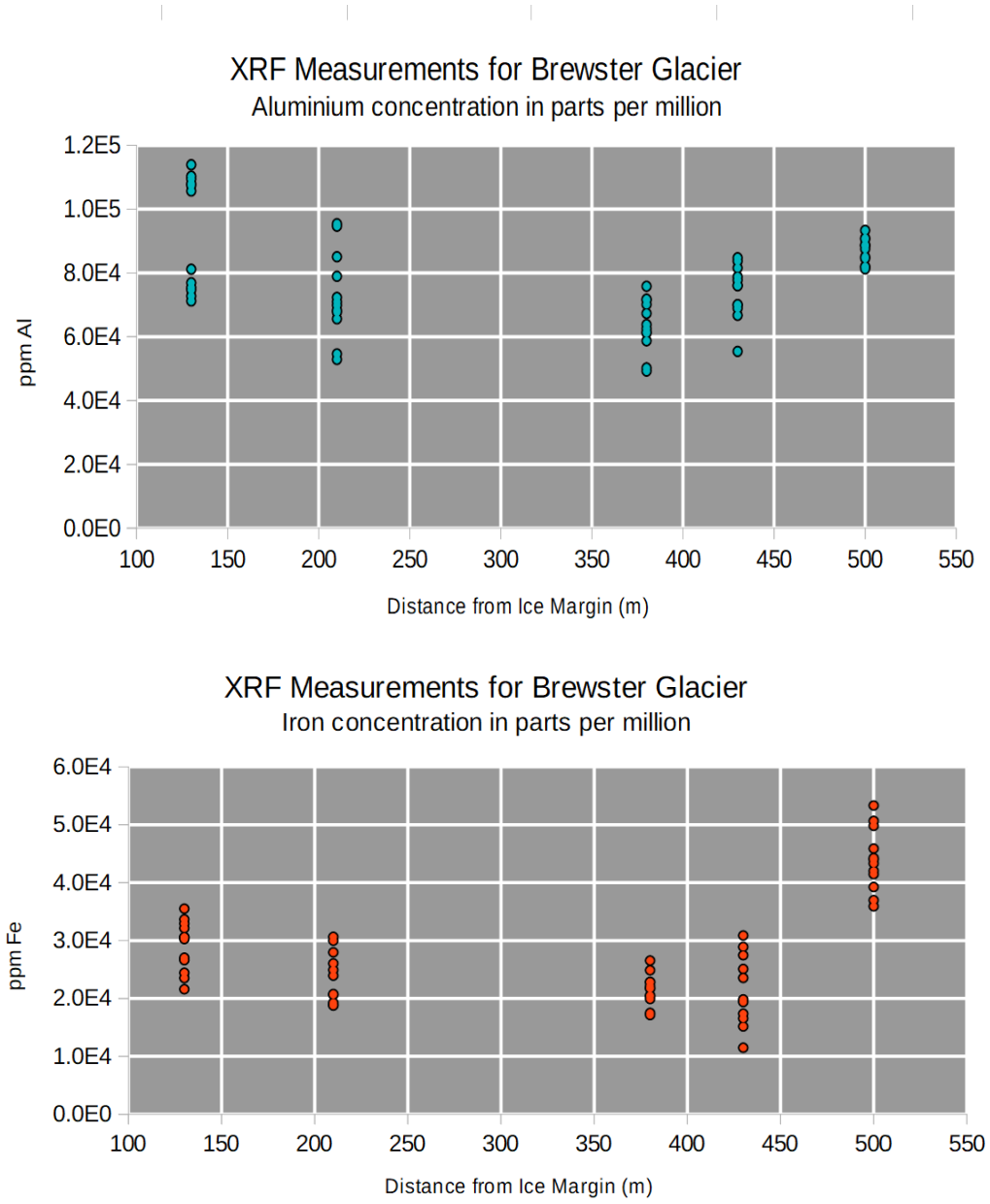

Figure 045
From top: Graphical representation of Aluminium and Iron trends, respectively, in samples from Brewster Glacier transect, grading from large to small displacement between sampling site and glacier terminus. Each sample site has 6 XRF Geochem readings at 10-40 kV, and 6 readings at 50kV.

Very immobile elements such as zirconium and yttrium are generally very difficult to weather from minerals, and as such are indicative of weathering intensities between samples of different exposures. An expected trend for a continuously weathering environment would see a steady increase of these elements in the rocks as the relative concentrations of the other more weatherable elements is reduced with increasing exposure age. However, looking at both elements in figure 046 this is not evident. Yttrium appears to exhibit a concave behavior of initial decrease followed by increase, while zirconium is showing the inverse relationship expected by gradually reducing in composition. Both of these apparent trends are encapsulated by the associated error of the spread of measurements, and as such are too weak to definitively establish behavior.

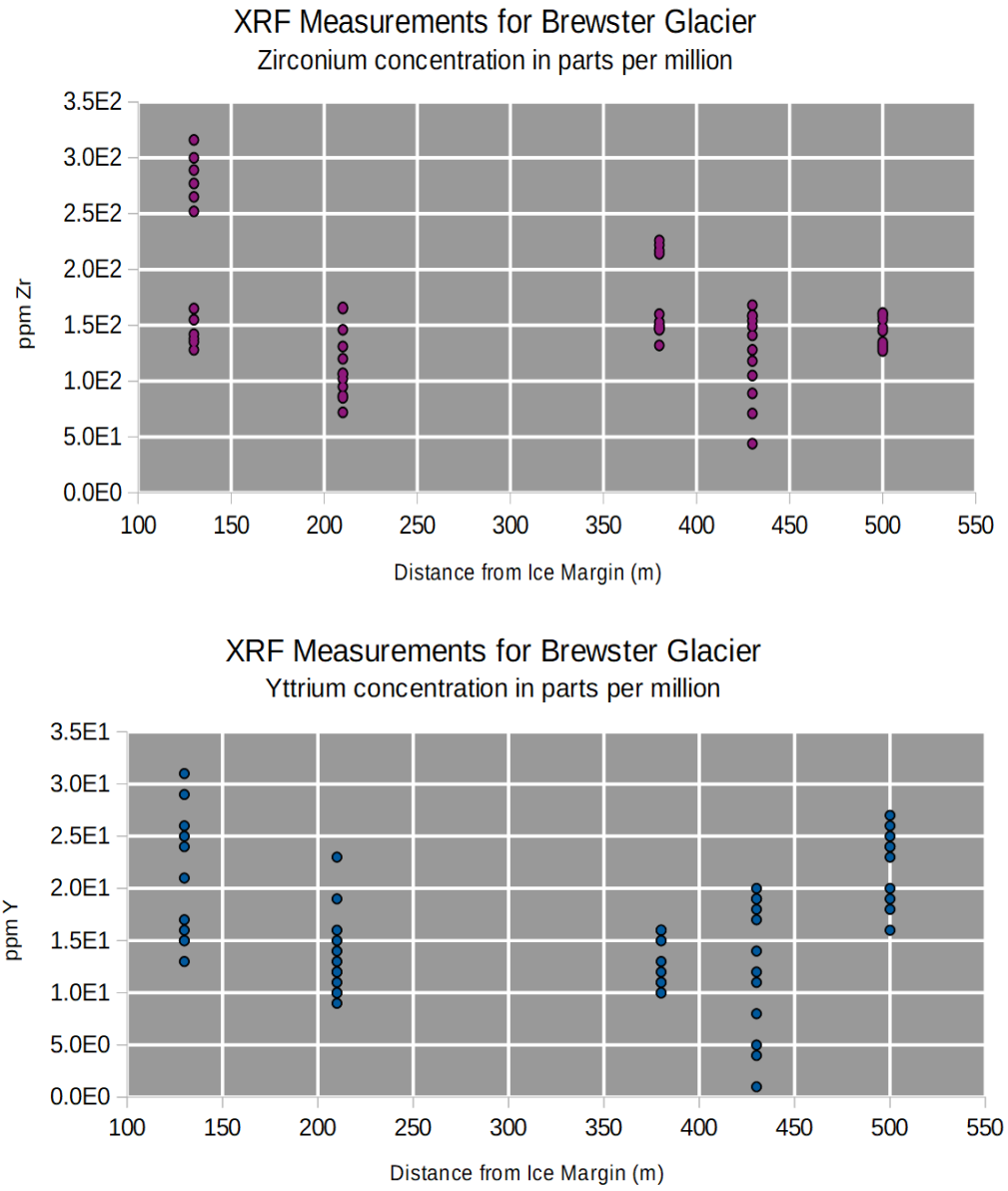

Figure 046
From top: Graphical representation of Zirconium and Yttrium trends, respectively, in samples from Brewster Glacier transect, grading from large to small displacement between sampling site and glacier terminus. Each sample site has 6 XRF Geochem readings at 10-40 kV, and 6 readings at 50kV.

Low ion lithophile elements (LILE) are elements which are traditionally incompatible with crustal rock forming elements as a result of their large ionic radius which makes them enriched in the crust as unbound elements (figure 047). High field strength elements (HFSE) are likewise incompatible with most crystal structures, though instead due to their small radius as a result of a high cationic charge (figure 048). LILEs are mobile in fluids as well as in response to hydrothermal influences. This can give a signal both from groundwater influences as well as potentially from forces during formation. The HFSEs are typically immobile, similar to Zr, Yt, etc., and typically will be representative of the original material. The relationships between the two can give insight into the weathering processes a given lithological sample has been exposed to. Both sets of elements appear to exhibit inverse behavior within each pair, providing weak evidence for trends generated through weathering (figure 047 and figure 048).

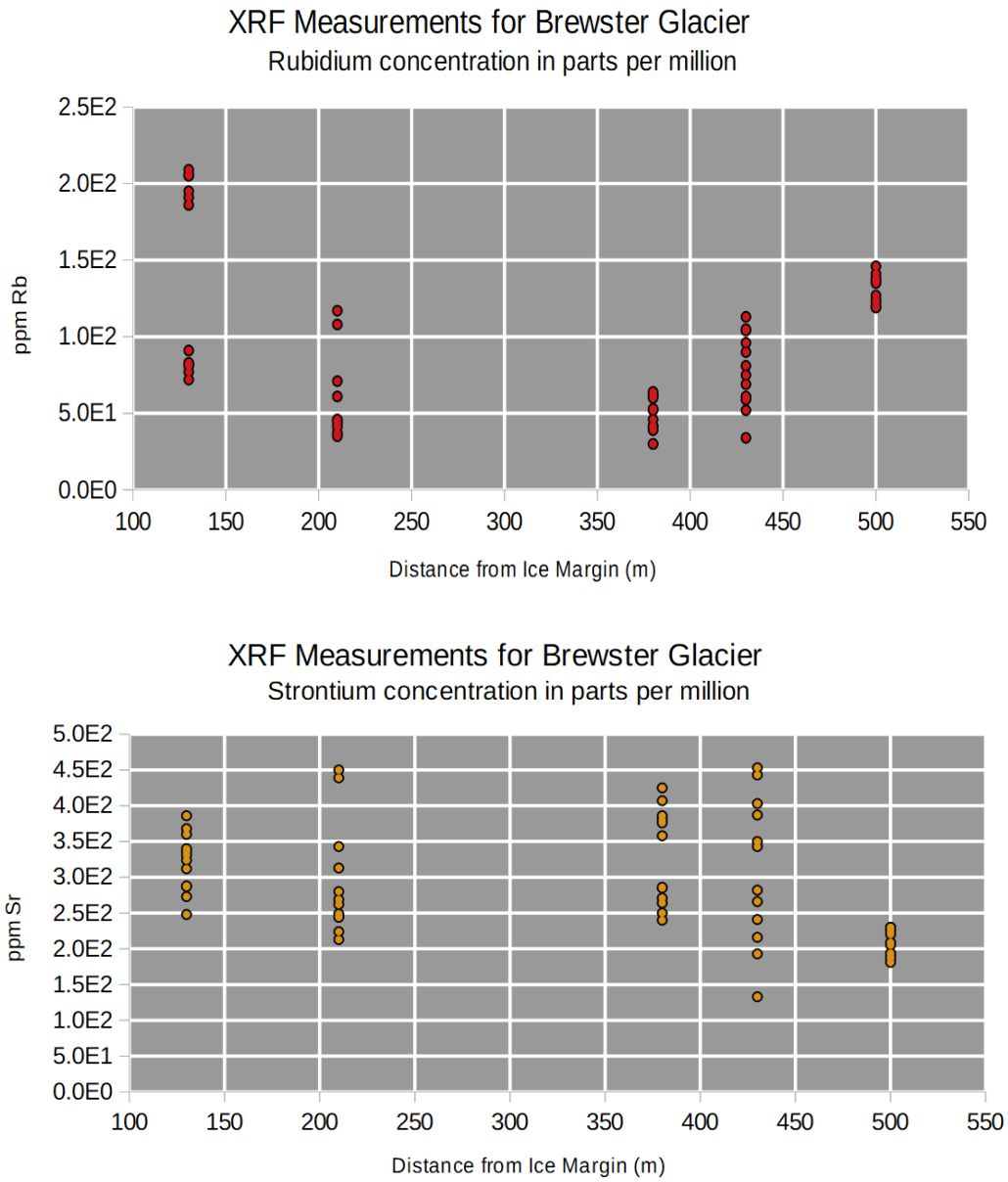

Figure 047

From top: Graphical representation of Rubidium and Strontium trends, respectively, in samples from Brewster Glacier transect, grading from large to small displacement between sampling site and glacier terminus. Each sample site has 6 XRF Geochem readings at 10-40 kV, and 6 readings at 50kV.

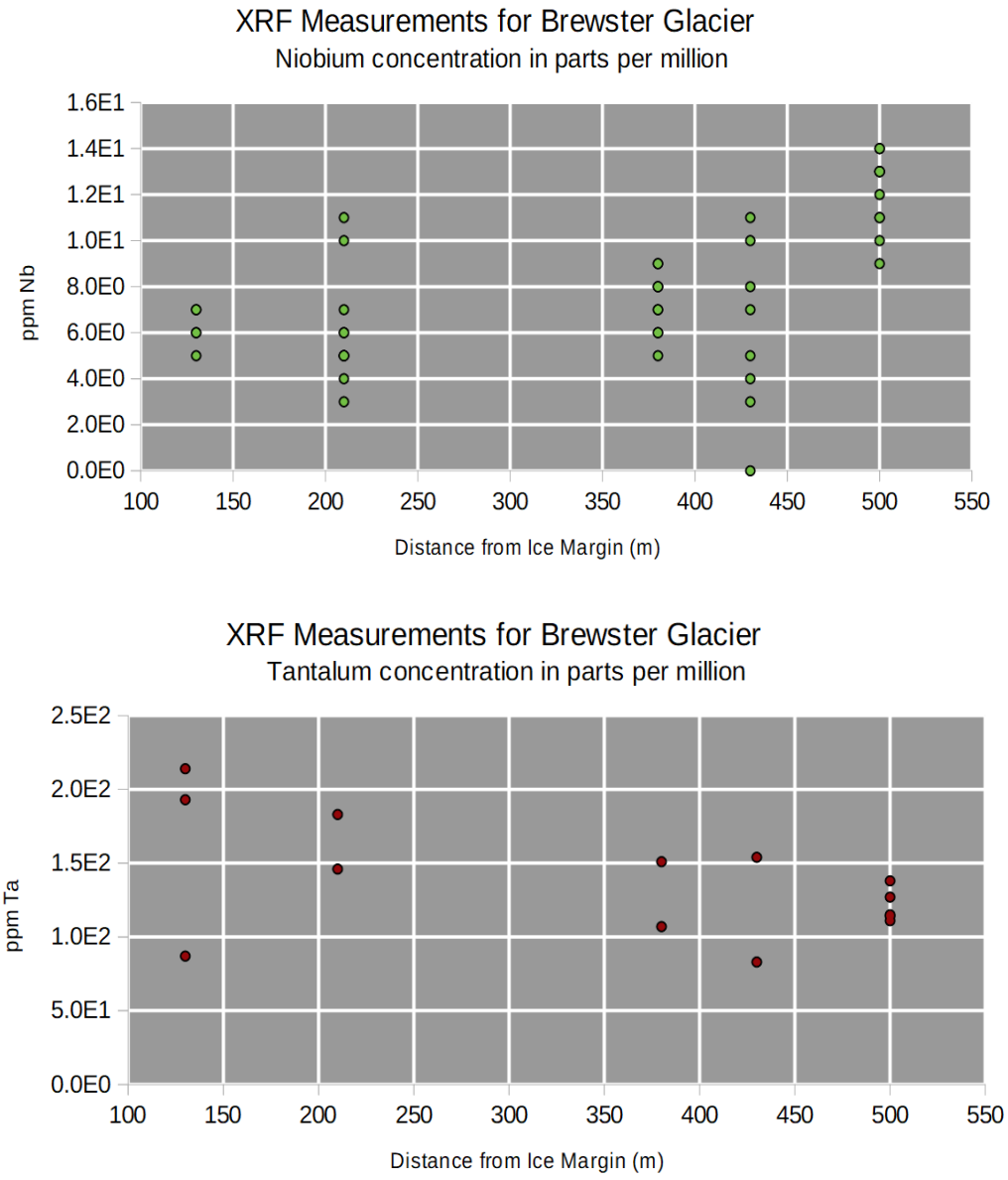

Figure 048
From top: Graphical representation of Niobium and Tantalum trends, respectively, in samples from Brewster Glacier transect, grading from large to small displacement between sampling site and glacier terminus. Each sample site has 6 XRF Geochem readings at 10-40 kV, and 6 readings at 50kV.

5.5. SEM Data

Each constituent mineral present in the samples was measured for percent composition through the optical determination process outlined in section 4.6. Each sample was analysed across at least three different magnification levels, and at between three and ten independent sites across the thin section of sample. As each sample was carefully prepared to contain a cross-section through the body and the surface, percent composition values were able to be determined for both the core of the sample and the top 100µm. The table of results can be found in appendix 9.3. Values acquired at the same magnification level were averaged, and graphed against each site to look for trends.

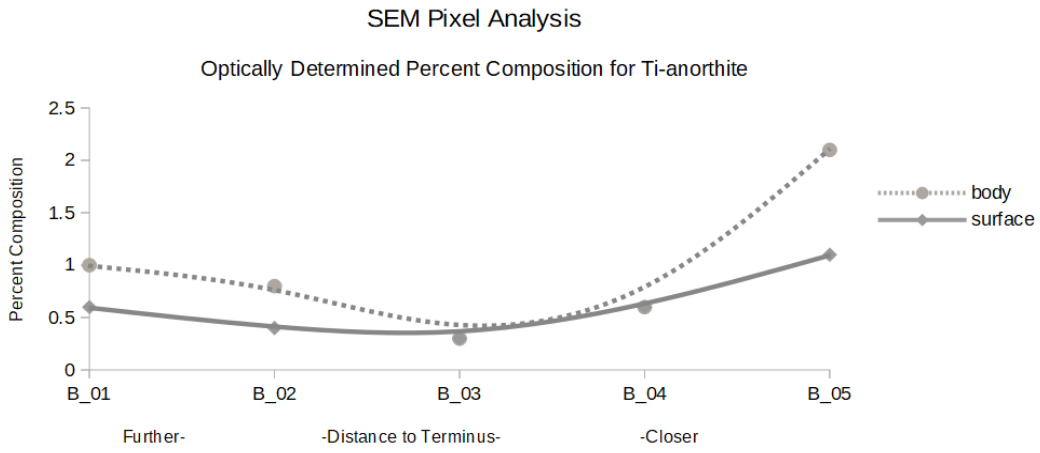

Figure 049
Percent composition of Ti-anorthite in samples as optically determined through false-color BSE Images. The percent composition was independently calculated for the surface (top 100µm) and the body (entire field of view minus top 100µm).

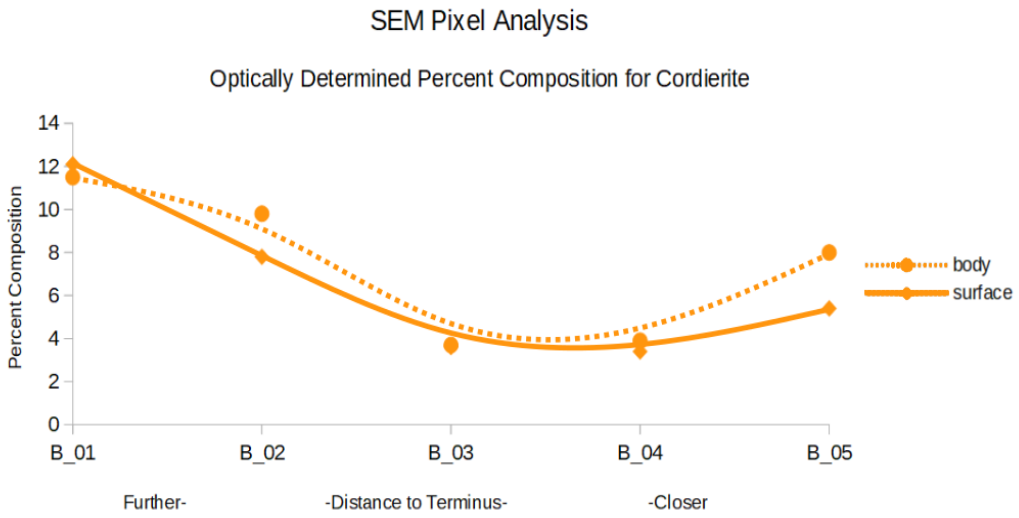

Figure 050

Percent composition of Cordierite in samples as optically determined through false-color BSE Images. The percent composition was independently calculated for the surface (top 100µm) and the body (entire field of view minus top 100µm).

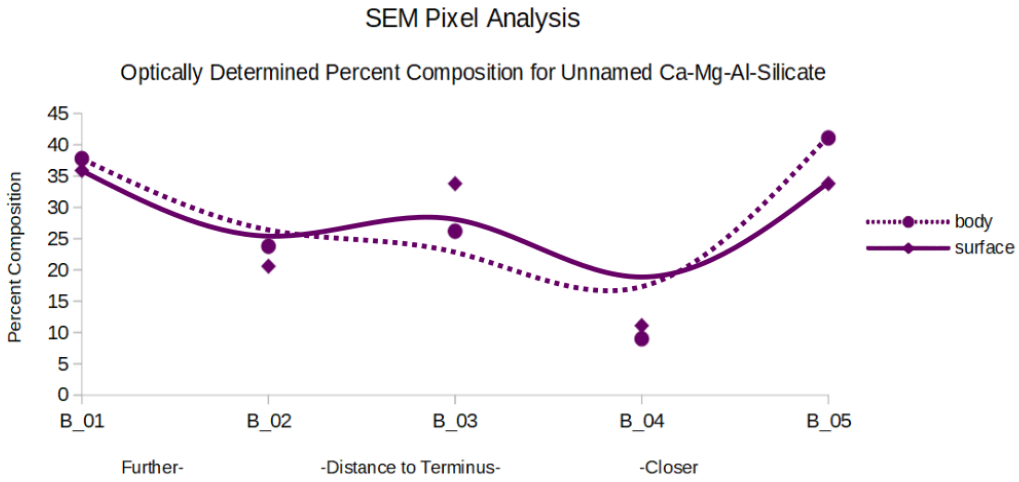

Figure 051

Percent composition of unnamed calcium-magnesium-aluminium-silicate in samples as optically determined through false-color BSE Images. The percent composition was independently calculated for the surface (top 100µm) and the body (entire field of view minus top 100µm).

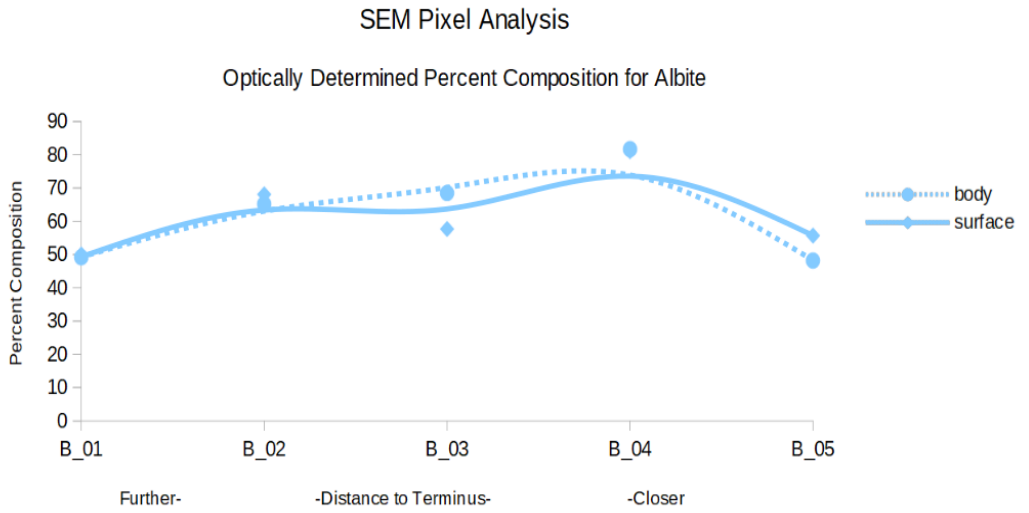

Figure 052

Percent composition of Albite in samples as optically determined through false-color BSE Images. The percent composition was independently calculated for the surface (top 100µm) and the body (entire field of view minus top 100µm).

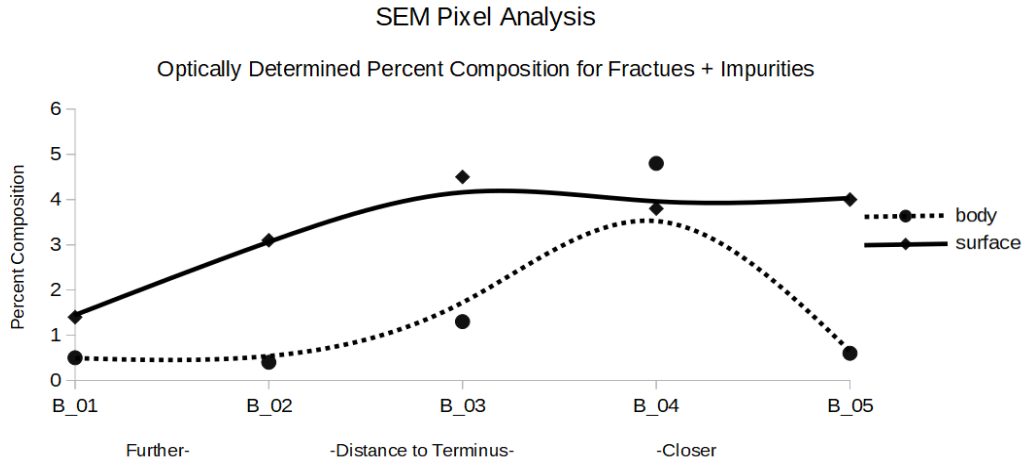

Figure 053

Percent composition of fractures and impurities in samples as optically determined through false-color BSE Images. The percent composition was independently calculated for the surface (top 100µm) and the body (entire field of view minus top 100µm).

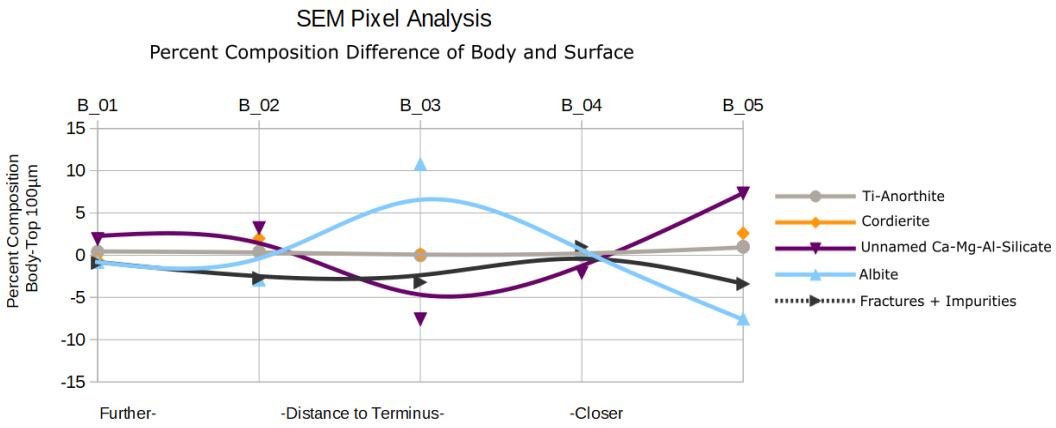

Figure 054

Difference in percent composition of each constituent mineral's body and surface values in samples, as optically determined through false-color BSE Images. The percent composition was independently calculated for the surface (top 100µm) and the body (entire field of view minus top 100µm). The surface values were subtracted from the body values to depict trends in compositional changes between the surface and body of samples.

6. Discussion

Proglacial areas contribute a significant amount of chemical weathering flux of ions to downslope environments, aiding in their soil formation and playing an important role in landscape evolution (Fairchild et al., 1999; Anderson et al., 2000; Anderson, 2005). The addition of large quantities of pulverised rock carried in suspension facilitates a substantial increase in the transport of weathered materials, as well as an increased dissolved load. With the exception of silicate weathering, it has been shown that this signal often only decreases down-system—making the proglacial areas the highest ion flux contributor. However, the results from this research on proglacial weathering sees no such pattern. Without a complete paradigm shift into how weathering is manifested, we are now left with the issue of determining a source for the chemical weathering rates observed by others.

Weathering rates are observed to decrease with greater residence times (White, 2008; White and Brantley, 2003). This disagrees with the traditional concept that greater weathering will generate increased surface area over time which will in turn feed back into increased weathering. Fundamentally, weathering should be directly proportional to the amount of surface area exposed, due to an increased number of reactive sites on the surface of a mineral for hydrolysis reactions (Luttge and Arvidson, 2007). This however, when studied in high relief areas with newly exposed bedrock, is only true for silicate weathering regimes rather than the sulfide oxidation and carbonate dissolution which make up the largest percentage of total dissolved solids in young areas. It has been shown for silicates that this expected trend is likely tied to down-valley changes in vegetative patterns rather than independent weathering variables (S. Anderson et. al, 2000). To further explore this observed pattern, White and others (2003) conducted a series of laboratory and field tests to simulate and measure weathering rates in various scenarios. It was found that aged rocks artificially exposed to laboratory weathering forces exhibited weathering rates which were an order of magnitude greater than similarly weathered rocks measured in the field. Furthermore, within the laboratory setting it was discovered that simulated fresh bedrock again weathered an order of

magnitude greater than the aged rocks in the laboratory setting. The observed discrepancy between laboratory weathering rates and those determined in the field can be partially attributed to a difference in thermodynamic solvent saturation (Maher 2010). This suggests that water interacting with the samples in a laboratory setting had levels of dissolved ions which were below its saturation threshold, providing a greater reactive capacity for chemical weathering than an in-situ water source which would likely be already carrying a high load of dissolved minerals. However, it cannot explain the order of magnitude discrepancy between fresh and weathered samples in the experimental dissolution setting. It is then proposed that the aged rocks, despite a greater available surface area, potentially exhibit a depletion of weatherable materials at their surfaces due to past exposure. This complicates the notion that while mineral roughness correlates positively with age, the hand in hand progression of chemical weathering and roughness likewise experiences an increase.

Nevertheless, the findings of White and Brantley (2003) point towards a scenario where fresh rock and fresh water should exhibit unexpectedly productive weathering rates, potentially up to two orders of magnitude greater than measured downfield counterparts. The flow of water beneath an active glacier is the best natural representation of this scenario. Perpetuating this logic, the reactions occurring subglacially should therefore comprise a large majority of the dissolved ion flux measured downstream as there is fresh water (thermodynamically unsaturated) at high flow rates, coming into contact with fresh rock that is continually being physically eroded beneath the ice. However, this is not a pattern that was made visible through the analysis of surficial bedrock weathering.

6.1. Measured Bedrock Weathering

Investigations at Franz Josef and Brewster Glacier show that while there are multiple strengths of weathering signals present at each site, there are no ubiquitous trends within the data of either correlation morphology, or site wide weathering

figure 055 and figure 056). In these plots, distance from modern ice surface represents the temporal component of weathering. The waveforms generated for each sample present information which does not support the presence of gradational landscape evolution along the sampled transect, nor are the irregular weathering patterns consistent between scales and analytical methods.

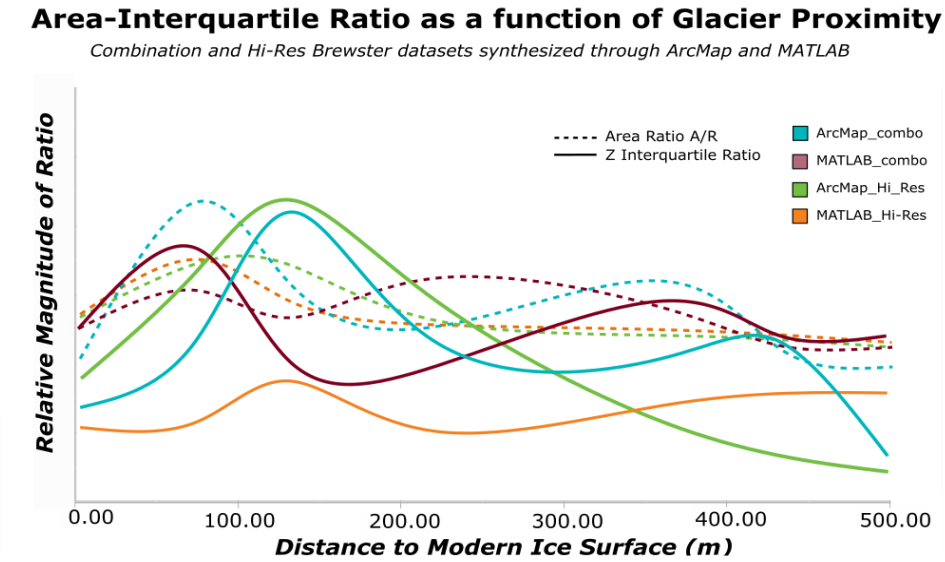

Figure 055
Overlay of area ratio and interquartile ratio model outputs generated for two scales of observation at Brewster Glacier, using both MATLAB and ArcMap. Tangential interpolation lines are used to represent data trends between the model output values. Referenced datapoints can be found in figure 038 and 039. Y axis is dimensionless as the magnitude of each ratio is likewise dimensionless and calculated in differential context.

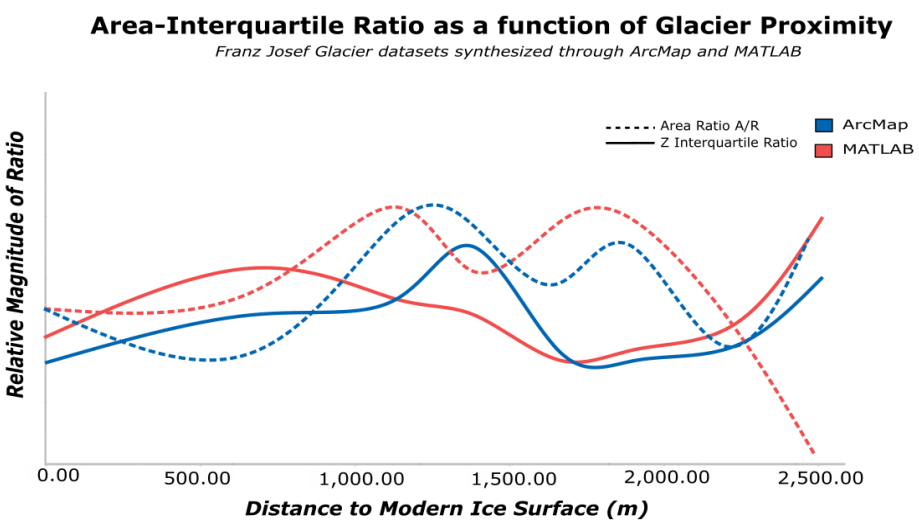

Figure 056
Overlay of area ratio and interquartile ratio model outputs generated for Franz Josef Glacier, using both MATLAB and ArcMap. Tangential interpolation lines are used to represent data trends between the model output values. Referenced datapoints can be found in figure 040 and 041. Y axis is dimensionless as the magnitude of each ratio is likewise dimensionless and calculated in differential context.

When investigating weathering trends over time between sites using the MCOC analysis method, as introduced in section 3.5.2., the patterns become more convoluted and show clear evidence of a lack of trends. Figure 057 shows the weathering history for Brewster Glacier through a plotted MCOC. MCOC figures for each sample site can be found in appendix 9.4.

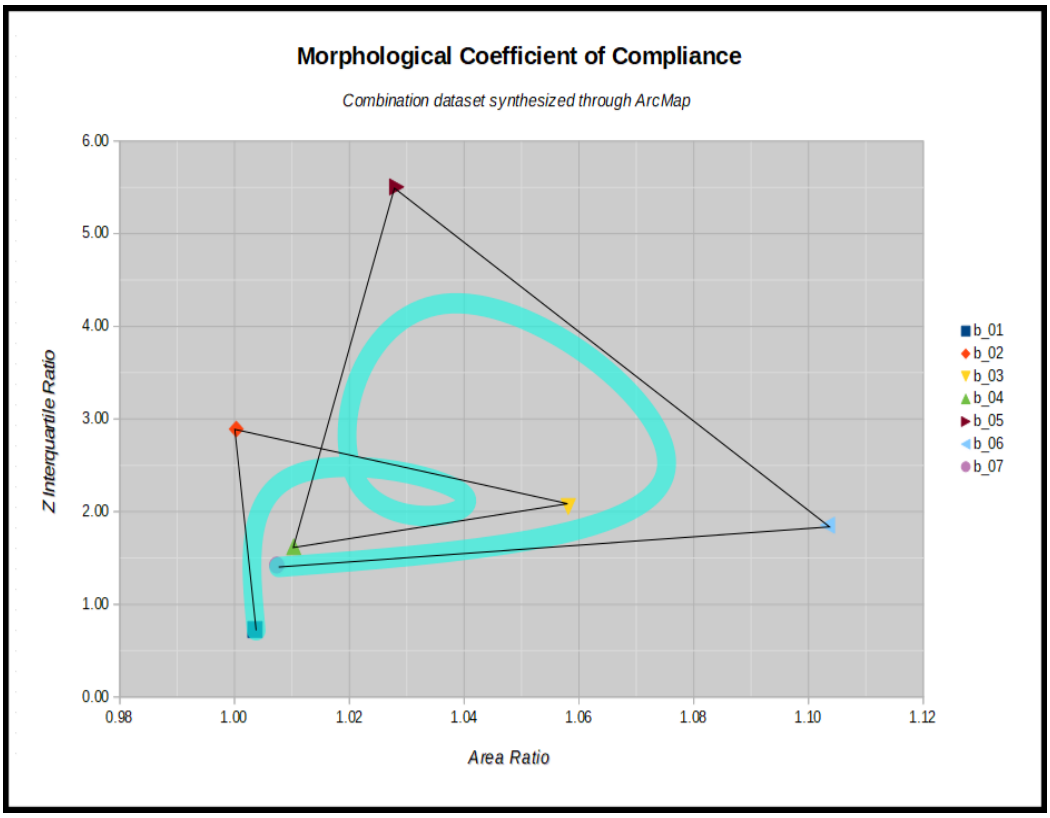

Figure 057
Morphological Coefficient of Compliance trend of the medium-scale combination dataset for Brewster Glacier. Tangential interpolation lines are used to represent data trends between the model output values, while the direct linear correlations can be seen by the black lines.

Beginning closest to the ice margin with the youngest exposure age, the weathering baseline occurs at B_07. Between B_07 and B_06, Z remains nearly the same while the A/R increases dramatically. This suggests an increase in weathering and surface roughness as a function of etch pit synthesis, adding new pits of the same size to existing features. Between B_06 and B_05, the area ratio dramatically decreases while Z increases by a significant amount. This is characteristic of a reduction in weathering signals, manifested by a smoothing of the surface with only large amplitude features surviving the transition. From this point to B_04, A/R continues to decrease slightly, while Z decreases significantly. Here we see a further reduction in surface roughness and a concurrent elimination of deep weathering artefacts. From B_04 to B_03 A/R increases while Z also marginally increases, suggesting

the inverse weathering scheme from the previous sample where new surface features are being generated, and existing features are increasing in size. The transition to B_02 sees a further increase in Z with a reduction of A/R, mirroring the behavior between B_06 and B_05 with a reduction of surface roughness by elimination of small artefacts. The last transition between B_02 and B_01 shows a slight increase of A/R with a steep decrease in Z, implying a mild synthesis of additional small surface features while eliminating the presence of large features. This behavior could also be exhibited by a surface which is physically denuded such that the small features are erased while the higher amplitude features are reduced in size until they become the smaller surface features on site.

The complex behavior exhibited by this sampling transect is similar to the other sampling areas tested (appendix 9.4.). While the irregularity of data can partially be attributed to parent material composition (discussed further in section 6.5.), the magnitude of weathering signals remains incompatible with continuous weathering.

6.2. Deep Weathering

It is evident that while established and proven metrics of weathering rate determination were utilised, there were no significant continuous patterns between outputs of the varied methodologies employed. The diversity and number of methods applied mostly precludes improper measurement techniques from being responsible for the incongruency of results, and presents two possible explanations for the lack of strong weathering signals.

1. That insufficient data and evidence were collected in the study for significant weathering trends or correlations to be observed. I.e. weathering occurred over larger scales.
2. That a lack of significant weathering was occurring in situ on exposed bedrock surfaces within proglacial areas. I.e. nothing to be measured/results were accurate and representative.

Though additional data is a welcomed addition to increase the robustness of any given research, a lack of data is not a viable explanation for the observations made here. Within the scope of this study, the data yielded—taking into account the amount of information collected and resolution of analyses performed—were sufficient to make empirically based interpretations (see results section 5.2., table 4). As discussed in the results section 5.2., metrics calculated and extrapolated upon such as Area Ratio are directly generated from first order analyses of the digital elevation models generated through Agisoft Photoscan. Thus, their associated error will be calculated based upon the error of the source data. With a spatial error of $1.0x10^{-1}$ mm, greater than two orders of magnitude below the minimum average feature size analysed, the generated models and subsequent calculations are well within the acceptable levels of error required for accurate analysis. By extension it can be concluded that the determination of negligible surficial bedrock weathering in proglacial areas is accurately formulated and indeed representative of the presently ongoing processes active in the studied proglacial regions.

The notion of limited bedrock weathering is not unheard of. In adjacent studies, this sentiment has been reiterated, where it is clear that surficial weathering of bare bedrock is often minimal to nonexistent, depending on the measurement techniques. As stated by Gabet and Mudd: “Indeed, intact patches of glacial polish exposed >10 ka by receding glaciers in the Sierra Nevada of California testify to negligible rates of weathering on vast bedrock surfaces.” (Gabet and Mudd, 2010).

This assessment of weathering at the studied proglacial field sites is further supported through compositional analysis. In specific environments, chemical weathering can operate without giving off ion concentrations to runoff and stream systems. In these situations the weathering occurs as mineral replacement in-situ where kaolinites and clays are generated within the crystalline structure. However, the chemical analyses performed in this thesis showcase that this is not the case at the field sites studied. The lack of physical and chemical responses to exposure age

and weathering forcings in an environment of high erosion, strongly suggests that the chemical weathering signatures observed are originating from elsewhere in the system.

This permits exploration of the second scenario, in which there is not enough surface weathering of bare bedrock to measure in any context. This implies that surface processes on bedrock in proglacial areas do not significantly contribute to chemical weathering. The large measured chemical weathering flux coming from proglacial environments, no longer attributable to surface weathering of exposed bedrock surfaces, must originate from two possible areas which we will explore in greater detail.

1. That subglacial processes account for 100% of the chemical weathering flux coming out of glacial basins.

Glaciers produce massive quantities of fine sediments through the grinding and fracturing of bedrock through subglacial processes, and as such present a strong case for their role in controlling the weathering signals from proglacial areas. These fine sub-glacially derived sediments have high ratios of surface area to unit mass, which promotes increases in reactive sites for chemical weathering throughout samples, and therefore a likely resultant increase in measured chemical denudation rates (R. Petrovich, 1981). However, as this behavior of the transition from physical weathering to chemical weathering evolves downstream from the proglacial area, it has little to no effect on incipient weathering in proglacial basins, particularly with respect to silicate weathering (Anderson et al., 2000).

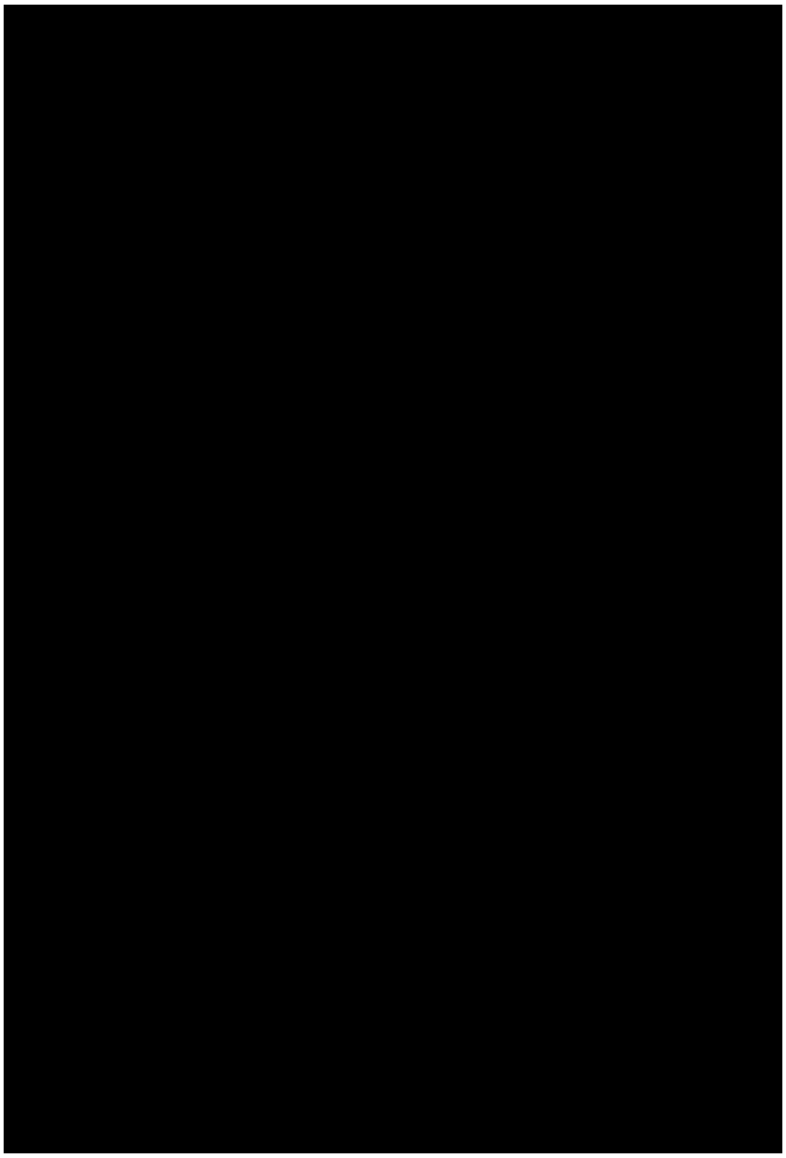

Figure 058
Fractional chemical composition of riverine fluxes investigated in the 2017 research of Torres and others. The blue data represent the measured values for glacial river loads from their dataset. Red data represent database sourced measurements from the world's largest rivers. Grey data represent the river load measurements from the GloRiCh database of 17,000 non-glaciated catchments. Figure sourced from 'Glacial weathering, sulfide oxidation, and global carbon cycle feedbacks' (Torres et al., 2017).

It is known that, while glaciated regions contribute higher chemical weathering fluxes to river loads than the global average for alpine basins, their chemical weathering rates are no greater than the rates found within non-glaciated alpine areas with similar hydrologic discharge rates (Hicks et al., 1990; S. Anderson et al.,

1997;Torres et al., 2017) (figure 058). Further, when measured at the basin scale for fractional contributions of subglacial and extra-glacial weathering, warm-based glaciers such as those studied here exhibit high dissolved loads from streams draining the glaciers as well as those adjacent to the glacial body, draining non-ice-covered regions of the basin. Though the subglacial streams show relatively higher chemical denudation rates, both subglacial and extra-glacial sources form integral parts in the overall denudation rate of the drainage basin (E. V. Axtmann et al., 1995). Based on this information, it is safe to treat the observed weathering products of the studied area as being at least partially generated from a source other than subglacial erosion.

2. Deep subsurface weathering.

If our sample area is independent of all (or as many as possible) external inputs such as dust flux and rainwater solutes, and there is no soil or vegetation present in the alpine glacial basin, then our weathering rates must come from subglacial processes, surface processes, or subsurface processes. As this far we have addressed the first two of these components and come to the conclusion that they exert negligible impacts on the weathering outputs of the studied system, we must further investigate the potential for active subsurface processes as having a role in generating the observed weathering signals.

Subsurface processes, also sometimes referred to as deep weathering, are the cumulative effects of active processes operating deeper than the soil mantle of a landscape surface (Riebe et al., 2016). These include though are not limited to; fracture plane weathering, mineral boundary dissolution, groundwater solute production, and many others. Deep weathering has, however, been poorly studied due mainly to limited access for observation and sampling (Riebe et al., 2016). “Overcoming this limitation is important, because deeper processes have profound implications for processes at the surface and for the overall function of the CZ.” (Riebe et al., 2016).

While the paradigm of kinetically limited soils remains dominant in the community, many papers in support fail to assess the components of the weathering system where deep weathering signals are active (Ferrier and Kirchner, 2008; Hilley et al., 2010).

It is recognized that the weathered zone of bedrock in certain environments can extend far below the soil mantle, yet many aspects of deep weathering are ignored as a function of convenience for sampling and analysis. Their exclusion can have potentially dramatic effects on gathered results and drawn conclusions. In a study by Jean Dixon and others, analysis of chemical depletion fractions of the soil, saprolite, and bedrock results in the conclusion that on steep slopes erosion is inversely related to weathering (Dixon et al., 2012). However, without the analysis of deep weathering below the bedrock surface, any deep weathering signals present in subterranean hydrological systems within rock fractures would have been missed, and potentially could have affected the outcomes of the research.

Often, the effects of deep weathering are visible at a lesser depth than in below-bedrock fracturing. In an earlier study , results showed that within the saprolite layer of the regolith that chemical weathering rates and intensity are tightly coupled in parallel with erosion rates (Dixon et al., 2009).

Nonetheless, it is critical that environments under examination for trends in weathering be tested in a manner that has sufficient sensitivity to recognize deep weathering signals, as its prevalence in diverse environments is becoming increasingly noted.

6.2.1. Global Evidence of Deep Weathering

Hahm and others recently discovered links between bedrock composition and local vegetation, leading to biosphere and landscape evolution controls on par with those currently held by regional climate variability (Hahm et al., 2014). Hahm and others (2014) studied landscapes in the Sierra Nevada mountains of California, and

observed strong correlations between the mineralogical composition of granitic bedrock, and the distribution of sequoia pine groves, noting two fold differences in weathering rates as a result. The variable nutrient availability and weatherability of the changing lithology in the study area influenced soil forming factors, and over time led to vastly differentiated regions of landscape morphology (figure 059).

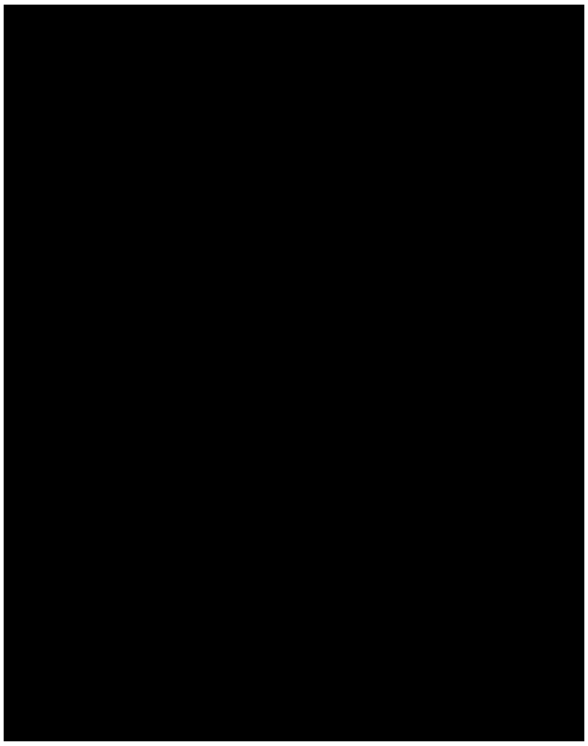

Figure 059
Graphic from the 2014 paper by Hahm and others, showing the strong correlations between bedrock composition, vegetation as expressed by tree canopy cover, and landscape morphology.

This evidence for bottom-up regulation of vegetation—and by extension, landscape evolution—presents a supporting case for the dominance of deep chemical weathering in propagating initial landscape modification. The regulation of surface characteristics begins far below the top of subsurface bedrock layers, and therefore likely precedes and is independent of soil formation. Progressing this idea, the lack of established soil horizons in high alpine proglacial areas would not preclude operation of deep bedrock weathering, presenting bare bedrock environments as sites for active subsurface weathering.

Empirical supporting data can be found in the study of deep weathering in a rapidly eroding Taiwanese mountain belt by Calmels and others (Calmels et al., 2010). River chemistry in a 7-year time series was analysed. Through annual rainfall variability and dissolved ion flux measured across diverse river discharge profiles, the team was able to separate three distinct chemical signals for different catchment water reservoirs. Relating to slow surface, rapid surface, and deep subsurface

groundwater sources, the chemical profiles of each yielded surprising results. The numbers revealed that not only was deep weathering a contributing component to the system, it in fact comprised the dominant chemical weathering signal for 75% of time, predominantly at low discharges. Even with higher discharges of chemical solutes related to heavy rainfall events and seasons, overall the deep weathering groundwater reservoir contributed around one third of the total system inputs due to chemical weathering, despite supplying only ~16% of volume discharge. These high concentrations originating from subsurface weathering suggest that even small reservoir inputs of this nature can have high impacts on the solute flux measurements taken in a system, and must be reconciled to generate representative regional weathering rates.

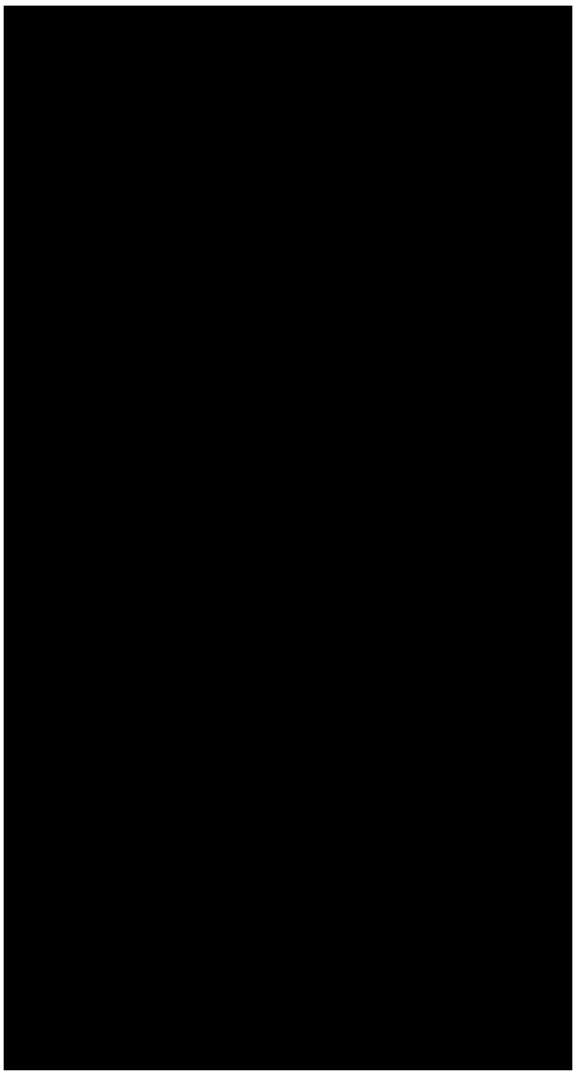

Figure 060
Figure from Calmels and others' research clearly delineating three independent reservoirs of chemical weathering waters. The graphs show: (a) Hydrograph separation and, (b) measured and modelled Sr isotopic composition of river runoff during a high discharge event. Slow surface runoff (SSR) provides a large weathering signal component initially, then becomes nearly negligible which is forced by event recharge water. A week after the typhoon event, the return to base flow discharge values is accompanied by an increasing contribution of the deep groundwater (DG) component, which exceeds the runoff levels of SSR. Figure sourced from (Calmels et al., 2010).

The work done by Calmels and others is particularly applicable, as the highly weatherable and rapidly eroding mountains studied in Taiwan closely resemble the metasedimentary mountain ranges of New Zealand, which have similarly high erosion rates resulting in the high angle morphology of their peaks (Fitzsimons and Veit, 2001). With more parallel study areas, methodological practices can be more easily adapted, and correlations more plausibly drawn.

The Sierra Nevada study conducted by Hahm and others demonstrates that the lithologic controls operate independently of altitude, slope, aspect, and previous glaciation (Hahm et al., 2014). The resilience of the bottom-up landscape evolution regime against past or present glacial controls presents further potential for parallels to be drawn between the study and the proglacial basins examined in this thesis.

Even though deep weathering has not been studied in NZ, previous works can be reevaluated in light of the findings of Hahm et al., (2014) and Camels at al. (2010). Research by Carey and others on river total organic carbon fluxes through multiple North Island and South Island small mountainous rivers in New Zealand has elucidated the trends of river fluxes in the local regions to the field sites studied in this thesis. Through an extended study of thirteen rivers, it was found that often contributing up to 75% of the total organic carbon flux of most NZ rivers, the dissolved component of river fluxes was far more important and consistent than the particulate loads. In many unexpected cases, the particulate organic carbon loads were very small, resulting in dissolved organic carbon flux comprising the majority of total organic carbon release (Carey et al., 2005).

Samples from ten major global rivers with headwaters in mountainous regions were analysed to serve as a global dissolved organic carbon and particulate organic carbon reference. The measurements captured for dissolved organic carbon loads in the New Zealand small mountainous rivers were consistent with the global references, as the dissolved organic carbon loads are scalable to any extents regardless of river volume or catchment size (Carey et al., 2005). However, it was

observed that the New Zealand rivers did not all have high particulate organic carbon transport loads to match their dissolved fractions. This unexpected observation places greater significance on the dissolved particulate carbon loads within the river systems to account for the total organic carbon content.

This increased role of dissolved river loads in these small alpine rivers supports the idea that weathering as represented by New Zealand rivers is present as dissolved river load fluxes, which have major contributions from the chemical weathering products present in groundwater (Calmels et al., 2010). The portion of compositions due to deep subsurface weathering remain mostly constant and are less affected by and much less responsive to rapid changes in precipitation regimes than other weathering signals. This consistent nature of deep subsurface derived dissolved weathering products suggests that weathering rates significantly coupled with deep subsurface weathering processes occurring across the drainage basin.

6.2.2. Local Evidence of Deep Weathering

Utilising information from these conclusions and applying the concepts to the data collected for this thesis, it can safely be assumed that deep weathering is indeed occurring in this area. The presence of strong weathering signals in a rapidly eroding alpine environment paired with negligible values of bedrock weathering in-situ at the surface points directly to a local and regional existence of deep weathering. This has several implications, first and foremost that while having a strong influence on overall chemical denudation rates, the existence of deep weathering in this type of barren bedrock environment, paired with the accepted bottom-up controls that we know lithology to have on more developed regions, means that our understanding of active weathering processes in a wide variety of environments which have underlying bedrock is incomplete.

With deep weathering acting in soil-mantled environments, the external perspective would show a kinetically limited weathering environment, where the soil profile dramatically thins with increased erosion (R. Anderson, 2002; A. White, 2008;

Norton and von Blackenburg, 2010; Dixon and von Blackenburg, 2012; Norton et al., 2014). However, with a change in scale of observation, the true chemical weathering flux will remain in relative balance, and often increase in response to the high erosional forcings (Anderson, 2005; Heimsath et al., 2012). This is because the cumulative weathering flux is in fact a summation of multiple components, of which both the traditionally studied regolith weathering patterns, and the new deep weathering regimes are distinct and decoupled components (Figure 061).

As the soil profile thins, less material is available for weathering and higher flow rates of solvent decrease residence time and saturation. However, with increased erosional factors the magnitude of deep weathering might increase in response through fracture propagation and presents a greater contribution to the overall chemical denudation of the system (Molnar et al., 2007; Clarke et al., 2010). It is worth noting that the Southern Alps of New Zealand are tectonically more active than fjordland, where much of the data came from in the 2010 study by Clarke and others. As a result, the Southern Alps will have a higher density of subsurface fractures, promoting a stronger weathering response (Cox et al., 1997; Little et al., 2002; Clarke et al., 2010). This is in accordance with the very rapid soil production rates that have been measured in the Southern Alps (Larsen et al., 2014).

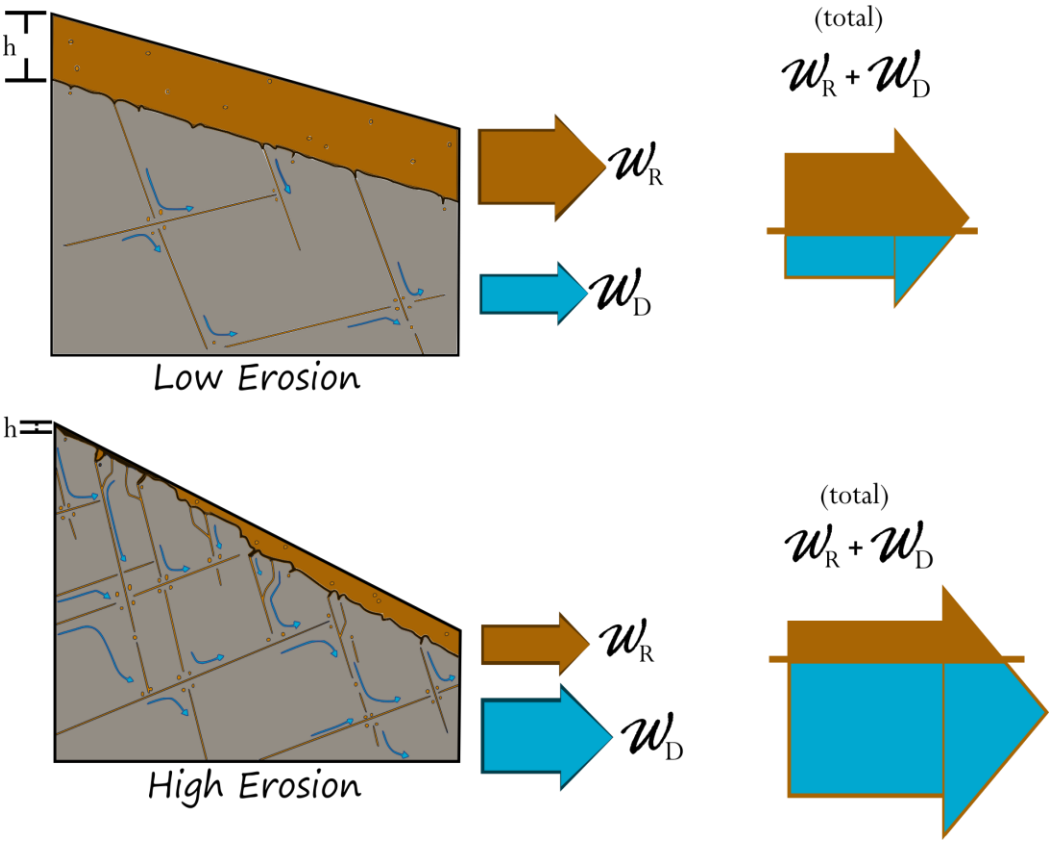

Figure 060
Diagrammatic representation of the independence of chemical weathering signals through soil mantles and deep subsurface weathering. While the chemical denudation rates observed increase with erosion, the distribution shifts between surface and groundwater processes as well. The soil depth is represented as "h", while the surface and soil-depth chemical weathering signal is marked as W_R and deep weathering as W_D.

In environments such as those demonstrated in figure 060, even with deep weathering acting in parallel, surface weathering will appear kinetically limited through observation and comply with a steady-state-soils equilibrium behavior. However, the basin scale solute fluxes will demonstrate otherwise, manifested through an increase in chemical denudation rates. Increased erosion rates driven through tectonics, uplift, and fracturing facilitate an increase in deep weathering rates. In many tectonically active environments, when deep subsurface weathering

is taken into account, the weathering zone has the potential to increase in size in an indefinitely scalable manner as a response to erosion rates.

The presence of this behavior helps to fill in the blanks for several previous studies. For example, Heimsath and others (2012) observed increasing soil production rates in parallel with increasing erosion rates. These measurements do not agree with the traditional kinetically-limited production scheme for soils, particularly with the weathering zone extending to a classically defined depth. The potential presence of a vertical weathering front into the subsurface as deep weathering offers a deeper explanation for their findings (Braun et al, 2016).

With deep weathering extant even in highly erosive alpine bedrock environments, the paradigm with no perceptible weathering on bedrock surfaces becomes plausible. It is known that chemical weathering occurs in these environments, and with deep weathering as a viable alternative to surface denudation, we can assess bedrock environments under a new lens with negligible surface weathering. As fast-eroding alpine bedrock regions are a critical source for weatherable silicate minerals and soil building materials across the globe, this new angle produces global weathering cycle implications.

6.3. Vegetation Interactions

One of the key conceptual components in this thesis is the targeted benefit gleaned by sampling in proglacial regions of eliminating several common sources of secondary weathering signals. These would otherwise distort the pure bedrock weathering signal and present challenging cases to resolve. Of these secondary sources, the biogeochemical interactions in the critical zone caused by plant life in vegetated areas is arguably by far the most significant (Drever, 1994). The Brewster Glacier exemplifies these ideas through sampling in a purely bedrock environment

devoid of soil mantles, while the ultimate transect made available at Franz Josef was less successful.

As visible in figure 005 of section 2.5., the mid-altitude region of the sampling transect at Franz Josef Glacier passed through and sampled within a vegetation-heavy region. The lower samples exist within the barren landscape of the recently retreated glacial body, while the higher samples reside in the high alpine zone with steeper gradients and lasting snow cover, precluding both portions of the sampled transect from the presence of vegetation.

When mapping the measurements for area ratio along the transect, a trend emerges of increasing surface roughness—and correspondingly weathering of surfaces—as exposure ages and distance from the glacier increases (figure 062).

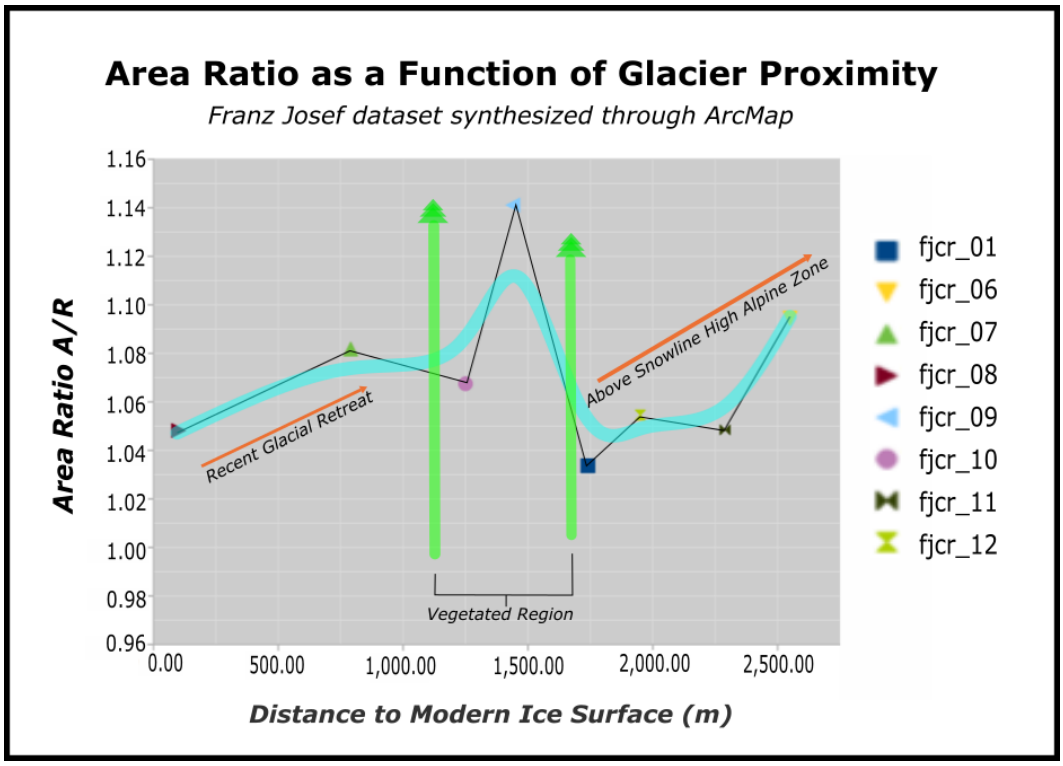

Figure 062
Changing area ratio as a function of exposure age and vector distance from the modern ice surface is presented. Weathering rate trends of increasing surface roughness parallel those of exposure age. The exception to this trend is clearly visible in the altered signal from the central group of sample sites. The trend inverts and begins to decrease before spiking as a rapid increase, followed by a rapid decrease after which the standard trend resumes, but with a lower starting value of surface roughness. Tangential interpolation lines are used to represent data trends between the calculated values shown by the data points.

The overall trend in weathering signal of increasing surface roughness with greater distance from the modern ice surface, as demonstrated by both end member ranges of the transect, is broken and inverted by the central region of the sampling transect which runs through a belt of vegetation. Through this region, the measured area ratio decreases. This decrease is coupled with a dip in interquartile range (Z) values (see figure 041, section 5.3.). Together, these paint a picture of decreasing weathering of surfaces through the vegetated region exhibited by exposed bedrock with less surface texture and a distribution towards smaller surface features,

resulting in a decrease in roughness as determined by the MCOC (see figures 055 and 056).

When applied to the higher resolution analysis of the dataset in MATLAB, a similar and more clear signal is present showing an inversion of the weathering processes as represented by morphological surface features (figure 063).

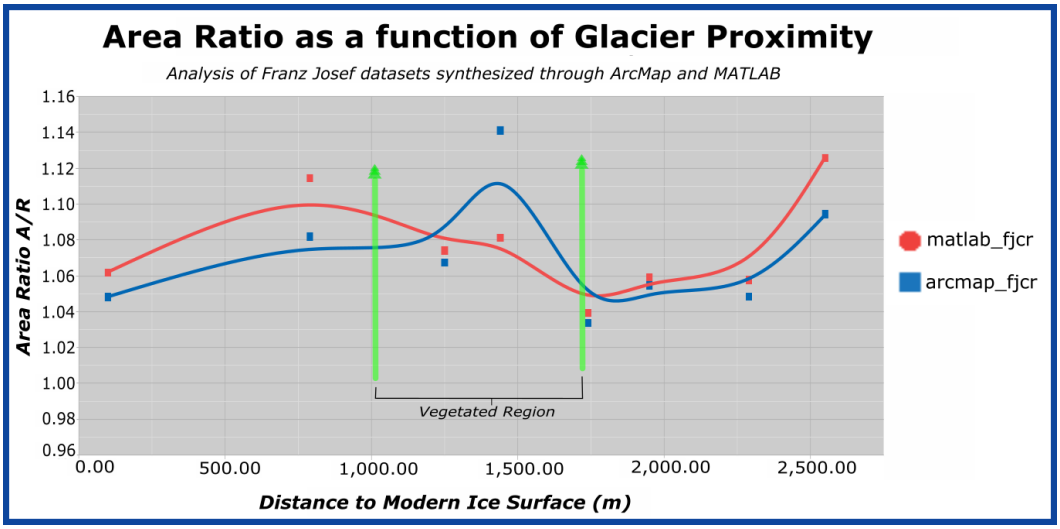

Figure 063
Changing area ratio as a function of exposure age and vector distance from the modern ice surface is presented. Patterns of the datasets appear to agree between the information synthesised via ArcMap and that generated through MATLAB. The blue lines and dots represent the ArcMap data, while the orange features represent those from MATLAB. Tangential interpolation lines are used to represent data trends between the calculated values shown by the dots.

The exact role of factors at play here are yet undetermined. As a region identified with having high lithological variability, the impact of bedrock structure and composition on vegetation growth is potentially more powerful of a factor than the forcings of vegetation on bedrock morphology. However, it is clear that there is a distinct correlation between vegetation and landscape morphology, where the nature of surface weathering is notably altered from that present in plain bedrock exposures. Further investigation into the relative impacts of weathering factors in these environments is merited to elucidate the nature of this apparent correlation.

6.4. Cosmogenics

One of the main aims for this research was to develop and test a novel field-technique for measuring weathering rates in-situ. In order to achieve this, the novel application of small-scale 3D modelling from unusual SFM perspectives and subsequent volumetric analysis would generate the difference in material volume between samples. In order to generate the final rates of weathering, absolute exposure ages would need to be gathered for the sites investigated. The well-established method of cosmogenic radionuclide surface exposure dating was to be used to calculate the differences in age between each sample, which could then be combined with the volumetric changes to garner an observed rate.

Unfortunately, due to the time-consuming nature of AMS analysis for cosmogenic radionuclide surface exposure dating, the results from processed samples have yet to be received from international laboratories. This represents a considerable issue, as without accurate dates the precision of volumetric analysis is nullified, and only relative rates may be obtained. However, it is possible that even with empirically determined sample ages, the uncertainty of dates would exceed the statistical significance needed for accurate determination at several of the sites. Because the anticipated ages at many of the sampling sites are of such small magnitude, the error associated is correspondingly large. This is due to small amounts of ^{10}Be in the samples simply as a result of the small accumulation period relative to production rates. For example, the lower two samples present at Franz Josef Glacier are estimated to be within 150 years of each other, with the lowest sample FJCR_08 being exposed for less than three quarters of a century. With local production rates of ~4 atoms g^{-1} yr^{-1} for the lowest sample, the concentration of <1000 atoms g^{-1} would be near the detection limit for this method.

However, even without absolute surface exposure ages, many of the sampling site ages can be constrained by relative age dating. Some of the sites at both Brewster Glacier and Franz Josef Glacier have been captured in historic photography from explorers and aerial photographs from map making expeditions long ago. These

historic resources can be used to reconstruct glacial position for a few of the samples. As seen in figure 064, the lowermost sample analysed at Franz Josef Glacier is beneath the glacier line in the photograph taken around 1916, and again remaining below the glacial extent in 1943, which constrains the age of the sample to between zero and 74 years. This gives the 3,389 mm^3m^{-2} difference between B_07 and B_08 duration, resulting in a relative weathering rate of 45.8 $mm^3m^{-2}a^{-1}$ (i.e. forty-five cubic millimeters per square meter per year).

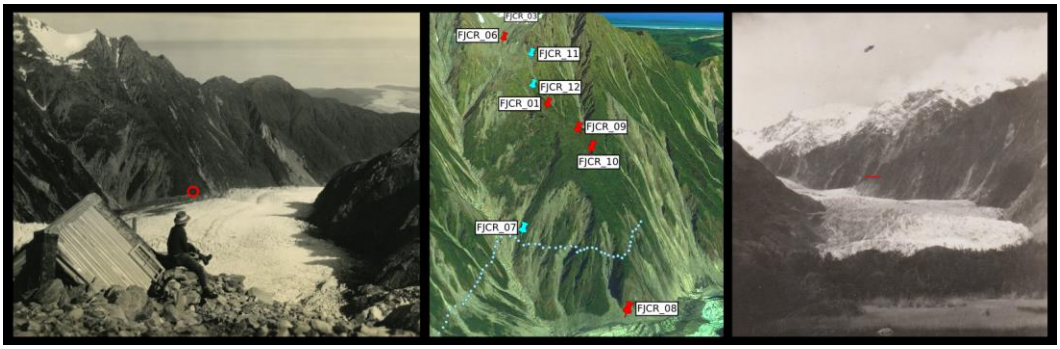

Figure 064
Historic photographs used to reconstruct approximate glacier altitudes. On left: A mountaineer enjoying the view down Franz Josef Glacier, the red circle surrounds the visible Defiance Hut with the ice nearly at its base (1916). In center: Oblique modified rendering of photo-overlay DEM sourced from Google Earth database. Perspective as if captured from Hende Ridge overlooking the Franz Josef field site of Castle Rocks on Cape Defiance Ridge. The light blue dotted markers are referenced with elevation data to show the glacial extent around 1916. On right: Photograph by H.C. Peart from August 1943 showing the extent of Franz Josef Glacier. Defiance ridge is becoming exposed, and the location of Defiance hut is marked by the red line segment.

6.5. Compositional Trend Analysis

XRF, SEM, and SEI trend analyses, as analogues to parent material composition were performed to contextualize the results gained from volumetric analysis, and to elucidate any patterns of preferential weathering in the areas studied with respect to mineralogical bias.

6.5.1. Scanning Electron Microscopy

As delineated in results section 4.6, the minerals present at Brewster Glacier as identified through the electron microprobe and BSE false color image analysis are most likely Ti-anorthite, cordierite, albite, and an unnamed calcium-magnesium-aluminum-silicate. As the rocks present are in close proximity to the Alpine Fault (section 2.4.1.) they are metamorphically transitional along a gradient that is variable depending on location. For example, the albite mineral under environments of high pressure and low temperature—conditions expected in a near-surface faulting environment—generates products of jadeite and quartz. In the false-color SEI images, this transitional albite is represented with the cyan color filter, and often its divergence to jadeite or quartz is small enough to escape detection on the greyscale and often is only notable with the microprobe point analysis (figure 065).

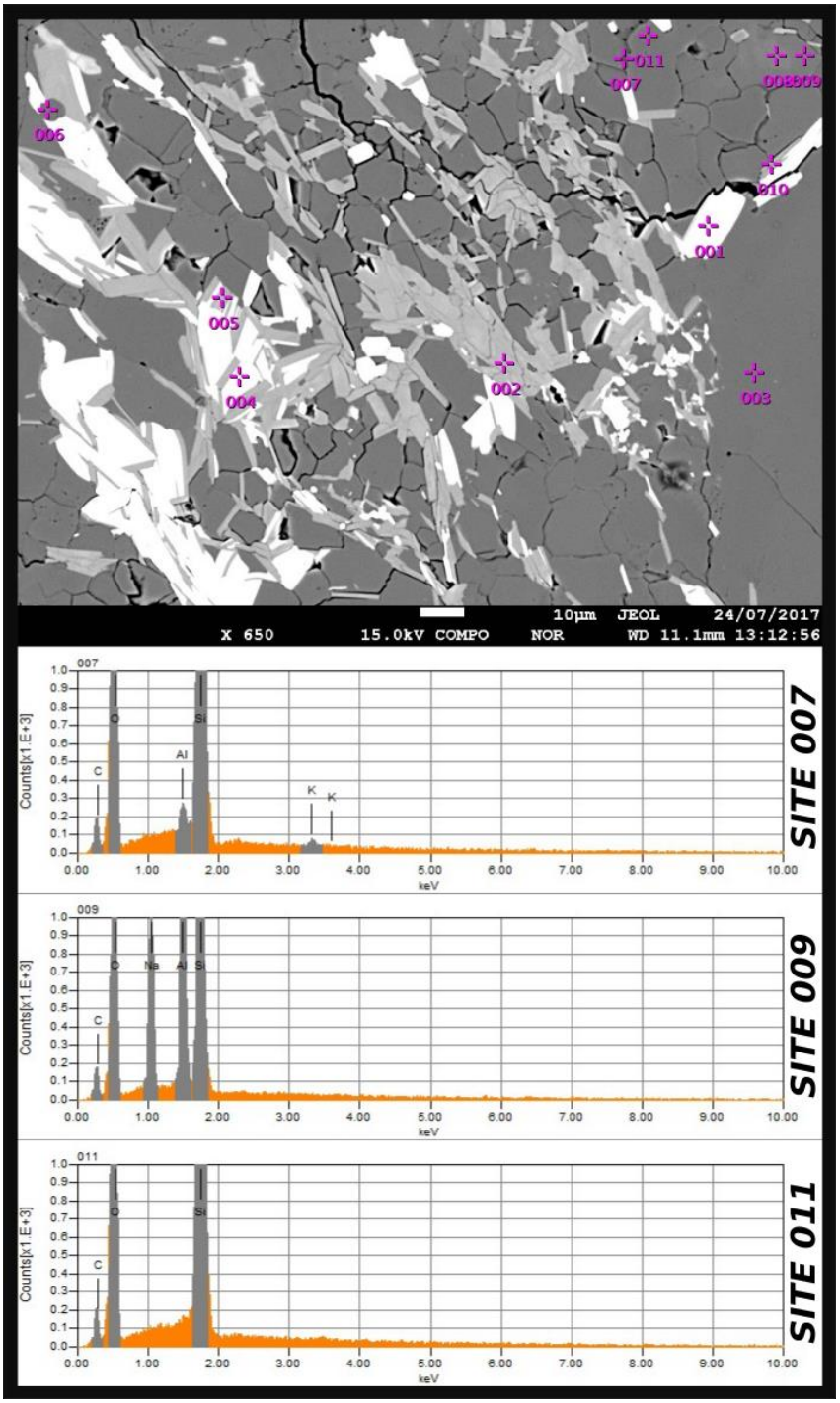

Figure 065
Greyscale BSE image of Brewster Glacier sample B_03. The brightness of each mineral is controlled by its mean atomic number, and therefore different mineral combinations will have different apparent brightnesses. Though the appear quite similar, as shown here site 007, 009, and 011 are entirely different minerals. However, sites 008 and 009 share the same composition, as do sites 003, 006, and 011.

The mineralogical percent composition analyses carried out through the optical determination process outlined in section 4.6. shows variable behavior between sites indicating that they are at varying states of weathered, yet demonstrates no clear patterns. As visible in results section 5.5. with figures 049, 050, 051, 052, and 053, there are no discernable trends of compositional variation along the sampling transect present either in the body or the top 100µm of surface (see also figure 066 below). This is a very important note to make, as it shows no supporting evidence for surface weathering patterns between samples.

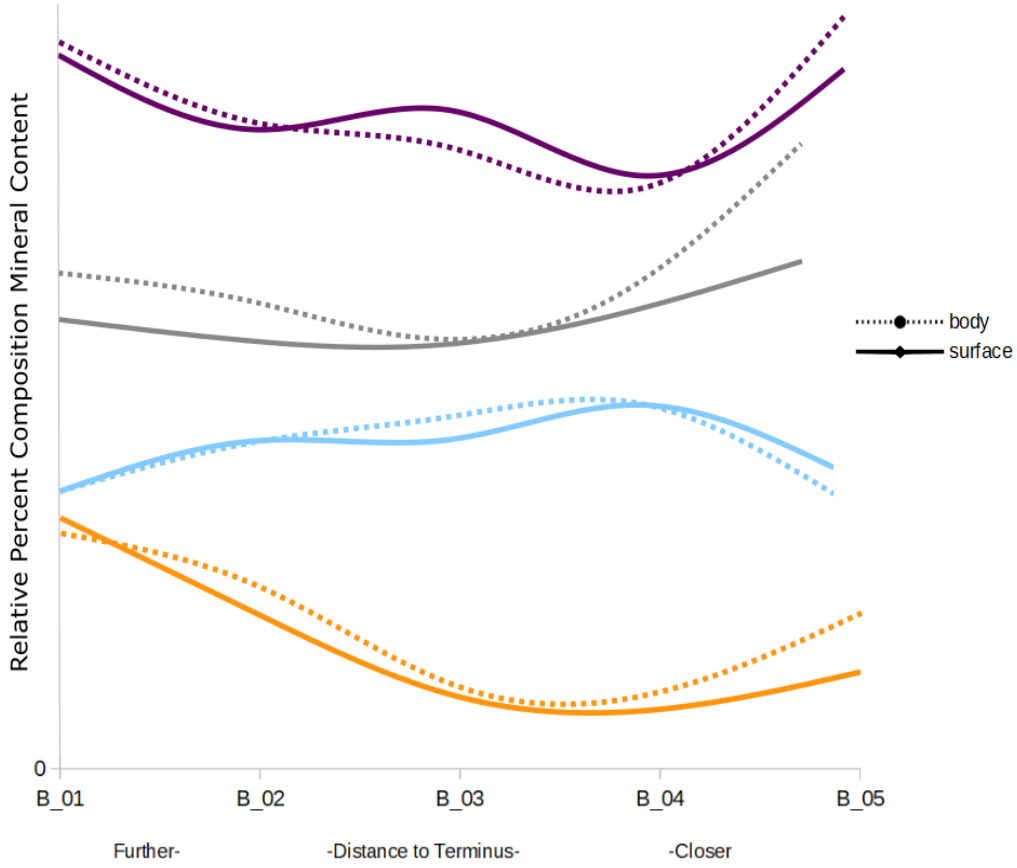

Figure 066

Relative percent composition mineral content of each sample along the transect of Brewster Glacier. Graphical representation illustrates the lack of continuous trends along the transect for all investigated minerals. Magenta corresponds to an unnamed calcium-magnesium-aluminum-silicate, grey corresponds to Titanium-anorthite, cyan corresponds to Albite, and the yellow corresponds to Cordierite.

Unfortunately, the local lithological variability casts doubt on the robustness of these findings, as the compositional variability from sample to sample could be entirely dictated by the parent material. However, the ability to distinguish between and generate analytical measurements independently for the body and surface of each sample allows an alternative analysis which is independent of compositional predispositions. By examining the differences in compositional makeup between the body and surface profiles for each mineral at each site, we can generate relative values for compositional variations which arise as a direct result of weathering. Examining figure 054 in results section 5.5., and again below, it is evident that along with no trends in surface-body mineralogical variations there is very little magnitude in variability between the body and surface of samples for all constituents investigated.

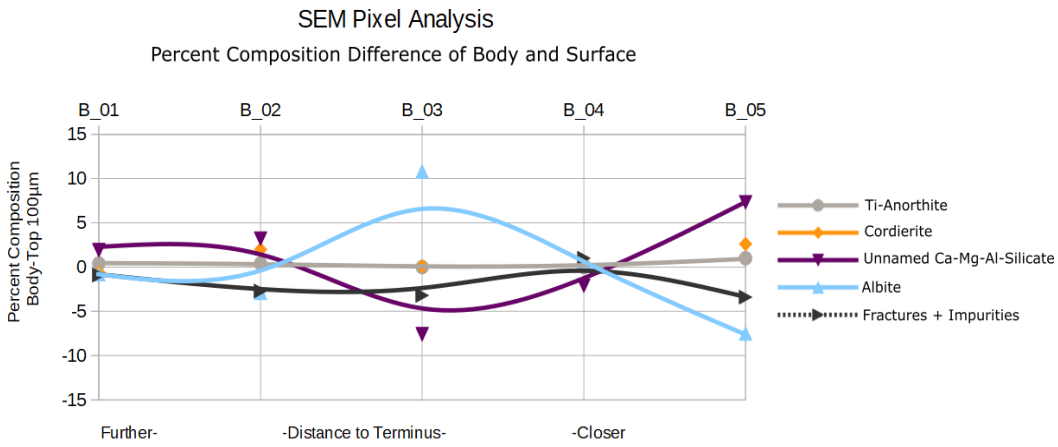

Figure 054
Difference in percent composition of each constituent mineral's body and surface values in samples, as optically determined through false-color BSE Images. The percent composition was independently calculated for the surface (top 100µm) and the body (entire field of view minus top 100µm). The surface values were subtracted from the body values to depict trends in compositional changes between the surface and body of samples.

The lack of trends apparent through both starting material and zone analyses fails to provide evidence of weathering at the surface of bedrock environments along the entire transect. This supports the concept that in the areas studied, little to no in-situ surficial weathering is occurring of the bedrock.

6.5.2. X-ray Fluorescence

XRF was carried out on each sample and analyzed for trends among groups of elements which commonly exhibit very different behaviors in response to weathering. Elements which are typically mobile such as: Ca, Na, Mg, K, as well as elements which are somewhat immobile, such as: Si, Mn, Ni and elements which are very much immobile in most weathering environments such as: Fe, Al, Ti, Y, Zr were investigated for compositional trends along the sampling transect. In addition, both high-field strength elements such as niobium and tantalum along with low ion lithophile elements such as rubidium and strontium were likewise analyzed for trends.

If a strong weathering force was acting upon the environment studied, we would expect to see a trend of decreasing composition of the mobile elements as they are being rapidly weathered, increasing in magnitude in parallel with the distance from modern ice margin. Additionally, we would expect to observe an increase in immobile elements as their relative percent composition is adjusted with the altered rocks.

Looking at figure 043 in the results section 5.4., and again below, the mobile element potassium decreases as expected through the first half of the transect, then begins to increase again for the second half of the sampling set. Calcium has a less pronounced increase in the second half of its compositional trend, and provides likely evidence for calcite dissolution. Though the spread of data points creates a magnitude of error and uncertainty that precludes a definitive explicit decreasing behavior, one is clearly suggestive. The expression of calcium weathering in this environment has significant implications. As anorthite is present as a prominent

mineral in-situ of the samples, the weathering of this mineral would traditionally explain the decrease in calcium concentrations. However, optical analysis with SEI imaging and microprobe spot analyses preclude this behavior by showing negligible signs of anorthite weathering. As a result, the signal is likely a function of calcite weathering. This has been shown to occur in similar environments, and has been known to function as an indicator of deep weathering (White et al., 1999; Price et al., 2013; Riebe et al., 2016).

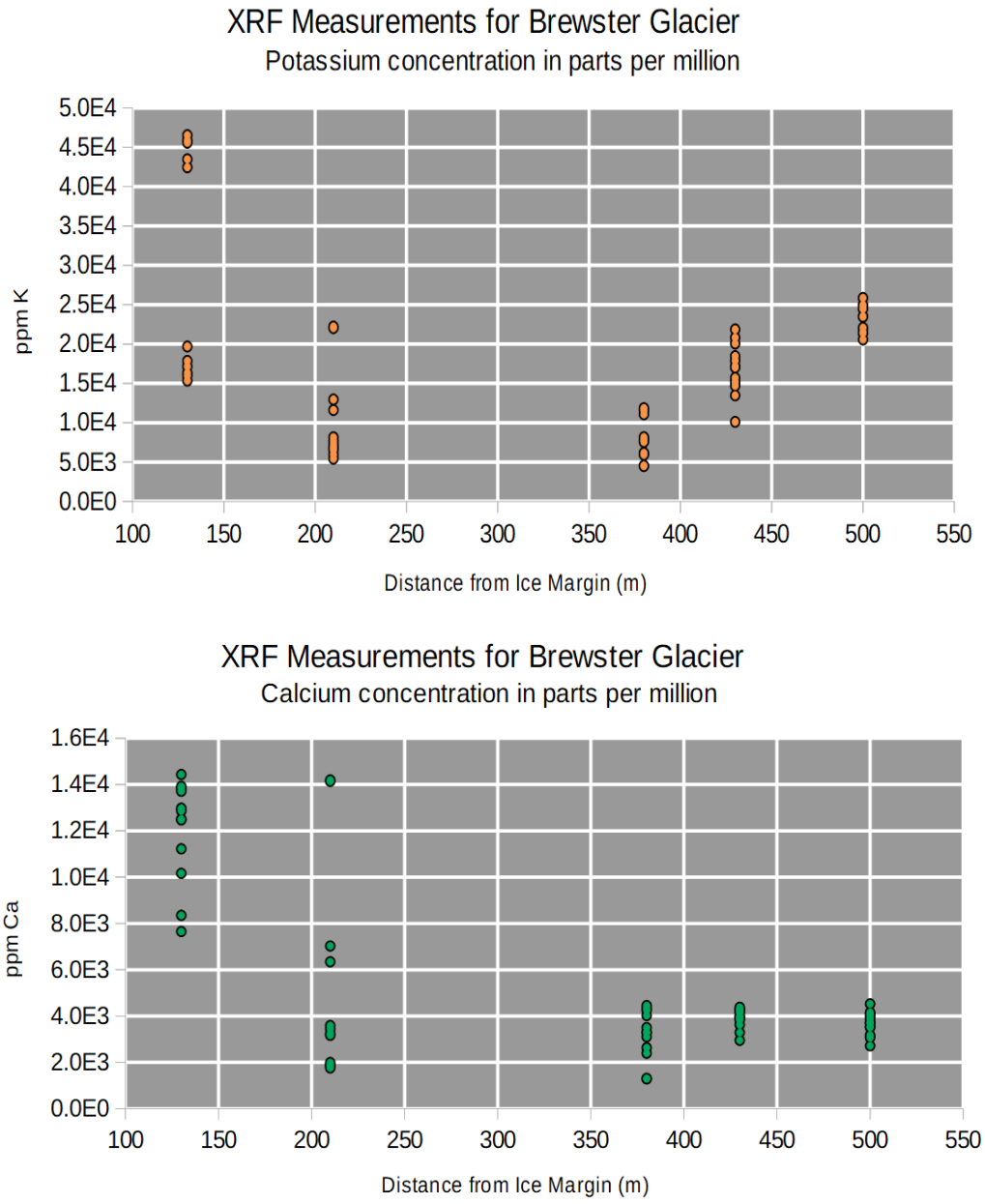

Figure 043
From top: Graphical representation of potassium and calcium trends, respectively, in samples from Brewster Glacier transect, grading from large to small displacement between sampling site and glacier terminus. Each sample site has 6 XRF Geochem readings at 10-40 kV, and 6 readings at 50kV.

The immobile elements all exhibit behavior somewhere along the spectrum between a flatline constant percent composition, and the inverse behavior of the mobile elements (figure 044, 045, and 046). This is to be expected with weathering

of any kind, though the perpetuated lack of progressive trend along the transect continues to fail for support of the case for significant active surface weathering on proglacial bedrock.

While we would expect to observe continuous trends within a progressively weathering environment, the results describe an environment with little to no weathering occurring at the surface, or where the weathering signals are so weak that they are indistinguishable from the noise generated by more dominant landscape evolution processes. However, it is clear that these environments are indeed weathering, and dramatically at that (Anderson et al., 1997).

Deep weathering and an overall lack of activity on surficial bedrock substrates produce compelling arguments to account for the disparity between measured river solute fluxes and discernable weathering processes. Yet an explanation for the variability and inconsistency of patterns in weathering signals observed across all analyses performed in this research has yet to be defined. The prevailing hypothesis entertained to account for the behavior of observations functions on the variable weatherability of surfaces as a function of lithologically discontinuous parent materials.

The small weathering signals that are detected often have little to no discernable trends, indicating that there are factors, external or intrinsic, which exhibit stronger controls on surface morphology than weathering. Inherent differences in material weatherability present an effective mechanism to alter the impacts of weathering in an environment.

As described in section 2.4.1., the entirety of the Southern Alps and particularly the field sites chosen exist in a region of metasedimentary rocks of mixed composition. To further lithological complexity, the close proximity to the Alpine fault generates a sharp metamorphic gradient that radiates outwards for kilometers. As a result, the rocks across the mountain range, and even within small regional areas of

observation exhibit relatively unpredictable levels of compositional variability. Take, for example, figure 067 below: in addition to undulating terrain generated through differential physical weathering and forces of glacial erosion, there are easily detectable bands of oxidation of surface material, dispersed throughout the landscape. Paired with the complex structural fabric of metasedimentary rocks that have undergone multiple metamorphic transformations, this produces clear evidence of locally variable lithology on a meter scale resolution.

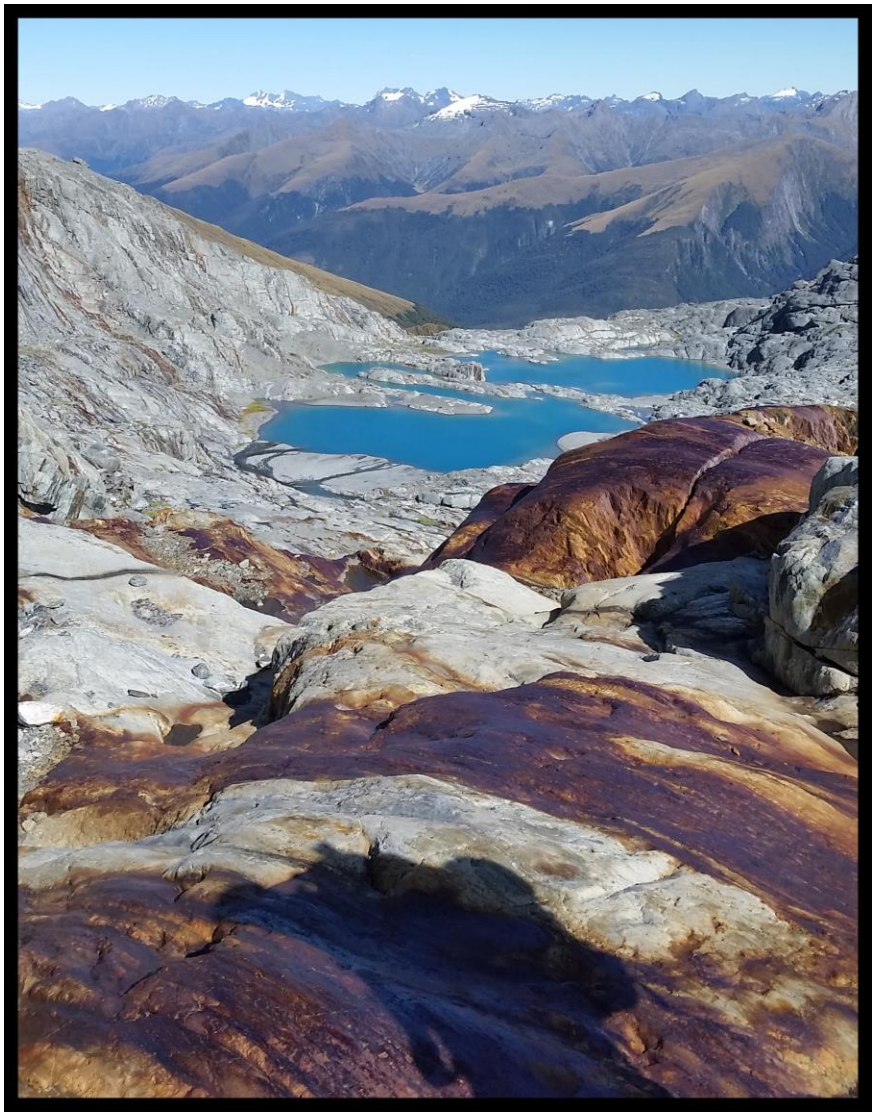

Figure 067
Local variability of bedrock lithology at Brewster Glacier easily distinguishable by the presence of iron oxide bands running parallel to the local structural fabric.

Returning to the X-ray Fluorescence results, when examining low ion lithophile elements such as rubidium and strontium, a vaguely inverse relationship is exhibited with coarse resolution with rubidium concentration reducing as a function of distance from ice margin, while strontium correspondingly experiences an increase in concentration. While rubidium and strontium aren't known to be particularly mobile elements in the context of weathering, we see a minorly associative trend between the two (Lanphere et al., 1964; Aronson, 1965). However, the trend is observed along the opposite gradient than one would expect. Classically strontium outcompetes rubidium in abundance within older rocks as both a matter of radioactive decay, and relative elemental mobility as a Low-Field-Strength-Element (LFSE). Yet we see a trend of increasing strontium and correspondingly decreasing rubidium as the rocks get *younger*, rather than *older* as we would expect. This could be due to many factors, but the lithological variability is most likely the responsible agent for these observations. While the trends in Rb-Sr abundances do not agree with exposure ages, the expected mechanisms for controlling the compositional relationships do not function on those timescales. Rather, the observed trends in LFSEs are characteristic of lithologic evolution as a function of metamorphosis (Lanphere et al., 1964; Aronson, 1965). Therefore, the elemental mobilities observed along the sampling transect are more likely to be a result of metamorphosis and diagenetic hydrothermal alteration of the parent material than surface weathering processes.

Variable parent material lithology as a function of metamorphic grade is further manifested in apparent manipulation of rock hardness. As metamorphic grades change through a formation, the properties of hardness and coherence are altered, in turn manipulating the material's inherent weatherability. This is most clearly visible through the analysis of prominence and magnitude thereof for in-situ quartz veins against the average surface elevation of the sample.

At most sites along the sampling transect within the Brewster Glacier basin, the quartz veins consistently possessed negative prominence when compared with the

rest of the sample, indicating that at least with respect to chemical denudation via etch pits, the material infill of the veins was the most weatherable component of the rock, likely a combination of calcite or zeolites with the quartz (figure 068). With closer proximity to the ice margin, samples at Franz Josef Glacier exhibited similar behavior. However, with increasing distance from the glacier, the rocks became more friable and the quartz veins assumed a positive amplitude from their surrounding surfaces, indicating that they were the least weatherable component of the rock (figure 068).

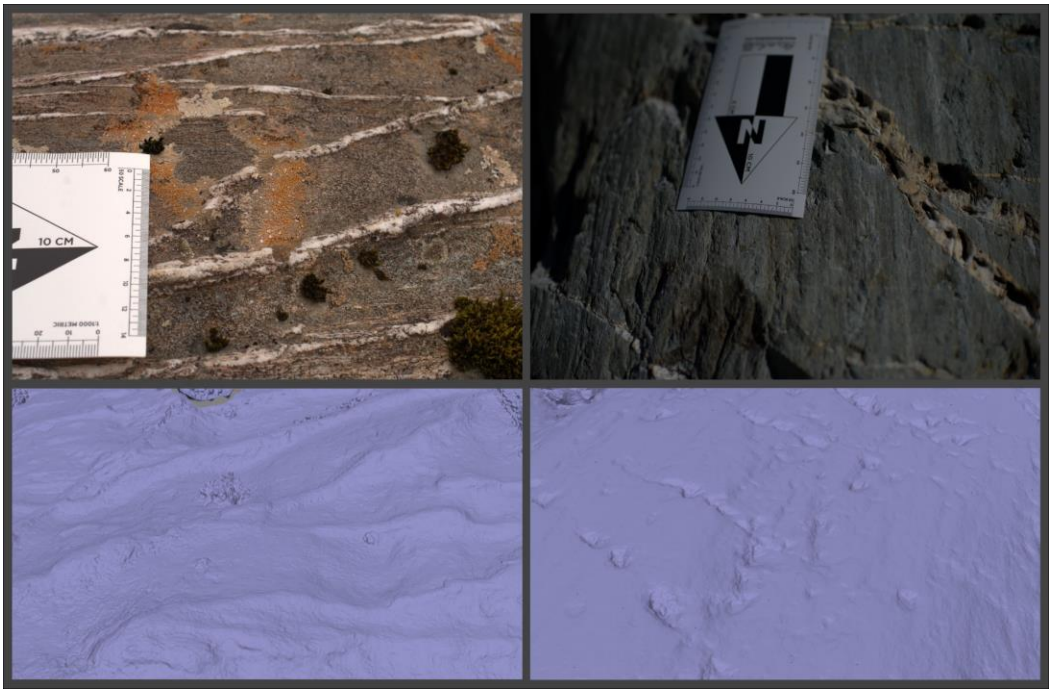

Figure 068
Intrinsic hardness, coherence, and weatherability of rock as evidenced by relative relief compared to in-situ quartz veins. Upper left: Image captured of sample FJCR_07 demonstrating the location and morphology of the quartz veins in sample. Lower left: Photoscan SFM TIN mesh model of sample FJCR_07 expressing the positive relief of quartz veins. Upper right: image captured of sample B_06 demonstrating the location and morphology of the quartz veins in sample. Lower right: Photoscan SFM TIN mesh model of sample B_06 expressing the negative relief of quartz veins.

Metamorphic grade as it relates to rock hardness has a profound impact on the weatherability of rocks. Areas of higher metamorphic grade will weather less than their lower grade counterparts, but the relationship is nonlinear. This results in a disparity of roughness which is amplified disproportionately to the difference in metamorphic grade, so that small changes in original material hardness can result in very large differences to landscape roughness (Day, 1980; McCarroll, 1991; Nicholson, 2009).

With respect to the higher elevation sites at Franz Josef Glacier, the dramatic shift in rock weatherability has a negative impact on the analytical methods employed. With regards to cosmogenic radionuclide dating, the surface exposure ages generated will be dramatically different from the actual date of exhumation, as the surface is being eroded at a rate that is faster than the accumulation of ^{10}Be. As a result, the ages received will underestimate the surface exposure age in the context of glacially-derived exposure. The age will, however, still provide an estimate for the length of time that the current surface has been exposed for. With lithological controls determining the trends of results, it is clear that this is a variable which will be imperative to control for future research.

6.6. Field Site Disparities

The two field sites in this study where chosen due to their differential time scales, yet similar characteristics. The main focus was an effort to establish similar observations of weathering patterns over multiple time resolutions, with the Brewster Glacier operating on a time scale of several thousand years, and the Franz Josef Glacier operating on a time scale of several tens of thousands of years. Initially an attempt to add Antarctic samples in the mix to add a hundred-thousand-year time scale to the mix was made, but insufficient data was available remotely to properly make comparative analyses.

The two regional sites would in an ideal setting have identical morphological characteristics with only time as a variable. Indeed, many common features were shared between the two sites. The sites both occur along a hillslope transect perpendicular to glacial flow, and are located along the western margin of the Southern Alps of New Zealand. However, while both Brewster and Franz Josef as field sites share the same rock type as a dominant feature in their lithologies, the very nature of greywacke is variable and heavily depends on the parent material, structural fabric, and grade of metamorphic deformation for trends in composition (Cummins, 1962). As such, the greywacke exposures studied at each field site differed slightly in their chemical and mineralogical constituents, and greatly in physical characteristics (e.g. hardness, weatherability, cleaved semischist vs foliated schist) with the rocks local to Franz Josef exhibiting less structural coherence and exhibiting a much higher weatherability. The higher samples along the transect at Franz Josef showed such signs of intense weathering that adjacent material was nearly friable by hand.

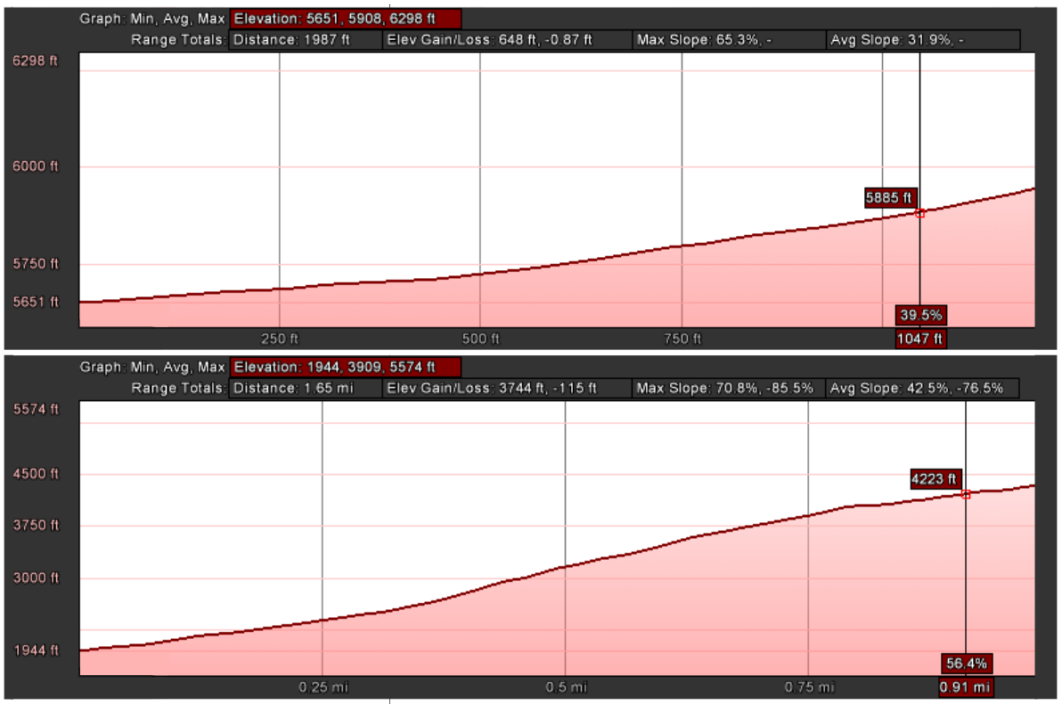

Figure 069
Partial elevation profile graphs for the field sites, showing distribution and magnitude of slopes. The upper graph represents the elevation profile for the sampling transect at Brewster Glacier, and the lower graph represents the Franz Josef Glacier transect. Note that the average slope at Franz Josef Glacier is a 10% steeper grade.

The main areas in which the two field sites differ from each other are biodiversity, aspect, slope, and geographic setting. Though the studied transects occur at similar elevations, Franz Josef has alpine vegetation that persists through sixty percent of the sampling area while Brewster Glacier had no flora or developed soil horizons at any of the sampling sites. The Franz Josef Glacier valley is nearly an order of magnitude deeper than the Brewster Glacier catchment, and has particularly steep slopes present as a function of glacier size, flow characteristics, local lithology, and timescale (figure 069). The result of this generates much more shielding of many sample sites, which impacts the collection of cosmogenic particles, as well as the magnitude of weathering forces. Further, due to the location of Franz Josef on the west coast of New Zealand, the region receives more frequent and severe weather patterns with an annual rainfall of ~12 m per year (Griffiths and McSaveney, 1983) when compared with the setting of Brewster Glacier which lies further inland with

an annual rainfall of ~6m per year (Anderson et al., 2010) and is shielded from the initial brunt of onshore weather events by an adjacent mountain range (section 2.4., 2.5) (Salinger, 1980; Ibbitt et al., 2000).

These disparities between field sites are important to note, as much of the analysis was performed without calculated calibrations against these external factors. Each one is likely to have a small measurable impact on the results generated through the application of most field techniques.

6.7. Computational Model Evaluation

Despite the complex environments being modeled, the computational analyses performed with a level of precision eligible for success. Though the variable lithology influenced results such that the data were challenging to interpret, the models themselves were evaluated to have functioned exceptionally well (see section 5.2.). However, as this research functions as the initial testing and review for these techniques, operations were not without shortcomings. From field collection to computational analysis, minor issues were noted which hindered analysis functionally or logistically.

It is noted that while four independent scales of observation per sample were intended for each sampling area, factors at both sites limited photography capture and model rendering. In following the photographic procedures outlined in 4.1.3. and referenced in 4.2., both field areas inhibited fulfillment of all the photography criteria for capturing the intermediate scales. Insufficient photographs were accurately captured at the Brewster field site, leaving the photosets for the two intermediate scales too thin to independently generate accurate 3D models within Photoscan. Luckily, the two scales are similar enough in their cross section of observational area and resolution, and as such were able to be combined for a single medium-scale model of very high accuracy (figure 070). At Franz Josef Glacier, the terrain and vegetation and most of the field sites was such that it was either too

dangerous to capture the furthest set of photographs in a 3-5m radius, or there was not enough adjacent land area to locate to for taking the photographs. For this reason, only a single high-resolution scale of analysis was performed.

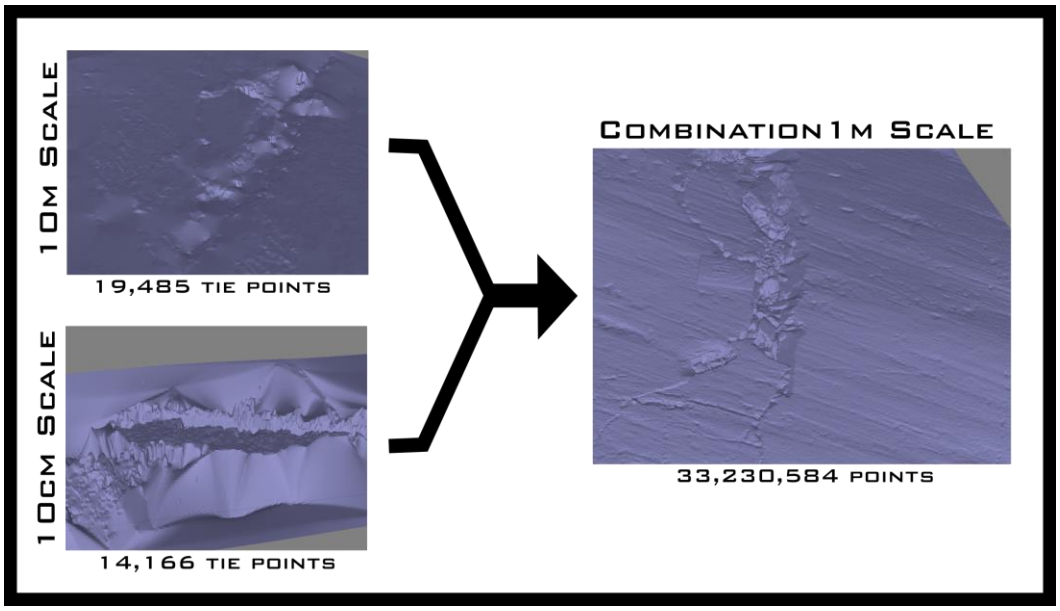

Figure 070
Point cloud TIN mesh models of the two resolutions with insufficient photography at Brewster Glacier sampling site B_02, which were combined to generate a high resolution intermediate scale. Note that though the number of photos used was simply doubled, the number of spatial reference points generated is increased by multiple orders of magnitude.

6.7.1. ArcMap

When utilising the ESRI ArcGIS program ArcMap, computational limitations by way of software programming were quickly realised. Due to its designed structure, ArcMap remains a single threaded 32-bit software program. Essentially, the software can only use a single core of a multi-core processor. This prevents the full or even partial utilisation of computational resources available. Particularly frustrating with 32 cores available on a high-performance cluster, when only one thread can be processed at a time, fixing computing time to a much larger time scale than necessary. Even on a small-capacity personal computer, these computational

limits are apparent, with several of the models investigated having point counts too excessive for the single thread processing to handle, given even an infinite amount of time. With the larger scale combination arrays generated for Brewster sites B_01, B_02, B_03, B_04, and B_07 composed of between 15-25 million points, regardless of parameters set or processing power supplied, the file exports would fail on every attempt. The only solution available to mitigate the issue while maintaining continuity of analysis was to interpolate the grid to assimilate a successfully run sample and dramatically reduce the resolution of each model. However, this then entirely prevented the continuity of resolution, rendering it unable to be performed while maintaining experimental integrity. The only solution available to mitigate the issue was to dramatically cut down the observational window to allow for the appropriate number of points to be present. This greatly reduced the magnitude to which the output files were representative of the entire surface studied. As a result, the data yielded maintained its accuracy, but the requirement to reduce resolution or window size and thus overall precision of calculations is an unacceptable course of action for mitigating shortcomings in software rather than raw data quality.

It is very important to note that there are two main points within this procedure where subjectivity is introduced by the researcher. With the current adaptive capacity of the model being limited as it is, these are a necessary course of action to ensure that the calculations are representative of the surfaces studied. This subjectivity is introduced when applying surface reconstruction methods, particularly in the event of differential global polynomial interpolation orders, and further at the time of break point classification of features within the DEM of Difference.

With the maximum global polynomial interpolation filter (GPI) being a 10th degree, and the lack of controls on polynomial targeting, there were departures from optimal fit on both ends of the roughness and weathering spectrum. With samples such as (B_01), the weathering pits were small and few, while the regional surface

had relatively smaller scale striations, which the 10th order polynomial was unable to account for. This required modifying the classification break threshold for features much smaller than ideal, as the striations were picked up prior to the majority of the smaller weathering features (figure 071). As a result, the detection limit for weathering features was negatively affected, and prevented a fully representative surface characterisation.

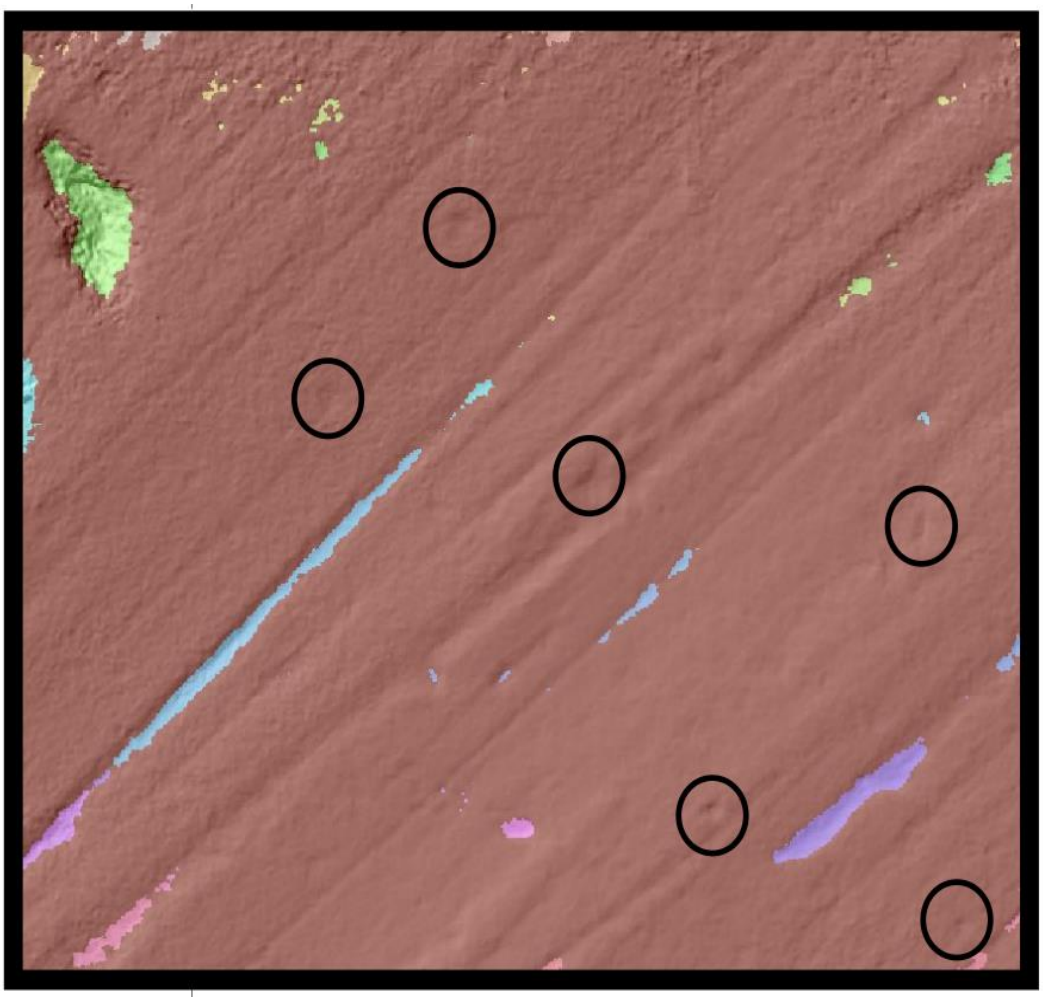

Figure 071
DEM of difference between the original sample and the polynomial interpolation surface, with pixels grouped into regions of individual features. Note the mis-identification of the linear striae features, while the individual etch pits circled in black were missed by the computational approach.

With samples such as (B_06), the opposing issue was present. While there was relatively larger scale low frequency features that the GPI could mitigate, the intensity of weathering signaled by high amplitude absolute pit depth measurements interfered with the GPI signal, resulting in biased and reduced depth values (figure 072). With the target weathering features being detected and influencing the GPI, a compromise without ideal outcomes must be reached, where the balance is established between proper background morphology noise reduction, poor feature identification, and reduction of pit depth measurements.

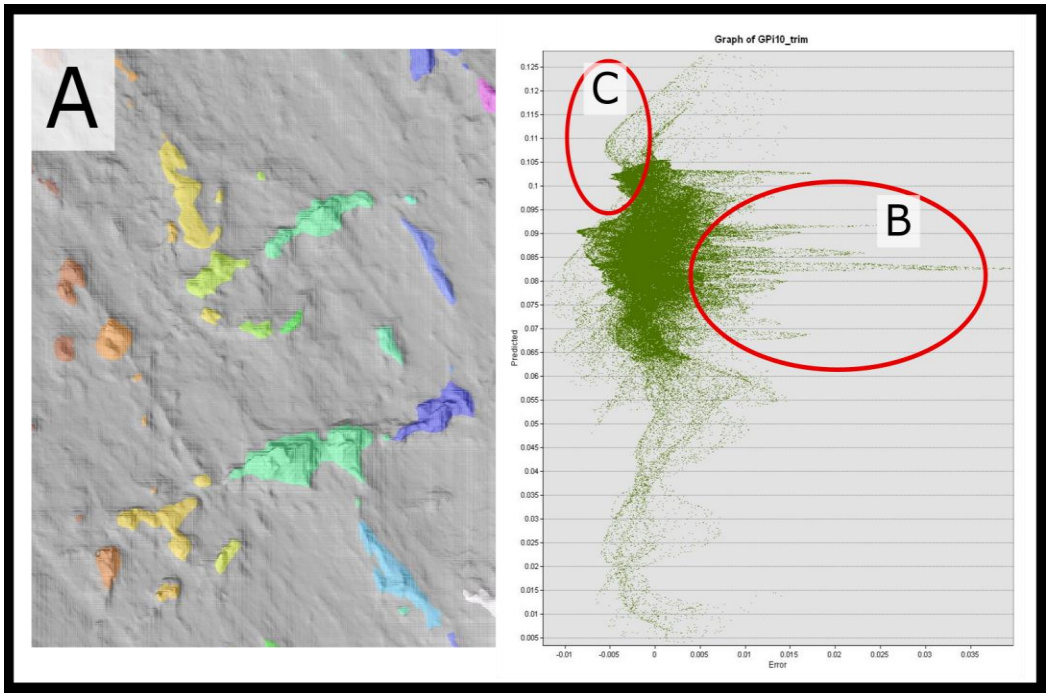

Figure 072
DEM of difference for sample B_06 and the graph of computational accuracy for the 10th order global polynomial interpolation function. It is clear in (a) that the large weathering pit features are perfectly isolated and accounted for, while there are abundant surface features of smaller amplitude that are skipped over. The cloud of points encircled in (b) are the negative relief inconsistencies generated by the interpolated surface, corresponding with the large pits. However, this weighted the entire dataset improperly, causing all of the points relating to smaller surface features, encircled at (c) to become positive relief features which are skipped over by subsequent processing.

One potential method of mitigation was to incorporate the ArcMap GPI interpolation outputs at the highest level without target feature distortion with the CWT functions to properly target the morphological erosion features desired. However, it was subsequently discovered that the continuous wavelet transform method is immune to geometrically dissimilar features regardless of scale.

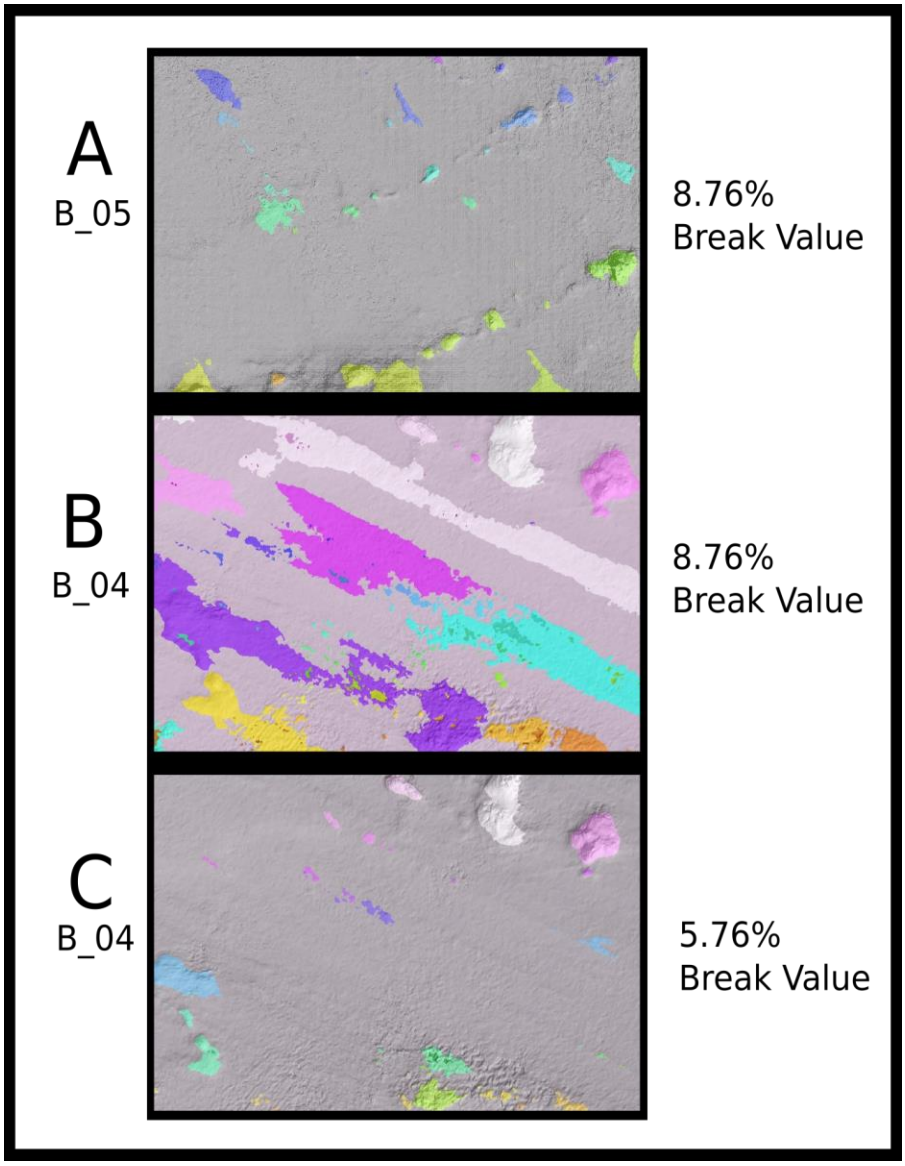

Figure 073
Discontinuity of DoD feature thresholding between samples represented by maintaining the break value from sample B_05 (A) through to sample B_04 (B), with the threshold manually adjusted for best fit on the same B_04 sample DoD (C).

The second and arguably most significant component of introduced analytical subjectivity occurs when manually setting the break points for classifying features. Due to the widely variable surface morphology present in the study areas and the inconsistent fit of GPI, the classification thresholds for targeted features need to be manually established. Figure 073 demonstrates this issue. Model (A) is shown for sample B_05 where the grouped regions accurately represent the desired etch pits, with the central break value for classification set at 8.76%. Yet when that same break value is applied to the next sample in (B), B_04, the threshold is too lax and allows low frequency surface features to fall into the same categories, obscuring the higher frequency targeted features. When the break value is adjusted by just 3% in (C), the proper features are brought back into focus. Optically determined by the researcher, the correct break values for each model are chosen as the compromise between inclusivity of all target features and exclusion of improper artefacts. This process is imperative for proper analytical modeling within the ArcMap approach, yet it is entirely subjective in its application.

6.7.2 MATLAB

The CWT artefact analysis was very effective at determining surface features independently of contextual morphology, and provided more accurate analysis of both frequency and artefact volumes than the ArcMap approach (figure 074).

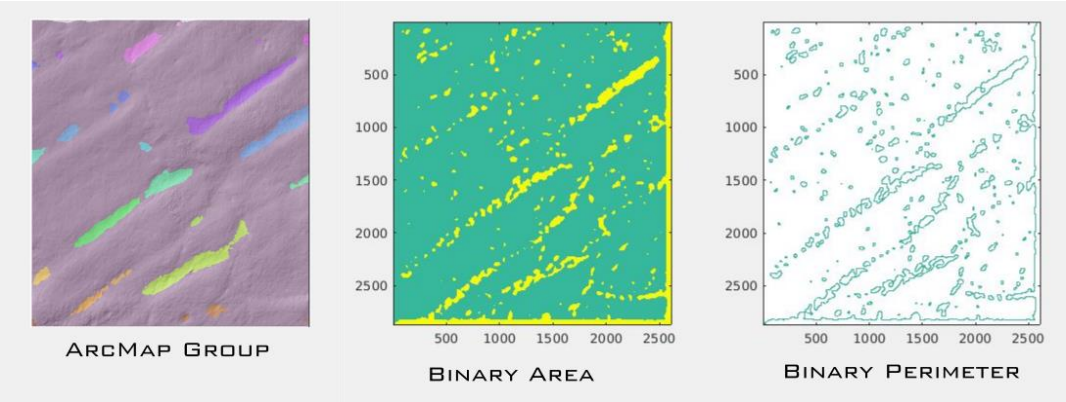

Figure 074
The same sample analysed for weathering pit features by ArcMap (on left), and MATLAB (at center). The precision and number of etch pits isolated through MATLAB are orders of magnitude more, seen clearly in the perimeter calculation step (on right).

However, when analysing many of the sites at Franz Josef Glacier, the high level of specificity designed into the algorithm made the characterisation of weathering surfaces difficult. This is largely due to the advanced states of weathering that many of the samples exhibited, which was expressed morphologically in different ways than initial weathering often presents itself, and as was targeted at Brewster Glacier (figure 075).

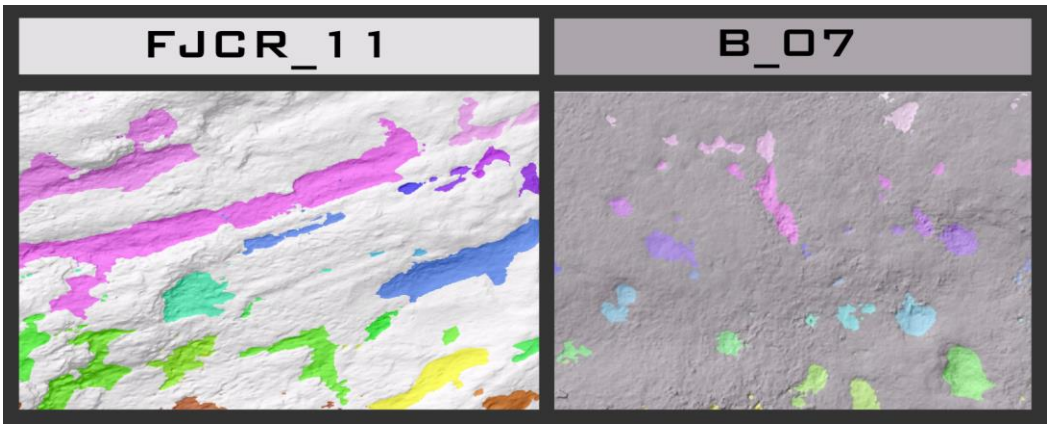

Figure 075
Hillshade models of the different morphology of weathering surfaces between the highly weathered rocks at Franz Josef Glacier (on left), and the incipient weathering etch pits at Brewster Glacier (at right).

As the surfaces present along the sampling transect progressively exhibit stronger signals of erosion, the geometry of surface artefacts differentiated further from the classical inversely parabolic etch pit to more complex and elongate features. As the models employed were specifically designed to target the morphology of incipient weathering features, their identification and characterisation of weathering artefacts on highly eroded features becomes less accurate. However, even with features of complex microtopography, overall the MATLAB models handle the artefacts and surface reconstruction remarkably well (figure 076).

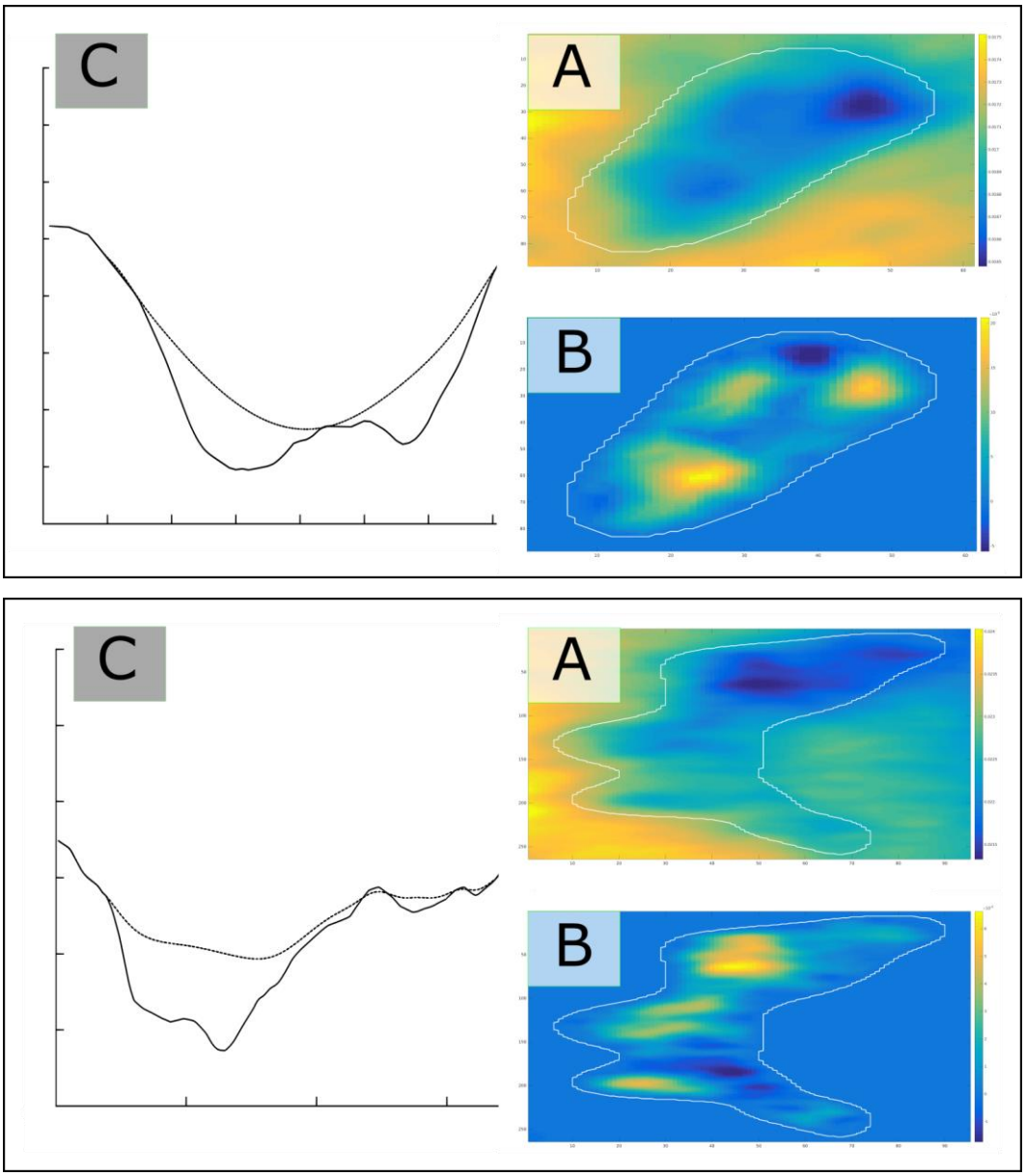

Figure 076
Output figures generated for two single weathering pit clusters from the 'pitstats2.m' script. The two features selected showcase the efficacy of the script to handle complex microtopography. The contour surface interpolation method takes into account the contextual morphology, and with the added handle of a +5% perimeter, approximates a pre-weathering surface of reasonable accuracy. The pit perimeter is located within the heightmap of the full DEM (A). The lower image (B) shows the same colour filter applied with the area outside the feature perimeter set to 'nan', and as such the range decreases to show morphology in higher detail. A cross section of the pit (C) is printed and shows the level of conformity for the new surface contour (dashed line).

6.8. Interquartile Ratio Accuracy

The application of interquartile ratio, as detailed in section 3.5.2. is such that it is utilised as a calibration metric to ensure the validity of area ratio calculations. However, as evidenced in figure 077, the interquartile ratio of surface feature amplitude frequency exhibits a remarkable parallel correlation behavior to area ratio. This is particularly interesting as the two metrics are generated using entirely different analytical components. The area ratio is a direct comparison between two and three-dimensional surface area, while the interquartile ratio is calculated by the ratio of median splits of each half of a dataset generated by organizing the amplitude of surface features into categories by frequency. The congruence of behavior between the two metrics not only validates the representative accuracy of calculated results, but also presents the interquartile range as a compelling standalone proxy for surface roughness.

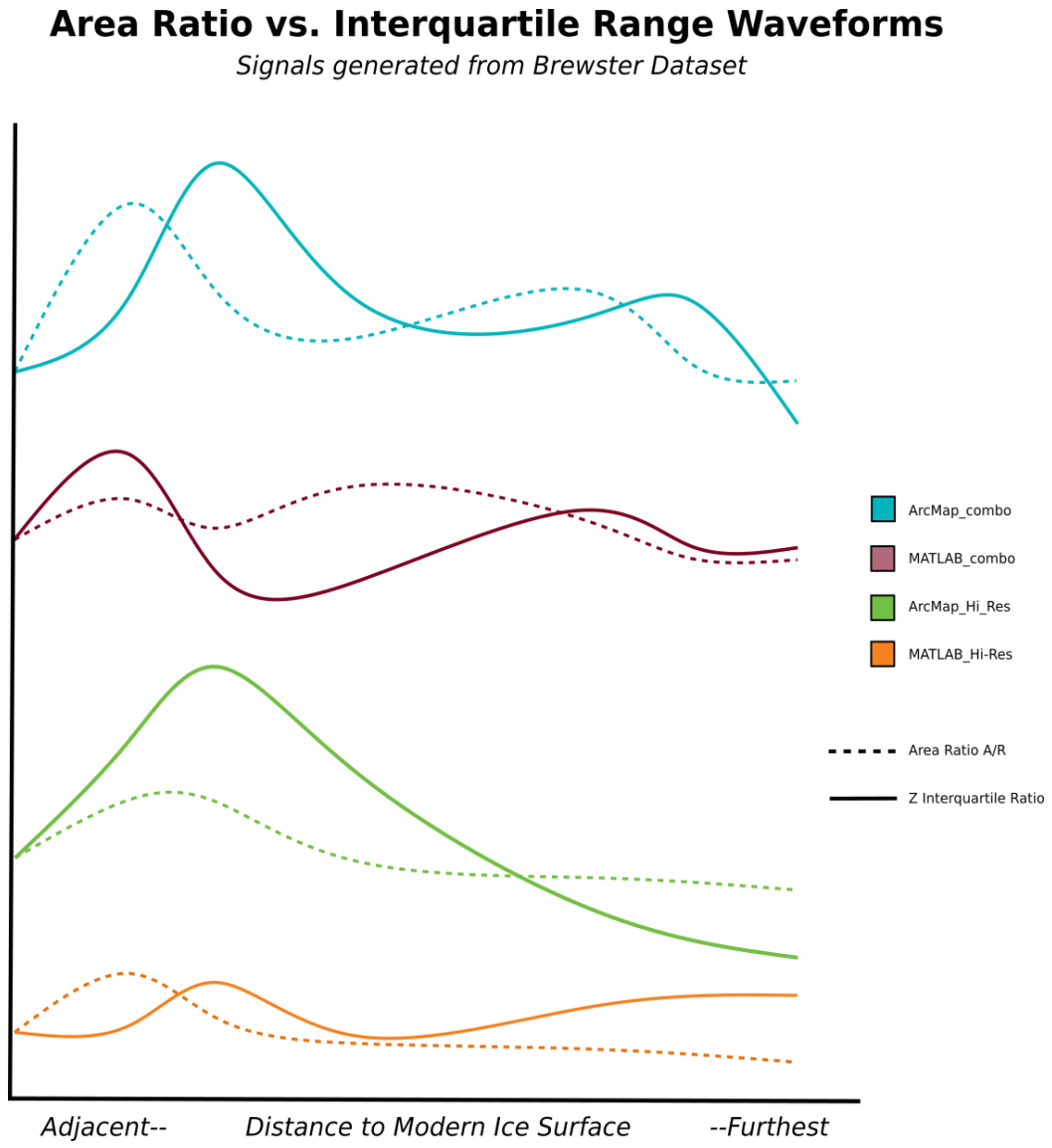

Figure 077
Waveform comparison between ArcMap and MATLAB generation of Aria Ratio and the Interquartile Range measurement, Z. As unitless metrics, the compatibility of A/R and Z cannot be quantified, and as such for this diagram, amplitude of waveforms can be ignored. Despite the vastly different components of generation, the signal behavior is very similar between the two metrics.

6.9. Experimental Error

The components that make up the Area Ratio (A/R) parameter produce significant output bias based on the properties of observed models. A/R lends itself towards comparing near-congruent models, as it has a high susceptibility of producing inaccurate results when presented with datasets of variable scale and resolution. Though scale modification does not affect the relative proportions of the area ratio as each component measurement has a geometric relationship with change in 2D area, the lack of uniformity and inherent fractal nature of geologic structures lead towards a scenario of feature exclusion as scale increases (Turcotte and Huang, 1995). With a sizeable enough step in window size, larger textural features come into view that were previously factored out as low-frequency background noise by the applied global polynomial. The relative underrepresentation of these features in smaller scale models must be accounted for in some way to ensure that accurate representations of true surface data are generated. Resolution incompatibility, on the other hand, presents a case with much stronger explicit manipulation of area ratio results. Acting on the same morphological principles as scale modification, where the morphology of natural features is essentially scalable in a near-infinite capacity limited only by the precision of observations, resolution disparities allow for a shift in area ratio that is non-linearly related to the magnitude of change in resolution. This is because by nature, the ratio of three-dimensional surface area to two-dimensional surface area is almost always greater than one. When observational scale changes, both parameters are modified with the same scaling parameter. However, when resolution is disparate between the two models, only the three-dimensional surface area is modified, and therefore fundamentally changes the properties of the surface area, in a manner which reduces the apparent roughness/texture. Thus, unlike scale modification where each component shares the same relationship between modified variable and outputs, resolution has the capacity to influence results in a non-linear capacity (Siu-Ngan Lam and Quattrochi, 1992). With two independent variables simultaneously acting on the same set of results with mathematically different behaviors, an arithmetic solution is as complicated and prone to error as it would seem.

The ideal conceptual model for roughness analysis would dictate congruent resolution and region size as a prerequisite for data inputs. Normalising the resolution can be performed in step 5 of the ArcMap procedure in section 4.7.2. where the cell size is set to the lowest resolution member. The region size can be modified following the complete model generation of each sample. This allows for a preservation of integrity for the feature identification of each sample, allowing the highest possible native resolution to be used prior to normalization. The DoD files should be imported into a single ArcMap project, and using the Spatial Analyst tool box, the "Extract by Mask" function of the "Extraction" tools can be used in a batch process to set the clip extent of each DEM to the same coordinates. This allows for each sample to be independently processed at its highest and most representative extent preserving detail, yet still be directly measured against adjacent samples without rendering entirely new ArcMap projects.

Normalisation, however, has its limits—as was discovered with the blanket calibration of every model in this study to the same standard—and there exists a finite point where the compatibility of data is nullified by the ever-increasing error of coarsening datasets. Combining the scale of the smallest model in planar space with the lowest resolution of the largest models, presents a misrepresentation of data that exhibits the smallest levels of distortion at the median of the dataset, and the highest levels of distortion at both the end members. This presents the case that a 100% normalisation of resolution and scale is truly only appropriate for suites of models with pre existing traits which exhibit low levels of variability.

In lieu of absolute normalisation, an effort was made to clarify the relationships between the resolution, scale, and outcomes of this specific study; in an attempt to account for the differences caused by these variables and to facilitate sample comparison. Scale and resolution were independently analysed by comparing the original sample datasets with those following a series of transformations. A full normalisation of samples across both sample sites with an aggressive 100%

compliance of parameters was carried out, providing a modified baseline for comparison. Each set of sample readings were converted to operate on the smallest observational area scale, at the lowest grid size resolution. A parallel set of results were generated with each sample independently operating at its native resolution, which is determined by the accuracy of the SFM generated model and the scale at which the features were observed. The first scale comparison investigated scale effects in situ, by comparing the Brewster sample sites of which each had both a model generated at a 10 cm scale, and a secondary combination model for a ~2 m scale (table 9). This was calculated by dividing the area ratio value for the smallest models, labeled as "Hi-Res" by the larger regional models labeled as "Combo", generating a percent variation that came in at just under 1%. Performed for the native and calibrated dataset, this helps generate more information on the effects of in-situ observational scale, and compare the accuracy of an aggressively normalised dataset with the same in-situ scale variations.

Table 9

Fit Metric Calculation

Hi-Res vs. Combo Dataset Comparison

Sample	Percent A/R change (HR/C)	Fit Metric to Local Avg.	Fit Metric to Global Avg.
B_01 Native	1.0092	0.0164	0.0057
B_01 Calibrated	1.0071	0.0143	0.0036
B_03 Native	0.9629	0.0309	0.0421
B_03 Calibrated	0.9410	0.0549	0.0663
B_04 Native	1.0075	0.0147	0.0040
B_04 Calibrated	1.0061	0.0133	0.0026
B_05 Native	1.0249	0.0314	0.0209
B_05 Calibrated	0.9752	0.0179	0.0289
B_06 Native	1.0470	0.0519	0.0416
B_06 Calibrated	0.9107	0.0900	0.1018
B_07 Native	1.0182	0.0251	0.0145
B_07 Calibrated	1.0023	0.0096	0.0011
Local Average Percent Change	0.9927	0.0309	0.0278

Furthering this, the fit metrics of the native and calibrated datasets to in-situ scale variation were iteratively compared through the same method, with the native resolution data as the divisor of the calibrated dataset. The percent difference in

effect due to coarse data normalisation was just 6/10,000 (six ten-thousandths) off from its derivative components at just under 1% variability as well (table 10—showing hi-res+combo native vs. calibrated).

Table 10

Fit Metric Calculation

Hi-Res+Combo Native vs. Hi-Res+Combo Calibrated Dataset Comparison

Sample	Percent A/R change (C/N)	Fit Metric to Local Avg.	Fit Metric to Global Avg.
B_01	0.9979	0.0347	0.0056
B_03	0.9772	0.0143	0.0268
B_04	0.9986	0.0354	0.0048
B_05	0.9515	0.0123	0.0545
B_06	0.8699	0.1073	0.1535
B_07	0.9844	0.0215	0.0193
Local Average Percent Change	0.9633	0.0376	0.0441

Lastly, the direct comparison between native and calibrated datasets was carried out independent of the in-situ scale change. This was accomplished through comparing each sample at both Franz Josef Glacier and Brewster glacier rendered at native resolutions and scales, directly across with their corresponding values as calculated through the normalisation of resolution and scale (table 11). It was shown that even in this direct analysis of calibrated observations of very different sampling environments, the average percent A/R change measured was 1.021%, only 2/1,000 (two thousandths) off of the previous comparison.

Table 11

Fit Metric Calculation

Native vs. Calibrated Dataset Comparison

Sample	Percent A/R change (C/N)	Fit Metric to Local Avg.	Fit Metric to Global Avg.
B_01_combo	1.0006	0.0204	0.0028
B_01_Hi_Res	0.9985	0.0226	0.0050
B_02_combo	1.0043	0.0166	0.0009
B_03_combo	1.0154	0.0056	0.0118
B_03_Hi_Res	0.9923	0.0290	0.0112
B_04_combo	0.9979	0.0232	0.0056
B_04_Hi_Res	0.9965	0.0247	0.0070
B_05_combo	1.0110	0.0099	0.0075
B_05_Hi_Res	0.9620	0.0614	0.0430
B_06_combo	1.0365	0.0149	0.0319
B_06_Hi_Res	0.9891	0.0323	0.0145
B_07_combo	1.0075	0.0134	0.0040
B_07_Hi_Res	0.9918	0.0295	0.0117
FJCR_01	1.0400	0.0182	0.0352
FJCR_06	1.0065	0.0144	0.0031
FJCR_07	1.0381	0.0165	0.0334
FJCR_08	0.9971	0.0240	0.0063
FJCR_09	1.0418	0.0200	0.0369
FJCR_10	1.0242	0.0031	0.0203
FJCR_11	1.0406	0.0188	0.0357
FJCR_12	1.2503	0.1834	0.1975
Local Average Percent Change	1.0210	0.0287	0.0250
Global Average Percent Change	1.0034	0.0324	0.0323

Each of these calculations were in turn analysed for accuracy of fit by averaging the percent influence of the variable on area ratio within each dataset, and performing the same comparison against this local average with each percent A/R change. For peace of mind, the process was repeated between analyses with a generated global average. Each calculation both locally and globally within the data expressed no more than a 4.5% variation, implying that there is an average of 97.8% of the data which agrees that within this study the scale of observation both in-situ and computationally has an average impact of just over 1% on the variability of calculated area ratio. This allows for a justified exclusion of scale as a variable on the performed calculations due to negligible statistical impact.

6.10. Fate of the Silicates

Global climate regulation driven via available mineral silica functions in two primary ways. The first, most commonly the subject of vigorous investigation within the field of geomorphology is the chemical weathering of silicate minerals, in which the chemical separation of silica into its constituent components results in a stoichiometric net loss of carbon dioxide. This fundamental process is incredibly well researched and understood, and the majority of past and current work has been to increase the knowledge of when, where, and how much of this type of reaction is occurring, in an effort to create a better approximation of Earth's ability to reduce atmospheric carbon dioxide along various timescales, playing an essential role in regulating global climates (Gillardet et al., 1999; Jacobson and Blum, 2003; Torres et al., 2017).

The primary mechanisms investigated through which these silicate minerals are released are physical and chemical weathering. Through the work demonstrated in this thesis, we can arrive at the conclusion that, at least in the glaciated Southern Alps, much of this weathering product does not occur in-situ at the surface of bedrock environments, and instead relies on deep subsurface weathering in conjunction with mechanical transport processes. These bring the material into lower regions for more complex biogeochemical interactions which might free up and break down the silicate components of the parent material.

Susanne Anderson and others have made observations which determine that while incipient weathering plays a role in separating the silicate minerals from their adjacent mineral constituents, the breakdown of these components occurs far later and further afield than the proglacial regions investigated (Anderson et al., 1997; Anderson et al., 2000; Anderson, 2005).

While we know these reactions occur, we also know that the breakdown of silicate minerals is often incomplete in nature when compared to the volume of material removed i.e. not all silicates are evolved before they are transported out of the

terrestrial sink (Walker et al., 1981; Raymo et al., 1988). However this unutilized portion of silica arguably plays an even more important role in climate change regulation once it reaches the ocean than its land-based counterparts.

Once present in the oceans as silica, these minerals are utilized to generate the exoskeletons of autotrophic phytoplankton known as diatoms (Bailleul et al, 2015). Diatoms are unique among phytoplankton in that they possess an obligate silicon requirement for growth (Lewin 1962). As a result, DSi concentrations in oceanic environments has been shown exert strong controls on diatom productions rates (Brzezinski et al., 1988). Diatoms are responsible for 20% of global primary photosynthetic production, and as a result have a profound impact on global atmospheric carbon dioxide reduction (Bailleul et al, 2015). Additionally, in terms of carbon fixing capacity and biomass, the production of the atmospheric oxygen that we use for respiration originates as much from their production as tropical rainforests (Bailleul et al, 2015).

In order to be available for diatom genesis, the silica must be present in the photic zone/surface waters, where such lifeforms exist. The oceanic silica cycle reintroduces these components to the surface waters through sediment-water interfaces and dissolved silica nutrient upwelling from deep benthic currents (Tréguer et al., 2017), while terrestrial components either arrive as dissolved silica in the form of silicic acid, or are deposited as mineral-bound silica which is quickly turned into silicic acid by the dissolved ion gradient present in oceanic waters (Siever 1991). Concentrations of silica in the surface waters of the ocean are often more than one order of magnitude undersaturated with respect to quartz and a further two orders of magnitude with respect to biogenic silica. This undersaturation is only explained by the presence of diatoms actively removing DSi, as standard equilibria and reaction kinetics cannot account for the observed concentrations (Conley, 2002). The net dissolved river load, while trivial in comparison to the volume of the oceanic silica cycle, comprises 80% of the dissolved inputs to the ocean (Tréguer et al., 1995).

Diatoms source their silica from the ocean around them, which is derived from the global oceanic silica cycle and perpetual contributions from the continental silica cycle as generated by river loads (Conley, 2002; Conley, 2003; Tréguer and De La Rocha, 2012; Cermeño et al., 2015). This provides a direct link between silicate mineral erosion and weathering to atmospheric carbon dioxide drawdown, and as a result establishes an additional relationship between landscape denudation rates and global climate regulation.

This link is particularly important with respect to alpine weathering environments close to oceanic bodies, with high transport rates as we see in NZ. Often the erosion and transport rates are so great that a larger percentage than is standard of silicate minerals are transported out of the terrestrial environment into the oceanic silica cycle before they have a chance to weather, and therefore play a stronger role in climate regulation (Conley, 2003; Jacobson and Blum, 2003).

A study from 2003 from Penna and others showed that diatoms could essentially directly utilize silica from crystalline sources (or dissolution processes directly adjacent) which showed that they preferentially replicate in the context of crystalline silica sources rather than biogenically generated silica (Penna et al., 2003). The affinity for diatoms to proliferate in environments with crystalline forms of silicates makes room for the potential of alternative landscape evolution mechanisms to influence the global silicate and carbon system. The idea of airbourne materials influencing oceanic diatom populations was introduced in 2000 by Harrison. The implication was that increased silicate-bearing sediments produced during glacial periods would subsequently generate a large supply of silicates to be transported to the oceans as dust. The additional silicate flux then lowers the CO_2 levels during the corresponding glacial-interglacial periods (Harrison, 2000).

7. Conclusion

Successful determination of weathering patterns within incipient weathering of proglacial areas has led to the discovery of active deep weathering in high alpine environments. This provides a substantiating case for the influence of deep weathering on actively evolving landscapes globally.

Novel micro-SFM photogrammetry techniques successfully generated the three-dimensional rendering of surface features utilised for surface weathering characterisation, with notable accuracy and precision. This provides additional support in favor of SFM as a low cost and high accuracy method for non-destructive three-dimensional characterisation of small scale features in the field.

The application of two novel analytical methods for surface characterisation provided a robust mechanism with which to generate and interpret surface weathering proxies based on features from the micro-SFM models. Global polynomial interpolation filtering proved more effective at isolating features present in samples with large, low frequency regional morphology identified for exclusion, rather than in regions with high frequency morphology approaching the size of target features. User-subjective classification of filters functioned to improve selection sensitivity, but compromises the integrity of results. Continuous wavelet transform analysis provided the most accurate surface feature characterisation, with sensitivity at sites of ideal morphology often an order of magnitude greater than the interpolation filtration method. The ability of the Mexican hat wavelet to select features based on three-dimensional geometry compatibility provided accurate determination of weathering artefacts without the need for subjective intervention.

The novel application of an interquartile ratio of surface feature amplitude frequencies combined with area ratio measurements provided metrics for detailed descriptions of surface roughness and analysis, indicative of the nature and magnitude of past weathering regimes. Additionally, the discovery of parallel

behavior between the independent roughness metrics of area ratio and interquartile ratio simultaneously increases the robustness of calculated results, but also presents the interquartile range as a compelling standalone proxy for surface roughness.

Compositional analysis with X-ray fluorescence and electron microprobe analysis provided mineralogical and elemental context for the spatial results. Determination of a general lack of chemical and structural alteration in materials provided robust support for the proposed weathering trends at the sampling sites. Compositional trends of mobile weathering elements direct focus towards calcite dissolution. With the presence of unaltered anorthite in-situ, this discovery provides further supporting evidence for the dominance of deep weathering in incipient weathering environments.

The greater understanding of initial weathering with respect to the generation of all weathering products, provides critical information towards adding robustness to forecasts on how the earth system will continue to evolve and respond to changes in the future.

8. References

Abramovich F., Benhamini Y. (1996)

Adaptive thresholding of wavelet coefficients. Computational Statistics & Data Analysis. Vol. 22, pp. 351-361.

Agisoft Inc.

Bounding Box to Coordinate System. Accessed on 12/4/2017. <http://wiki.agisoft.com/wiki/Bounding_Box_to_Coordinate_System.py>

Agisoft Inc.

Photoscan Memory Requirements. Accessed on 09/10/2017. <http://www.agisoft.com/pdf/tips_and_tricks/PhotoScan_Memory_Requirements.pdf#page=1&zoom=auto,-312,591>

Amusan, A. A. (2002)

Incipient weathering of granite-gneiss and soil development in Southwestern Nigeria. West African Journal of Applied Ecology. Vol. 3, pp. 55-68.

Anderson B., Mackintosh A., Stumm D., George L., Kerr T., Winter-Billington A., Fitzsimons S. (2010)

Climate sensitivity of a high-precipitation glacier in New Zealand. Journal of Glaciology. Vol. 56, no. 195, pp. 114-128.

Anderson, R. (2002)

Modeling the tor-dotted crests, bedrock edges, and parabolic profiles of high alpine surfaces of the Wind River Range, Wyoming. Geomorphology. Vol. 46, issue 1-2, pp. 35-58.

Anderson, Suzanne Prestrud, James I. Drever, Neil F. Humphrey (1997)

Chemical weathering in glacial environments. Geology. Vol. 25, No. 5. Pp. 399-402.

Anderson, S., J. Drever, C. Frost, P. Holden (2000)

Chemical weathering in the foreland of a retreating glacier. Geochimica et Cosmochimica Acta. Vol. 64, issue 7, pp.1173-1189.

Anderson, S. (2005)

Glaciers show direct linkage between erosion rate and chemical weathering fluxes. Geomorphology. Vol. 67, pp. 147-157.

Argoul, F., A. Arnéodo, G. Grasseau, Y. Gagne, E. J. Hopfinger & U. Frisch (1989)

Wavelet analysis of turbulence reveals the multifractal nature of the Richardson cascade. Nature, vol. 338, pp. 51–53.

Aronson, James L. (1965)

Reconnaissance rubidium—strontium geochronology of New Zealand plutonic and metamorphic rocks. New Zealand Journal of Geology and Geophysics. Vol. 8, issue 3, pp. 401-423.

Axtmann, Ellen V., Robert F. Stallard (1995)

Chemical weathering in the South Cascade Glacier basin, comparison of subglacial and extra-glacial weathering. Biogeochemistry of Seasonally Snow-Covered Catchments (Proceedings of a Boulder Symposium, July 1995). IAHS publication no. 228. Pp. 431-439.

Benjamin Bailleul, Nicolas Berne, Omer Murik, Dimitris Petroutsos, Judit Prihoda, Atsuko Tanaka, Valeria Villanova, Richard Bligny, Serena Flori, Denis Falconet, Anja Krieger-Liszkay, Stefano Santabarbara, Fabrice Rappaport, Pierre Joliot, Leila Tirichine, Paul G. Falkowski, Pierre Cardol, Chris Bowler & Giovanni Finazzi (2015)

Energetic coupling between plastids and mitochondria drives CO2 assimilation in diatoms. Nature. DOI: 10.1038/nature14599

Baoping Tang, Wenyi Liu, Tao Song (2010)

Wind turbine fault diagnosis based on Morlet wavelet transformation and Wigner-Ville distribution. Renewable Energy. Vol. 35, issue 12, pp. 2862-2866.

Barnard, V. E., P. Vielva, D. P. I. Pierce-Price, A. W. Blain, R. B. Barreiro, J. S. Richer, C. Qualtrough (2004)

The very bright SCUBA galaxy count: looking for SCUBA galaxies with the Mexican hat wavelet. Monthly Notices of the Royal Astronomical Society, Vol. 352, issue 3, pp. 961–974.

Bathurst, J.C. (2004)
Roughness. Encyclopedia of Geomorphology. Volume 1+2. Page 884.

Bartier, Patrick M., C. Peter Keller (1996)
Multivariate interpolation to incorporate thematic surface data using inverse distance weighting (IDW). Computers & Geosciences. Volume 22, issue 7, August 1996, pp. 795-799

Baumeister, J.L., Elisabeth M. Hausratha, Amanda A. Olsen, Oliver Tschaunera, Christopher T. Adcock, Rodney V. Metcalf (2015)
Biogeochemical weathering of serpentinites: An examination of incipient dissolution affecting serpentine soil formation. Applied Geochemistry. Vol. 54, pp. 74-84.

Berner E. K. and Berner R. A. (1996)
Global Environment: Water, Air and Geochemical Cycles. Prentice Hall.

Branley, S. L., Goldhaber, M. B., Ragnarsdottir, K. V. (2007)
Crossing disciplines and scales to understand the critical zone. Elements. Vol. 3, issue 5, pp. 307-314.

Braun J, Mercier J, Guillocheau F, Robin C. (2016)
A simple model for regolith formation by chemical weathering. Journal of Geophysical Research: Earth Surface:1–81. DOI:10.1002/2016JF003914.

Brzezinski M. A., Villareal T. A., Lipschultz F. (1998)
Silica production and the contribution of diatoms to new and primary production in the central North Pacific. Marine Ecology Progress Series. Vol. 167, pp. 89-104.

Burke MJ and Nasor M (2004)
Wavelet based analysis and characterization of the ECG signal. Journal of Medical Engineering & Technology. Vol. 28, issue 5, pp. 227.

Calmels, D., A. Galy, N. Hovius, M. J. Bickle, A. J. West, M.-C. Chen, H. J. Chapman (2010)
Deep chemical weathering in a rapidly eroding mountain belt, Taiwan. Earth and Planetary Science Letters. Vol. 303, pp. 48–58.

Carey, A. E., Christopher B. Gardner, Steven T. Goldsmith, W. Berry Lyons, D. Murray Hicks (2005)

Organic carbon yields from small, mountainous rivers, New Zealand. Geophysical Research Letters, an AGU journal. Vol. 32, issue 15. 10 August 2005.

Carvalho, D., A. Rocha, C. Santos,R. Pereira (2013)

Wind resource modelling in complex terrain using different mesoscale–microscale coupling techniques. Applied Energy, vol. 108, pp. 493-504.

Cermeño P., Paul G. Falkowski, Oscar E. Romero, Morgan F. Schaller, and Sergio M. Vallina (2015)

Continental erosion and the Cenozoic rise of marine diatoms. Proceedings of the National Academy of Sciences of the United States of America. Col. 112, issue 14, pp. 4239-4244.

Chaudhary, M., Anupma Dhamija (2013)

A brief study of various wavelet families and compression techniques. Journal of Global Research in Computer Science. Vol. 4, no. 4, pp. 43-49.

Chandler J. (1999)

Effective application of automated digital photogrammetry for geomorphological research. Earth Surface Processes and Landforms, vol. 24, pp.51-63.

Clarke, B. A., Douglas W. Burbank (2010)

Bedrock fracturing, threshold hillslopes, and limits to the magnitude of bedrock landslides. Earth and Planetary Science Letters. Vol 297, pp. 577-586.

Conley D. J. (2002)

Terrestrial ecosystems and the global biogeochemical silica cycle. Global Biogeochemical Cycles. Vol. 15, no. 4, 1121, doi:10.1029/2002GB001894.

Conley D. J. (2003)

Riverine contribution of biogenic silica to the oceanic silica budget. Limnology and Oceanography. Vol. 42, issue 4, pp.774-777.

Cox, S. C., D. Craw, and C. P. Chamberlain (1997)
Structure and fluid migration in a late Cenozoic duplex system forming the Main Divide in the central Southern Alps, New Zealand, N. Z. J. Geol. Geophys., 40, 359– 373.

Cox, S.C.; Barrell, D.J.A. (compilers) (2007)
Geology of the Aoraki Area. Institute of Geological & Nuclear Sciences 1:250 000 geological map 14. 1 sheet + 71 p. Lower Hutt, New Zealand. GNS Science. ISBN 0-478-09962-2

Cremeens DL, Brown RB, Huddleston JH. (1994)
Whole Regolith Pedology, SSSA Special Publication 34. SSSA; Madison, WI.

Cummins, W. A. (1962)
The Greywacke problem. Geological Journal. Vol. 3, issue 1, pp. 51-72.

CZO (2018)
Critical Zone Observatories, a U.S. NSF National Program. Criticalzone.org webpage, research tab. Accessed April, 2018. <http://criticalzone.org/national/research/the-critical-zone-1national/>

Daubechies, Ingrid. (1988)
Orthonormal Bases of Compactly Supported Wavelets. Communications of Pure and Applied Mathematics. Vol. 41, pp. 909-996.

Davis, P.T., Bierman, P., Marsella, K.A., Caffee, M.W. & Southon, J.R. (1999)
Cosmogenic analysis of glacial terrains in the eastern Canadian Arctic; a test for inherited nuclides and the effectiveness of glacial erosion. Annals of Glaciology. Vol. 28, pp. 181-188.

Day, Michael J. (1980)
Rock Hardness: Field Assessment and Geomorphic Importance. The Professional Geographer. Vol. 32, issue 1, pp. 72-81.

Dixon, J. C., Sean W. Campbell, Colin E. Thorn and Robert G. Darmody (2005)
Incipient weathering rind development on introduced machine-polished granite discs in an Arctic alpine environment, northern Scandinavia. Earth Surface Processes and Landforms. Vol. 31, pp. 111-121.

Dixon, J. L., Heimsath, A. M., Amundson, R. (2009)
The critical role of climate and saprolite weathering in landscape evolution. Earth Surface Processes and Landforms 34: 1507–1521

Dixon, J. L., Hartshorn, A. S., Heimsath, A. M., DiBiase, R. A. & Whipple, K. X. (2012)
Chemical weathering response to tectonic forcing: A soils perspective from the San Gabriel Mountains, California. Earth Planet. Sci. Lett. 323-324, 40–49

Dixon, J. L., and F. von Blanckenburg (2012)
Soils as pacemakers and limiters of global silicate weathering, C. R. Geosci., 344(11–12), 597–609. Doi:10.1016/j.crte.2012.10.012.

Drever, J.I. (1994)
The effect of land plants on weathering rates of silicate minerals. Geochimica et Cosmochimica Acta. Vol. 58, issue 10, pp. 2325-2332.

Dunai, Tibor J. (2010)
Cosmogenic Nuclides. Principles, Concepts and Applications in the earth sciences. Cambridge University Press. December 2010/ ISBN:9780511804519.

Durand, P., Colin Neal, Francois Lelong (1991)
Anthropogenic and natural contributions the rainfall chemistry of a mountainous area in the Cevennes National Park (Mont-Lozere, southern France). Journal of Hydrology. Vol 130, pp.71-85.

Elfouly, F. H., Mohamed I. Mahmoud, Moawad I. M. Dessouky, and Salah Deyab (2008)
Comparison between Haar and Daubechies Wavelet Transformations on FPGA Technology. World Academy of Science, Engineering and Technology International Journal of Electronics and Communication Engineering. Vol. 2, no. 1, pp. 96-101.

Fairchild, Ian J., Jacque A. Killawee, Martin J. Sharp, Baruch Spiro, Bryn Hubbard, Regi D. Lorrain, Jean-Louis Tison (1999).
Solute generation and transfer from a chemically reactive alpine glacial-proglacial system. Earth Surface Processes and Landforms. Vol. 24, pp. 1189-1211.S

Falkowski, Michael J., Alistair M.S. Smith, Andrew T. Hudak, Paul E. Gessler, Lee A. Vierling (2006)

Automated estimation of individual conifer tree height and crown diameter via two-dimensional spatial wavelet analysis of lidar data. Canadian Journal of Remote Sensing. Vol. 32, no. 2, pp. 153-161.

Ferrier, K. L. & Kirchner, J. W. (2008)

Effects of physical erosion on chemical denudation rates: A numerical modeling study of soil-mantled hillslopes. Earth Planet Sci. Lett. 272, 591–599

Fitzsimons, S.J. and H. Veit (2001)

Geology and Geomorphology of the European Alps and the Southern Alps of New Zealand; A Comparison. Mountain Research and Development Vol 21 No 4 Nov 2001: 340–349.

Furukawa, Y., Ponce, J. (2010)

Accurate, dense, and robust multiview stereopsis. IEEE Transactions on Pattern Analysis and Machine Intelligence, vol. 32, pp. 1362–1376.

Gabet, Emmanuel J., and Simon M. Mudd (2010)

Bedrock erosion by root fracture and tree throw: A coupled biogeomorphic model to explore the humped soil production function and the persistence of hillslope soils. Journal of Geophysical Research. Vol. 115, F04005, doi:10.1029/2009JF001526.

Gadre, V., V.P. Dimitri, E. Chandraskehar (2008)

Wavelets and Fractals in Earth System Sciences. Pp. 286. ISBN 1-4665-5360-X

Gaillardet, J.; Dupré, B.; Louvat, P.; Allègre, C.J. (1999)

Global silicate weathering and CO2 consumption rates deduced from the chemistry of large rivers. Chemical Geology. Vol. 159, issue 1-4, pp. 3-30.

Graham T. (1864)

XXXV.- On the properties of silicic acid and other analogous colloidal substances. Journal of the Chemical Society. Issue 0, 1864.

Grohmann, C. H. and Riccomini, C. (2009)
Comparison of roving-window and search-window techniques for characterising landscape morphometry. Computers & Geosciences, vol. 35, pp. 2164-2169.

Grohmann, Smith, M.J., C.H., Riccomini, C., (2011)
Multi-scale Analysis of Topo-graphic Surface Roughness in the Midland Valley, Scotland.
IEEE Transactions on Geoscience and Remote Sensing. 49:1200-1213. DOI:10.1109/TGRS.2010.2053546

Gupta S. (2014)
Wavelet Based Techniques for Speckle Noise Reduction in Ultrasound Images. Nishtha Attlaset al Int. Journal of Engineering Research and Applications. Vol. 4, Issue 2, pp.508-513. (14) Wavelet Based Techniques for Speckle Noise Reduction in Ultrasound Images. Available from: https://www.researchgate.net/publication/276061449_Wavelet_Based_Techniques_for_Speckle_Noise_Reduction_in_Ultrasound_Images [accessed May 04 2018].

Hahm, W. J., Clifford S. Riebe, Claire E. Lukens and Sayaka Araki (2014)
Bedrock composition regulates mountain ecosystems and landscape evolution. Proceedings of the National Academy of Sciences of the United States of America. Proc Natl Acad Sci U S A. 2014 Mar 4; 111(9): 3338–3343.

Heller, P. N. (1995)
Rank M Wavelets with N Vanishing Moments. Society for Industrial and Applied Mathematics Journal on Matrix Analysis and Applications. Vol. 16, issue 2, pp. 502-519.

Herman, Frédéric., Brian Anderson, Sébastien Leprince (2011)
Mountain glacier velocity variation during a retreat/advance cycle quantified using sub-pixel analysis of ASTER images. Journal of Glaciology, Vol. 57, No. 202, pp. 197-207.

Herman, Frédéric., Champagnac, Jean-Daniel (2016)
Plio-Pleistocene increase of erosion rates in mountain belts in response to climate change. Terra Nova. Vol. 28, pp.2-10.

Herzfeld, U. C., Mayer, H., Feller, W., and Mimler, M. (2000)
Geostatistical analysis of glacier-roughness data. Annals of Glaciology, vol. 30, pp. 235-242.

Hilley, G. E., Chamberlain, C. P., Moon, S., Porder, S. & Willett, S. D. (2010)
Competition between erosion and reaction kinetics in controlling silicate-weathering rates. Earth Planet. Sci. Lett. 293, 191–199

Hobson, R. D. (1967)
FORTRAN IV programs to determine the surface roughness in topography for the CDC 3400 computer. Computer Contribution State Geol. Survey Kansas, vol. 14, pp. 1-28.

Ibbitt, R. P., R. D. Henderson, J. Copeland, D. S. Wratt. (2000)
Simulating mountain runoff with meso-scale weather model rainfall estimates: A New Zealand experience. Journal of Hydrology. Vol. 239, issues 1-4, pp. 19-32.

Imaging-Resource (2018)
Pentax 35mm f/2.8 Macro Limited HD DA. <https://www.imaging-resource.com/lenses/pentax/35mm-f2.8-macro-limited-hd-da/review/> Accessed on 02/02/18.

Jacobson, A. D., J. Blum, P. Chamberlain, D. Craw, P. Koons (2003)
Climatic and tectonic controls on chemical weathering in the New Zealand Southern Alps. Geochimica et Cosmochimica Acta. Vol. 67, issue 1, pp. 29-46.

John C. Gosse, Fred M. Phillips (2001)
Terrestrial in situ cosmogenic nuclides: theory and application. Quaternary Science Reviews, vol. 20, pp. 1475-1560.

Josso, Bruno, Burton, David R, Lalor, Michael J (2002)
Frequency normalised wavelet transform for surface roughness analysis and characterisation. Wear. Vol. 252, pp. 491-500.

J.D. Milliman, R.H. Meade (1983)
World-wide delivery of river sediments to the oceans. J. Geology, pp. 1- 21

Gaillardeta J., B.Dupréb, P.Louvata, C.J.Allègrea, (1999)
Global silicate weathering and CO_2 consumption rates deduced from the chemistry of large rivers. The Journal of Chemical Geology. Vol. 159, Iss. 1-4, pp.3-30.

Griffiths, G.A., McSaveney, M.J. (1983)
Distribution of mean annual precipitation across some steepland regions of New Zealand. NZ Journal of Science 26, 197–209.

Harrison K. G. (2000)
Role of increased marine silica input on paleo-pCO_2 levels. Paleoceanography. Vol. 15, issue 3, pp. 292-298.

Heimsath, A. M., Roman A. DiBiase, Kelin X. Whipple (2012)
Soil production limits and the transition to bedrock-dominated landscapes. Nature Geoscience. DOI: 10.1038/NGEO1380

Heyman, J., Arjen P. Stroeven, Jonathan M. Harbor, Marc W. Caffee (2011)
Too young or too old: Evaluating cosmogenic exposure dating based on an analysis of compiled boulder exposure ages. Earth and Planetary Science Letters. Vol. 302, issues 1-2, pp.71-80.

Hicks M., McSaveney M. J., Chinn T. J. H. (1990)
Sedimentation in Proglacial Ivory Lake, Southern Alps, New Zealand. Arctic and Alpine Research., Vol. 22, No. 1 (Feb., 1990), pp. 26-42.

Hopkinson C., Chasmer L. E., Sass G., Creed I. F., Sitar M. Kalbfleisch W., Treitz P. (2014)
Vegetation class dependent errors in lidar ground elevation and canopy height estimates in a boreal wetland environment. Canadian Journal of Remote Sensing. Vol. 31, issue 2, pp. 191-206.

Hyslip, J., Vallejo, L. (1997)
Fractal analysis of the roughness and size distribution of granular materials. Engineering Geology, vol: 48 (3-4), pp: 231-244.

Hyyppä J., Inkinen M.(2009)
Detecting and estimating attributes for single trees using laser scanner. The Photogrammetric Journal of Finland, vol. 16, pp. 27-42.

Krizbergs, J., A. Kromanis (2006)

Methods for prediction of the surface roughness 3D parameters according to technological parameters. 5th International DAAAM Baltic Conference. Industrial Engineering-Adding Innovation Capacity of Labour Force and Entrepreneurs. April 2006, Tallinn, Estonia.

Kelly, P.J., S.P. Anderson, A. Blum (2012)

Rock strength reductions during incipient weathering. American Geophysical Union, Fall Meeting 2012, abstract id. EP43B-0868.

Koutsoudis A., Blaž Vidmar, George Ioannakis, Fotis Arnaoutoglou, George Pavlidis, Christodoulos Chamzas (2014)

Multi-image 3D reconstruction data evaluation. Journal of Cultural Heritage. Vol. 15, issue 1, pp. 73-79.

Andrew C. Kurtz, Louis A. Derry, Oliver A. Chadwick (2002)

Germanium-silicon fractionation in the weathering environment. Geochimica et Cosmochimica Acta. Vol. 66, issue 9, pp. 1525-1537. ISSN 0016-7037. https://doi.org/10.1016/S0016-7037(01)00869-9.

Lal, D. (1991)

Cosmic ray labeling of erosion surfaces: in situ nuclide production rates and erosion models. Earth and Planetary Science Letters. Vol. 104, pp. 424-439.

Larsen I. J., Almond P.C., Eger A., Stone J. O., Montgomery D. R., Malcom B. (2014)

Rapid soil production and weathering in the Southern Alps, New Zealand. Science. Vol. 343, pp.637-640.

Lanphere, M. A. and Wasserburg, G. J. F. and Albee, A. L. and Tilton, G. R. (1964)

Redistribution of Strontium and Rubidium Isotopes during Metamorphism, World Beater Complex, Panamint Range, California. In: Isotopic and Cosmic Chemistry. North Holland , Amsterdam, pp. 269-320.

Lewin, J. C. (1962)

Physiology and Biochemistry of Algae. Silicification, 00.445-455. Ed. Academic Press, New York, NY.

Little, T. A., R. J. Holcombe, and B. R. Ilg (2002)
Kinematics of oblique collision and ramping inferred from microstructures and strain in middle crustal rocks, central Southern Alps, New Zealand, J. Struct. Geol., 24, 219– 239.

Lubis, M.Z., Pujiyati S., Hestirianoto T. and Wulandari P.D. (2016)
Haar Wavelet Method to Spectral Analysis Continuous Wavelet Transform 1D Using Whistle Sound to Position of Dolphins (Tursiops aduncus). Journal of Applied & Computational Mathematics, vol. 5, issue 2, pp. 1-8.

Luttge A. and Arvidson R. S. (2007)
The mineral-water interface. In Kinetics of Geochemical Systems (ed. S. L. Brantley. S. L., J. Kubicki, and A. F. White).

Maher, K. (2010)
The dependence of chemical weathering rates on fluid residence time. Earth and Planetary Science Letters. Vol. 294, pp.101-110.

Mathworks. 2-D continuous wavelet transform. Accessed in January, 2018.
<https://au.mathworks.com/help/wavelet/ref/cwtft2.html>

Mathworks. Wavelet Toolbox Overview. Accessed in March, 2018.
<https://au.mathworks.com/videos/wavelet-toolbox-overview-115893.html>

Mavris, C., Markus Egli, Michael Plötze, Joel D. Blum, Aldo Mirabella, Daniele Giaccai, Wilfried Haeberli (2010)
Initial stages of weathering and soil formation in the Morteratsch proglacial area (Upper Engadine, Switzerland). Geoderma. Vol. 155, pp. 359-371.

McCarroll, Danny (1991)
The schmidt hammer, weathering and rock surface roughness. Short Communication. Vol. 16, issue 5, pp. 477-480.

Mendiguchía C., Moreno C., García-Vargas M. (2007)
Evaluation of natural and anthropogenic influences on the Guadalquivir River (Spain) by dissolved heavy metals and nutrients. Chemosphere. Vol. 69, issue 10, pp. 1509-1517.

Miles, Evan S., Jakob F. Steiner, Fanny Brun (2017)
Highly variable aerodynamic roughness length (z_0) for a hummocky debris-covered glacier. Journal of Geophysical Research: Atmospheres. 2017 American Geophysical Union. Pp. 8447-8466. 10.1002/2017JD026510.

Molnar, P., Robert S. Anderson, Suzanne Prestrud Anderson (2007)
Tectonics, fracturing of rock, and erosion. Journal of geophysical research. Vol. 112, F03014, doi:10.1029/2005JF000433.

Moses C., Robinson D., Barlow J. (2014)
Methods for measuring rock surface weathering and erosion: A critical review. Earth-Science Reviews. Vol. 135, pp. 141-161.

N. J. Cullen, B. Anderson, P. Sirguey., D. Stumm, A. Mackintosh, J.P. Conway, H.J. Horgan, R. Dadic, S.J. Fitzsimons, and A. Lorrey. (2017)
An 11-year record of mass balance of Brewster Glacier, New Zealand, determined using a geostatistical approach. Journal of Glaciology. Vol. 63, Iss. 238, pp. 199–217. https://doi.org/10.1017/jog.2016.128

Nicholson, Dawn T. (2009)
Holocene microweathering rates and processes on ice-eroded bedrock, Roldal area, Hardangervidda, southern Norway. Geological Society London Special Publications. Vol. 320, issue 1, pp. 29-49.

Nikolov I., Madsen C. (2016)
Benchmarking Close-range Structure from Motion 3D Reconstruction Software Under Varying Capturing Conditions. EuroMed 2016, part 1, LNCS 100058, pp. 15-26.

Norton, K.P., von Blanckenburg, F. (2010)
Silicate weathering of soil-mantled slopes in an active Alpine landscape. Geochimica et Cosmochemica Acta. Vol. 74, pp. 5243–5258.

Norton, K.P., Molnar, P., Schlunegger, F. (2014)
The role of climate-driven chemical weathering on soil production. Geomorphology. Vol. 204,pp. 510–517.

Norton, K. P., Schlunegger, F. (2017)
Lack of a weathering signal with increased Cenozoic erosion? Terra Nova. Vol. 29, pp. 265-272.

Oleschko K., Parrot J., Ronquillo G., Shoba S., Stoops G., Marcelino V. (2004)
Weathering: Toward a Fractal Quantifying. Mathematical Geology. Col. 36, issue 5, pp. 607-627.

Okrusch, M., Siegfried Matthes (2005)
Mineralogie - Eine Einführung in die spezielle Mineralogie, Petrologie und Lagerstättenkunde. Springer-Verlag, Berlin Heidelberg New York Tokyo. ISBN 3-540-23812-3

Ortega, Rengifo. (2012)
Modelling potential debris flows from SRTM data in the upper Chama river watershed, northwestern Venezuela. Revista Geografica Venezolana, vol. 53, pp. 93-108.

Pastia, L., B. Walczak, D. Massart, P. Reschiglian (1999)
Optimization of signal denoising in discrete wavelet transform. Chemometrics and Intelligent Laboratory Systems. Vol. 48, issue 1, pp. 21-34

Pavich M. J. (1986)
Processes and rates of saprolite production and erosion on a foliated granitic rock of the Virginia Piedmont. In Rates of Chemical Weathering of Rocks and Minerals (ed. S. M. Dethier and D. P. Coleman), pp. 551-590. Academic Press.

Penna A., Magnani M., Fenoglio I, Fubini B., Cerrano C., Giovine M., Bavestrello G. (2003)
Marine diatom growth on different forms of particulate silica: Evidence of cell/particle interaction. Aquatic Microbial Ecology. Vol. 32, issue 3, pp.299-306.

Petrovich, Radomir (1981)

Kinetics of dissolution of mechanically comminuted rock-forming oxides and silicates—II. Deformation and dissolution of oxides and silicates in the laboratory and at the Earth's surface. Geochimica et Cosmogeochimica Acta. Vol. 45, issue 10, pp.1675-1686.

Price JR, Rice KC, Szymanski DW. (2013)

Mass-balance modeling of mineral weathering rates and CO2 consumption in the forested, metabasaltic Hauver Branch watershed, Catoctin Mountain, Maryland, USA. Earth Surface Processes and Landforms. Vol. 38, pp. 859–875.

Purdie, H., Brian Anderson, Trevor Chinn, Ian Owens, Andrew Mackintosh, Wendy Lawson (2014)

Franz Josef and Fox Glaciers, New Zealand: Historic length records. Global and Planetary Change vol. 121, pp. 41–52.

Racoviteanu A. E., Manley W. F., Arnaud Y., Williams M. W. (2007)

Evaluating digital elevation models for glaciologic applications: An example from Nevado Coropuna, Peruvian Andes. Global and Planetary Change. Vol. 59, issues 1-4, pp. 110-125.

Raich, J. W., Schlesinger, W. H. (1992)

The global carbon dioxide flux in soil respiration and its relationship to vegetation and climate. Tellus. Vol. 44, issue 2, pp.81-99.

Raymo, M. E., Ruddiman, W. F. & Froelich, P. N. (1988)

Influence on late Cenozoic mountain building on ocean geochemical cycles. Geology. Vol. 16, pp. 649-653.

Raja, J., B. Muralikrishnan, Shengyu Fu (2002)

Recent advances in separation of roughness, waviness and form. Precision Engineering, Volume 26, Issue 2,Pages 222-235. ISSN 0141-6359.

Rattenbury, M.S.; Jongens, R.; Cox, S.C. (compilers) (2010)

Geology of the Haast area. Institute of Geological & Nuclear Sciences 1:250 000 geological map 14. 1 sheet + 58 p. Lower Hutt, New Zealand. GNS Science. ISBN 978-0-478-19745-7

Riebe C. S., Kirchner J. W. and Finkel R. (2003)
Long-term rates of chemical weathering and physical erosion from cosmogenic nuclides and geochemical mass balance. Geochim. Cosmochim. Acta. Vol. 67,pp. 4411–4427.

Riebe C. S., Kirchner J. W., Granger D. E. and Finkel R. (2001)
Minimal climatic control on erosion rates in the Sierra Nevada, California. Geology. Vol. 29,pp. 447–450.

Riebe, Clifford S., W. Jesse Hahm, and Susan L. Brantley (2016)
Controls on deep critical zone architecture: a historical review and four testable hypotheses. Earth Surface Processes and Landforms. Vol. 42, pp. 128-156.

Rioul, O., P. Duhamel (1992)
Fast Algorithms for Discrete and Continuous Wavelet Transforms. IEEE Transactions on Information Theory. Vol. 38, no. 2, pp. 569-586.

Rosso, B., D.R. Burton, M.J. Lalor (2001)
Wavelet strategy for surface roughness analysis and characterisation. Computer Methods in Applied Mechanics and Engineering. Vol. 191, pp.829-842.

Roy, S., J. Gaillardeta, C.J. Allègrea (1999)
Geochemistry of dissolved and suspended loads of the Seine River, France: anthropogenic impact, carbonate and silicate weathering. Geochimica et Cosmochimica Acta. Vol. 63, Issue 9, pp. 1277-1292.

Salinger, M. J. (1980)
New Zealand Climate: I. Precipitation Patterns. Monthly Weather Review. Vol. 108, issue 11, pp. 1892-1904.

Schwikowski, Margit (2004)
Reconstruction of European Air Pollution from Alpine Ice Cores. Earth Paleoenvironments: Records Preserved in Mid- and Low-Latitude Glaciers. Pages 95-119. ISBN 978-1-4020-2146-6.

Siever, R. (1991)
Silica in the oceans: Biological-geochemical interplay. Scientists on Gaia, pp. 287 – 295, MIT Press, Cambridge, Mass.

Sidhik S. (2015)
Comparative study of Birge–Massart strategy and unimodal thresholding for image compression using wavelet transform. Optik. Vol. 126, pp. 5952-5955.

Siu-Ngan Lam, N., Dale A. Quattrochi (1992)
On the Issues of Scale, Resolution, and Fractal Analysis in the Mapping Sciences. Professional Geographer. Vol. 44, issue 1, pp. 88-98.

Smith B., Warke P., McGreevy J., Kane H (2005)
Salt-weathering simulations under hot desert conditions: agents of enlightenment or perpetuators of preconceptions? Geomorphology. Vol. 62 (1-2), pp. 211-227.

Stephenson and Kirk (1996)
Measuring erosion rates using the micro-erosion meter: 20 years of data from shore platforms, Kaikoura Peninsula, South Island, New Zealand. Marine Geology. Vol. 131, issues 3-4, pp. 209-218.

Stone, R. O. and Dugundji, J. (1965)
A study of microrelief - its mapping, classification and quantification by means of a Fourier analysis. Engineering Geology, vol.1, pp. 89-187.

Stonestrom D. A., White A. F., and Akstin K. C. (1998)
Determining rates of chemical weathering in soils-solute transport versus profile evolution. J. Hydrology 209, 331-345.

Tingbo Hou, Hong Qin (2012)
Continuous and discrete Mexican hat wavelet transforms on manifolds. Graphical Models. Vol. 74, issue 4, pp. 221-232.

Thompson, EH. (1965)
Review of methods independent model aerial triangulation. The Photogrammetric
Record, vol. 5, pp. 72–79.

Tomás, R., Z. Li, J. M. Lopez-Sanchez, P. Liu, A. Singleton (2016)
Using wavelet tools to analyse seasonal variations from InSAR time-series data: a case study of the Huangtupo landslide. Landslides, vol. 13, issue 3, pp. 437–450.

Torres, M. A., Nils Moosdorf, Jens Hartmann, Jess F. Adkins, A. Joshua West (2017)
Glacial weathering, sulfide oxidation, and global carbon cycle feedbacks. Proceedings of the National Academy of Sciences of the United States of America. Vol. 114, issue 33, pp. 8716-8721.

Tréguer PJ, De La Rocha CL (2012)
The world ocean silica cycle. Annual Review of Marine Science. Vol. 5, pp. 477-501.

Turcotte D.L., Huang J. (1995)
Fractal Distributions in Geology, Scale Invariance, and Deterministic Chaos. In: Barton C.C., La Pointe P.R. (eds) Fractals in the Earth Sciences. Springer, Boston, MA

Vargo, L., B. Anderson, H. Horgan (2017)
Using structure from motion photogrammetry to measure past glacier changes from historic aerial photographs. Journal of Glaciology. Vol.63, Iss.242, pp. 1105-1118.

Victoria University of Wellington SGEES
Electron probe microanalysis facility webpage. Accessed April, 2018. <https://www.victoria.ac.nz/sgees/research/facilities/microanalysis-facility>

Vastaranta M., T. Melkas, M. Holopainen, H. Kaartinen, J. Hyyppä, H. Hyyppä (2009)
Laser-based field measurements in tree-level forest data acquisition. The Photogrammetric journal of Finland, vol. 112009, pp. 51-61.

Walker, J.C.G., Hays, P.B., Kasting, J.F. (1981)

A negative feedback mechanism for the long- term stabilization of Earth's surface temperature. J. Geophys. Res.- Oceans Atmos. Vol. 86, pp. 9776–9782

Wavelet.org

The scaling and shifting process of the DWT. Accessed on 15/02/2018. <http://www.wavelet.org/tutorial/wbasic.htm>

Ward, Peter D. and Brownlee, Donald (2000)

Rare Earth. Springer, New York, NY. ISBN: 978-0-387-21848-9. DOI: https://doi.org/10.1007/b97646

Washtell, J., Carver, S., and Arrell, K. (2009)

A Viewshed Based Classification of Landscapes Using Geomorphometrics. In Purves, R., Gruber, S., Straumann, R., and Hengl, T., editors, Geomorphometry 2009 Conference Proceedings, pages 44-49. University of Zurich, Zurich.

Weatherill, N. P. and Hassan, O. (1994)

Efficient three-dimensional Delaunay triangulation with automatic point creation and imposed boundary constraints. Int. J. Numer. Meth. Engng., vol. 37, pp. 2005–2039. doi:10.1002/nme.1620371203

Webster T. L., Dias G. (2006)

An automated GIS procedure for comparing GPS and proximal LIDAR elevations. Computers & Geosciences. Vol. 32, issue 6, pp. 713-726.

Westoby M. J., J. Brasington, N. F. Glasser, M. J. Hambrey, J. M. Reynolds, (2012)

'Structure-from-Motion' photogrammetry: A low-cost, effective tool for geoscience applications. Geomorphology, vol. 179, 15 December 2012, pp. 300-314.

White A. and Blum A. (1995)

Effects of climate on chemical weathering in watersheds. Geochimica et Cosmochimica Acta. Vol. 59, issue 9, pp. 1729-1747.

White A. F., Blum A. E., Schulz M. S., Vivit D. V., Larsen M., and Murphy S. F. (1998)

Chemical weathering in a tropical watershed, Luquillo Mountains, Puerto Rico: I. Long-term versus short-term chemical fluxes. Geochim Cosmochim Acta 62, 209- 226.

White A., Bullen T. D., Vivit D. V., Schulz M. S., Clow D. W. (1999)

The role of disseminated calcite in the chemical weathering of granitoid rocks. Geochimica et Cosmochimica Acta. Vol. 63, issues 13–14, pp. 1939-1953. ISSN 0016-7037.

White A. F. and Brantley S. L. (2003)

The effect of time on the weathering of silicate minerals: Why to weathering rates differ in the laboratory and field? Chemical Geology. Vol. 190, pp. 69-89.

White, A. (2008)

Quantitative approaches to characterizing natural chemical weathering rates. Kinetics of Water-Rock Interaction. Pp. 469-543.

White, Kevin; Bryant, Rob; Drake, Nick (1998)

Techniques for measuring rock weathering: Application to a dated fan segment sequence in Southern Tunisia. Earth Surfaces Processes and Landforms. Vol. 23, pp. 1031-1043.

Wieler R., Graf T. (2001)

Cosmic Ray Exposure History of Meteorites. In: Peucker-Ehrenbrink B., Schmitz B. (eds) Accretion of Extraterrestrial Matter Throughout Earth's History. Springer, Boston, MA. ISBN: 978-1-4613-4668-5.

Willenbring, J. K., Jerolmack, D. J. (2016)

The null hypothesis: globally steady rates of erosion, weathering fluxes and shelf sediment accumulation during late cenozoic mountain uplift and glaciation. Terra Nova. Vol. 28, issue 1, pp. 11-18.

Willsman A., Chinn T., and Macara G. (2015)

New Zealand glacier monitoring: end of summer snowline survey 2015. National Institute of Water & Atmospheric Research Ltd, Auckland.

Wilson, M. F. J., O'Connell, B., Brown, C., Guinan, J. C., and Grehan, A. J. (2007)

Multiscale Terrain Analysis of Multibeam Bathymetry Data for Habitat Mapping on the Continental Slope. Marine Geology, vol. 30, pp. 3-35.

Wright J., Smith B., Whalley B. (1998)

Mechanisms of loess-sized quartz silt production and their relative effectiveness: laboratory simulations. Geomorphology. Vol. 23, issue 1, pp. 15-34.

Young, Randy K. (1993)

Wavelet Theory and Its Applications. Kluwer international series in engineering and computer science. SECS, Vol. 189. ISBN 0-7923-9271-X

Zanner CW, Graham RC. (2005)

Deep regolith: exploring the lower reaches of soil. Geoderma 126: 1–3.

Zhaouani H., S-H. Lee, R. Vargiolu, T.G. Mathia. (1999)

The multiscale mathematical microscopy of surface roughness. Incidence in Tribology. Lubrication at the Frontier: The Role of the Interface and Surface Layers in the Thin Film and Boundary Regime. Volume 36, 1st Edition, pp. 379-390. eBook ISBN: 9780080535661.

Zweck, C., Marek Zreda, Darin Desilets (2013)

Snow shielding factors for cosmogenic nuclide dating inferred from Monte Carlo neutron transport simulations. Earth and Planetary Science Letters, vol. 379,pp. 64–71.

9. Appendices

9.1. Photoscan Python Script for Model Orientation

```
#rotates model coordinate system in accordance of bounding box for active chunk
#scale is kept
#compatibility: Agisoft PhotoScan Professional 1.1.0

import PhotoScan
import math

doc = PhotoScan.app.document
chunk = doc.chunk

R = chunk.region.rot            #Bounding box rotation matrix
C = chunk.region.center         #Bounding box center vector

if chunk.transform.matrix:
        T = chunk.transform.matrix
        s = math.sqrt(T[0,0] ** 2 + T[0,1] ** 2 + T[0,2] ** 2)          #scaling
        S = PhotoScan.Matrix().diag([s, s, s, 1]) #scale matrix
else:
        S = PhotoScan.Matrix().diag([1, 1, 1, 1])

T = PhotoScan.Matrix( [[R[0,0], R[0,1], R[0,2], C[0]], [R[1,0], R[1,1], R[1,2], C[1]],
[R[2,0], R[2,1], R[2,2], C[2]], [0, 0, 0, 1]])

chunk.transform.matrix = S * T.inv()            #resulting chunk transformation matrix
```

9.2. MATLAB Scripts

9.2.1. Wavelet Transform Analysis

```
%%%%%%%%%%%%%%%%%%%%%%%%%%%%%%%%%%%%%%%%%%%%%%%%%%%%%%%%%%%%%%%%%%%%%%%%
% dem_analysis2
%
% a script to perform wavelet analysis on a micro-scale DEM
% a continuous wavelet decompostion is performed to ...
% a discrete wavelet decompositions at a series of levels is
% undertaken to identify erosion features
%%%%%%%%%%%%%%%%%%%%%%%%%%%%%%%%%%%%%%%%%%%%%%%%%%%%%%%%%%%%%%%%%%%%%%%%

% choose which analysis to do by commenting out one of these
%analysis='continuous';
analysis='discrete';

% DEM file format - 'tif' = GeoTIFF
format='tif';

% directory where the DEMs are
dir_name='\F:\ALL_THE_DATA\Brewster\DEM\Final_hi_res_DEMs\'

% a list of DEMs to process
im_name={'sqclip_B_04_Hi_Res'};
% each one has a row to plot cross profiles on
profile_row=[200];

% step through each DEM to do analysis
 for ii=1:length(im_name)
    % read DEM
    im_file=[dir_name,im_name{ii},'.',format];
    dem=imread(im_file);

    % deal with no-data values (come as -32768 from photoscan)
    dem(dem<-1000)=NaN;
    % wavelet analysis does not like NaN
    dem(isnan(dem))=0;

    switch analysis

        case 'discrete'

            % use stationary wavelet transform so that the DEM is
not decimated
            % https://au.mathworks.com/help/wavelet/gs/analysis-
with-the-discrete-wavelets.html


            wavelet_name='db20';
```

```
            % find number of levels of transform we can do
            [lb ub]=wavsupport(wavelet_name);
            disp(['wavelet support ',num2str(lb),' ->
',num2str(ub)])

            maxlev=wmaxlev(size(dem),wavelet_name)
            disp(['wavelet max level ',num2str(maxlev)])

            % pick your scaling parameter
            % setting to maxlev does maximum number of levels
            level=maxlev;

            % make a DEM the correct size
            % 2^Level has to divide the size of the DEM
            nrows=ceil(size(dem,1)/2^level)*2^level;
            ncols=ceil(size(dem,2)/2^level)*2^level;

            % splice the DEM into an array of zeros the correct
size
            dem0=zeros(nrows,ncols);
            dem0(1:size(dem,1),1:size(dem,2))=dem;

            cod_dem0 = dem0;
            % do the wavelet transform
            [ca,chd,cvd,cdd] = swt2(dem0,level,wavelet_name);

            % plot data
            % first a profile across the DEM
            ph=[];
            figure(1)
            clf
            hold on
            ph(1)=plot(1:size(dem0,2),cod_dem0(profile_row,:));
            leg_txt{1}='dem';
            for jj=1:level
                % extract data for each level
                cod_dem = ca(:,:,jj)/2^jj;

                % and plot it

ph(jj+1)=plot([1:size(dem0,2)],cod_dem(profile_row,:));
                leg_txt{jj+1}=['level ',num2str(jj)];
            end

            legend(ph,leg_txt)

            figure(2)
            clf
            % plot difference which could be used for roughness
analysis
            hi_freq=dem0-cod_dem0;
            % plot without edges
            imagesc(hi_freq(10:end-10,10:end-10));

        case 'continuous'
```

```
            % set up wavelet
            wav.name='mexh';
            wav.param={[2]  [1]  [1]};

            % do wavelet transform
            cwtmexh = cwtft2(dem,'wavelet',wav,'scales',[1 2 4 8
16 32 64 128]);

            % plot data
            % a series of lines at each decomposition level
            % plotted across the profile line
            figure(1)
            clf
            hold on
            ph=[];
            ph(1)=plot(1:size(dem,2),dem(profile_row,:));

ph(2)=plot(1:size(dem,2),(real(cwtmexh.cfs(profile_row,:,1,1))));

ph(3)=plot(1:size(dem,2),(real(cwtmexh.cfs(profile_row,:,1,2))));

ph(4)=plot(1:size(dem,2),(real(cwtmexh.cfs(profile_row,:,1,3))));

ph(5)=plot(1:size(dem,2),(real(cwtmexh.cfs(profile_row,:,1,4))));

ph(6)=plot(1:size(dem,2),(real(cwtmexh.cfs(profile_row,:,1,5))));

legend(ph,'DEM','wavelet1','wavelet2','wavelet3','wavelet4','wave
let5')

            % plot 4 panes with difference levels of
decomposition
            figure(2)
            clf
            subplot(2,2,1)
            % plot without edges
            imagesc(real(cwtmexh.cfs(100:end-100,100:end-
100,1,3)));
            caxis([-0.0001 0.0001])
            subplot(2,2,2)
            imagesc(real(cwtmexh.cfs(100:end-100,100:end-
100,1,4)));
            caxis([-0.001 0.001])
            subplot(2,2,3)
            imagesc(real(cwtmexh.cfs(100:end-100,100:end-
100,1,5)));
            caxis([-0.01 0.01])
            subplot(2,2,4)
            imagesc(real(cwtmexh.cfs(100:end-100,100:end-
100,1,6)));
            caxis([-0.01 0.01])

            % plot thresholded values - note different thresholds
for different scales
```

```
            figure(3)
            clf
            subplot(2,2,1)
            imagesc(real(cwtmexh.cfs(100:end-100,100:end-
100,1,3))>1e-4);
            caxis([-0.0001 0.0001])
            subplot(2,2,2)
            imagesc(real(cwtmexh.cfs(100:end-100,100:end-
100,1,4))>1e-3);
            caxis([-0.001 0.001])
            subplot(2,2,3)
            imagesc(real(cwtmexh.cfs(:,:,1,5))>1e-2);
            caxis([-0.01 0.01])
            subplot(2,2,4)
            imagesc(real(cwtmexh.cfs(100:end-100,100:end-
100,1,6))>1e-1);
            caxis([-0.01 0.01])
            %print('-dpng','-r300',[im_name{ii},'_thresh.png'])

            % store the results in a variable which will be read
in pitstats2.m
            in_pitstat_a=real(cwtmexh.cfs(:,:,1,5))>1e-2;

    end
 end
```

9.2.2. Identified Feature Analysis

```
`%%%%%%%%%%%%%%%%%%%%%%%%%%%%%%%%%%%%%%%%%%%%%%%%%%%%%%%%%%%%%%%%%%%%%%%
% pitstats2
%
% a script take a 2D continuous wavelet transform
% and calculate statistics on erosion pits.
% this script expects the output of the transform to be in
% the variable 'in_pitstat_a', from dem_analysis2
%%%%%%%%%%%%%%%%%%%%%%%%%%%%%%%%%%%%%%%%%%%%%%%%%%%%%%%%%%%%%%%%%%%%%%%

marg=5; % margin around pit taken for interpolation

% in_pitstat_a comes from dem_analysis2
% and is the thresholded, 5th level CWT of the DEM
A = in_pitstat_a ;

originalDEM = dem; % From dem_analysis2

rowvec = (1:size(originalDEM,1))';
colvec = (1:size(originalDEM,2))';
rows=(1:size(originalDEM,1))'*ones(1,size(originalDEM,2));
cols=ones(size(originalDEM,1),1)*(1:size(originalDEM,2));

bwimg=abs(A-1); % Logical image (use for masking and perimeters)

% DEMedit is the original DEM, with erosion features removed
DEMedit=double(originalDEM.*bwimg);
DEMedit(DEMedit==0)=nan;

% Now let's find the perimeters in the binary image
%  If needed this can be run in cell mode
pflag = 0 % plotflag

maxDepth = []; % maximum depth of each pit
pitVol = [];
pitArea = [];
% use imcontour for speed
[cnt h]=imcontour(bwimg,[1 1]);
% weird vector output format
not_done=1;
ind=1;
num=0
% step through each contour, which corresponds to an erosion
feature
while not_done
    cnt_level=cnt(1,ind);
    cnt_count=cnt(2,ind);
    disp(['contour at: ',num2str(cnt_level),' count:
',num2str(cnt_count)])
    cnt_data=cnt(:,ind+1:ind+cnt_count);
    % see if its a closed contour
```

```
    if cnt_data(1,end)==cnt_data(1,1) &&
cnt_data(2,end)==cnt_data(2,1)
        num=num+1;
        % grid fit these data
        % find extents, and clip a little DEM for interpolation
        % take a margin around the extents to ensure a boundary
around the feature
        min_j=min(cnt_data(1,:))-marg;
        min_i=min(cnt_data(2,:))-marg;
        max_j=max(cnt_data(1,:))+marg;
        max_i=max(cnt_data(2,:))+marg;
        % check the margin doesn't put us outside the extents of
the DEM

        % clip edited and orignal DEM to bounds of this pit
        mini_DEMedit=DEMedit(min_i:max_i,min_j:max_j);
        mini_originalDEM=originalDEM(min_i:max_i,min_j:max_j);
        rowvec = (1:max_i-min_i+1)';
        colvec = (1:max_j-min_j+1)';
        rows=(1:max_i-min_i+1)'*ones(1,max_j-min_j+1);
        cols=ones(max_i-min_i+1,1)*(1:max_j-min_j+1);
        % use grid fit to interpolate a 'pre-erosion surface'
across the pit

newDEM=gridfit(cols(:),rows(:),mini_DEMedit,colvec,rowvec,'smooth
ness',0.1);
        subsetDEM=newDEM-mini_originalDEM;

        % max absolute depth of pit
        maxDepth(end+1) = max(abs(subsetDEM(:)));
        % pit volumes
        pitVol(end+1) = sum(abs(subsetDEM(~isnan(subsetDEM))));
        % number of pixels (* by pixel size for area)
        pitArea(end+1) = sum(sum(isnan(mini_DEMedit)));

        % now plot data, if requested
        if pflag

            % plot the identified pit
            figure(1)
            clf
            imagesc(mini_originalDEM)
            hold on
            plot(cnt_data(1,:)-min_j+1,cnt_data(2,:)-min_i+1,'w-
','linewidth',2)
            colorbar
            print('-dpng','-r200',['pit_',num2str(num)]);

            % plot the identified pit as difference from pre-
erosion surface
            clf
            imagesc(subsetDEM)
            hold on
            plot(cnt_data(1,:)-min_j+1,cnt_data(2,:)-min_i+1,'w-
','linewidth',2)
            colorbar
```

```
            print('-dpng','-r200',['pit_diff_',num2str(num)]);

            % plot cross-profile of the identified - pre-erosion
surface and pit
            clf
            hold on
            plot(mini_originalDEM(:,floor((max_j-min_j)/2)),'k')
            plot(newDEM(:,floor((max_j-min_j)/2)),'k--')
            print('-dpng','-r200',['pit_profile_',num2str(num)]);
        end

    else
        % there may be some unclosed contours on the boundary -
can't process them
        disp('not closed')
    end

    ind=ind+cnt_count+1;
    if ind>size(cnt,2) break; end

end
```

9.3. SEM Mineral Analysis by Sample

SEM Percent Composition Analysis

Sample	Magnification	Total Pixels	# White Pix	% White Pix	# Yellow Pix	% Yellow Pix	# Magenta	% Magenta	# Cyan	% Cyan	# Extra	% Extra
B_01 Z-08	40x	671182	1529	0.2	25224	3.8	225087	33.5	411737	61.3	7605	1.1
B_01	body	680031	6626	1	78518	11.5	257344	37.8	334513	49.2	3030	0.4
B_01	surface (top 100µm)	198678	1291	0.6	24105	12.1	71282	35.9	99282	50	2718	1.4
B_02 Z-06	40x	691078	1783	0.3	31954	4.6	227197	32.4	428236	62.5	1908	0.3
B_02	body	638496	5356	0.8	62262	9.8	151918	23.8	416544	65.2	2416	0.38
B_02	surface (top 100µm)	185335	751	0.4	14476	7.8	38244	20.6	126161	68.1	5703	3.1
B_03 Z-07	250x	642243	1597	0.3	26361	4.1	188670	29.4	401189	62.5	24426	3.8
B_03 Z-09	40x	665241	0	0	46415	7	137226	20.6	463350	69.7	18250	2.7
B_03 Z-12	40x	817210	6705	0.8	53757	6.6	144391	17.7	573340	70.2	39017	4.8
B_03	body	364455	1066	0.3	13494	3.7	95593	26.2	249660	68.5	4642	1.3
B_03	surface (top 100µm)	284869	889	0.3	10339	3.6	96306	33.8	164397	57.7	12938	4.5
B_04 Z-08	40x	956393	3475	0.4	38960	4.1	129473	13.5	723963	75.7	60522	6.3
B_04 Z-11	40x	603579	1034	2	25158	4.2	81115	13.4	418260	69.3	78012	12.9
B_04	body	862147	4915	0.6	33968	3.9	77690	9	704068	81.7	41506	4.8
B_04	surface (top 100µm)	193853	1152	0.6	6677	3.4	21588	11.1	157284	81.1	7152	3.7
B_05 Z-10	40x	260074	1361	0.52	6047	2.33	143282	55.09	104574	40.21	4810	1.79
B_05 Z-10R	40x	843344	6383	0.8	124903	14.8	324036	38.4	384462	45.6	3560	0.4
B_05 Z-07	40x	207452	5954	2.87	5876	2.83	73585	35.5	117044	56.42	4993	2.41
B_05 Z-07R	40x	616975	6978	1.1	35151	5.7	227913	36.9	344446	55.8	2487	0.4
B_05 Z-13R	65x	728873	13933	1.9	30615	4.2	279775	38.4	397035	54.5	7515	1
B_05 Z-14	230x	334164	20238	6.06	11998	3.59	84683	25.34	205805	61.59	11440	3.42
B_05 Z-13	65x	279325	18463	6.61	8825	3.16	96492	35.54	148099	53.02	7446	2.67
B_05 Z-15	950x	367680	12727	3.46	21708	5.9	76002	20.67	252698	68.73	4545	1.24
B_05	body	716965	14933	2.1	57061	8	294866	41.1	345706	48.2	4399	0.6
B_05	surface (top 100µm)	225261	2456	1.1	12241	5.4	76162	33.8	125565	55.7	8837	3.9

9.4. Additional Model Output Trends

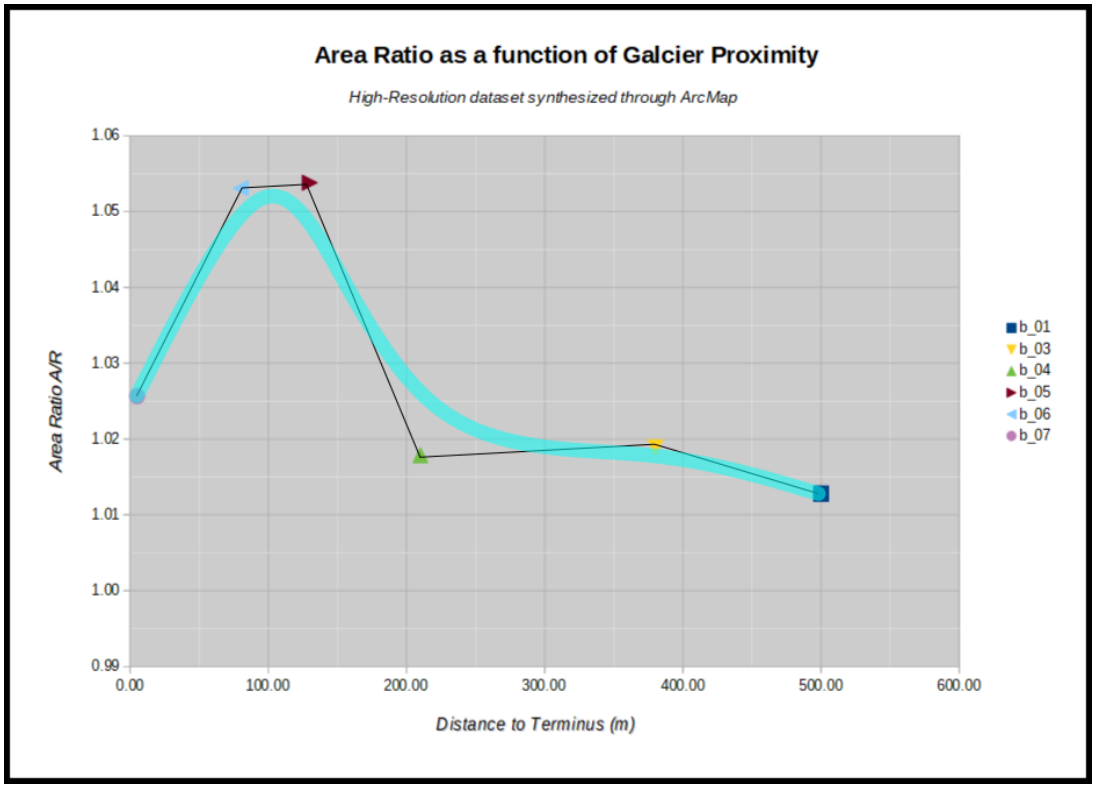

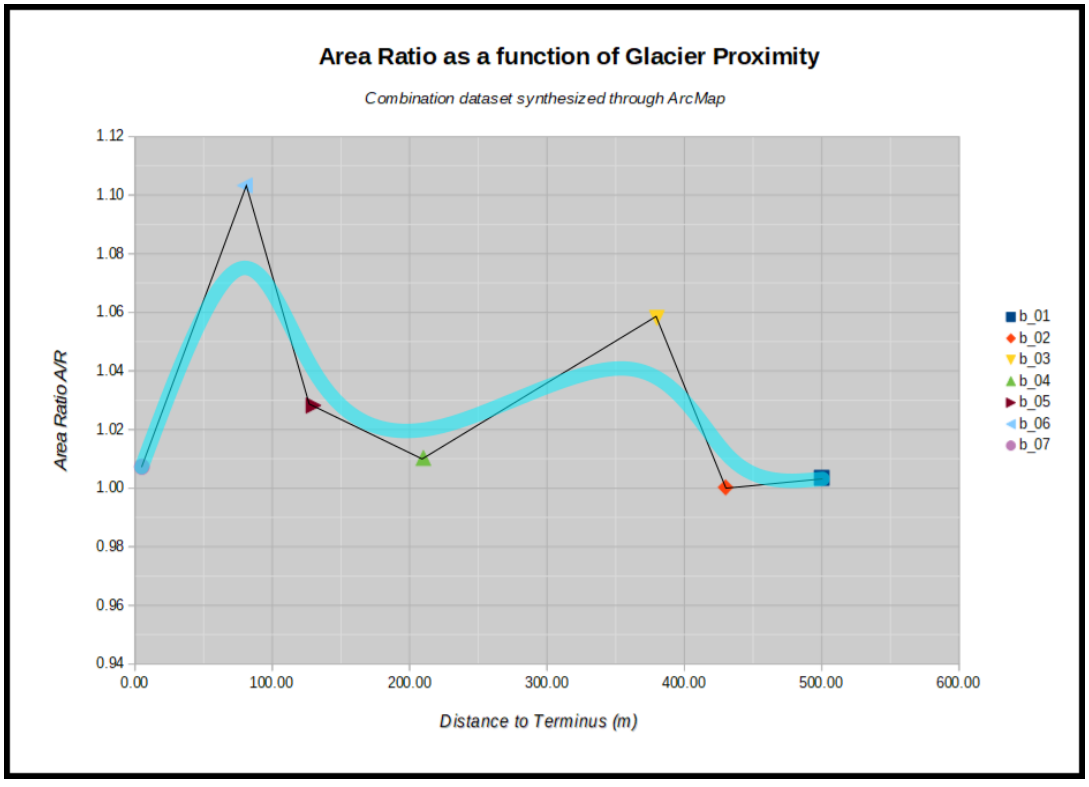

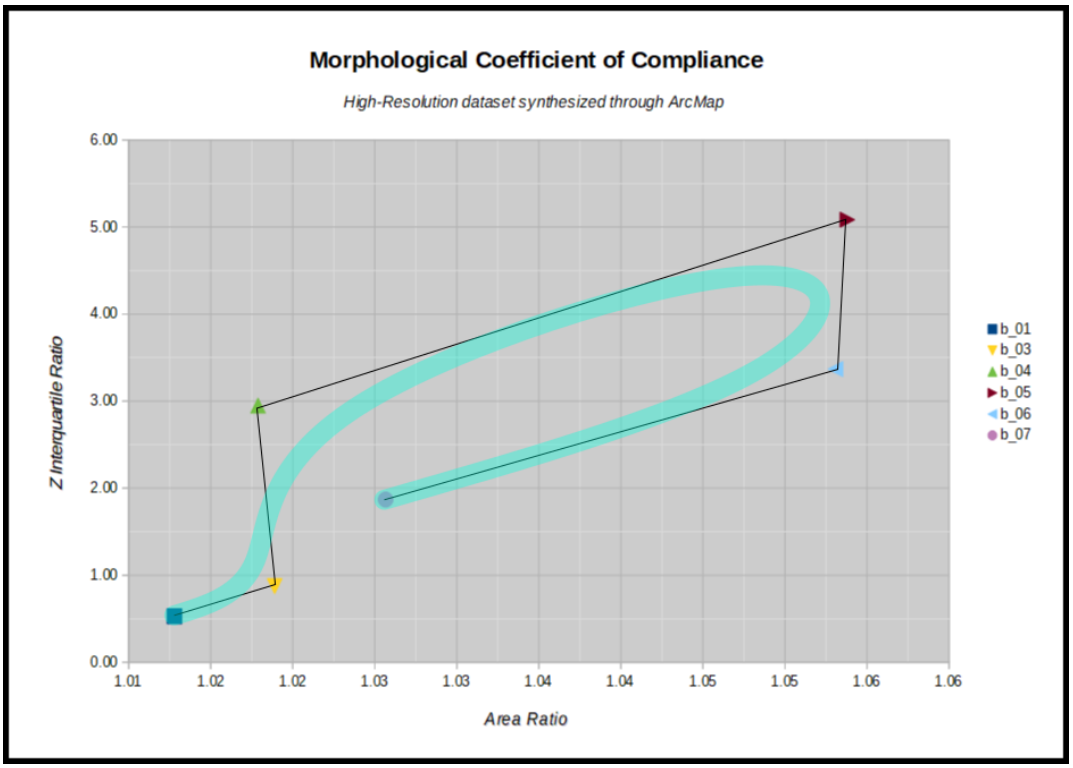
Morphological Coefficient of Compliance
High-Resolution dataset synthesized through ArcMap
Z Interquartile Ratio
Area Ratio
6.00
5.00
4.00
3.00
2.00
1.00
0.00
1.01
1.02
1.02
1.03
1.03
1.04
1.04
1.05
1.05
1.06
1.06
b_01
b_03
b_04
b_05
b_06
b_07

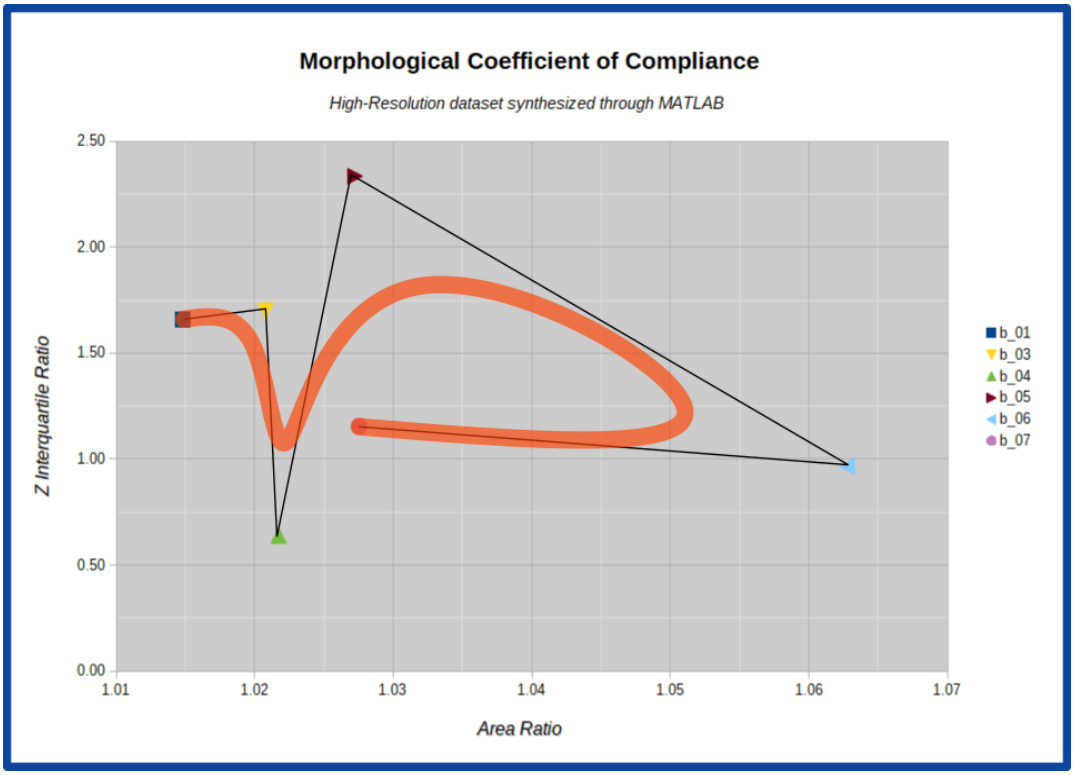
Morphological Coefficient of Compliance
High-Resolution dataset synthesized through MATLAB
Z Interquartile Ratio
Area Ratio
2.50
2.00
1.50
1.00
0.50
0.00
1.01
1.02
1.03
1.04
1.05
1.06
1.07
b_01
b_03
b_04
b_05
b_06
b_07

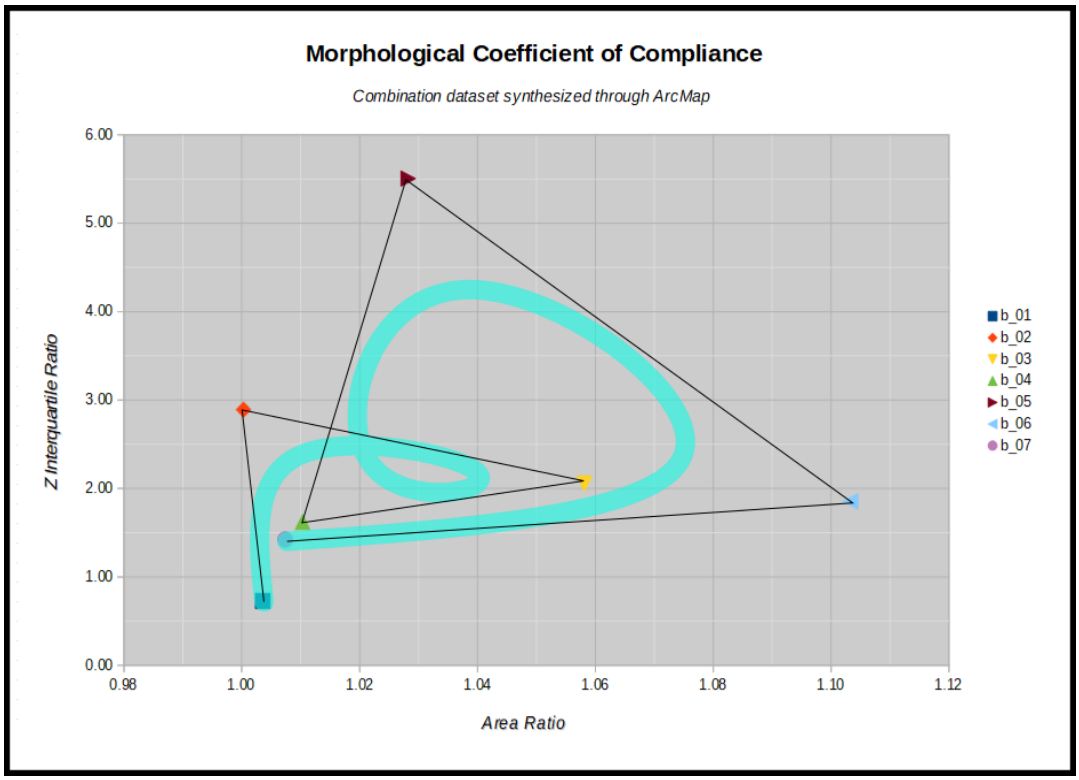
Morphological Coefficient of Compliance
Combination dataset synthesized through ArcMap
Z Interquartile Ratio
Area Ratio
6.00
5.00
4.00
3.00
2.00
1.00
0.00
0.98
1.00
1.02
1.04
1.06
1.08
1.10
1.12
b_01
b_02
b_03
b_04
b_05
b_06
b_07

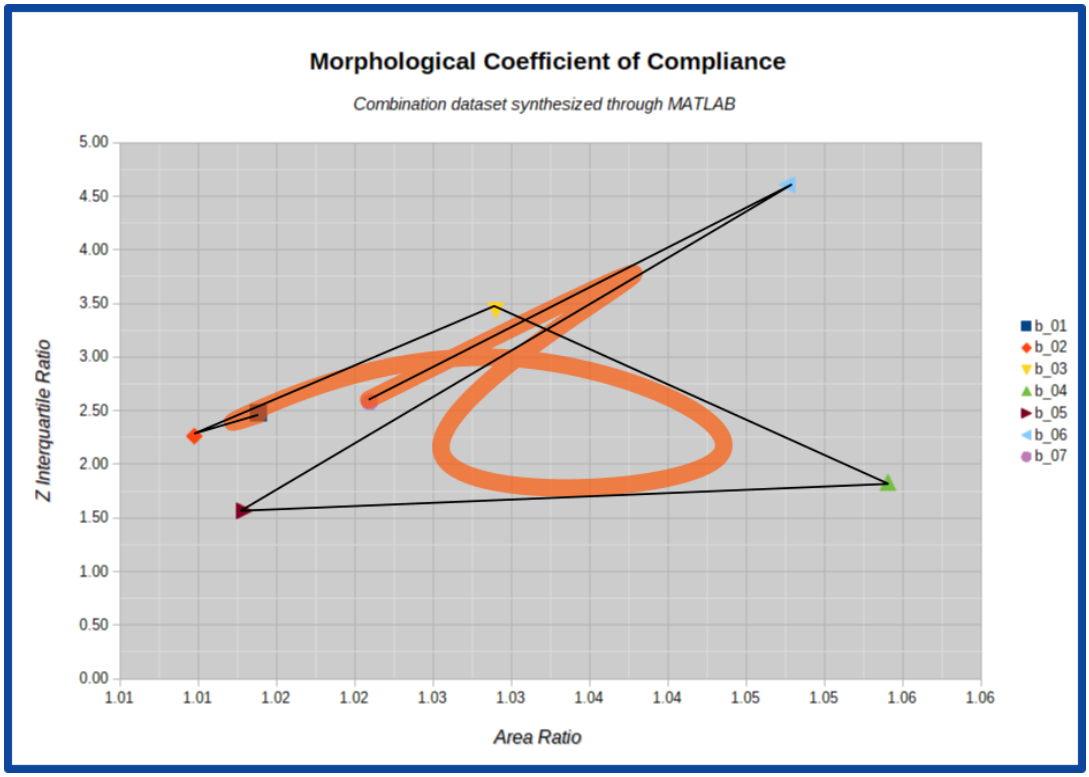
Morphological Coefficient of Compliance
Combination dataset synthesized through MATLAB
Z Interquartile Ratio
Area Ratio
5.00
4.50
4.00
3.50
3.00
2.50
2.00
1.50
1.00
0.50
0.00
1.01
1.01
1.02
1.02
1.03
1.03
1.04
1.04
1.05
1.05
1.06
1.06
b_01
b_02
b_03
b_04
b_05
b_06
b_07

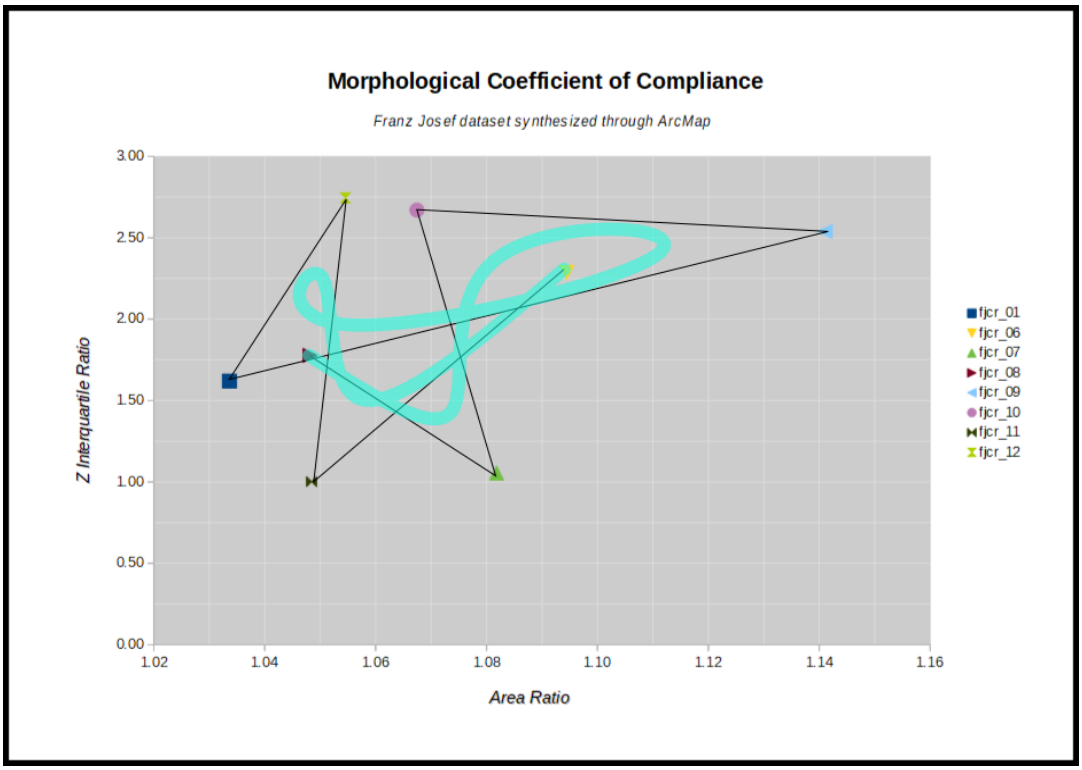
Morphological Coefficient of Compliance
Franz Josef dataset synthesized through ArcMap
Z Interquartile Ratio
Area Ratio
3.00
2.50
2.00
1.50
1.00
0.50
0.00
1.02
1.04
1.06
1.08
1.10
1.12
1.14
1.16
fjcr_01
fjcr_06
fjcr_07
fjcr_08
fjcr_09
fjcr_10
fjcr_11
fjcr_12

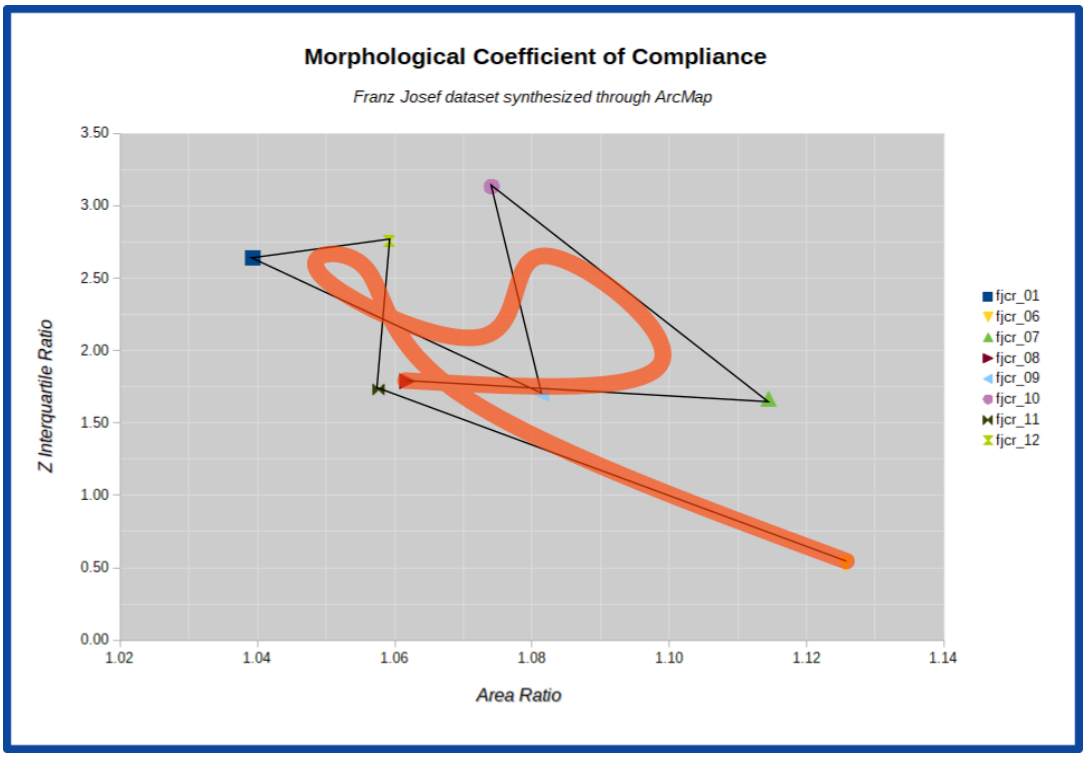
Morphological Coefficient of Compliance
Franz Josef dataset synthesized through ArcMap
Z Interquartile Ratio
Area Ratio
3.50
3.00
2.50
2.00
1.50
1.00
0.50
0.00
1.02
1.04
1.06
1.08
1.10
1.12
1.14
fjcr_01
fjcr_06
fjcr_07
fjcr_08
fjcr_09
fjcr_10
fjcr_11
fjcr_12

9.5. Global Polynomial Interpolation Filter Analysis Results

10th Order Global Polynomial Interpolation Filter Analysis Results
Sample: Brewster B_01_combo

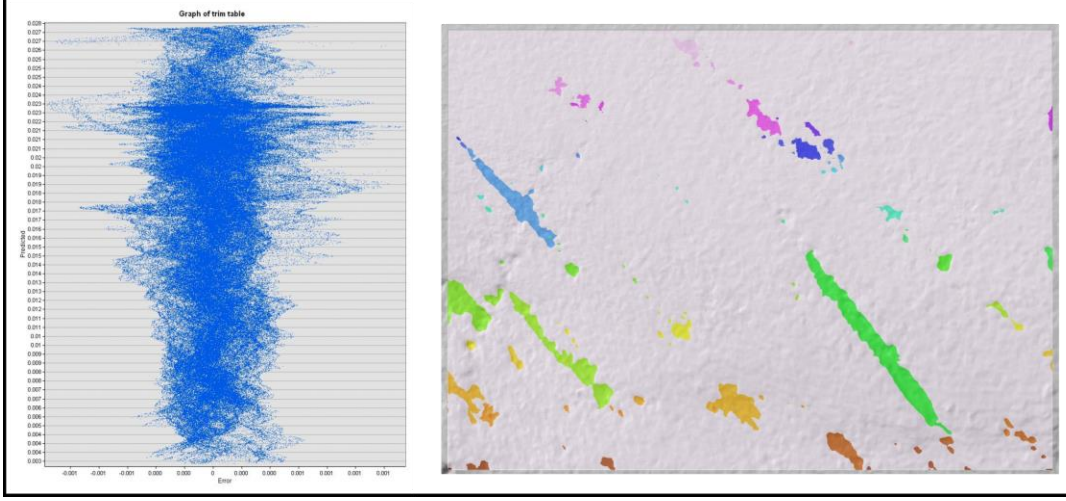

10th Order Global Polynomial Interpolation Filter Analysis Results
Sample: Brewster B_01_Hi-Res

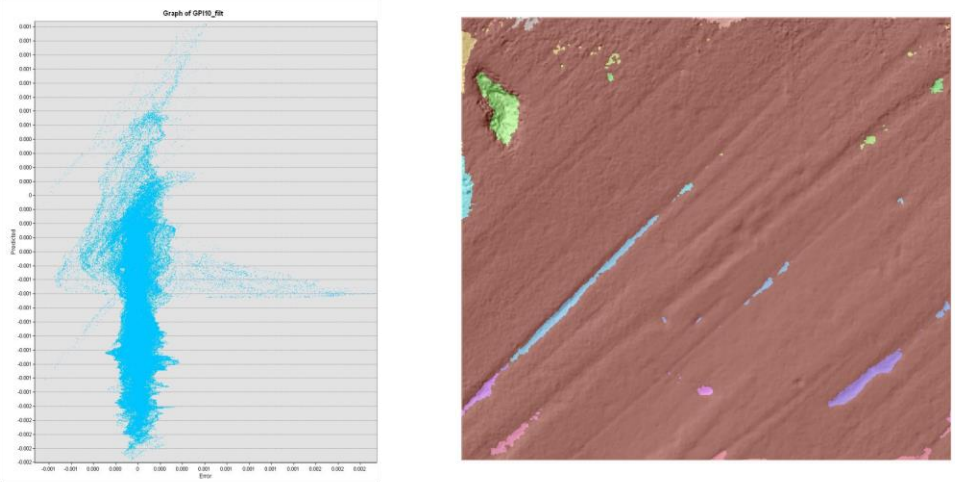

10th Order Global Polynomial Interpolation Filter Analysis Results
Sample: Brewster B_02_combo

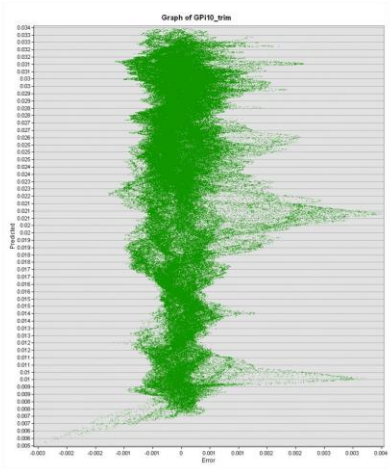

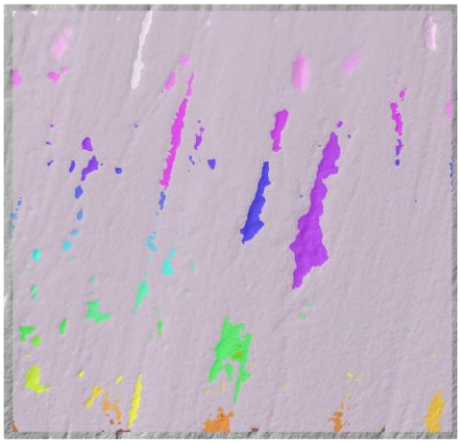

10th Order Global Polynomial Interpolation Filter Analysis Results
Sample: Brewster B_03_combo

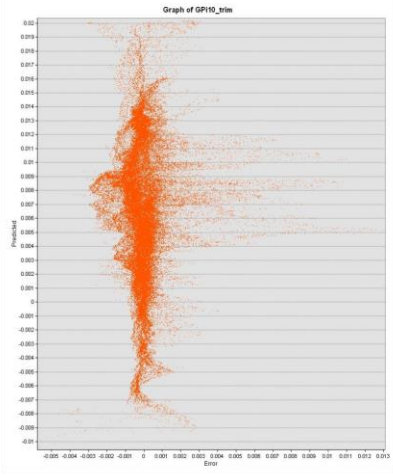

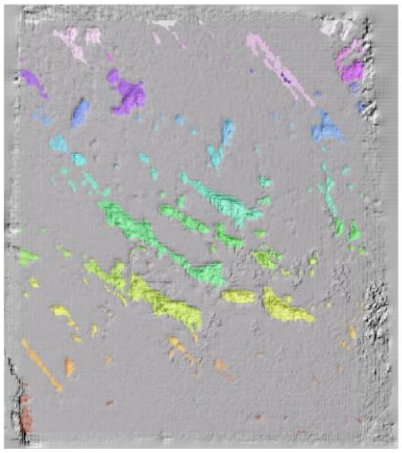

10th Order Global Polynomial Interpolation Filter Analysis Results
Sample: Brewster B_03_Hi-Res

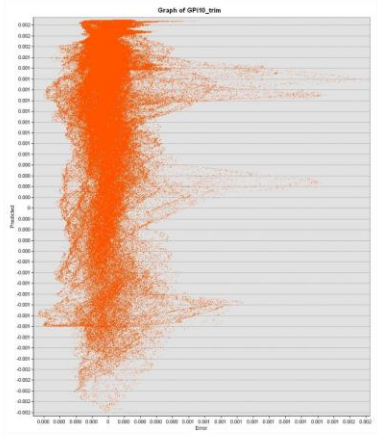

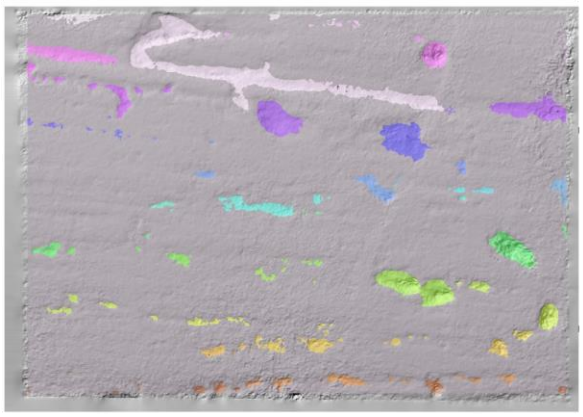

10th Order Global Polynomial Interpolation Filter Analysis Results
Sample: Brewster B_04_combo

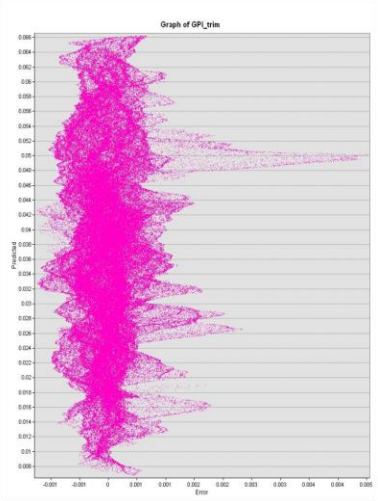

10th Order Global Polynomial Interpolation Filter Analysis Results
Sample: Brewster B_04_Hi-Res

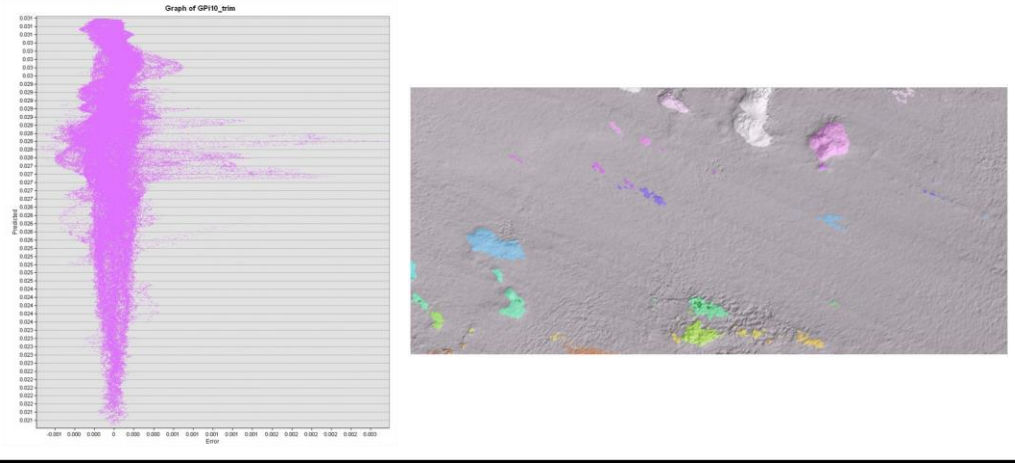

10th Order Global Polynomial Interpolation Filter Analysis Results
Sample: Brewster B_05_combo

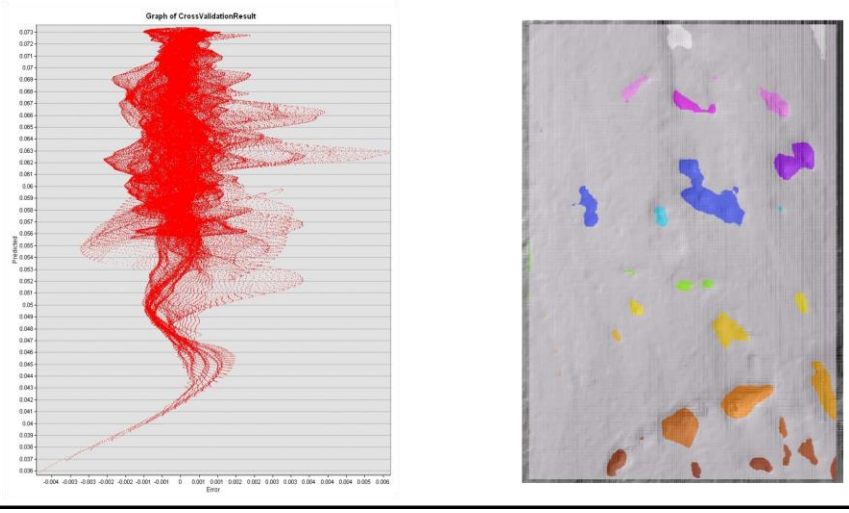

10th Order Global Polynomial Interpolation Filter Analysis Results
Sample: Brewster B_05_Hi-Res

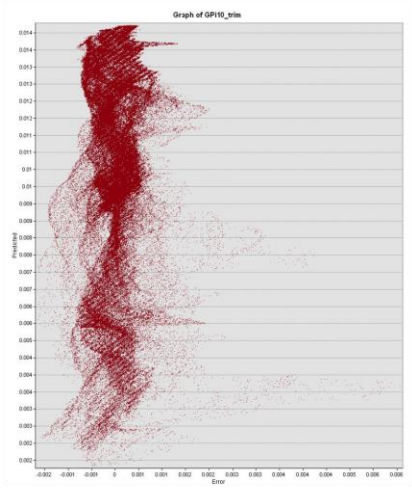

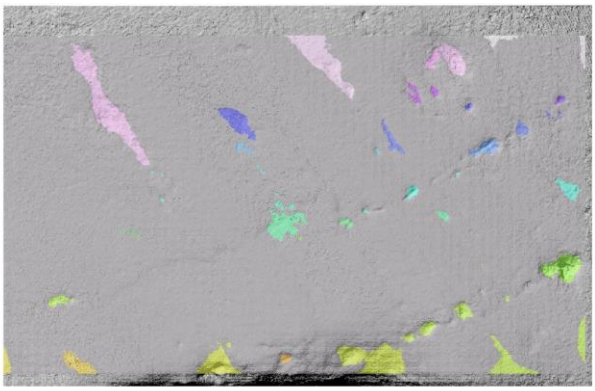

10th Order Global Polynomial Interpolation Filter Analysis Results
Sample: Brewster B_06_combo

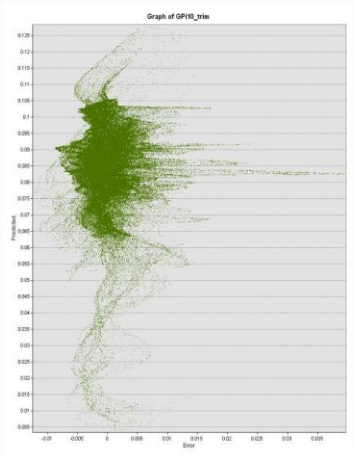

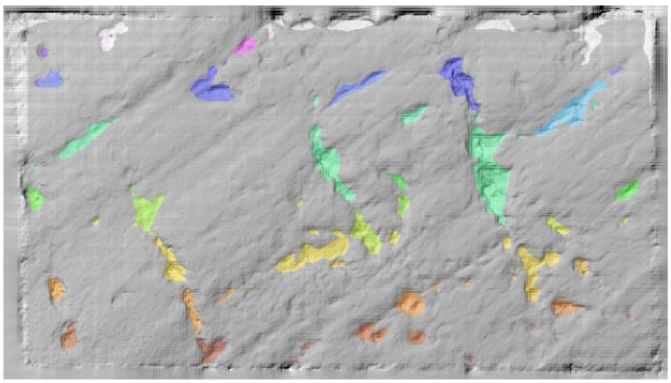

10th Order Global Polynomial Interpolation Filter Analysis Results
Sample: Brewster B_06_Hi-Res

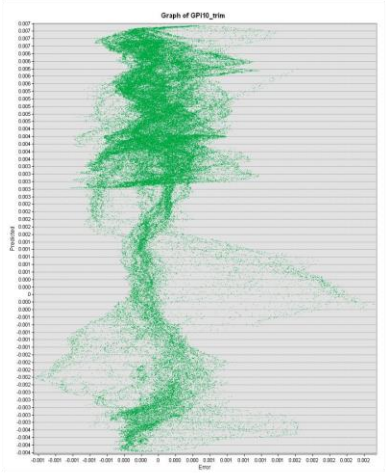

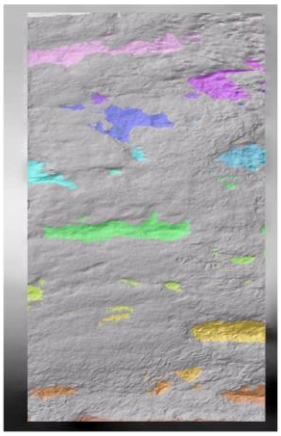

10th Order Global Polynomial Interpolation Filter Analysis Results
Sample: Brewster B_07_combo

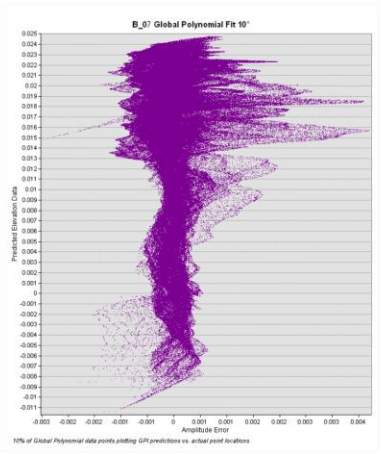

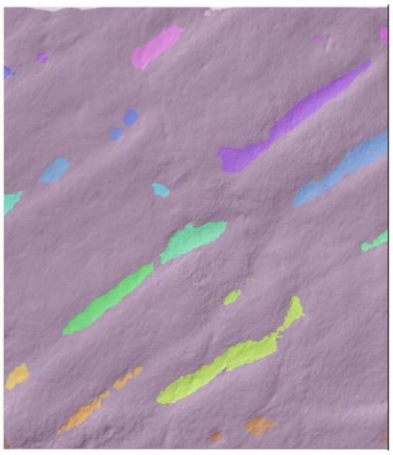

10th Order Global Polynomial Interpolation Filter Analysis Results
Sample: Brewster B_07_Hi-Res

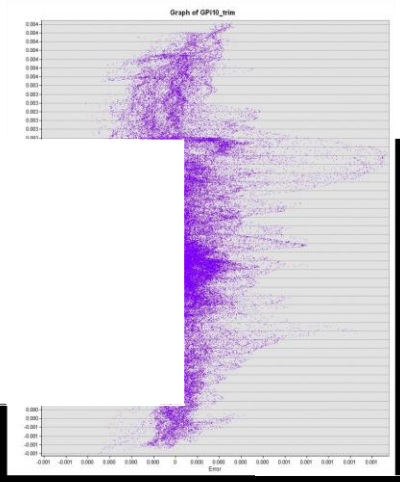

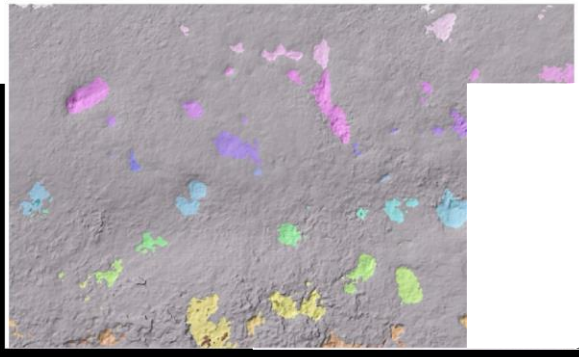

10th Order Global Polynomial Interpolation Filter Analysis Results
Sample: Franz Josef FJCR_01

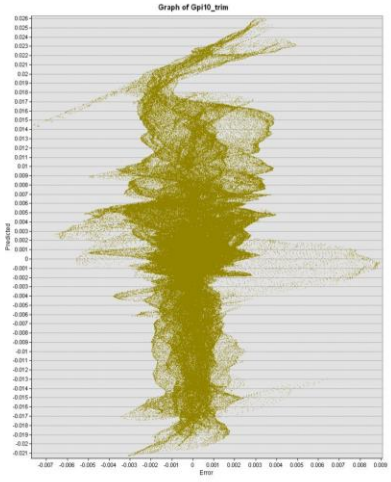

10th Order Global Polynomial Interpolation Filter Analysis Results
Sample: Franz Josef FJCR_06

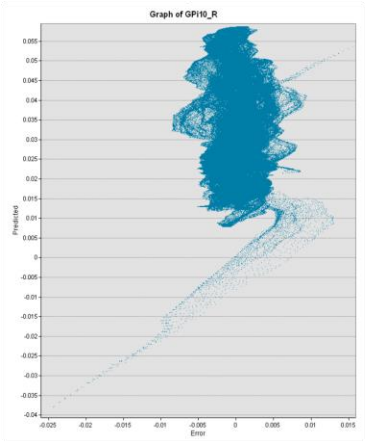

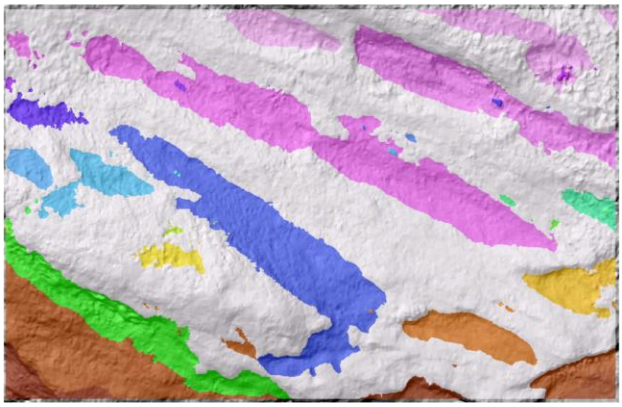

10th Order Global Polynomial Interpolation Filter Analysis Results
Sample: Franz Josef FJCR_07

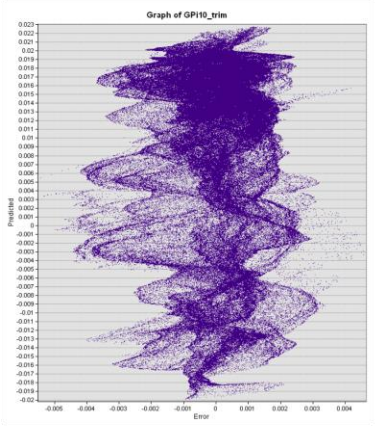

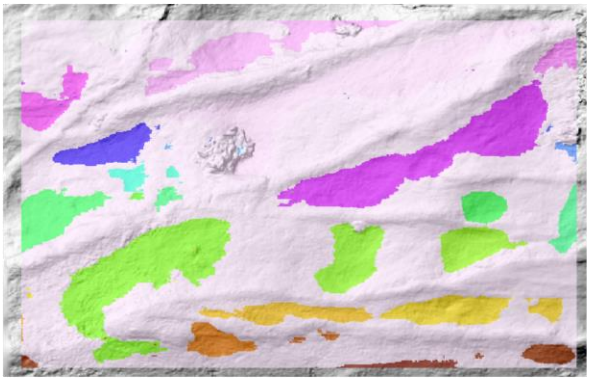

10th Order Global Polynomial Interpolation Filter Analysis Results
Sample: Franz Josef FJCR_08

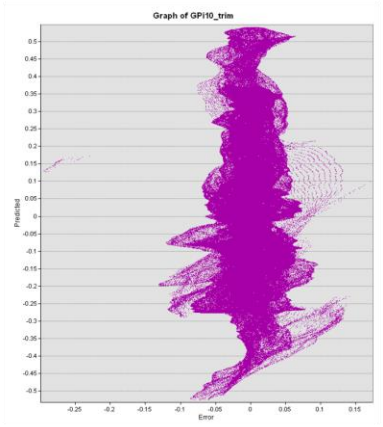

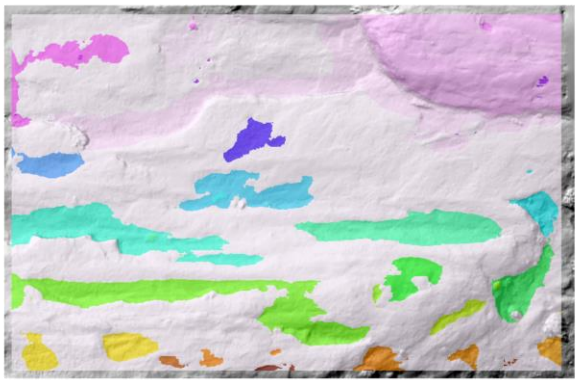

10th Order Global Polynomial Interpolation Filter Analysis Results
Sample: Franz Josef FJCR_09

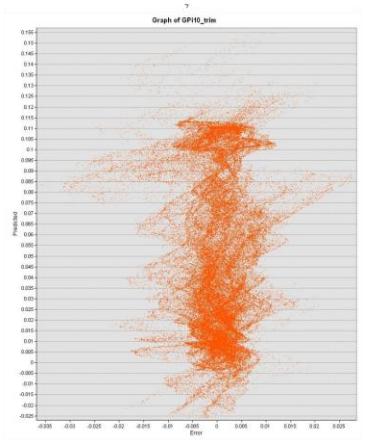

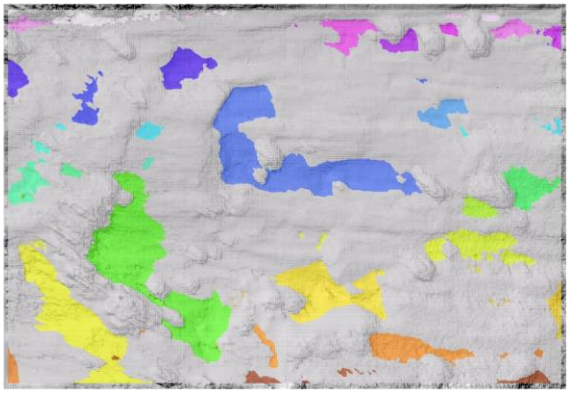

10th Order Global Polynomial Interpolation Filter Analysis Results
Sample: Franz Josef FJCR_10

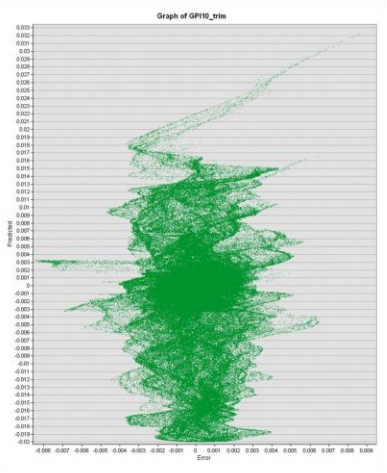

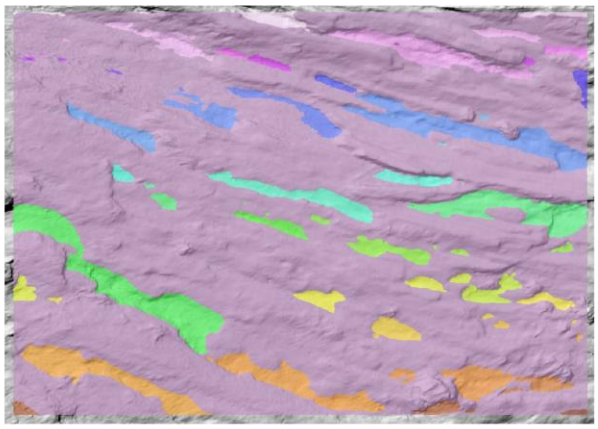

10th Order Global Polynomial Interpolation Filter Analysis Results
Sample: Franz Josef FJCR_11

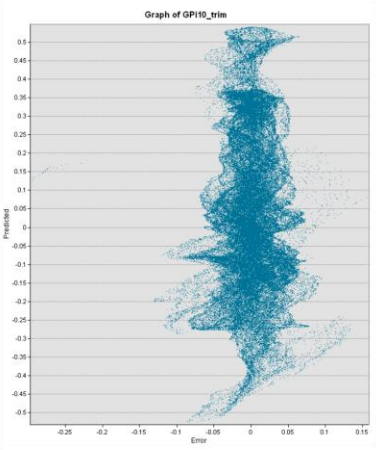

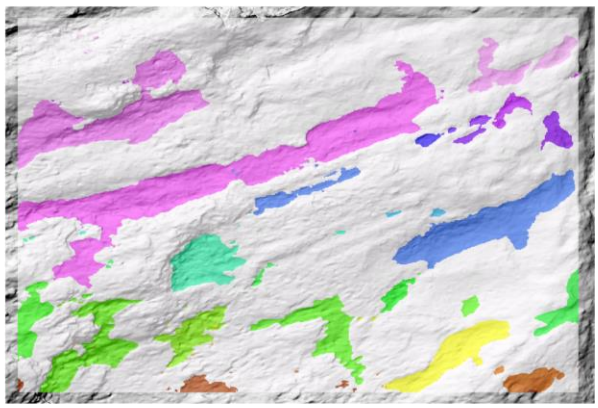

10th Order Global Polynomial Interpolation Filter Analysis Results

Sample: Franz Josef FJCR_12

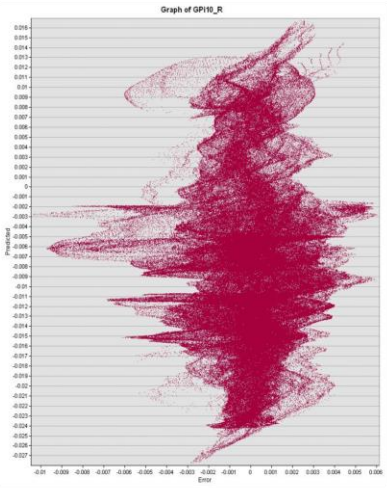

9.6. Continuous Wavelet Transform Analysis Results

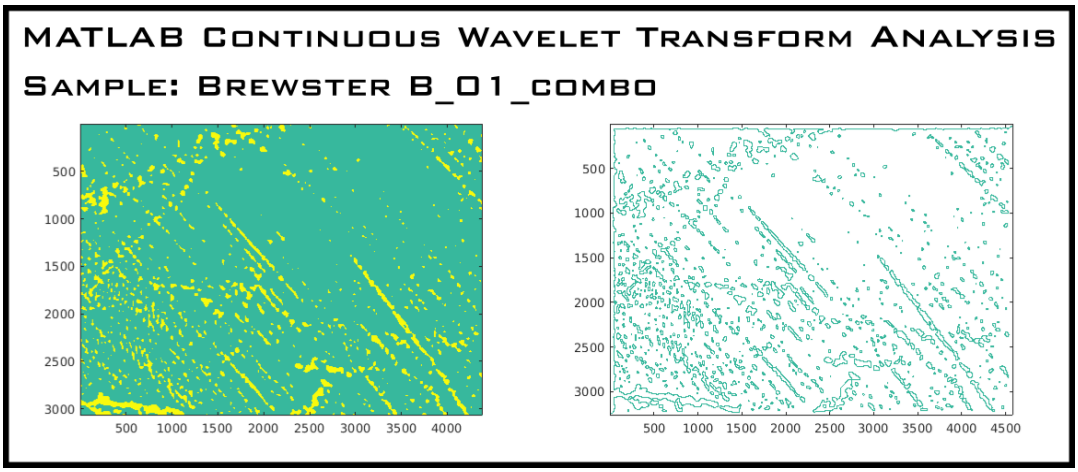

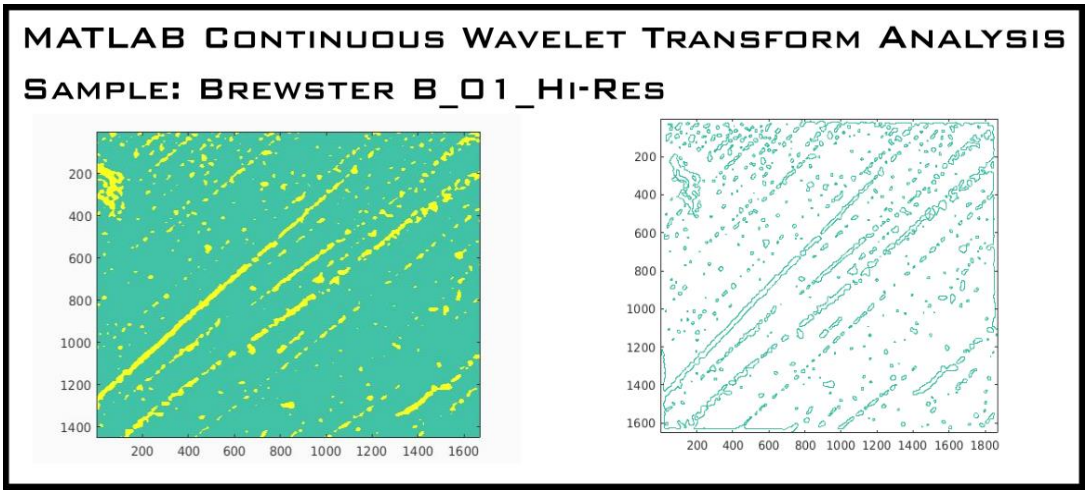

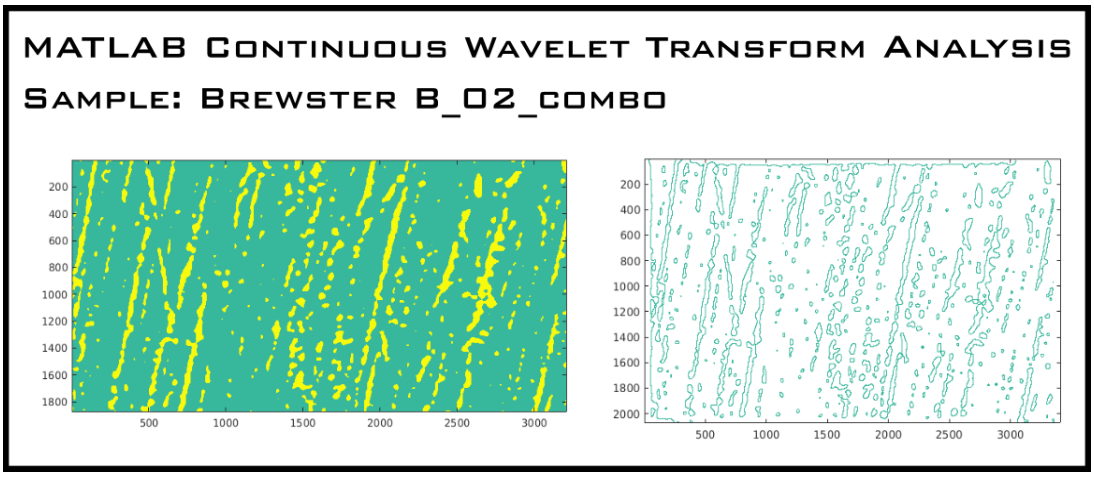

MATLAB Continuous Wavelet Transform Analysis
Sample: Brewster B_03_Hi-Res

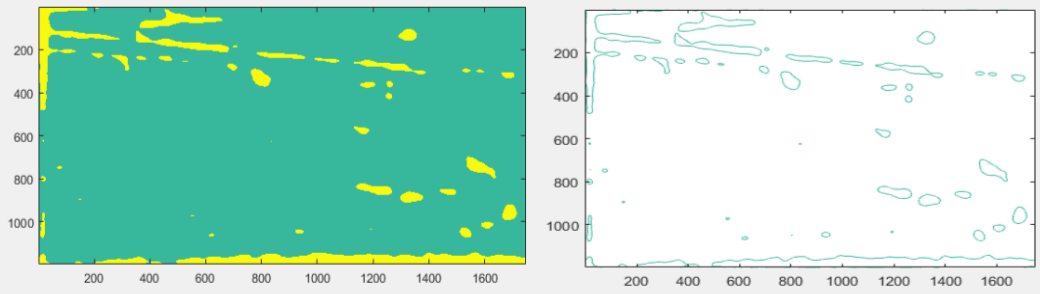

MATLAB Continuous Wavelet Transform Analysis
Sample: Brewster B_03_combo

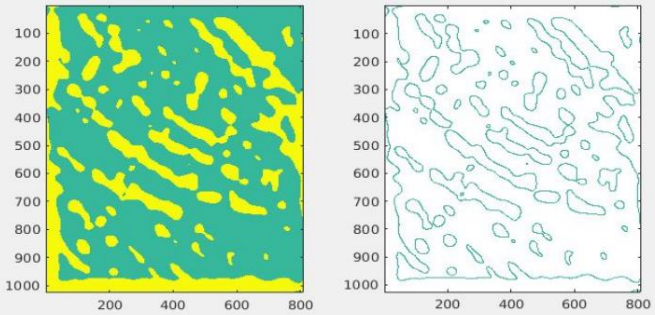

MATLAB Continuous Wavelet Transform Analysis
Sample: Brewster B_04_combo

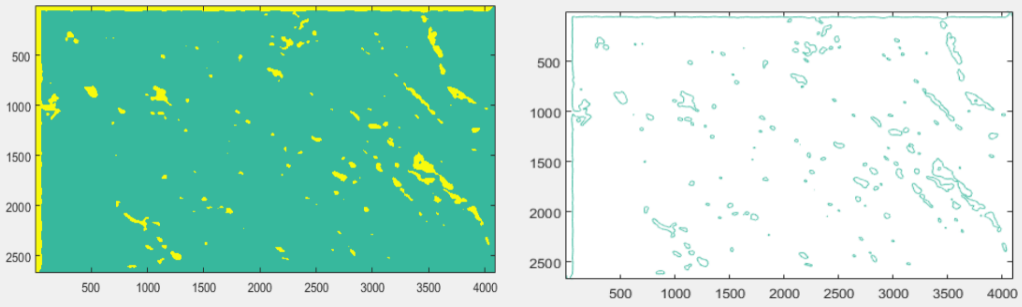

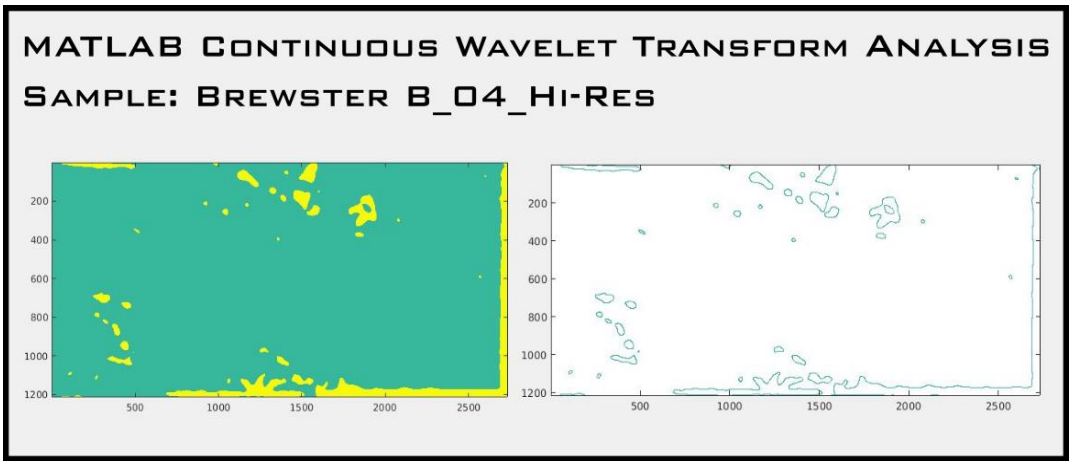
MATLAB Continuous Wavelet Transform Analysis
Sample: Brewster B_04_Hi-Res
200
400
600
800
1000
1200
500
1000
1500
2000
2500

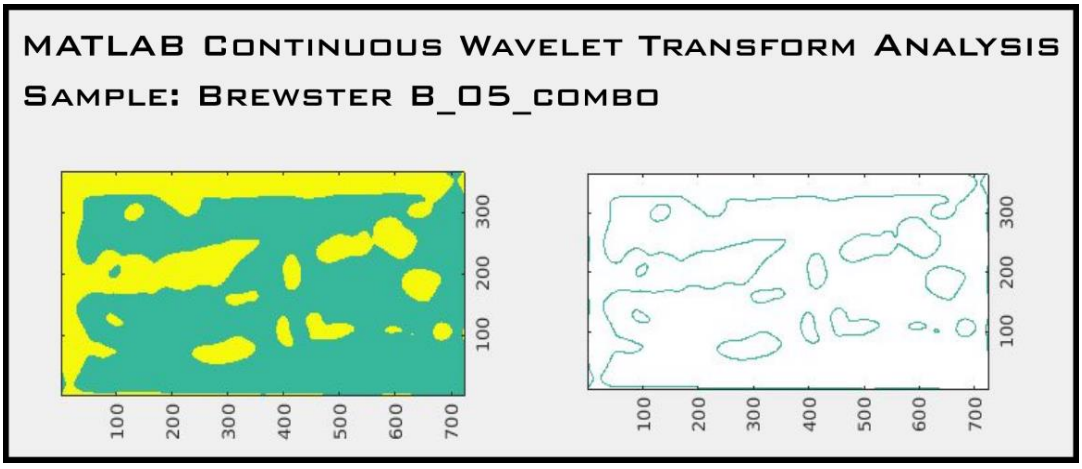
MATLAB Continuous Wavelet Transform Analysis
Sample: Brewster B_05_combo
100
200
300
400
500
600
700

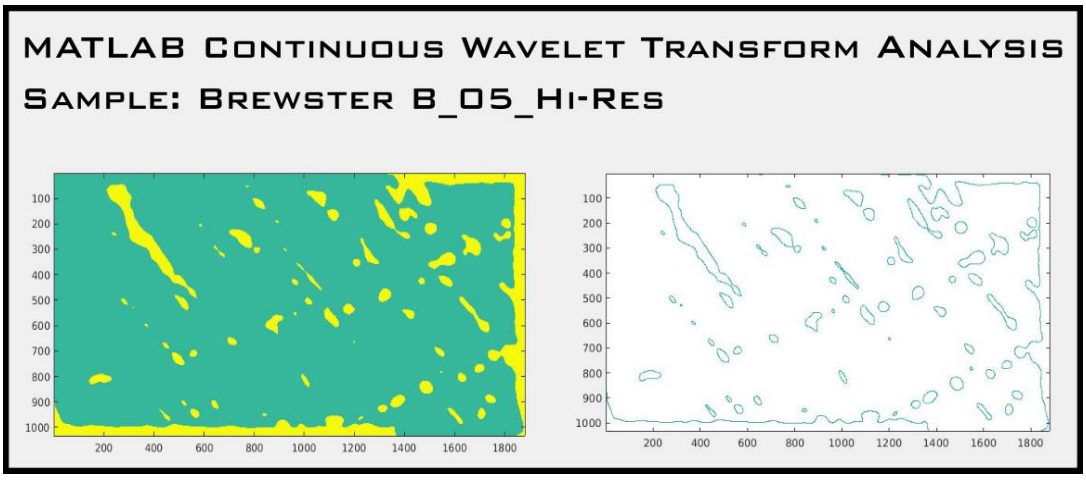
MATLAB Continuous Wavelet Transform Analysis
Sample: Brewster B_05_Hi-Res
100
200
300
400
500
600
700
800
900
1000
1200
1400
1600
1800

MATLAB Continuous Wavelet Transform Analysis
Sample: Brewster B_06_combo

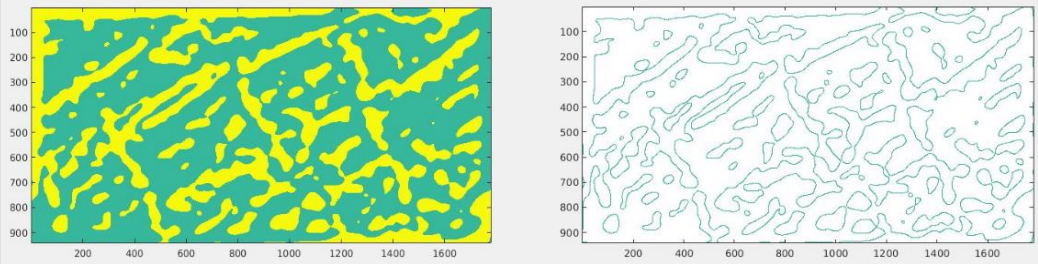

MATLAB Continuous Wavelet Transform Analysis
Sample: Brewster B_06_Hi-Res

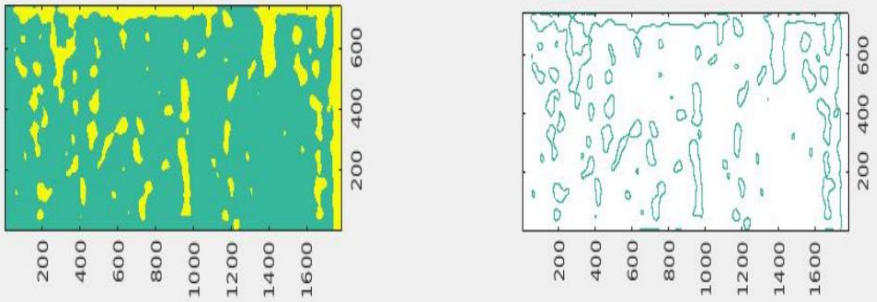

MATLAB Continuous Wavelet Transform Analysis
Sample: Brewster B_07_combo

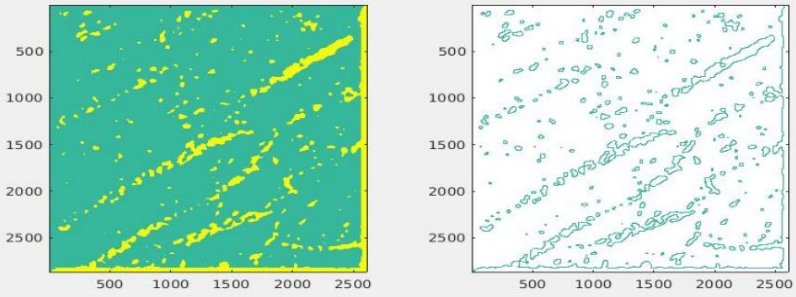

MATLAB Continuous Wavelet Transform Analysis
Sample: Brewster B_07_Hi-Res

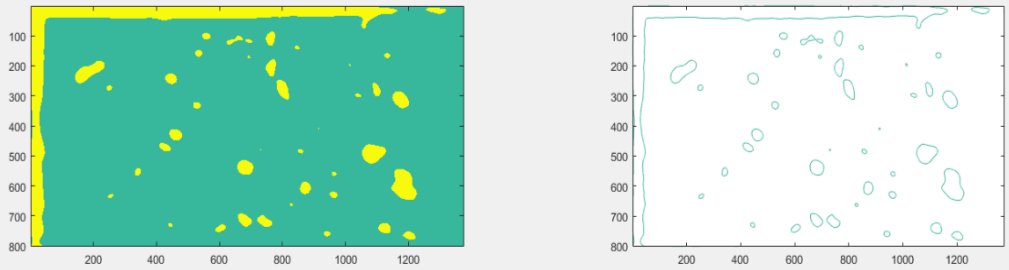

MATLAB Continuous Wavelet Transform Analysis
Sample: Franz Josef FJCR_01

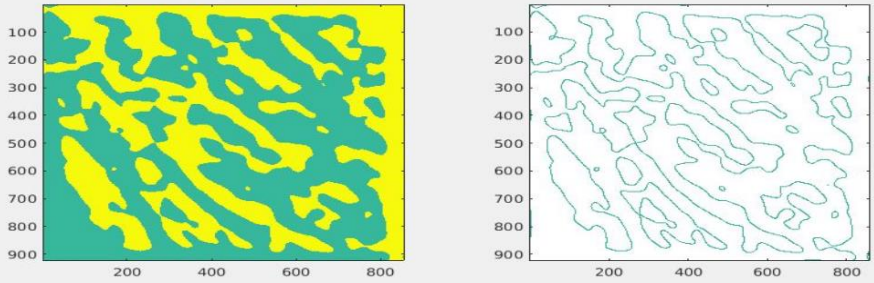

MATLAB Continuous Wavelet Transform Analysis
Sample: Franz Josef FJCR_06

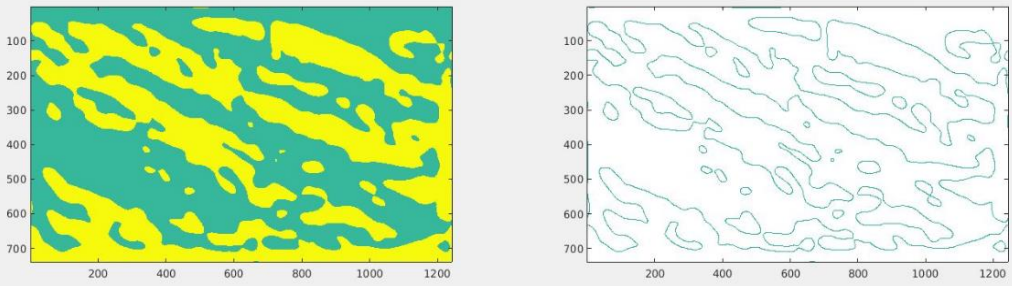

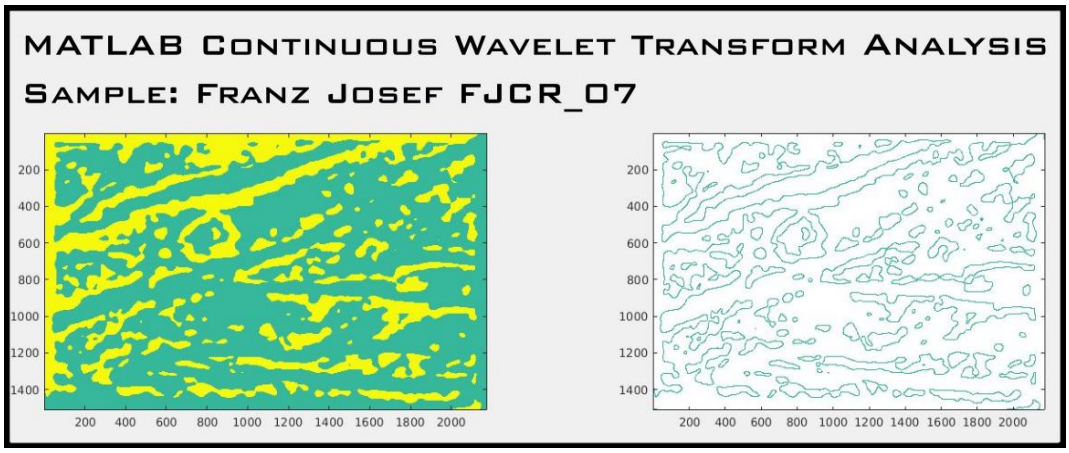
MATLAB Continuous Wavelet Transform Analysis
Sample: Franz Josef FJCR_07
200 400 600 800 1000 1200 1400
200 400 600 800 1000 1200 1400 1600 1800 2000
200 400 600 800 1000 1200 1400
200 400 600 800 1000 1200 1400 1600 1800 2000

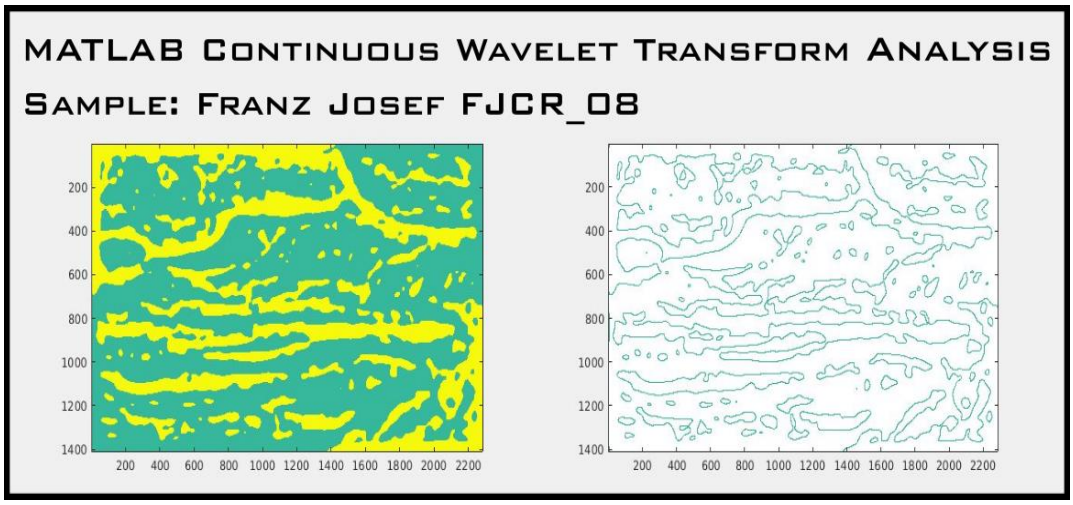
MATLAB Continuous Wavelet Transform Analysis
Sample: Franz Josef FJCR_08
200 400 600 800 1000 1200 1400
200 400 600 800 1000 1200 1400 1600 1800 2000 2200
200 400 600 800 1000 1200 1400
200 400 600 800 1000 1200 1400 1600 1800 2000 2200

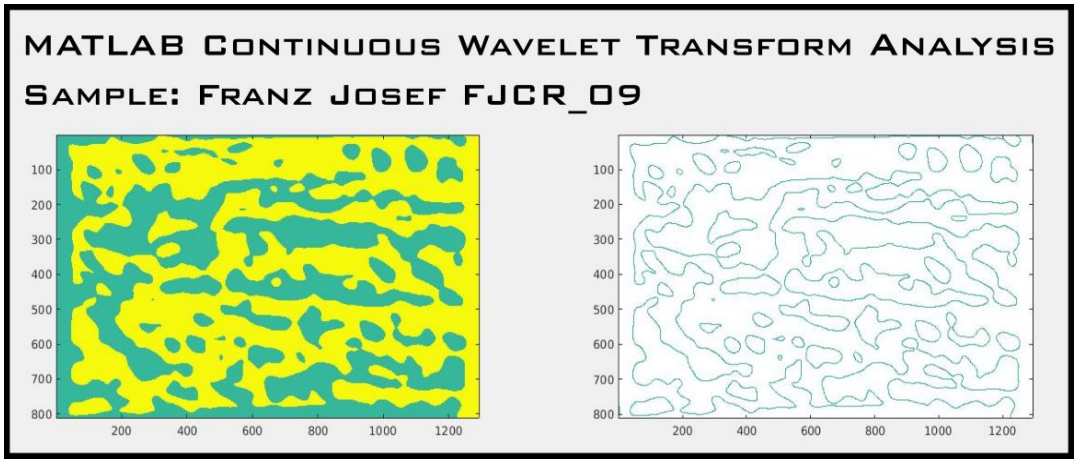
MATLAB Continuous Wavelet Transform Analysis
Sample: Franz Josef FJCR_09
100 200 300 400 500 600 700 800
200 400 600 800 1000 1200
100 200 300 400 500 600 700 800
200 400 600 800 1000 1200

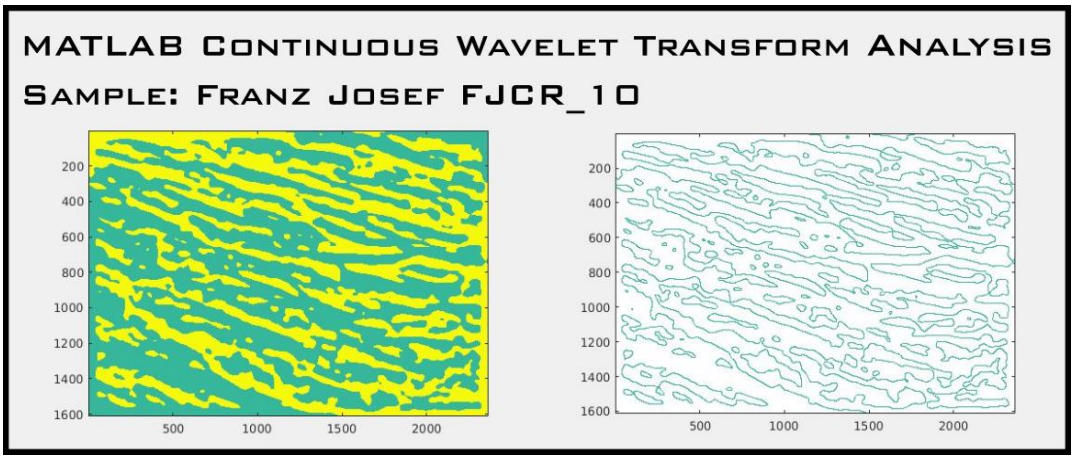
MATLAB Continuous Wavelet Transform Analysis
Sample: Franz Josef FJCR_10
200
400
600
800
1000
1200
1400
1600
500
1000
1500
2000

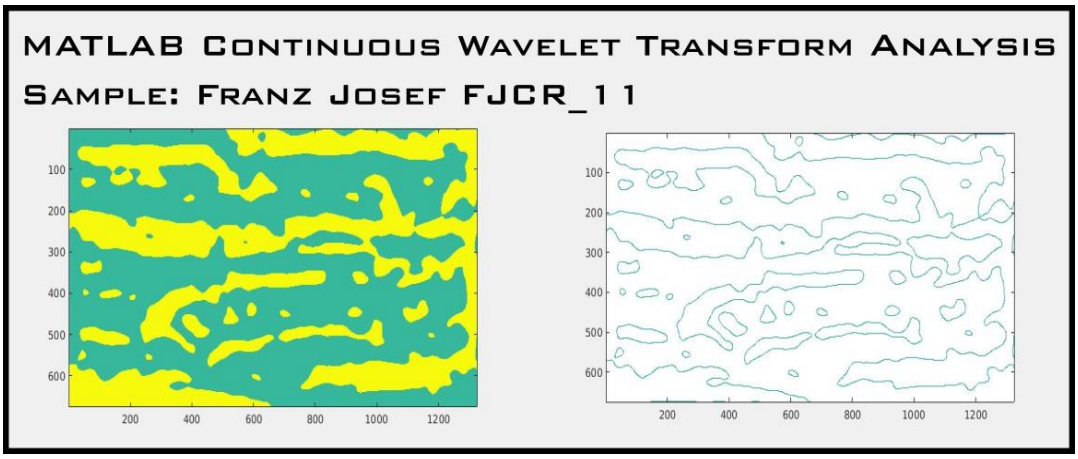
MATLAB Continuous Wavelet Transform Analysis
Sample: Franz Josef FJCR_11
100
200
300
400
500
600
200
400
600
800
1000
1200

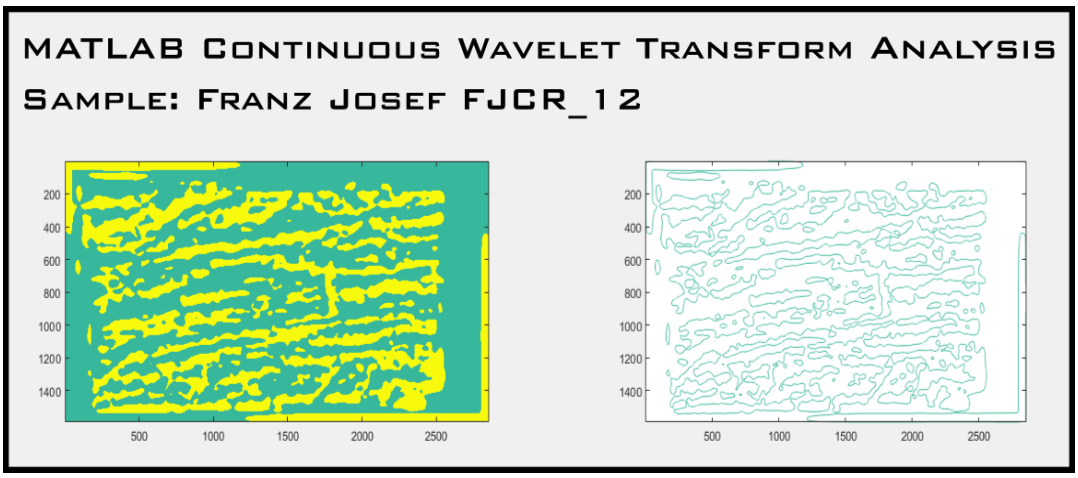
MATLAB Continuous Wavelet Transform Analysis
Sample: Franz Josef FJCR_12
200
400
600
800
1000
1200
1400
500
1000
1500
2000
2500

9.7. Additional XRF Measurement Trends

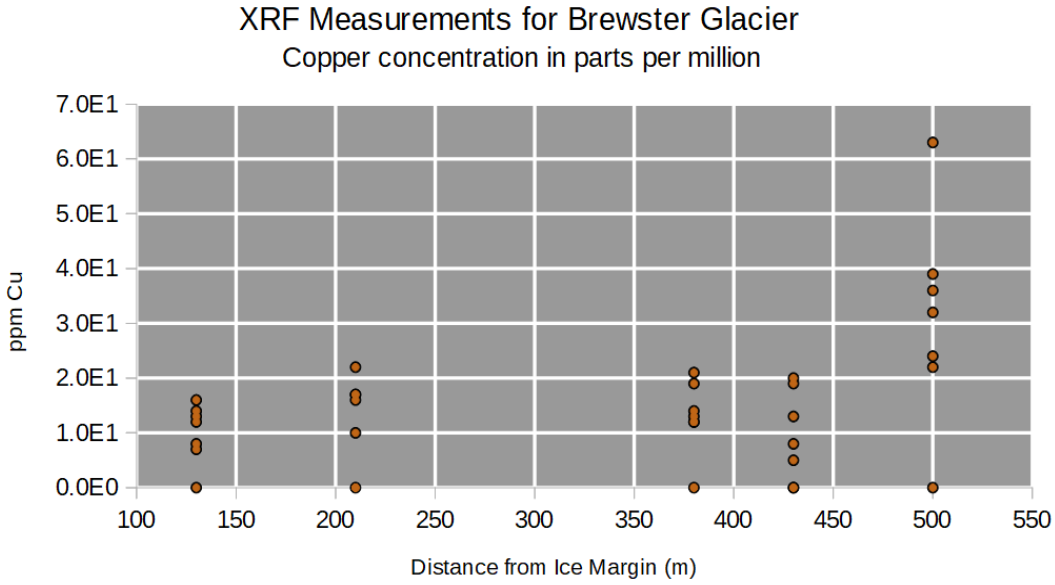

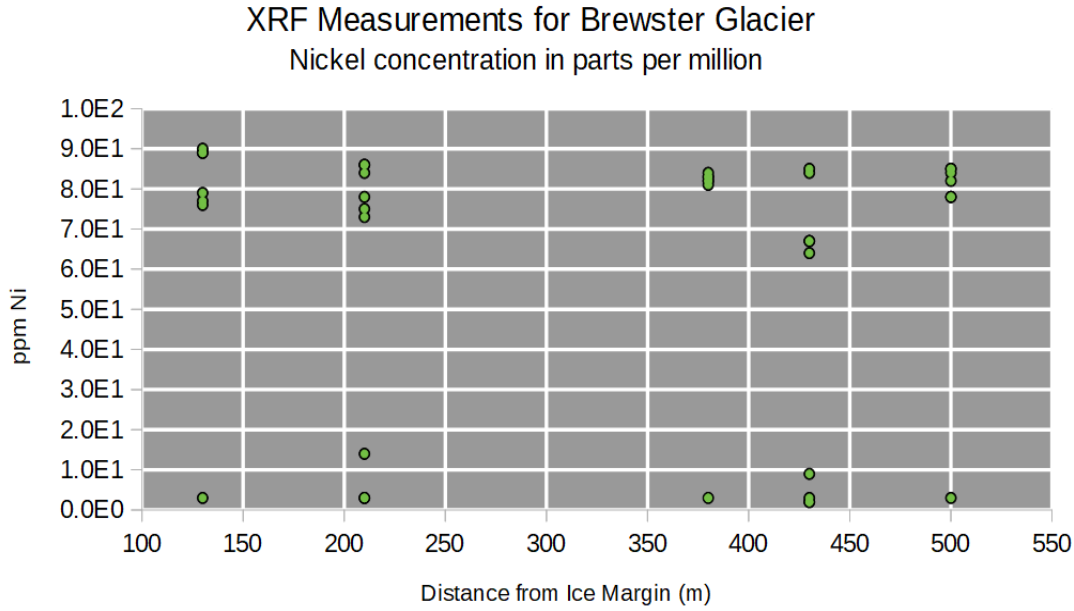

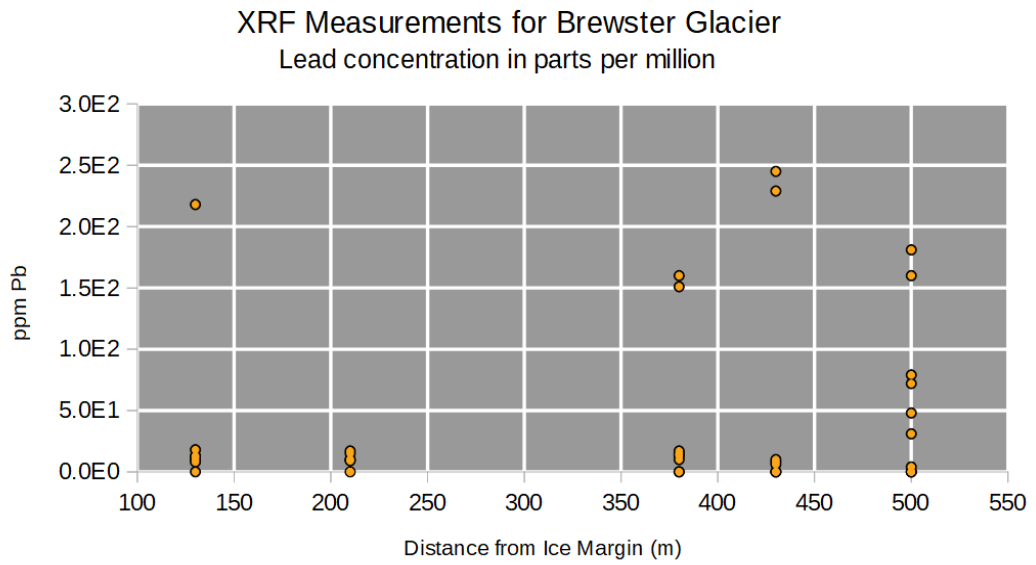
XRF Measurements for Brewster Glacier
Lead concentration in parts per million
ppm Pb
3.0E2
2.5E2
2.0E2
1.5E2
1.0E2
5.0E1
0.0E0
100
150
200
250
300
350
400
450
500
550
Distance from Ice Margin (m)

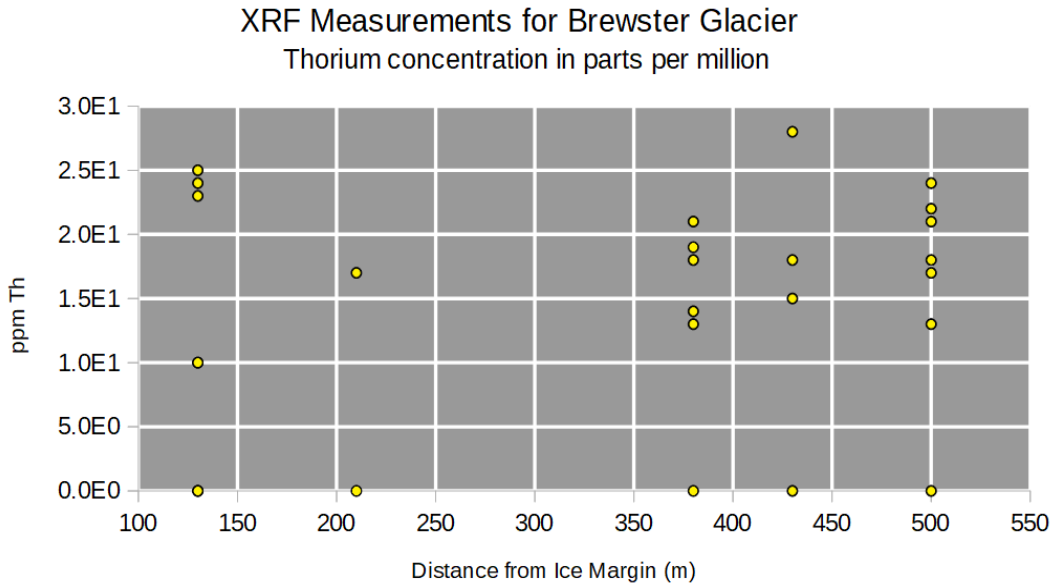
XRF Measurements for Brewster Glacier
Thorium concentration in parts per million
ppm Th
3.0E1
2.5E1
2.0E1
1.5E1
1.0E1
5.0E0
0.0E0
100
150
200
250
300
350
400
450
500
550
Distance from Ice Margin (m)

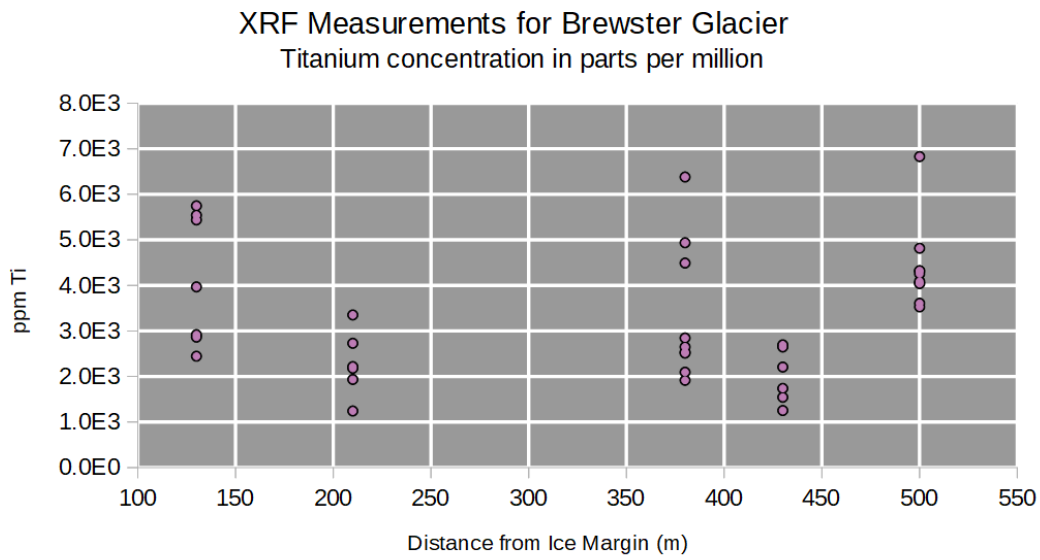
XRF Measurements for Brewster Glacier
Titanium concentration in parts per million
ppm Ti
8.0E3
7.0E3
6.0E3
5.0E3
4.0E3
3.0E3
2.0E3
1.0E3
0.0E0
100
150
200
250
300
350
400
450
500
550
Distance from Ice Margin (m)

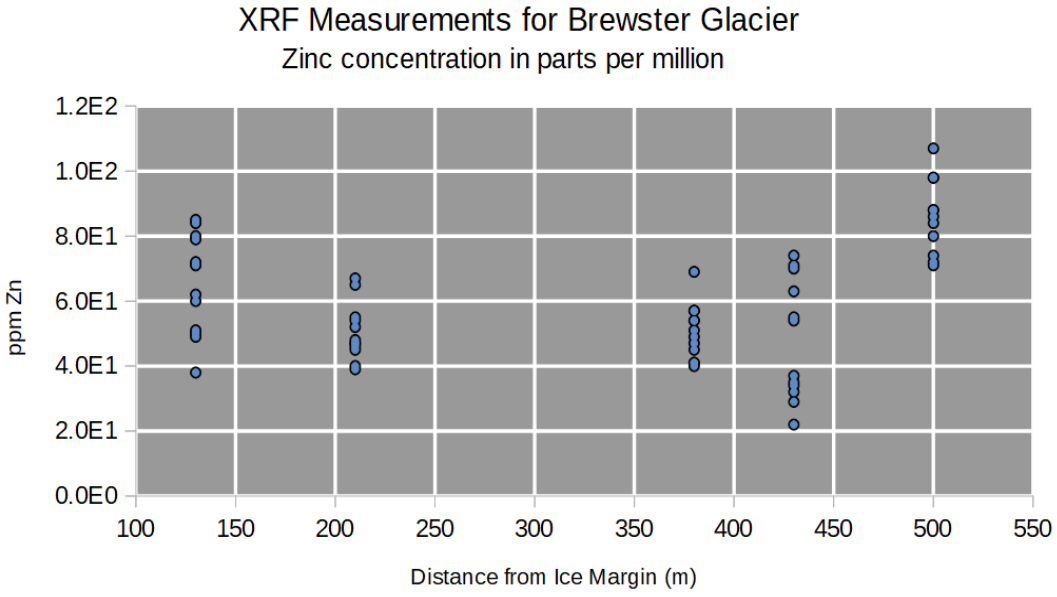
XRF Measurements for Brewster Glacier
Zinc concentration in parts per million
ppm Zn
1.2E2
1.0E2
8.0E1
6.0E1
4.0E1
2.0E1
0.0E0
100
150
200
250
300
350
400
450
500
550
Distance from Ice Margin (m)

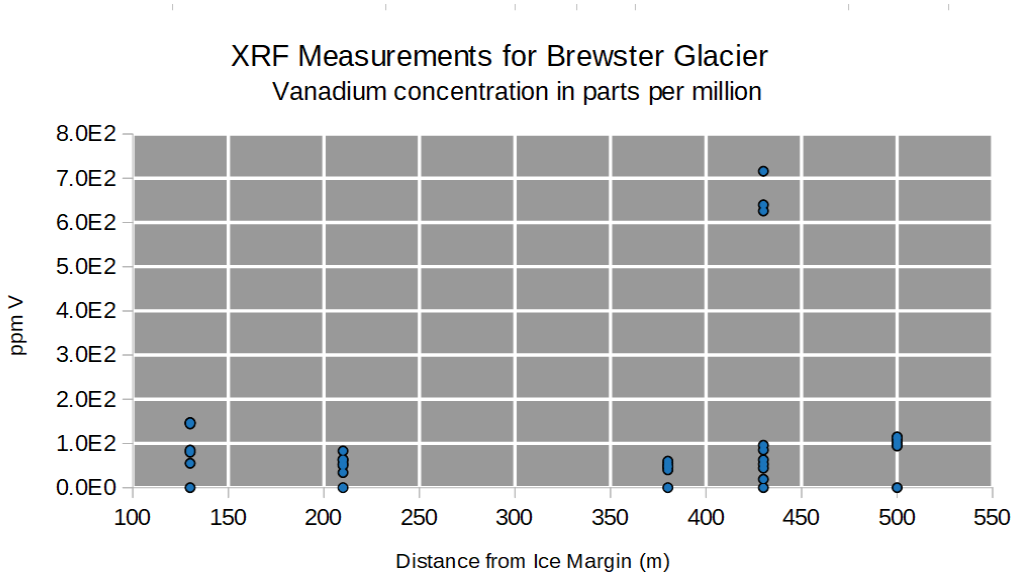
XRF Measurements for Brewster Glacier
Vanadium concentration in parts per million
ppm V
8.0E2
7.0E2
6.0E2
5.0E2
4.0E2
3.0E2
2.0E2
1.0E2
0.0E0
100
150
200
250
300
350
400
450
500
550
Distance from Ice Margin (m)

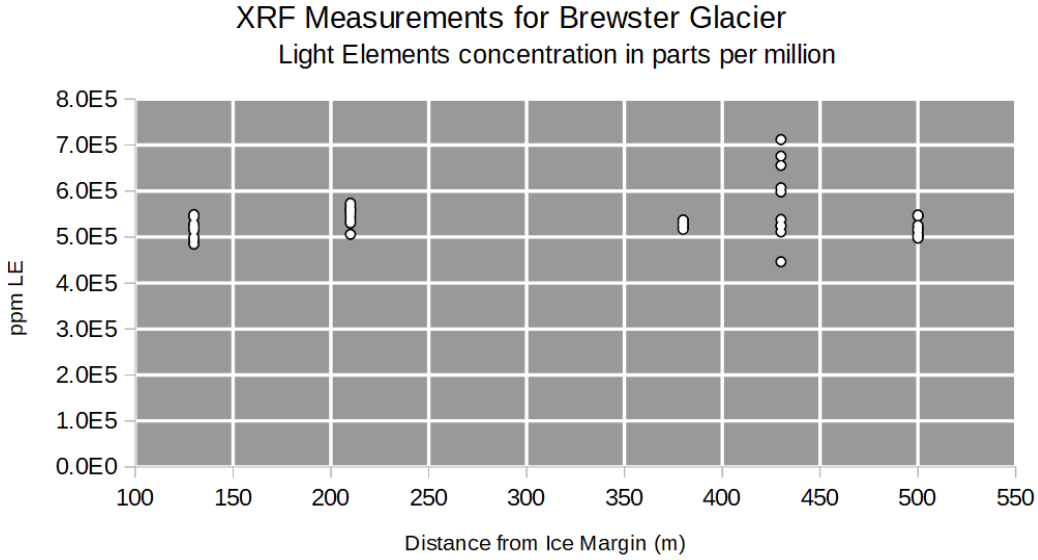
XRF Measurements for Brewster Glacier
Light Elements concentration in parts per million
ppm LE
8.0E5
7.0E5
6.0E5
5.0E5
4.0E5
3.0E5
2.0E5
1.0E5
0.0E0
100
150
200
250
300
350
400
450
500
550
Distance from Ice Margin (m)

9.8. XRF Raw Data

XRF Raw Data as averaged for each sample from twelve separate readings, six at the preset voltage and six at the higher 50kV setting.

Reading #	B01 Avg	B02 Avg	B03 Avg	B04 Avg	B05 Avg
Method Name	Geochem(2)	Geochem(2)	Geochem(2)	Geochem(2)	Geochem(2)
Collimation Status	No	No	No	No	No
Units	ppm	ppm	ppm	ppm	ppm
Al Concentration	89487.83	71614.83	64829.17	73159.50	94171.33
Al Error 1s	564.00	456.50	472.00	486.17	559.17
Si Concentration	329376.83	298829.83	374938.83	335827.83	315040.50
Si Error 1s	697.83	587.67	724.83	680.50	687.50
K Concentration	24283.17	15987.83	8407.00	10214.83	31870.83
K Error 1s	70.83	47.83	39.83	42.33	88.17
Ca Concentration	3874.33	3688.83	3260.67	5222.83	12579.00
Ca Error 1s	38.83	30.00	33.50	36.50	53.50
Ti Concentration	4061.50	2015.17	2426.00	2276.67	4159.50
Ti Error 1s	68.17	47.00	56.50	54.00	69.50
V Concentration	106.33	60.00	49.50	57.83	109.67
V Error 1s	7.67	5.67	6.83	6.17	8.00
Mn Concentration	485.50	331.50	580.00	455.33	438.33
Mn Error 1s	12.50	9.00	12.50	11.33	11.83
Fe Concentration	46268.00	21426.00	21998.50	23600.50	30490.17
Fe Error 1s	116.00	59.67	65.67	68.67	87.83
Ni Concentration	21.83	11.00	14.00	12.33	22.83
Ni Error 1s	3.00	3.67	3.00	4.83	3.00
Cu Concentration	36.00	10.83	15.17	16.50	11.67
Cu Error 1s	2.17	2.33	2.00	2.00	2.00
Zn Concentration	90.33	47.83	51.00	51.17	72.00
Zn Error 1s	2.00	1.50	1.83	2.00	2.00
Rb Concentration	137.33	74.33	49.17	56.00	145.67
Rb Error 1s	1.00	0.83	1.00	1.00	1.00
Sr Concentration	222.50	304.83	338.17	297.83	344.17
Sr Error 1s	1.00	1.50	1.50	1.33	1.83
Y Concentration	25.33	11.00	14.00	13.83	22.33
Y Error 1s	1.00	0.50	1.00	1.00	1.00
Zr Concentration	157.17	119.00	174.83	115.00	226.67
Zr Error 1s	1.00	1.00	1.00	1.00	1.50

Reading #	B01 Avg	B02 Avg	B03 Avg	B04 Avg	B05 Avg
Method Name	Geochem (2)	Geochem (2)	Geochem (2)	Geochem (2)	Geochem (2)
Nb Concentration	13.17	4.67	8.00	6.17	11.00
Nb Error 1s	1.00	8.83	1.00	1.00	1.00
Pb Concentration	44.17	4.00	13.83	11.83	12.33
Pb Error 1s	1.50	9.67	1.00	1.00	1.00
Th Concentration	19.17	10.17	17.33	2.83	15.33
Th Error 1s	3.00	46.00	2.83	100.83	23.33
LE Concentration	500883.00	585371.83	522810.50	548444.17	508835.00
LE Error 1s	959.50	769.83	876.33	866.17	977.67

Reading #	B01 Avg	B02 Avg	B03 Avg	B04 Avg	B05 Avg
Method Name	Geochem (2)-50kV	Geochem (2)-50kV	Geochem (2)-50kV	Geochem (2)-50kV	Geochem (2)-50kV
Collimation Status	No	No	No	No	No
Units	ppm	ppm	ppm	ppm	ppm
Al Concentration	84393.50	76711.83	62508.33	72942.00	90346.00
Al Error 1s	650.00	583.17	526.33	574.00	659.33
Si Concentration	315486.83	309254.17	372401.33	345358.83	306070.83
Si Error 1s	1550.00	1436.83	1719.83	1610.33	1457.33
K Concentration	22153.50	17757.50	8060.50	10384.83	29593.33
K Error 1s	117.50	91.50	51.33	62.17	150.17
Ca Concentration	3471.50	4119.67	3057.17	5226.00	11440.83
Ca Error 1s	38.17	37.17	34.50	43.83	69.00
Ti Concentration	3248.33	0.00	2634.67	0.00	661.33
Ti Error 1s	837.67	148.83	707.17	144.33	347.33
V Concentration	0.00	330.33	0.00	0.00	0.00
V Error 1s	355.17	256.00	355.83	343.83	357.17
Mn Concentration	0.00	368.00	0.00	407.67	69.33
Mn Error 1s	446.17	253.50	379.00	167.67	389.83
Fe Concentration	41555.67	23014.00	21047.00	23499.50	27664.33
Fe Error 1s	335.67	223.00	222.83	236.33	262.67
Ni Concentration	0.00	0.00	0.00	0.00	0.00
Ni Error 1s	82.00	75.17	82.50	80.33	83.33
Cu Concentration	0.00	0.00	0.00	0.00	0.00
Cu Error 1s	78.67	70.67	78.50	78.00	79.17

Reading #	B01 Avg	B02 Avg	B03 Avg	B04 Avg	B05 Avg
Method Name	Geochem (2)-50kV	Geochem (2)-50kV	Geochem (2)-50kV	Geochem (2)-50kV	Geochem (2)-50kV
Zn Concentration	83.67	48.17	49.83	49.67	58.17
Zn Error 1s	11.17	9.17	9.67	9.67	10.33
Rb Concentration	123.67	82.17	47.67	58.33	134.00
Rb Error 1s	4.00	2.67	2.33	2.50	4.00
Sr Concentration	192.00	313.50	316.50	290.67	298.00
Sr Error 1s	4.00	4.67	5.17	4.67	5.17
Y Concentration	20.00	13.67	12.83	13.50	18.50
Y Error 1s	2.00	1.50	1.00	1.33	1.50
Zr Concentration	133.33	128.33	169.00	115.33	200.33
Zr Error 1s	3.00	3.00	3.33	3.00	3.83
Nb Concentration	11.33	6.00	6.67	5.83	10.00
Nb Error 1s	1.00	1.00	1.00	1.00	1.00
Ta Concentration	100.83	39.50	43.00	54.83	82.33
Ta Error 1s	88.67	222.83	245.83	230.83	194.83
Pb Concentration	40.00	4.00	15.00	10.33	11.67
Pb Error 1s	17.67	43.17	4.00	24.33	16.83
Th Concentration	9.00	3.00	3.17	0.00	7.67
Th Error 1s	12.50	42.33	48.33	68.17	24.50
LE Concentration	527966.50	566675.33	529054.50	540972.17	532016.33
LE Error 1s	2295.83	1993.17	2168.83	2122.50	2199.83

9.8.1. XRF Error

XRF Instrument Measurement Error			
Element	Average Capture Error 1s (ppm)	Element	Average Capture Error 1s (ppm)
K	76.1666	**Cu**	39.5500
Ca	41.5000	**Ni**	42.0833
Si	1115.2666	**Pb**	99.2666
Mn	169.3333	**Th**	754.3666
Al	553.0666	**Ti**	248.0500
Fe	167.8333	**Zn**	5.9333
Zr	2.1666	**V**	170.2333
Y	1.1833	**Le**	511.6333
Rb	2.0333		
Sr	3.0833		
Nb	1.7833		
Ta	32.6923		

9.9. Sampling Site Coordinates

Sampling Site Coordinate Locations			
Sample ID	**Latitude**	**Longitude**	**Elevation (m)**
B_01	44° 4'59.37"S	169°26'16.92"E	1,863
B_02	44° 4'58.37"S	169°26'15.11"E	1,838
B_03	44° 4'57.22"S	169°26'13.70"E	1,823
B_04	44° 4'55.81"S	169°26'7.39"E	1,762
B_05	44° 4'55.47"S	169°26'4.07"E	1,746
B_06	44° 4'54.80"S	169°26'2.96"E	1,740
B_07	44° 4'53.53"S	169°25'59.85"E	1,736
FJCR_03	43°27'1.27"S	170° 9'19.14"E	1,708
FJCR_06	43°27'11.06"S	170° 9'23.98"E	1,564
FJCR_11	43°27'8.43"S	170° 9'33.40"E	1,480
FJCR_12	43°27'10.82"S	170° 9'41.45"E	1,336
FJCR_01	43°27'10.37"S	170° 9'48.57"E	1,261
FJCR_09	43°27'9.20"S	170°10'1.08"E	1,184
FJCR_10	43°27'9.00"S	170°10'6.96"E	1,114
FJCR_07	43°27'23.28"S	170°10'14.02"E	828
FJCR_08	43°27'16.16"S	170°10'38.25"E	637